

**Using a small expansion chamber to characterise ice  
nucleation by high-latitude mineral dusts and volcanic ash**

Leon King

Submitted in accordance with the requirements for the degree of Doctor of Philosophy

The University of Leeds  
School of Earth and Environment

May 2024

## **Declaration**

The candidate confirms that the work submitted is his own, except where work which has formed part of jointly authored publications has been included. The contribution of the candidate and the other authors to this work has been explicitly indicated below. The candidate confirms that appropriate credit has been given within the thesis where reference has been made to the work of others.

**Ponsonby, J., King, L., Murray, B. J. and Stettler, M. E. J.: Jet aircraft lubrication oil droplets as contrail ice-forming particles, *Atmos. Chem. Phys.*, 24(3), 2045–2058, doi:10.5194/acp-24-2045-2024, 2024.** This publication includes measurements of the temperature and humidity conditions at which citric acid aerosol activates to liquid droplets or homogeneously freezes. These measurements of citric acid were performed by Leon King as part of chapter 2 of this thesis and were published in the above publication as method justification and for comparisons with other results.

This copy has been supplied on the understanding that it is copyright material and that no quotation from the thesis may be published without proper acknowledgement.

The right of Leon King to be identified as Author of this work has been asserted by him in accordance with the Copyright, Designs and Patents Act 1988.

© 2019 The University of Leeds and Leon King

## **Acknowledgements**

First and foremost, I would like to thank my supervisors Benjamin Murray and Ryan Neely III for their support and guidance throughout the duration of my project; this thesis would not exist without them. Also, the members of the University of Leeds ice nucleation group for their company and assistance: Mike Adams, Mark Tarn, Sarah Barr, Martin Daily, Alberto Sanchez-Marroquin, Grace Porter, Elena Maters, Sandy James, Seb Sikora, Beth Wyld, Joe Robinson, Erin Raif, Katie Thompson, Polly Foster, Nina Kinney and Ross Herbert. I would also like to thank the Cohen Lab staff for supporting my lab work, in particular Andy Hobson for his general day-to-day assistance and Lesley Neve for XRD measurements. Thank you as well to the NERC Panorama DTP for funding my project.

Aside from those at the University of Leeds, I am also thankful to have worked with people from other institutions. From Karlsruhe Institute of Technology, I would like to thank Ottmar Möhler, Larissa Lacher, Franziska Vogel, Pia Boger, Jens Nadolny and Nicole Büttner as well as Achim Hobl from Bilfinger Noell GmbH for their help with all things related to the PINE instrument. From Imperial College London, I would like to thank Joel Ponsonby and Marc Stettler for making use of the methods I developed during my project and applying them to your own science.

I am also grateful for those who have been friends to me during this time, to the many fellow members of SEE who have provided me with company and entertainment during lunch breaks and to my past housemates who made my life at home, particularly during lockdown, all the more entertaining.

I would like to give a special thank you to Lena Chen for being a constant source of comfort and encouragement and helping me to stay mentally positive during the toughest periods of this project. Also, a big thank you to my family for their lifelong support, my mum, dad, brother and sister.

**Abstract**

Ice-nucleating particles (INPs) can influence the radiative properties of clouds and therefore climate. There are many different types of INPs including mineral dusts, biological aerosols and combustion aerosols, these different types can nucleate ice at different temperatures and through different mechanisms. Therefore, an understanding of the ice-nucleating activity (INA) of each of the different types of INPs is needed to fully understand their effect on the climate system. In this thesis I use the Portable Ice Nucleation Experiment (PINE), a small cloud expansion chamber, to characterise the INA high-latitude mineral dusts and volcanic ashes.

In order to achieve this, I first characterise the temperature inside the PINE and determine that the calculated adiabatic temperature is an accurate representation of the temperature inside the PINE on the timescales and conditions used in this thesis. Measurements of the INA of high-latitude dusts from Greenland and Alaska show that they have different INAs from one another. By using the PINE to measure the INA of volcanic ash samples aged in water, aged in acid and unaged, I find that the ageing generally decreases the INA of the ashes, but to varied extents depending on the ash and the type and length of ageing. The INA results for both high-latitude dust and volcanic ash are consistent with measurements of similar samples at warmer temperatures using a cold stage measurement technique. These new PINE measurements extend the previously existing measurements to lower temperatures than was possible using the cold stage technique. The results of this thesis highlight the differences between different INP types and provide underpinning knowledge that might be used in the future to predict the effect that high-latitude dusts and volcanic ashes may have on the radiative properties of clouds.

<b>DECLARATION</b>	<b>2</b>
<b>ACKNOWLEDGEMENTS</b>	<b>3</b>
<b>ABSTRACT</b>	<b>4</b>
<b>FIGURES</b>	<b>9</b>
<b>TABLES</b>	<b>18</b>
<b>LIST OF ABBREVIATIONS</b>	<b>19</b>
<b>1 INTRODUCTION</b>	<b>20</b>
1.1 CLOUDS & THEIR IMPACT ON CLIMATE	20
1.2 ICE NUCLEATION	22
1.2.1 Homogeneous classical nucleation theory	22
1.2.2 Heterogeneous classical nucleation theory	25
1.2.3 The singular approximation of heterogeneous ice nucleation	25
1.3 MODES OF ATMOSPHERIC ICE NUCLEATION	29
1.4 TYPES & SOURCES OF ICE-NUCLEATING PARTICLES	31
1.4.1 Mineral dust	32
1.4.2 Bioaerosols	33
1.4.3 Black carbon	34
1.4.4 Volcanic ash	34
1.5 INSTRUMENTS FOR MEASUREMENTS OF ICE NUCLEATION	35
1.5.1 Cloud expansion chambers	35
1.5.2 Continuous flow diffusion chambers	36
1.5.3 Cold stages	39
1.5.4 Comparing the results of different ice nucleation measurement methods	40
1.6 THE PORTABLE ICE NUCLEATION EXPERIMENT CHAMBER	41
1.7 THESIS OBJECTIVES AND OUTLINE	43

1.8	PUBLICATION STRATEGY	44
1.9	OTHER WORK – PONSONBY OIL PAPER	45
1.10	REFERENCES	47
<b>2</b>	<b>CHARACTERISING TEMPERATURE IN A PORTABLE CLOUD EXPANSION CHAMBER DESIGNED FOR COUNTING ICE-NUCLEATING PARTICLES</b>	<b>86</b>
2.1	BACKGROUND	86
2.2	METHODS	87
2.2.1	Test aerosol preparation and size distributions	88
2.2.2	Portable Ice Nucleation Experiment (PINE)	91
2.2.3	Adiabatic temperature calculation	92
2.2.4	Relative humidity calculation	94
2.2.5	Active site density	94
2.3	RESULTS & DISCUSSION	96
2.3.1	Comparison of the measured and dry adiabatic temperatures	96
2.3.2	Onset of cloud particle formation using non-ice-nucleating aerosol	99
2.3.3	The optimal expansion flow rate	102
2.3.4	Homogeneous ice nucleation in cloud droplets	104
2.3.5	Heterogeneous ice nucleation of K-feldspar	107
2.4	CONCLUSIONS	110
2.5	APPENDIX	111
2.5.1	Aerosol particle transmission efficiency	111
2.5.2	Thermocouple response time	113
2.5.3	Relative humidity at the start of expansions	115
2.6	REFERENCES	117

<b>3</b>	<b>USING A SMALL CLOUD EXPANSION CHAMBER TO CHARACTERISE THE ICE-NUCLEATING ACTIVITY OF NORTHERN HIGH-LATITUDE MINERAL DUSTS</b>	<b>122</b>
3.1	BACKGROUND	122
3.2	MATERIALS AND METHODS	126
3.2.1	High-latitude dust sample collection	126
3.2.2	Mineral composition of samples	126
3.2.3	Ice nucleation measurements	128
3.3	SAMPLE CHARACTERISATION	128
3.3.1	Sample mineralogy	128
3.3.2	Aerosol size distributions	129
3.4	RESULTS & DISCUSSION	131
3.4.1	High-latitude dust ice-nucleating activities	131
3.4.2	Comparison to cold stage measurements	138
3.4.3	High-latitude dust ice-nucleating activity parameterisation	141
3.5	CONCLUSIONS	147
3.6	APPENDIX	149
3.7	REFERENCES	155
<b>4</b>	<b>CHARACTERISING THE ICE-NUCLEATING ACTIVITY OF VOLCANIC ASH AND THE EFFECTS OF WATER AND ACID AGING</b>	<b>161</b>
4.1	CONTRIBUTIONS STATEMENT	161
4.2	BACKGROUND	161
4.3	METHODS	165
4.3.1	Volcanic ash samples and ageing process	165
4.3.2	PINE-1B ice nucleation measurements	166
4.3.3	Droplet freezing assay measurements	166

4.4	RESULTS & DISCUSSION	167
4.4.1	Sample aerosol and expansion cloud size distributions	167
4.4.2	Determination of volcanic ash ice-nucleating activity	172
4.4.3	Effect of ageing on volcanic ash ice-nucleating ability	174
4.4.4	Comparison between PINE-1B and $\mu$ L-NIPI measurements	176
4.5	CONCLUSIONS	180
4.6	APPENDIX	181
4.7	REFERENCES	190
<b>5</b>	<b>CONCLUSIONS</b>	<b>194</b>
5.1	OVERVIEW	194
5.1.1	Objective 1: The use and development of tools and methods for measuring ice nucleation – the PINE-1B instrument	194
5.1.2	Objective 2: Use PINE to characterise the ice-nucleating activity of high-latitude mineral dusts across a range of temperatures relevant for mixed-phase clouds	197
5.1.3	Objective 3: Use PINE to characterise the ice-nucleating activity of volcanic ash and the effect of aging processes	199
5.2	PROJECT CONCLUSIONS	200
5.2.1	PINE-1B temperature measurement range and consistency with cold stage measurements	200
5.2.2	Limitations of PINE	201
5.3	REFERENCES	203

## Figures

**Figure 1.1:** Illustration of the 10 different genera of clouds and the typical altitudes at which they are seen in temperate regions (WMO, 2017). The z axis refers to altitude above sea level. Figure 1.3 from Lohmann et al. (2016), reproduced with permission of Cambridge University Press through PLSclear. 20

**Figure 1.2:** Illustration of cloud responses to Earth surface warming. Figure 7.9 from Forster et al. (2023). 21

**Figure 1.3:** Plot of Gibbs free energy for the formation of an ice cluster (black line) in supercooled water at  $-20\text{ }^{\circ}\text{C}$ . Blue and red lines respectively show the individual surface and volume terms as given in Equation 1.1. Ice density of  $919\text{ kg m}^{-3}$  (Carnahan et al., 2021) and  $\gamma$  of  $25\text{ mJ m}^{-2}$  (Piaggi et al., 2022) used for calculations. Dotted lines indicate the critical cluster radius and Gibbs free energy given by the maximum Gibbs free energy for cluster formation. 24

**Figure 1.4:** Images showing the locations (black circles) at which ice nucleation began to occur in droplets placed on microcline feldspar surfaces. Below each image is a plot showing the nucleation temperature of each individual freezing measurement run and above the characteristic nucleation temperature,  $T_c$ , is given, which is the average temperature at which each droplet froze. The numbers at each circle give the individual runs in which nucleation originated at that site. The bracketed numbers in the top right of the images are the cleavage planes. Figure 3 from Holden et al. (2019). 28

**Figure 1.5:** Diagram showing the main different modes of atmospheric ice nucleation and the temperature and relative humidity conditions at which they can occur. Figure 1-1 from Kanji et al., (2017). 29

**Figure 1.6:** Plot showing estimated global average immersion mode ice-nucleating particle concentrations of different types of atmospheric aerosol as a function of temperature. Figure 19 from Murray et al. (2012). 31

**Figure 1.7:** Map showing erodible soil fraction across the globe. Figure 1 from Groot Zwaaftink et al. (2016). 32

**Figure 1.8:** Schematic showing the AIDA facility. Figure 1 from Wagner et al. (2009). 36

**Figure 1.9:** Schematic of the Zurich ice nucleation chamber, a CFDC instrument. Figure 2 from Stetzer et al. (2008). 37

**Figure 1.10:** Diagram showing the  $\mu\text{L}$ -NIPI cold stage instrument. Figure 1 from Whale et al. (2015). 39

**Figure 1.11:** Photograph of a commercial PINE instrument making continuous INP measurements in Oklahoma. Side panels are removed to show the internal workings of the PINE. Figure A7 from Möhler et al. (2021). 42

**Figure 1.12:** Plot showing the temperature and relative humidity with respect to ice conditions under which  $\sim 100$  nm diameter jet lubrication oil droplets activated to cloud droplets measured using the PINE-1B.  $T_{\text{in}}$  is the average initial temperature at the start of expansions for each set of measurements. Adapted from Figure 4 (a) from Ponsonby et al. (2024). 46

**Figure 2.1:** Schematic of the experimental setup used for measurements in this study. Compressed air was used to fill a  $0.73 \text{ m}^3$  aerosol chamber with sample. The size distribution of the aerosol sample in the chamber from  $0.01$  to  $20 \mu\text{m}$  was measured by combining measurements from a TSI model 3938 SMPS and a TSI model 3321 APS. The PINE-1B system measured INP concentrations in the chamber as described in the text. Valves and MFCs were used to control the direction and rate of the various flows through the system. 88

**Figure 2.2:** Examples of aerosol size distributions measured by APS and SMPS of citric acid and K-feldspar test aerosols. APS and SMPS measured diameters were converted into volume equivalent sphere diameters as in Möhler et al, (2008) in order to compare the two different instruments. Grey points show the measurements which were not used in further analysis due to the overlap between the APS and SMPS size ranges. 90

**Figure 2.3:** Plot of an expansion using K-Feldspar aerosol to illustrate the operation of PINE and show the difference between the measured and calculated adiabatic temperatures. Dashed lines show the conditions calculated according to an adiabatic expansion while solid lines show the conditions measured in the case of temperature and pressure and calculated from these measurements in the case of  $\text{RH}_i$ . Top, middle and bottom temperature lines refer to the positions of the thermocouples inside the PINE chamber. Blue points represent individual particles measured by the OPC. Vertical dotted

line indicates the time at which cloud particles are first measured by the OPC, referred to as the onset. 97

**Figure 2.4:** Plot showing the  $RH_i$  and temperature conditions under which cloud particle formation onset is observed. Each individual point represents a single expansion at 4.0 slpm such as the one shown in Figure 2.3. Solid circles represent conditions calculated according to a dry adiabatic expansion while crossed squares represents conditions calculated from temperature and pressure measurements in the chamber. Red points represent citric acid aerosol while black points represent smoke aerosol, green points represent ambient aerosol measured by the PINE-04-03. Solid blue line represents water saturation (100 %  $RH_w$ ) conditions, dashed green line represents parameterisation of homogeneous ice nucleation according to Koop et al. (2000). Error bars represent conditions at  $\pm 0.5$  seconds from the time at which onset is observed. Grey dotted lines represent calculated dry adiabatic conditions through expansions. 100

**Figure 2.5:** Plot showing the adiabatic  $RH_i$  at the onset of cloud droplet activation of citric acid aerosol relative to water saturation  $RH_i$  for different expansion flow rates. The black dotted line represents a ratio of 1.0. Coloured points represent individual expansions. Box and whisker plots include all expansions at a given flow rate, grey shaded box area represents 25 to 75 %, horizontal black line represents mean value, and whiskers span 5 to 95 %. 102

**Figure 2.6:** Illustration showing the conditions in the PINE chamber during the expansions measuring the homogeneous ice nucleation of citric acid aerosol. Solid blue line represents water saturation (100 %  $RH_w$ ) conditions, dashed red line represents the trajectory of the conditions through the expansion, with arrows indicating the direction with time. Blue shaded area represents the temperature range in which homogeneous ice nucleation is expected (defined as 0.1 to 50 % of droplets frozen) to occur based upon the parameterisation from Tarn et al. (2021), assuming liquid particles with a diameter of 2  $\mu\text{m}$ . Blue circle represents expected conditions for the formation of liquid droplets and grey hexagon for homogeneous ice nucleation. 105

**Figure 2.7:** Plot showing the homogeneous ice nucleation onset temperatures for citric acid aerosol. Solid circle points represent conditions calculated according to an adiabatic expansion while crossed square points represents conditions calculated from temperature and pressure measurements in the chamber. Coloured shaded areas represent the temperature range in which homogeneous ice nucleation is expected to occur (defined as

0.1 to 50 % of droplets frozen) based upon three different parameterisations for homogeneous ice nucleation (Espinosa et al., 2016; Koop and Murray, 2016; Tarn et al., 2021), assuming liquid particles with a diameter of 2  $\mu\text{m}$ . 106

**Figure 2.8:** Size distribution of particles measured by the Welas OPC during an expansion using K-feldspar test aerosol at expansion starting temperature of  $-13\text{ }^{\circ}\text{C}$  and flow rate of 4.0 slpm. Black dashed line indicates the ice diameter threshold; all particles larger than this threshold were considered ice crystals and all particles smaller than this threshold were considered not ice crystals. 108

**Figure 2.9:** Plot showing the surface area density of active sites as a function of adiabatic temperature for K-Feldspar aerosol. Each point represents a measurement from a single expansion. The different shapes for the red points represent different surface area concentrations of K-Feldspar aerosol in the aerosol chamber during measurements. Purple line represents a parameterisation for K-feldspar by Harrison et al. (2019) and purple shaded area represents standard deviation of the parameterisation. The temperature (x-axis) uncertainty for adiabatic points represents adiabatic temperatures at  $\pm 0.5$  seconds from the minimum expansion temperature. Uncertainty for active site density (y-axis) is calculated from the uncertainty associated with the counting statistics of ice particles during expansions. 109

**Figure 2.10:** Plot showing **a)** aerosol size distribution of K-feldspar aerosol measured by the APS from the aerosol chamber and between the diffusion driers and the PINE chamber inlet. **b)** Transmission efficiency of particles from the aerosol chamber to the PINE chamber as a function of the volume equivalent diameter, measured using the APS. Horizontal dashed line shows a 100 % transmission efficiency where no particles are lost. 112

**Figure 2.11:** **a)** Comparison between the temperature measurements from the bottom PINE-1B gas thermocouple and an additional wire thermocouple inserted into the bottom of the PINE chamber during 4 expansions. The first two expansions were performed at a flow rate of 2.0 slpm and the second two at 4.0 slpm. **b)** Rate of temperature change for the two thermocouples averaged over 10 seconds. 114

**Figure 2.12:** Plot showing the effect of introducing a pause before expansions has on the onset  $\text{RH}_i$  of homogeneous freezing of citric acid haze droplets, calculated from temperature and pressure measurements in the PINE-1B chamber. Each point represents a single expansion with a starting temperature of  $-40\text{ }^{\circ}\text{C}$  and an expansion flow rate of

2.0 slpm. Error bars represent the standard deviation of the results at 0 minutes, equal to  $\pm 0.75\%$  RH. 116

**Figure 3.1:** Map showing locations of known high-latitude dust sources. Brown and green stars highlight the Copper River Valley, Alaska, and Kangerlussuaq, Greenland, respectively. Adapted from figure 1 from Meinander et al. (2022) 123

**Figure 3.2:** **a)** MODIS Aqua satellite image of dust plume from the Copper River valley on 04/10/2012, taken from figure 8 from Bullard et al. (2016). **b)** Photograph showing airborne dust at the surface at Kangerlussuaq, photograph taken by Bethany Wyld. 125

**Figure 3.3:** Sampling locations of the **a)** Copper River ( $60^{\circ}27'43''\text{N}$   $145^{\circ}02'26''\text{W}$ ) and **b)** Kangerlussuaq ( $67^{\circ}00'26''\text{N}$   $50^{\circ}40'53''\text{W}$ ) surface sediments used in this study. Satellite images taken from Google Earth on 26/02/2024, maps include data from CNES/Airbus, Landsat/Copernicus, Maxar Technologies, TerraMetrics, IBCAO, Airbus and U.S. Geological Survey. 127

**Figure 3.4:** Example aerosol size distribution measurements of the Copper River and Kangerlussuaq dust samples in the aerosol chamber. The diameters measured by the SMPS and APS were converted to a volume-equivalent diameter to be merged (Möhler et al., 2008). Grey APS points are measurements which were not used in further analysis. 130

**Figure 3.5:** Cloud size distributions measured by the Welas OPC during PINE expansions with **a)** too few ice crystals, **b)** a balance of ice crystals and liquid droplets, **c)** too many ice crystals. Dashed black line indicates size threshold above which all particles are counted as ice crystals. **a)** and **b)** are from expansions using the Kangerlussuaq sample and **c)** is from an expansion using the Copper River sample. 132

**Figure 3.6:** Time series of PINE expansion measurements of Copper River aerosol sample. Each point represents a single expansion. **a)** Minimum adiabatic temperature inside PINE chamber during expansion, **b)** concentration of ice particles measured by PINE during expansion, **c)** surface area concentration of sample in aerosol chamber measured by SMPS and APS, **d)** active site density, calculated by dividing  $N_{\text{ice}}$  by the aerosol surface area. Grey points indicate expansions which were not included in further analysis due to a lack of confidence in the measured number of ice crystals, explained further in main text. 134

**Figure 3.7:** INAs of Copper River and Kangerlussuaq HLD samples as measured by the PINE-1B. K-feldspar measurements from chapter 2 and parameterisation from Harrison et al. (2019) are shown for comparison. Each point represents a single expansion, apart from Kangerlussuaq points above -20 °C and at -33, -29 and -28 °C which are averages of multiple expansions. Error bars represent the estimated value uncertainties. For individual expansions, the adiabatic temperature uncertainty is calculated by combining the fractional thermocouple measurements uncertainty ( $\pm 0.1$  °C) with the fractional pressure measurement uncertainty ( $\pm 0.5$  %). The active site density uncertainty is calculated from the Poisson error of the number of ice crystals measured. For averaged points, the adiabatic temperature uncertainty is calculated using the same method as for individual expansions and the active site density uncertainty is the standard deviation of the averaged values. 135

**Figure 3.8:** INAs of **a)** Copper River and **b)** Kangerlussuaq samples in comparison to parameterisations of the activities of the mineral components of the samples (Harrison et al., 2019; Hiranuma et al., 2015). Parameterisations are scaled according to the compositions determined by QXRD. 137

**Figure 3.9:** Comparison of the INA of Copper River dust measured in this study using the PINE and by Barr et al. (2023) using the  $\mu$ L-NIPI, including heat treated samples. **a)**  $\mu$ L-NIPI data separated into size segregated filter samples, **b)** average of all size fractions. 139

**Figure 3.10:** Comparison of the INA of Kangerlussuaq dust measured in this study using the PINE and by Wyld et al. (preprint) using the  $\mu$ L-NIPI, including heated samples. 140

**Figure 3.11:** INAs of Copper River and Kangerlussuaq dusts measured by the PINE-1B and  $\mu$ L-NIPI (Barr et al., 2023; Wyld et al., preprint). Parameterisations of K-feldspar from Harrison et al. (2019) are scaled according to the quantities in each sample as determined by QXRD. 142

**Figure 3.12:** Best fits of Equation 3.2 to the data from **a)** Copper River, **b)** Kangerlussuaq. Red line shows the parameterisation which represents the INA of the HLD, and black and blue dashed lines show the two individual components which are added together produce the parameterisation. 143

**Figure 3.13:** Parameterisation of the INA of HLDs (Equation 3.2) fit to the data shown. Black and blue dashed lines show the two individual components which are added together produce the parameterisation. 144

**Figure 3.14:** a) Comparison of HLD INA measurements from multiple locations (Paramonov et al., 2018; Porter et al., 2020; Sanchez-Marroquin et al., 2020). b) Comparison of data from panel a to the HLD parameterisation from this study (Equation 3.2) and previous parameterisations of HLD (Sanchez-Marroquin et al., 2020) and LLD (Ullrich et al., 2017). 146

**Figure 3.15:** Duplicate of Figure 3.7 but without any averaging of data points. 154

**Figure 4.1:** Schematic showing the presence of volcanic ash particles in the eruption plume, eruption cloud and meteorological clouds following a volcanic eruption. From Maters et al. (2020). 162

**Figure 4.2:** Diagram showing the different classifications of volcanic rock based upon their silica and alkali content. From Le Maitre et al. (1989) 163

**Figure 4.3:** Aerosol size distribution measurements of the Fuego volcanic ash aged in acid for 24 hours, aerosolised in the aerosol chamber. Star points show the size distribution at the start of the measurements, when the sample is first aerosolised. Circle points show the size distribution after 4 hours of measurements. Hollow square points show the size distribution after 7 hours of measurements. The diameters measured by the SMPS and APS were converted to volume-equivalent diameters to be merged (Möhler et al., 2008). A diameter of  $0.4 \mu\text{m}$  was used below which only SMPS measurements were used and above which only APS measurements were used, as illustrated by the grey points which are the unused measurements. 168

**Figure 4.4:** Aerosol size distributions measured by SMPS and APS for each volcanic ash sample used in this study from when the surface area concentration of the sample was approximately  $1.0 \times 10^{-6} \text{ cm}^2 \text{ cm}^{-3}$ . Sample names in the legend indicate type of ash, type of ageing and length of ageing. 169

**Figure 4.5:** Aerosol surface area size distribution of unaged Astroni volcanic ash. Blue points are the values measured by the SMPS and APS and hollow black circles are the adjusted APS values. 170

**Figure 4.6:** Cloud size distributions measured by the Welas OPC during PINE-1B expansions using 24-hour acid-aged Fuego volcanic ash sample aerosol. Star points show

the size distribution at the start of the measurements, when the is first aerosolised. Circle points show the size distribution after 4 hours of measurements. Hollow square points show the size distribution after 7 hours of measurements. Dashed black line indicates size threshold above which all particles are counted as ice crystals. 171

**Figure 4.7:** Series of expansion measurements of Fuego volcanic ash aged in acid for 24 hours, each blue point represents a single expansion. **a)** concentration of ice crystals measured by the PINE-1B, **b)** ash aerosol surface area concentration measured by SMPS and APS, **c)** active site density of the ash calculated by dividing a by b. Vertical dashed lines at 14:10 and 19:00 enclose the period during which the value of  $n_s$  remains constant. Horizontal dashed lines in panel b enclose the range of aerosol surface area concentration values during the constant period of  $n_s$  values ( $2 \times 10^{-6}$  to  $1 \times 10^{-8} \text{ cm}^2 \text{ cm}^{-3}$ ). Error bars in panel a represent the uncertainty associated with the counting statistics of ice particles, error bars in panel b represent the 10 % uncertainty associated with the undercounting of particles by the APS, error bars in panel c represent the combination of the uncertainties in  $N_{\text{ice}}$  and aerosol surface area concentration. 173

**Figure 4.8:** Comparison of ice-nucleating ability of Fuego (FUE) (red), Astroni (AST) (blue) and Eyjafjallajökull (EYJ) (green) volcanic ashes and the effects of ageing in  $\text{H}_2\text{O}$  and  $\text{H}_2\text{SO}_4$ . Each box plot consists of all expansions with a minimum adiabatic temperature of  $-31.2 \pm 0.5 \text{ }^\circ\text{C}$  and ash sample surface area concentrations between  $2 \times 10^{-6}$  and  $1 \times 10^{-8} \text{ cm}^2 \text{ cm}^{-3}$ . Black diamonds represent the mean active site density and horizontal lines represent the median active site density. Coloured boxes represent the interquartile range of active site density values and whiskers show the range of values which were within 1.5 times of the interquartile range. Sample names indicate type of ash, type of ageing and length of ageing. 175

**Figure 4.9:** Comparison between the INA of unaged Fuego and Astroni volcanic ashes measured using the PINE-1B in this study (filled symbols) and the  $\mu\text{L-NIPI}$  by Fahy et al. (2022) (hollow symbols). 177

**Figure 4.10:** Comparison between the INA of unaged **a)** Fuego and **b)** Astroni volcanic ashes measured using the PINE-1B in this study (filled symbols) and  $\mu\text{L-NIPI}$  by Fahy et al. (2022) (hollow symbols). Sample names indicate type of ash, type of ageing and length of ageing. 178

**Figure 4.11:** Same as Figure 4.7 but for unaged Fuego volcanic ash. 181

<b>Figure 4.12:</b> Same as Figure 4.7 but for 10-minute water-aged volcanic ash.	182
<b>Figure 4.13:</b> Same as Figure 4.7 but for 24-hour water-aged Fuego volcanic ash.	183
<b>Figure 4.14:</b> Same as Figure 4.7 but for 1-hour acid-aged Fuego volcanic ash.	184
<b>Figure 4.15:</b> Same as Figure 4.7 but for 4-hour acid-aged Fuego volcanic ash.	185
<b>Figure 4.16:</b> Same as Figure 4.7 but for unaged Astroni volcanic ash.	186
<b>Figure 4.17:</b> Same as Figure 4.7 but for 10-minute water-aged Astroni volcanic ash.	187
<b>Figure 4.18:</b> Same as Figure 4.7 but for 10-minute acid-aged volcanic ash.	188
<b>Figure 4.19:</b> Same as Figure 4.7 but for unaged Eyjafjallajökull volcanic ash.	189

**Tables**

**Table 3.1:** Mineral composition of high-latitude dust samples from Copper River, Alaska and Kangerlussuaq, Greenland. Quantified using QRXD with relative intensity ratio using corundum reference. Samples were sieved to 45  $\mu\text{m}$  prior to analysis. The unknown % composition includes the minerals which were not able to be quantified, these unquantified minerals include amphiboles in both samples. 129

**Table 3.2:** Values used in Equation 3.2 to produce the parameterisation fits shown in Figure 3.12 and Figure 3.13. 145

**Table 3.3:** Key results for each expansion used in this study, each line represents a single expansion (a.k.a. run). Runs are not included if there was no distinguishable ice threshold or if the minimum adiabatic expansion temperature was below  $-36\text{ }^{\circ}\text{C}$  since the number of ice crystals could not be accurately determined (see Figure 3.5 and related text). Kan = Kangerlussuaq, CR = Copper River. 149

**List of abbreviations**

INP	Ice-Nucleating Particle
INA	Ice-Nucleating Activity
PINE	Portable Ice Nucleation Experiment
CRE	Cloud Radiative Effect
CNT	Classical Nucleation Theory
RH	Relative Humidity
PCF	Pore Condensation and Freezing
BC	Black Carbon
AIDA	Aerosol Interactions and Dynamics in the Atmosphere
OPC	Optical Particle Counter
CFDC	Continuous Flow Diffusion Chamber
$\mu$ LNIPI	microliter Nucleation by Immersed Particles Instrument
HLD	High-Latitude Dust
MFC	Mass Flow Controller
SMPS	Scanning Mobility Particle Sizer
APS	Aerodynamic Particle Sizer
LLD	Low-Latitude Dust
XRD	X-Ray Diffraction
QXRD	Quantitative X-Ray Diffraction

## 1 Introduction

### 1.1 Clouds & their impact on climate

Clouds are made up of liquid cloud droplets, solid ice crystals or a mix of both, known as mixed-phase clouds. Clouds form throughout the troposphere at different altitudes and under different conditions, which can lead to their different properties. Satellite measurements show that the global annual average cloud coverage is almost 70 % (Rossow and Schiffer, 1999). The World Meteorological Organisation splits clouds into low-, middle- and high-levels, the exact altitudes of these levels can vary due to different temperatures in different regions (WMO, 2017). The different genera of clouds and the levels at which they are typically seen are shown in Figure 1.1, with altitudes typical for a temperate region.

The cloud radiative effect (CRE) is the difference between the top of atmosphere radiative flux of the Earth with and without clouds, it therefore represents the radiative effect attributable to clouds (Ramanathan et al., 1989). The CRE is a balance between the cooling clouds cause by reflecting incoming shortwave radiation (an albedo effect) and the warming they cause by trapping outgoing longwave radiation (a greenhouse effect).

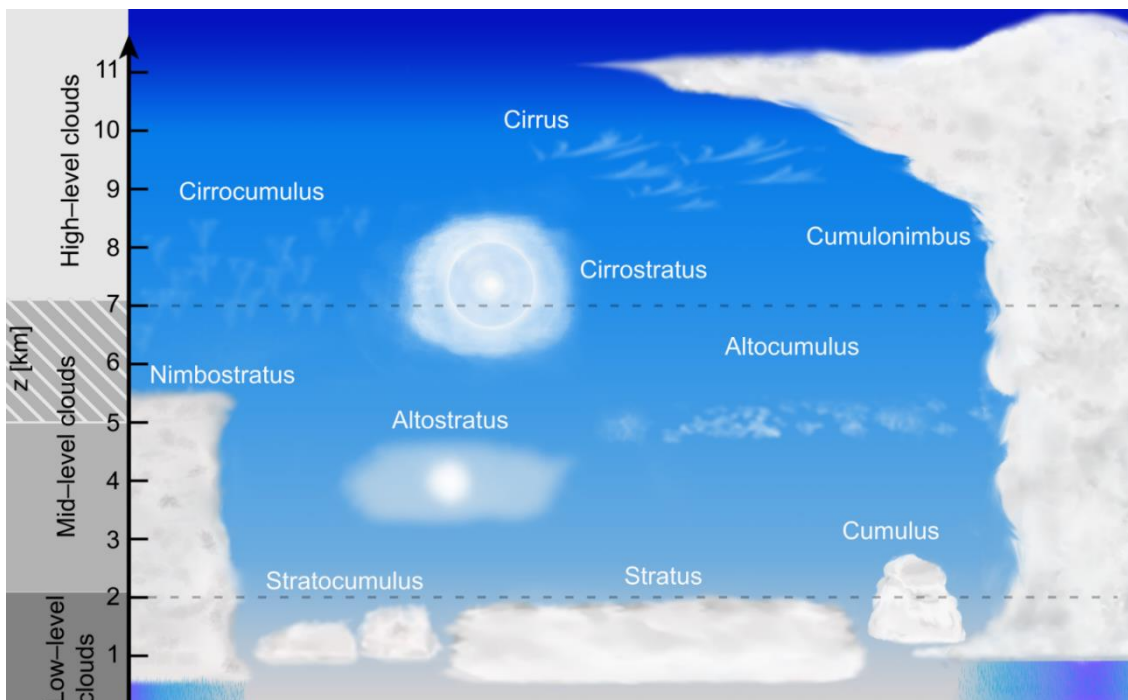


**Figure 1.1:** Illustration of the 10 different genera of clouds and the typical altitudes at which they are seen in temperate regions (WMO, 2017). The z axis refers to altitude above sea level. Figure 1.3 from Lohmann et al. (2016), reproduced with permission of Cambridge University Press through PLSclear.

The present-day global average CRE is estimated to be approximately  $-17 \text{ W m}^{-2}$  (Loeb et al., 2009), overall cooling the climate with the albedo effect outweighing the greenhouse effect. The net radiative effect of a cloud depends on its location within the atmosphere and its optical properties. The change in albedo caused by a cloud partly depends on the albedo at the Earth's surface under the cloud, for example over darker surfaces such as oceans the presence of a cloud will result in a greater increase in albedo than over brighter surfaces such as ice or snow (Schneider, 1972). Because of this, the CRE is dependent on the geographical location of cloud cover, with clouds at lower latitudes typically having a more negative radiative effect due to the Earth's surface having lower albedo. The amount of longwave radiation emitted by clouds depends on their cloud top temperature, with lower temperatures resulting in less emission, therefore clouds at higher altitudes with lower cloud top temperatures have a stronger greenhouse effect by more effectively trapping longwave radiation (Schneider, 1972). Aside from a cloud's location in the atmosphere, its optical properties can also influence its net radiative effect. The optical thickness of a cloud is a measure of how much radiation can pass through the cloud, with thicker clouds allowing less radiation through due to a mixture of reflection, scattering and absorption. The majority of the total global CRE is caused by low-level clouds due to their high optical thickness, while for mid- and high-level clouds, their net CRE depends on their optical thickness, with thicker clouds having a more negative CRE and thinner clouds having a slightly positive CRE (Chen et al., 2000; Hartmann et al., 1992).

The net cloud feedback is a combination of multiple different changes to cloud properties, locations and coverage that occur as a result of increasing surface temperature. Figure 1.2

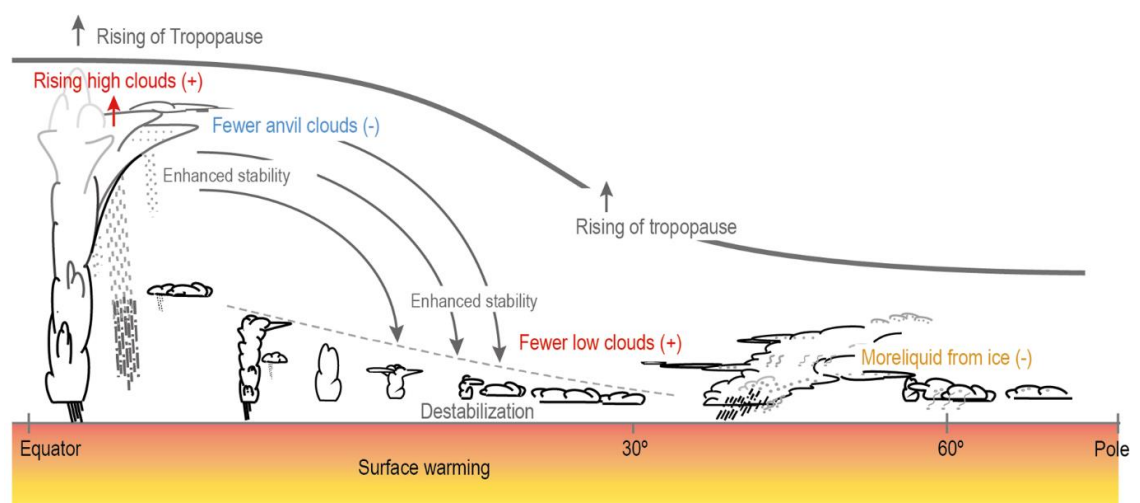


**Figure 1.2:** Illustration of cloud responses to Earth surface warming. Figure 7.9 from Forster et al. (2023).

(Forster et al., 2023) illustrates some of the main cloud feedbacks, some of which are positive such as increasing cloud top altitudes (Yoshimori et al., 2020), and some negative such as the increase in liquid water content in mixed-phase clouds (Murray et al., 2021). Overall, the net cloud feedback is estimated to be positive, but there is a high degree of uncertainty and spread between model simulations due to the complexity of the interplay between the multiple different feedbacks (Forster et al., 2023; Vial et al., 2013).

## **1.2 Ice nucleation**

In the atmosphere, cloud droplets can supercool to temperatures well below the melting point of ice. Cloud droplets will begin to freeze homogeneously at  $-33\text{ }^{\circ}\text{C}$  and below (Herbert et al., 2015), but they can heterogeneously freeze at higher temperatures if the right types of particles, known as ice-nucleating particles (INPs), are present. The freezing of cloud droplets can lead to a change in the optical properties and lifetime of a cloud (Lohmann and Feichter, 2005). As ice crystals nucleate in a cloud they will grow at the expense of liquid droplets via the Bergeron-Findeisen process since ice is the more stable phase at supercooled temperatures (Murphy and Koop, 2005). This process results in the cloud becoming composed of a smaller number of larger ice crystals, which decreases the albedo of the cloud and has a positive radiative effect (Lohmann and Feichter, 2005). Therefore, the way in which the liquid droplets in a cloud undergo ice nucleation, in particular the number of ice crystals that nucleate at a certain temperature, has an impact on the radiative effect of the cloud.

### **1.2.1 Homogeneous classical nucleation theory**

Homogenous ice nucleation occurs when liquid water freezes without the interference of a solid surface. For droplets on the micron scale, this occurs with increasing probability below about  $-33\text{ }^{\circ}\text{C}$  (Herbert et al., 2015). Supercooled water is metastable, meaning that it is a thermodynamically unstable phase, but is kinetically stable due to an energy barrier for transition to the thermodynamically stable phase of ice (Ickes et al., 2015). This energy barrier comes from the decrease in entropy when water molecules cluster together to form an ordered ice lattice. The formation of a small ice cluster within liquid water requires the creation of a surface between the ice and the water, which is endergonic, but at the same time the formation of stronger bonds between the molecules in the ice cluster is exergonic, and the number of these bonds increases with cluster volume. This results in the thermodynamics of ice nucleation being a balance between a surface and a volume factor,

as cluster size increases the surface area to volume ratio decreases, increasing the relative importance of the volume factor. The size at which the volume factor outweighs the surface factor is the critical cluster size, at this point the addition of further molecules to the cluster is exothermic, since the energy gained from forming the bonds outweighs the energy lost from creating new surface, and so ice growth becomes spontaneous. This is described in the equation for the Gibbs free energy of forming a cluster,  $\Delta G_{cl}$ , as shown:

$$\Delta G_{cl} = \underbrace{4\pi r^2 \gamma}_{\text{surface term}} - \underbrace{\frac{4\pi r^3}{3v} kT \ln S}_{\text{volume term}} \quad (\text{Eq. 1.1})$$

Where  $r$  is the cluster radius,  $\gamma$  is the interfacial energy between water and ice,  $v$  is the volume of a water molecule in the condensed ice phase,  $k$  is the Boltzmann constant,  $T$  is temperature and  $S$  is the saturation ratio with respect to the condensing ice phase. Figure 1.3 shows an example of the different terms in Equation 1.1 for when  $T = -20$  °C. The surface term is positive and proportional to  $r^2$ , while the volume term is negative while  $S$  is above 1 and is proportional to  $r^3$ , meaning that as  $r$  increases,  $\Delta G_{cl}$  becomes less positive until it eventually becomes negative and cluster growth becomes spontaneous.

Classical nucleation theory (CNT) provides a numerical description of the thermodynamics and kinetics of the homogenous freezing of water based on macroscopically measurable properties (Ickes et al., 2015). It can be used to predict quantities such as the critical cluster radius,  $r_{ccl}$ , and the rate of homogenous nucleation as a function of temperature and saturation. The radius of the critical cluster,  $r_{ccl}$ , is equal to  $r$  when  $d\Delta G_{cl}/dr = 0$  and so can be calculated using the following equation:

$$r_{ccl} = \frac{2\gamma v}{kT \ln S} \quad (\text{Eq. 1.2})$$

The Gibbs free energy needed to reach the critical cluster,  $\Delta G_{ccl}$ , is the energy barrier for the nucleation of ice in water and can be calculated by substituting equation 1.2 into equation 1.1 to give:

$$\Delta G_{ccl} = \frac{16\pi\gamma^3 v^2}{3(kT \ln S)^2} \quad (\text{Eq. 1.3})$$

The rate of homogeneous nucleation,  $J_{\text{hom}}$ , can be calculated using an Arrhenius equation as shown:

$$J_{\text{hom}} = A \cdot \exp\left(-\frac{\Delta G_{\text{ccl}}}{kT}\right) \quad (\text{Eq. 1.4})$$

Where  $A$  is the pre-exponential factor which represents the frequency with which individual water molecules attach to an ice cluster, this attachment frequency depends on quantities such as the liquid viscosity and there are multiple different expressions in the literature which estimate  $A$  at different temperatures (Huang and Bartell, 1995).

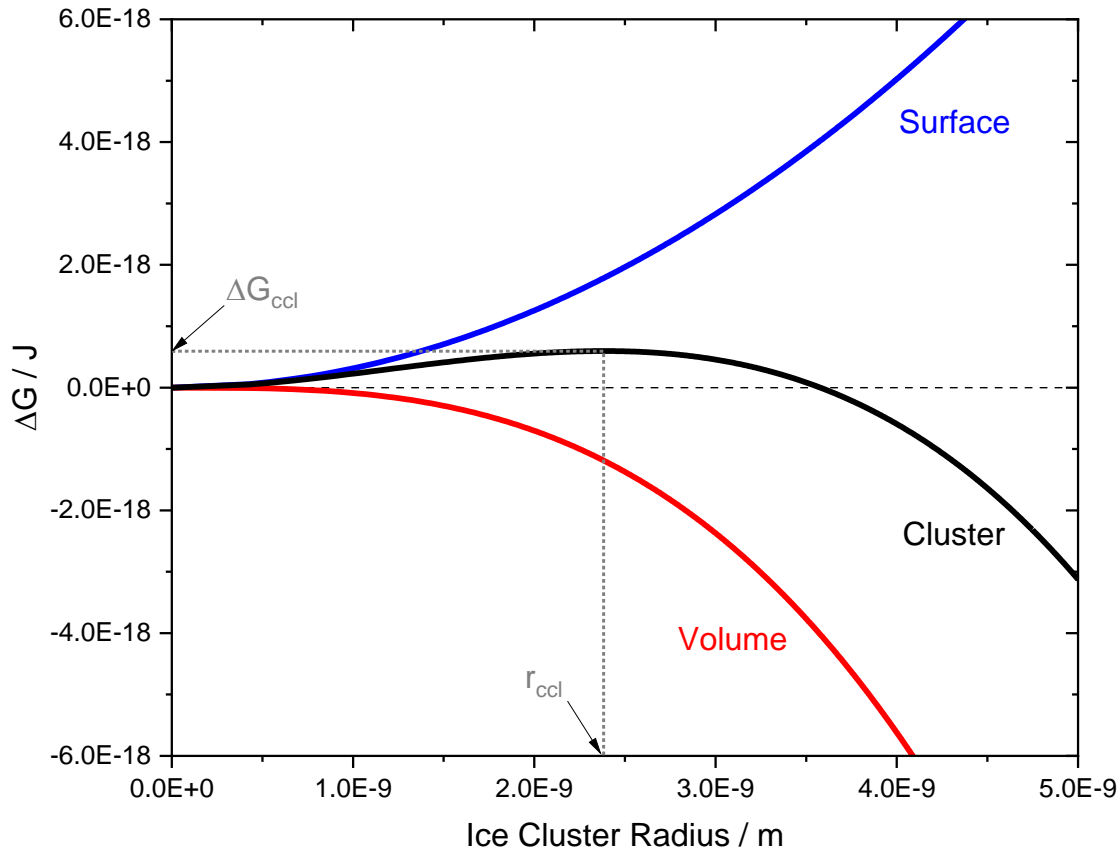


**Figure 1.3:** Plot of Gibbs free energy for the formation of an ice cluster (black line) in supercooled water at  $-20\text{ }^{\circ}\text{C}$ . Blue and red lines respectively show the individual surface and volume terms as given in Equation 1.1. Ice density of  $919\text{ kg m}^{-3}$  (Carnahan et al., 2021) and  $\gamma$  of  $25\text{ mJ m}^{-2}$  (Piaggi et al., 2022) used for calculations. Dotted lines indicate the critical cluster radius and Gibbs free energy given by the maximum Gibbs free energy for cluster formation.

By substituting equation 1.3 into equation 1.4, the following equation is given:

$$J_{\text{hom}} = A \cdot \exp\left(-\frac{16\pi\gamma^3\nu^2}{3k^3T^3(\ln S)^2}\right) \quad (\text{Eq. 1.5})$$

Equation 1.5 shows that lowering temperature and increasing saturation increases nucleation rate by decreasing the critical cluster size and therefore increasing the likelihood of a cluster forming (Murray et al., 2012).

### 1.2.2 Heterogeneous classical nucleation theory

The energy barrier for ice nucleation can be reduced by interaction with a solid surface, known as heterogeneous ice nucleation. Equation 1.5 can be modified to account for heterogeneous nucleation to give a heterogeneous nucleation rate,  $J_{\text{het}}$ , as shown:

$$J_{\text{het}} = A_{\text{het}} \cdot \exp\left(-\frac{\Delta G_{\text{ccl}}\varphi}{kT}\right) \quad (\text{Eq. 1.6})$$

Where  $A_{\text{het}}$  is the pre-exponential factor for heterogeneous nucleation and  $\varphi$  is a factor between 1 and 0 which accounts for the effect the solid surface has on the nucleation energy barrier, with a value of 1 meaning the surface has no effect and a value of 0 meaning that the surface reduces the energy barrier to 0. The value of  $\varphi$  can be related to the contact angle,  $\theta$ , between the nucleus and the flat surface, with  $\theta$  being between  $180^\circ$  and  $0^\circ$  (Murray et al., 2012). By reducing the energy barrier for ice nucleation, a solid surface can catalyse the nucleation of supercooled water to ice at higher temperatures than it otherwise would homogeneously nucleate. The greater the energy barrier reduction, the more effective the surface is at facilitating heterogeneous ice nucleation and the higher the temperature at which ice nucleation can occur.

### 1.2.3 The singular approximation of heterogeneous ice nucleation

Ice nucleation is known to be a stochastic process, with nucleation having a time dependence as described by the rate coefficient in CNT, and experimental studies have demonstrated the stochastic nature of heterogeneous ice nucleation. For example, Vonnegut and Baldwin (1984) showed that a 10  $\mu\text{L}$  water sample containing silver iodide particles held at a constant supercooled temperature would freeze after a seemingly random length of time, for example anywhere from 0 to 400 seconds when held at  $-5.5^\circ\text{C}$ .

This study showed that, when using a consistent sample, heterogeneous ice nucleation can occur after a range of lengths of time or at a range of different temperatures, demonstrating that there is a stochastic element to heterogeneous ice nucleation, which arises from the random nature of the formation of an ice cluster of critical size as described by CNT.

Despite this stochastic element of heterogeneous ice nucleation, studies measuring the repeated freezing of arrays of droplets containing random distributions of particles have shown that the variation in the freezing temperatures of the different droplets was much greater than the variation in the freezing temperature of single specific droplets (Vali, 1994, 2008; Vali and Stansbury, 1966). For example, Vali (2008) measured the freezing temperatures of arrays of 100 to 144 droplets of  $\sim 10 \mu\text{L}$  volume containing soil particles by repeating a cycle of cooling the droplets at a rate of  $1 \text{ }^\circ\text{C min}^{-1}$  until all the droplets froze, warming them to thaw them and then cooling them again. They found that the different droplets froze over a temperature range of  $-6$  to  $-24 \text{ }^\circ\text{C}$  but for specific droplets, changes in freezing temperature across the different cycles was  $> 1 \text{ }^\circ\text{C}$  for over 80 % of the droplets. These results indicated that in non-idealised situations where droplets can contain a range of different particle types or concentrations, such as in the atmosphere, the variation in freezing temperature that occurs due to stochastic effects is of secondary importance compared to the range of freezing temperatures that arises due to differences in droplet contents.

The singular approximation is a model which simplifies the description of heterogeneous ice nucleation by removing the time dependence. The singular approximation is based on the idea that heterogeneous nucleation occurs at specific sites on a particle's surface, commonly known as active sites. These active sites are thought to have specific temperature below which they can facilitate nucleation, related to how effectively they reduce the energy barrier for nucleation. A study by Holden et al. (2019) provided strong evidence in support of the existence of active sites by using video microscopy to observe the ice nucleation of  $1 \mu\text{L}$  volume water droplets resting on mineral surfaces. They showed that ice nucleation in droplets repeatedly occurred at a small number ( $\sim 5$ ) of specific locations on the mineral surfaces, as shown in Figure 1.4. Scanning electron microscopy and atomic force microscopy measurements of these mineral surfaces showed that all the sites at which nucleation occurred had micron-scale surface features such as pores or steps, suggesting that such features may have unique properties which favour the formation of ice clusters to grow to the critical size needed for ice nucleation. Holden et

al. (2019) also measured the freezing temperatures of arrays of droplets placed on the microcline feldspar surfaces and found that individual droplets repeatedly froze at consistent temperatures while the different droplets froze across a range of -8 to -14 °C. These droplet assay results showed that across the mineral surface there are active sites with a range of different characteristic nucleation temperatures and that these temperatures for each active site remain consistent across repeat measurements, further supporting the singular approximation.

The variety in active site nucleation temperatures across the surface area of a material is also seen in studies which measure ice nucleation by suspending the sample particles in water droplets and then cool the droplets to measure the freezing temperatures. These studies typically find that when using different concentrations of the suspended sample, higher sample surface area concentrations result in higher freezing temperatures (Broadley et al., 2012; Marcolli et al., 2007) since at higher surface area concentrations there is a higher probability of there being a rarer active site with a higher nucleation temperature than the more common active sites. Because of this surface area concentration dependence, results from heterogeneous ice nucleation measurements are commonly normalised to the surface area concentration of the sample to determine the temperature dependent active site density,  $n_s(T)$ , of the sample which is a measure of the concentration of sites across the sample's surface which can act as active sites for heterogeneous ice nucleation at a given temperature (Murray et al., 2012). The active site density can be used to compare the ice-nucleating activity (INA) of different materials.

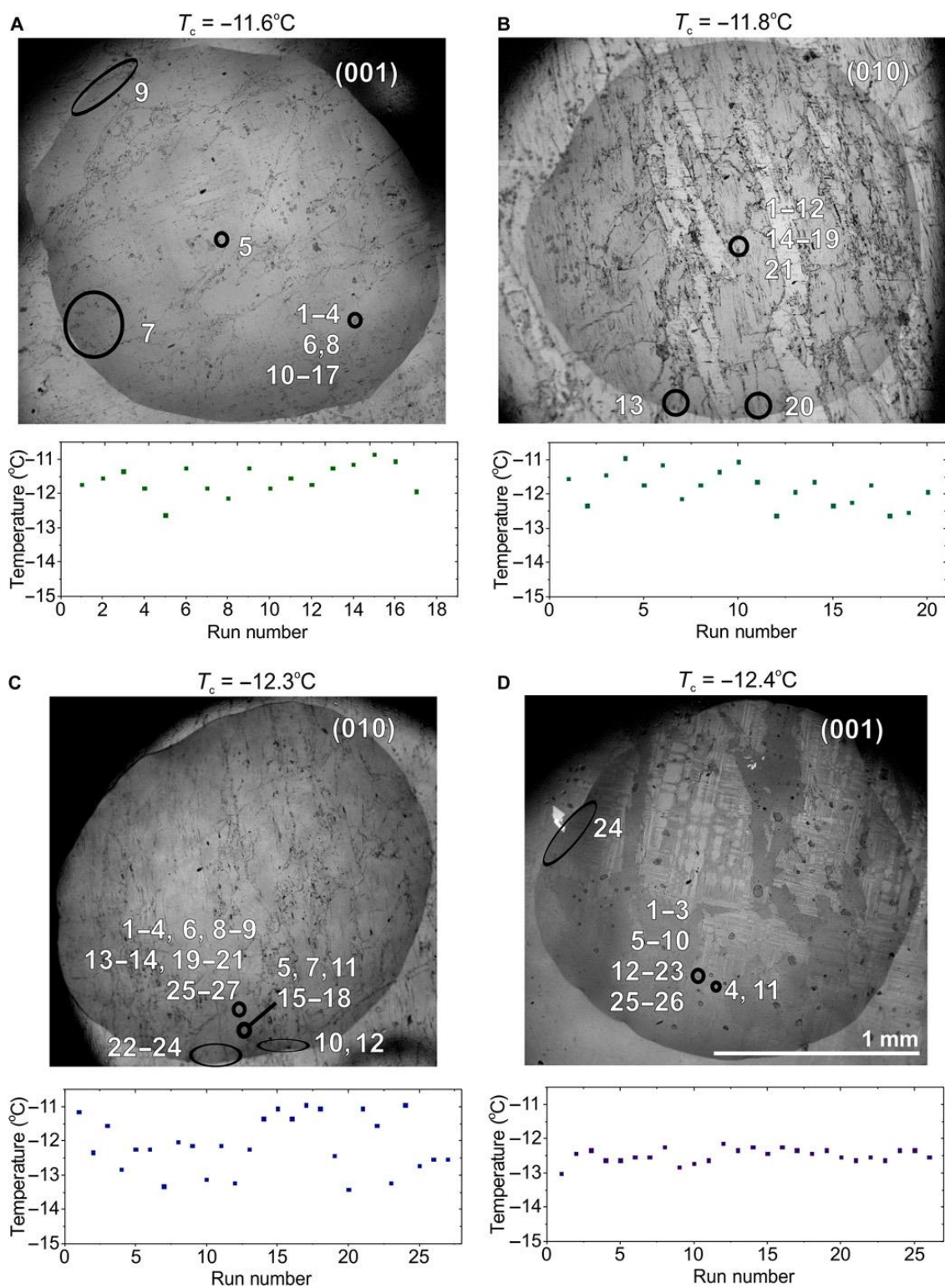


**Figure 1.4:** Images showing the locations (black circles) at which ice nucleation began to occur in droplets placed on microcline feldspar surfaces. Below each image is a plot showing the nucleation temperature of each individual freezing measurement run and above the characteristic nucleation temperature,  $T_c$ , is given, which is the average temperature at which each droplet froze. The numbers at each circle give the individual runs in which nucleation originated at that site. The bracketed numbers in the top right of the images are the cleavage planes. Figure 3 from Holden et al. (2019).

### 1.3 Modes of atmospheric ice nucleation

In the atmosphere, solid particles which can induce heterogeneous ice nucleation are known as INPs. There are multiple different pathways via which ice nucleation can occur in the atmosphere, often referred to as “modes” of ice nucleation, with different modes requiring different temperature and relative humidity (RH) conditions as well as potentially specific INP properties. Figure 1.5 illustrates the main modes of primary ice nucleation that occur in the atmosphere and shows the typical temperature and RH conditions required.

Immersion mode ice nucleation is when an INP triggers heterogeneous ice nucleation while immersed in a supercooled liquid droplet, the freezing can occur when the temperature is at or below the temperature at which the particle is active as an INP. Since liquid water droplets are a prerequisite for this mode of ice nucleation, the relative humidity with respect to water ( $RH_w$ ) must be at least 100 % for immersion freezing to occur. Remote sensing observations of mid-level clouds in tropical (Ansmann et al., 2009), subtropical (Ansmann et al., 2008), temperate (Westbrook and Illingworth, 2011) and Arctic (De Boer et al., 2011) regions have shown that the majority of clouds at

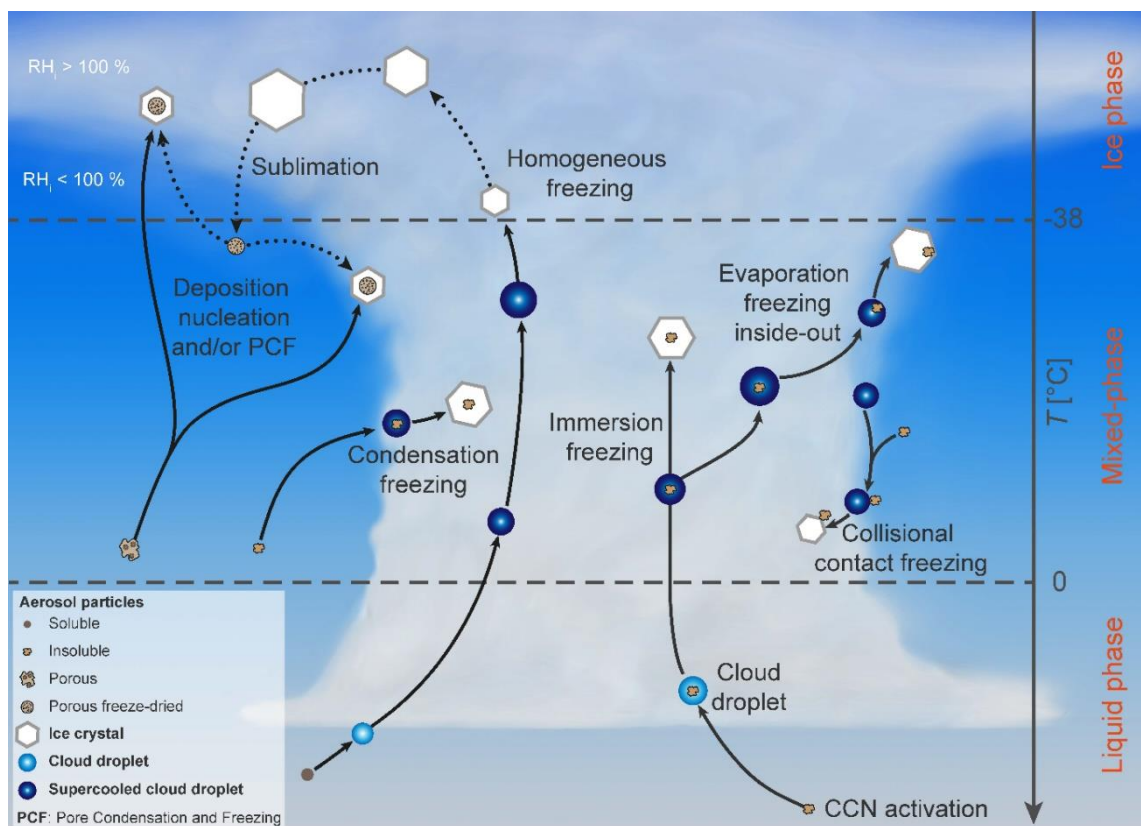


**Figure 1.5:** Diagram showing the main different modes of atmospheric ice nucleation and the temperature and relative humidity conditions at which they can occur. Figure 1-1 from Kanji et al., (2017).

temperatures  $>-25$  °C are mixed-phase and that supercooled liquid water droplets are required for ice production, indicating that immersion nucleation is the dominant mode of ice nucleation in the atmosphere at these temperatures. These observations also showed that ice particle concentration was primarily dependant on temperature, supporting the singular approximation of heterogeneous ice nucleation. Therefore, by characterising the temperatures at which different atmospheric aerosol types can nucleate ice and the concentrations of INPs present in the atmosphere, heterogeneous ice nucleation in mixed-phase clouds can be predicted and simulated in climate models.

Pore condensation and freezing (PCF) is a process in which liquid water in the pores (or any other inward surface feature such cracks and steps) on a particle's surface freezes and the ice grows out of the pores through the deposition of water vapour. Water can condense into these pores below water saturation as described by the inverse Kelvin equation, which shows that the vapour pressure over water condensed in a pore is less than over bulk water due to the concave curvature of the air-water interface, meaning the water more readily condenses in the pore. This effect is stronger for narrower pores, so the RH required for water condensation decreases with decreasing pore width. Marcolli (2014) suggested that PCF is the dominant ice nucleation mechanism below water saturation and that cases previously believed to be deposition nucleation (where ice directly deposits onto a particle's surface) were instead PCF. This is supported by measurements showing that at conditions below water saturation, many clays and mineral dusts have a much higher INA below  $\sim-38$  °C than at higher temperatures (David et al., 2020; Marcolli, 2014), this specific temperature dependence is inexplicable by deposition nucleation but can be attributed to the homogenous freezing of water in pores. Studies using materials with characterised pores have shown that the conditions at which PCF occurs depends on the size (David et al., 2020; Nichman et al., 2019), shape (Campbell and Christenson, 2018) and wettability (David et al., 2020; Mahrt et al., 2018) of the pores and that multiple pores close to one another on the particle's surface may be needed for ice to grow out of the pores and onto the surface of the particle (David et al., 2019). While it may be possible to predict the INA of a material under PCF-relevant conditions based upon its porosity and the structure of its pores, most of these studies use materials synthesised to have precise porosities, which may not be representative of the aerosol found in the atmosphere at conditions relevant for PCF.

Solutes decrease the melting temperature of ice (Rasmussen, 1982) by stabilising the liquid phase through an increase in entropy. Koop et al. (2000) showed experimentally

that water activity is the dominant factor in determining the homogenous freezing temperature of water droplets, referred to as the “water-activity criterion”. The ability to calculate homogenous nucleation rates solely from water activity, which at equilibrium is defined by RH, allows for homogenous freezing in clouds to be simulated using a simple calculation without any knowledge of the composition of the droplets.

#### 1.4 Types & sources of ice-nucleating particles

In the ambient atmosphere there are a variety of different types of aerosol particles which are known to act as INPs, including mineral dusts, bioaerosols, carbonaceous particles, ashes, organic particles, salt particles and metals (Kanji et al., 2017). The relative abundance of these different types of INP depends on location since the different types of INPs are linked to different sources. For example, measurements of ice crystal residuals over North America and Europe have shown mineral dust to be the dominant type of INP present (Cziczo et al., 2013; Kamphus et al., 2010; Pratt et al., 2009; Richardson et al., 2007), whereas in marine environments INPs from sea spray such as salts and marine organics become increasingly abundant (Cziczo et al., 2013). An estimation of the global average concentrations of different types of immersion mode INPs are shown in Figure 1.6 (Murray et al., 2012), which highlights that the different types of INP can be active at different temperatures.

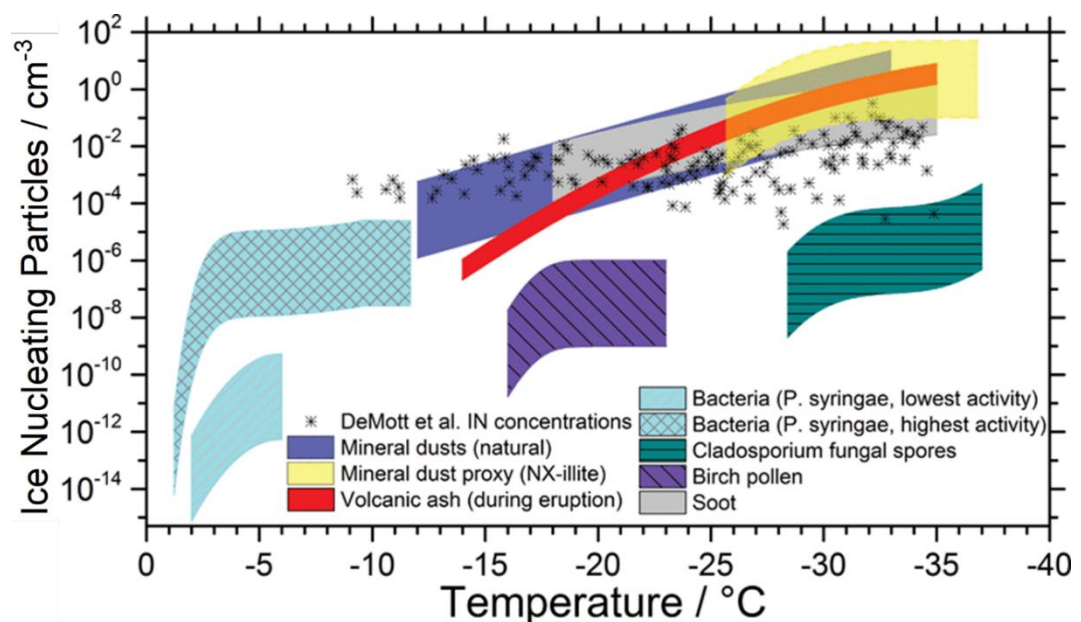


**Figure 1.6:** Plot showing estimated global average immersion mode ice-nucleating particle concentrations of different types of atmospheric aerosol as a function of temperature. Figure 19 from Murray et al. (2012).

### 1.4.1 Mineral dust

Global emissions of mineral dusts are estimated to be from 1000 to 5000 Tg y<sup>-1</sup> (Engelstaedter et al., 2006; Zender et al., 2004). The main source of atmospheric mineral dust is known as the Dust Belt, which ranges from the Sahara in northern Africa to the Gobi Desert in northern China and southern Mongolia (Prospero et al., 2002), as shown in Figure 1.7. This region primarily consists of arid deserts remote from human civilisation, but anthropogenic influences on the environment such as desertification are estimated to be responsible for 30 % to 50 % of the global average atmospheric mineral dust loading (Tegen and Fung, 1995). A global modelling study by Hoose et al. (2010) found that mineral dust particles made up 77 % of the global distribution of INPs active between 0 and -38 °C. Atmospheric dust is composed of various different minerals, an average composition from various XRD measurements of atmospheric dust samples collected at mid- to low-latitude locations was 47 % clays, 29 % quartz, 13 % feldspar and also other minerals including calcite, gypsum, goethite, haematite, palygorskite and halite (Murray et al., 2012). Of the minerals commonly found in atmospheric dust, potassium-rich feldspar (K-feldspar) has been shown by laboratory studies to have the highest INA, and is thought to be the most important mineral for controlling the INA of atmospheric dusts at temperatures below -15 °C under mixed-phase cloud conditions (Atkinson et al., 2013; Harrison et al., 2019).

High-latitude ( $\geq 50^{\circ}\text{N}$  and  $\geq 40^{\circ}\text{S}$ ) locations are also known to be sources of atmospheric dust, as shown in Figure 1.7, with approximately 1 to 5 % of the global dust emissions estimated to be from high-latitude sources (Bullard et al., 2016; Meinander et al., 2022).

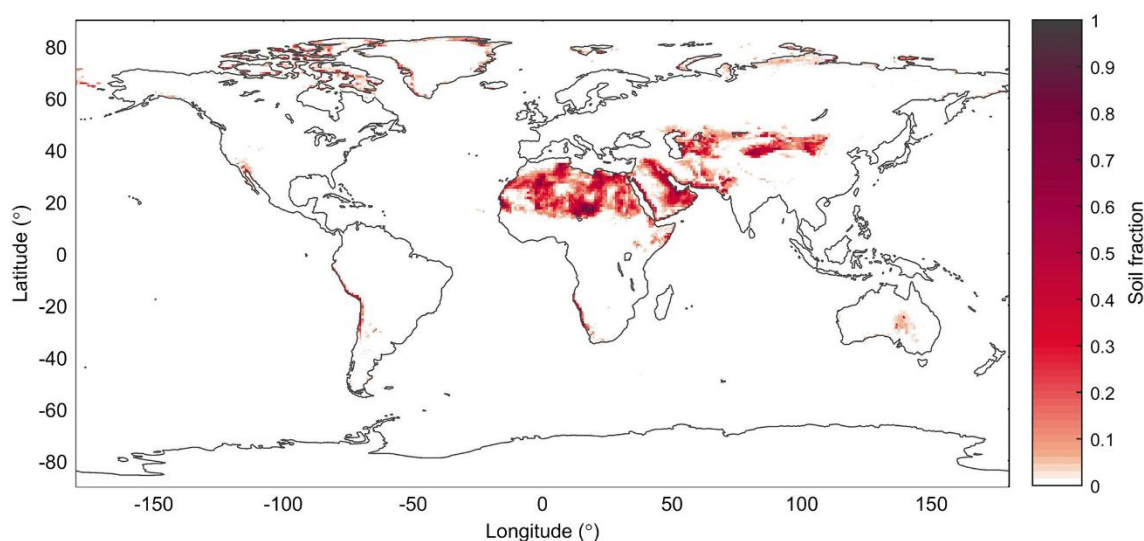


**Figure 1.7:** Map showing erodible soil fraction across the globe. Figure 1 from Groot Zwaaftink et al. (2016).

Dust emissions from these locations are seasonal, with specific environmental conditions such as low river discharge and low snow/ice cover being required (Bullard and Mockford, 2018; Crusius et al., 2011). As the climate warms, future emissions of dust from high latitudes are expected to increase due to more exposed sediment as glaciers melt (Amino et al., 2021).

#### **1.4.2 Bioaerosols**

Bioaerosols, also known as primary biological aerosol particles are solid particles from living organisms, they can be dead or alive and include fragments of biological material (Matthias-Maser and Jaenicke, 1995). Many bioaerosols such as pollen and fungal spores are emitted into the atmosphere from organisms as part of their propagation mechanisms (Jones and Harrison, 2004), while other biological material such as plant and animal fragments can be emitted during decay (Després et al., 2012). Whole microorganisms such as bacteria and viruses can also be aerosolised by processes such as bubble bursting from water or wind from land (Delort et al., 2010). The total global emission of bioaerosols is estimated to be  $1000 \text{ Tg y}^{-1}$  (Jaenicke, 2005), and bioaerosol is estimated to account for roughly 25 % of the number concentration of atmospheric aerosol over land (Jaenicke et al., 2007; Jones and Harrison, 2004; Matthias-Maser and Jaenicke, 1995). Bioaerosols have been measured in ice crystal and precipitation residuals (Creamean et al., 2013; Pratt et al., 2009), indicating that they are likely involved in ice nucleation in the atmosphere. The capability of various types of bioaerosols including bacteria (Möhler et al., 2008a), viruses (Adams et al., 2021), fungi (Kieft, 1988; Pouleur et al., 1992), pollen (Duan et al., 2023) and algae (Ickes et al., 2020) to heterogeneously nucleate ice has been demonstrated by laboratory studies. The ability of certain bacteria (Morris et al., 2004; Pandey et al., 2016) and fungi (Schwidetzky et al., 2023) to nucleate ice at temperatures up to  $\sim -2 \text{ }^\circ\text{C}$  has been linked to specific proteins which catalyse the nucleation of ice by favourably orienting water molecules.

Heat treatment of samples is often used as a method for identifying the presence of biogenic INPs in a sample based upon the assumption that the biogenic INPs will have their INA decreased by processes such as protein denaturation while other types of INP will be unaffected. A systematic study of the effect of heat treatment on mineral and biogenic INPs by Daily et al. (2022) found that, depending on the conditions used, certain minerals including K-feldspar were sensitive to heat treatment and non-proteinaceous biogenic INPs such as pollen and cellulose did not always decrease in INA after treatment. Therefore, heat tests are not a fool proof method of identifying the presence of biogenic

INPs in a sample and careful consideration of the heat treatment conditions is needed when using this method.

### **1.4.3 Black carbon**

Combustion processes emit a wide variety of gases and particles including CO<sub>2</sub>, NO<sub>x</sub>, ash and black carbon (BC) particles and a range of organic compounds that can go on to form secondary organic aerosol in the atmosphere (Bruns et al., 2015; Xu et al., 2011). Most studies indicate that BC is not an important INP in mixed-phase clouds (Chen et al., 2018; Hammer et al., 2018; Vergara-Temprado et al., 2018), but it has been suggested that it may be important in clouds that form close to BC sources (Levin et al., 2014; Twohy et al., 2010). However, BC has been shown to be able to nucleate ice via PCF, relevant for high-altitude clouds, with a wide variety in INA, most likely due to variety in porosity between the different aggregates (Mahrt et al., 2018; Nichman et al., 2019). Combustion ash particles have been shown to be immersion nucleation (Umo et al., 2015) and PCF active (Umo et al., 2019), indicating their potential importance in both mixed-phase and high-altitude clouds.

### **1.4.4 Volcanic ash**

The estimated average emissions of aerosol and precursor gases from volcanoes of ~10 to 15 Tg y<sup>-1</sup> (Dentener et al., 2006) is much lower than other atmospheric aerosol sources due to the sporadic nature of volcanic eruptions. However single eruption events can emit up to tens of thousands of teragrams of ash (Williams and Self, 1983), which can be transported tens of thousands of kilometres from the source and impact climate via direct and indirect aerosol effects (Durant et al., 2010; Engwell and Eychenne, 2016; Vernier et al., 2016). Similarly to mineral dusts, volcanic ashes are composed of a variety of minerals, with silicate minerals being the most common (Nakagawa and Ohba, 2003). The ability of volcanic ash aerosol to heterogeneously nucleate ice in the atmosphere has been suggested by studies linking volcanic eruption events to local increases in INP concentrations (Hobbs et al., 1971; Isono et al., 1959) and laboratory studies have shown volcanic ashes to have similar INAs to mineral dusts (Durant et al., 2008; Jahn et al., 2019; Mangan et al., 2017; Steinke et al., 2011). Volcanic eruptions also emit gases such as H<sub>2</sub>O, SO<sub>2</sub> and HCl which can coat and interact with volcanic ash particles in the eruption plume (Delmelle et al., 2007). Studies by Maters et al. (2020) and Fahy et al. (2022) showed that by interacting with other compounds emitted during eruptions, the INA of volcanic ashes can either be increased or decreased depending on the source of

the ash as well as the specific compound mixtures that it interacts with. The susceptibility of volcanic ash particles to have their INA altered by the compounds they are commonly emitted alongside adds a layer of complexity to predictions of the INA of volcanic ashes in the atmosphere.

## **1.5 Instruments for measurements of ice nucleation**

There are several different instruments and methods that are used to measure concentrations and the characteristics of INPs, including both online and offline techniques. Online methods generally have the advantage of being able to make measurements with higher time resolution but come with the offset of requiring more specialised equipment and having stricter requirements for making measurements, for example most online instruments require mains electricity to run, limiting the locations at which they can make measurements.

### **1.5.1 Cloud expansion chambers**

Cloud expansion chambers (Demott and Rogers, 1990; Möhler et al., 2021; Wagner et al., 2009b) are vessels used to simulate atmospheric conditions by controlling and monitoring conditions such as temperature, pressure and humidity. Cloud expansion chambers can be used to measure ice nucleation by undergoing expansions, where a decrease in the pressure inside the vessel leads to a decrease in temperature and rise in RH, leading to conditions which may allow for ice nucleation to occur. The Aerosol Interactions and Dynamics in the Atmosphere (AIDA) facility, shown in Figure 1.8, at the Karlsruhe Institute of Technology is an 84.3 m<sup>3</sup> chamber which can be temperature controlled from 60 °C to -90 °C. Particles, including liquid droplets and ice crystals, inside the chamber are measured using two Welas 2000 optical particle counters (OPCs) which are configured in measurement ranges of 0.7 to 40 and 2.3 to 104 µm to cover a large range of particle diameters (Wagner et al., 2009b). These OPCs are used to measure the concentration of ice crystals throughout an expansion, the ice crystals are distinguished from other particles based upon the measured diameter (Benz et al., 2005) since ice crystals grow at a faster rate than water droplets. The large size of the AIDA chamber allows measurements to be conducted over several days due to the long residence time of particles in the chamber (Saathoff et al., 2003). This capability for longer measurements allows for processes such as the atmospheric aging of aerosols to be measured with the AIDA. The downside of the large size of the AIDA chamber is that it is fixed in place,

therefore it cannot make online measurements of ambient aerosol at any location other than Karlsruhe, Germany.

### 1.5.2 Continuous flow diffusion chambers

Continuous Flow Diffusion Chambers (CFDCs) (Castarède et al., 2023; Chou, 2011; Friedman et al., 2011; Garimella et al., 2016; Jones et al., 2011; Kanji and Abbatt, 2009; Lacher et al., 2017; Rogers, 1988; Stetzer et al., 2008) are instruments which measure the ice-nucleating ability of aerosol samples by flowing the sample between two ice-covered walls which are cooled to different temperatures, a schematic of the Zurich ice nucleation chamber CFDC (Stetzer et al., 2008) is shown in Figure 1.9. The temperature difference between the two walls results in a linear temperature and vapour pressure gradient, but due to the exponential relationship between temperature and the saturation vapour pressure of water and ice (Murphy and Koop, 2005), the region in between the two walls is supersaturated with respect to ice. The greater the temperature difference between the two walls, the greater the supersaturation, and supersaturation with respect to water can be achieved with a large enough temperature gradient. By independently controlling the temperatures of the two walls, the temperature and RH conditions experienced by the sample aerosol can be accurately tuned, allowing for ice nucleation measurements to be made at conditions both subsaturated and supersaturated with respect to water. Alongside

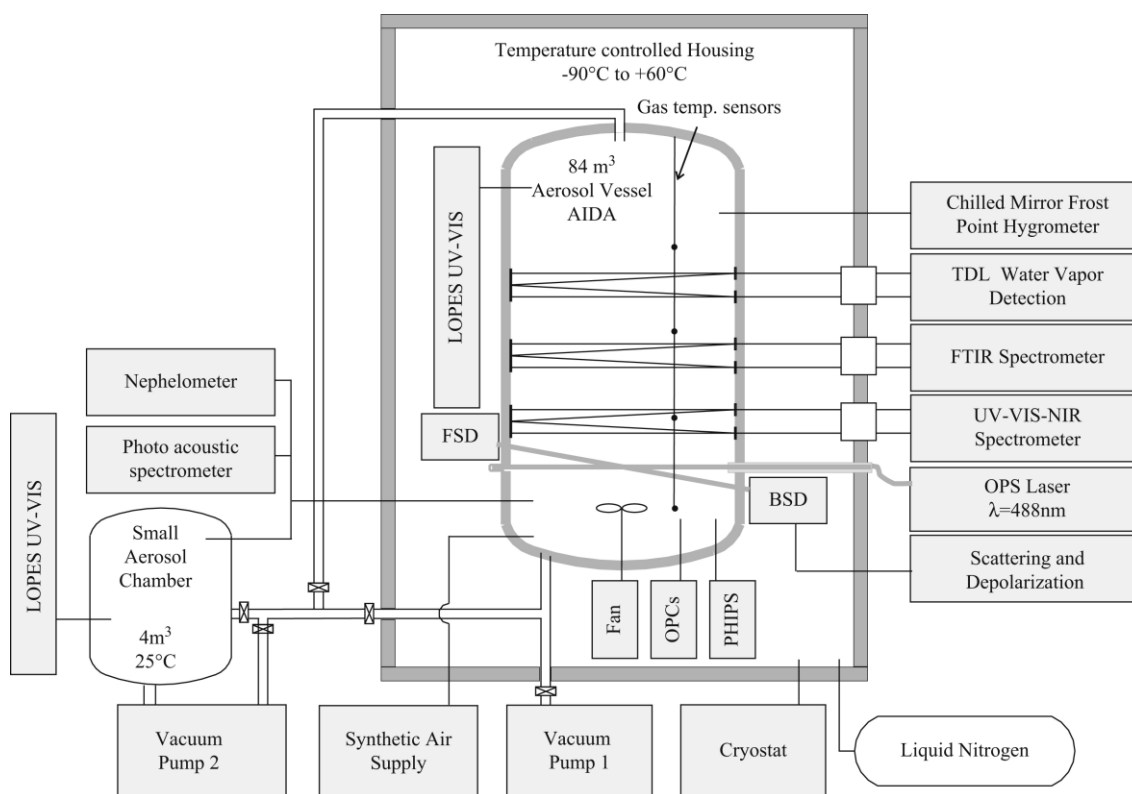


**Figure 1.8:** Schematic showing the AIDA facility. Figure 1 from Wagner et al. (2009).

the sample flow, a sheath flow of particle-free air is used to keep the sample in a narrow area with well-defined conditions. In most cases, an OPC is used at the outlet of a CFDC to measure the particles exiting the chamber, ice crystals are distinguished from liquid droplets and aerosol particles based upon their measured diameters due to the faster growth of ice crystals at temperatures below 0 °C (Rogers, 1988). To further increase the size difference between ice crystals and liquid droplets, and therefore improve the accuracy of ice crystal determination, most CFDC include an evaporation section towards the end of the chamber in which the RH is set to below water saturation so that unfrozen droplets will evaporate and decrease in size. Other methods for distinguishing between ice crystals and liquid droplets, such as depolarization detectors, are also sometimes incorporated (Castarède et al., 2023; Zenker et al., 2017).

CFDCs are designed to be portable so that they can be used to make online field measurements. There have been many different CFDCs designed, with the main differences being the geometry of the ice-covered walls and the orientation at which the instrument is designed to be operated. Wall geometries of concentric cylinders (Jones et al., 2011; Rogers, 1988) and flat parallel plates (Castarède et al., 2023; Chou, 2011;

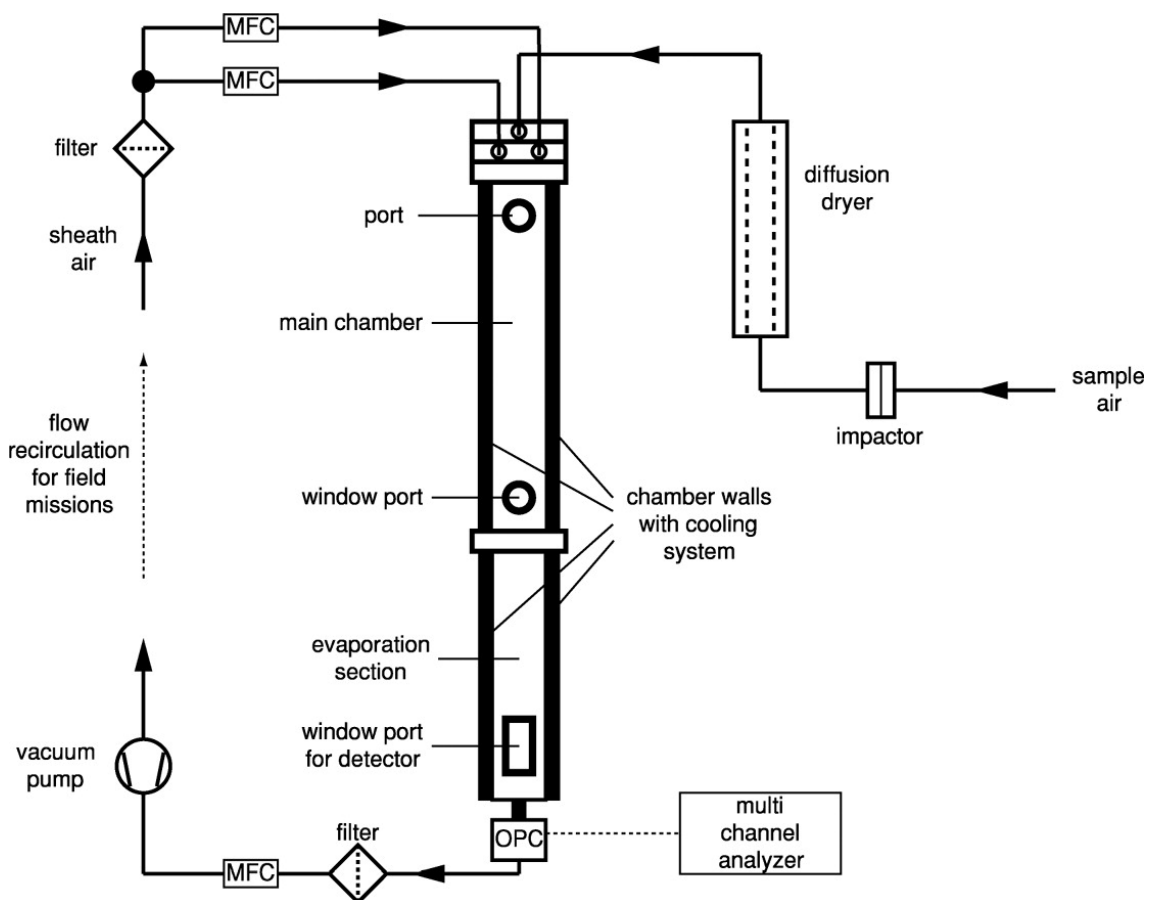


**Figure 1.9:** Schematic of the Zurich ice nucleation chamber, a CFDC instrument. Figure 2 from Stetzer et al. (2008).

Friedman et al., 2011; Garimella et al., 2016; Kanji and Abbatt, 2009; Lacher et al., 2017; Stetzer et al., 2008) have been used, with the flat plate design being more common due to having the advantage of being easier to manufacture and effectively cool (Stetzer et al., 2008). CFDCs can be operated either vertically (Castarède et al., 2023; Chou, 2011; Friedman et al., 2011; Garimella et al., 2016; Jones et al., 2011; Rogers, 1988; Stetzer et al., 2008), where the airflow is downwards, or horizontally (Kanji and Abbatt, 2009; Lacher et al., 2017), where the airflow is horizontal. The advantage of a vertical orientation is that particles are not lost by gravitational settling, but the disadvantage is that the horizontal temperature gradient between the walls results in an uneven buoyancy between the warmer and colder walls which can induce air circulation and shift the flow of the sample (Rogers, 1988). Horizontally oriented CFDCs minimise this buoyant circulation by having the warmer wall above the colder wall (Kanji and Abbatt, 2009). Different CFDCs also have different lengths, typically between 50 and 150 cm, with longer instruments having the advantage of longer particle residence times and therefore greater ice crystal growth while shorter instruments are more easily transported. Further additions and modifications to CFDCs include conditioning chambers in which aerosols are activated to droplets prior to being subjected to ice-nucleating conditions so that immersion nucleation can be exclusively measured without other nucleation modes (Kohn et al., 2016; Kulkarni et al., 2020).

The need for the walls of CFDCs to be coated in ice can result in background concentrations of ice crystals from the walls to be measured (Chou, 2011) which limits the lower detection limit of ice crystals in CFDCs. Also the ice layers can build up over the course of measurements which can increase background concentrations and so the ice walls need to be melted and reapplied after a few hours of measurements (Chou, 2011), limiting the capability of CFDCs to be used for continuous long-term measurements.

### 1.5.3 Cold stages

Cold stage instruments are used to measure the temperatures at which an array of droplets containing a sample undergo ice nucleation, a diagram of the microliter Nucleation by Immersed Particle Instrument ( $\mu\text{L-NIPI}$ ) (Whale et al., 2015) is shown in Figure 1.10. A typical cold stage experiment involves generating an array of droplets from a solution or suspension of the sample being investigated onto a hydrophobic slide, often by either nebulising (Murray et al., 2011) or pipetting (Budke and Koop, 2015; Tobo, 2016; Whale et al., 2015) the stock solution/suspension. The droplets are then cooled at a controlled rate on a cold stage and observed using a camera and in some cases a microscope, the time and temperature at which each droplet freezes is recorded based upon a change in appearance of the droplet which occurs when it freezes (Murray et al., 2010b; Whale et al., 2015). Different cold stage instruments are designed for different volume droplets ranging from pico- and nanolitre scale (Murray et al., 2011; O’Sullivan et al., 2014; Peckhaus et al., 2016; Wright and Petters, 2013) to microlitre scale (Budke and Koop, 2015; Tobo, 2016; Whale et al., 2015) droplets. The advantage of using larger droplets is that, for a given sample concentration, each droplet will contain more sample surface area and therefore will be more likely to contain a rare active site capable of ice nucleation at higher temperatures. This higher probability of nucleation at higher temperatures allows

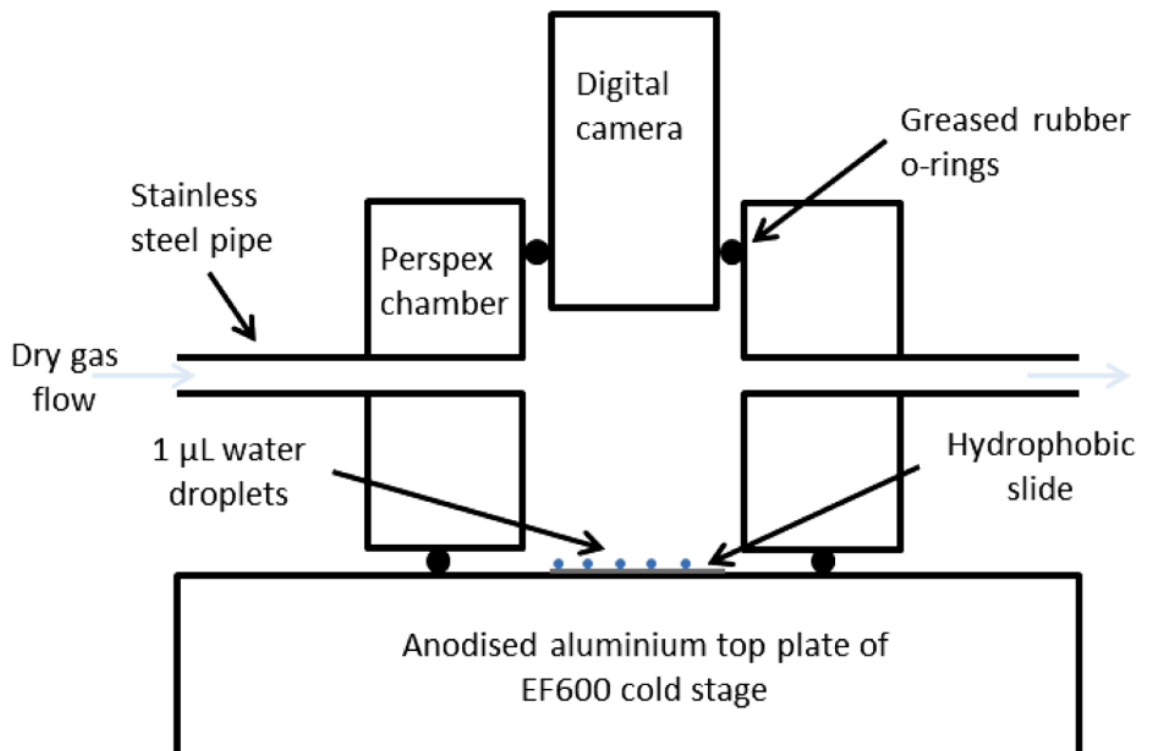


**Figure 1.10:** Diagram showing the  $\mu\text{L-NIPI}$  cold stage instrument. Figure 1 from Whale et al. (2015).

for measurements of a sample's INA to be made at these higher temperatures (Whale et al., 2015). Conversely, using smaller droplets allows for the INA at lower temperatures down to the homogeneous freezing range of pure water to be measured due to the lower probability of droplets containing active sites (O'Sullivan et al., 2014). Microfluidic techniques have been used to autonomously generate arrays of monodisperse picolitre volume droplets (Reicher et al., 2018) and further autonomize the droplet freezing process by passing the generated droplets over a cold stage held at a set temperature and observing the fraction of droplets that freeze (Tarn et al., 2020).

#### **1.5.4 Comparing the results of different ice nucleation measurement methods**

Since different instruments use different methods to measure ice nucleation, comparisons between the results of different instruments are useful for assessing the accuracy and limitations of different measurement methods. There have been several studies which have focused on the intercomparison of results from different ice nucleation measurement methods using specific control samples (DeMott et al., 2018; Hiranuma et al., 2015, 2019; Wex et al., 2015). During these intercomparison studies, the different methods are typically split into two different groups: methods that measure the sample in the aerosol phase (a.k.a. dry dispersion) and methods which measure the sample in an aqueous suspension (a.k.a. wet suspension). These two groups are analogous to online and offline instruments respectively, since online instruments typically directly sample an aerosol while offline techniques need to first collect a sample on a substrate and then remove the collected sample, typically by suspending it into water. The intercomparison studies have shown that the agreement of results from different measurement methods is dependent on the test material used. For Snomax<sup>®</sup> (a source of biological INPs) (DeMott et al., 2018; Wex et al., 2015) and soil dusts (DeMott et al., 2018) the different instruments' results agreed closely with one another but for mineral dusts (DeMott et al., 2018; Hiranuma et al., 2015) and cellulose (Hiranuma et al., 2019) the instruments' results showed more variation. In the cases where the variation between instruments was greater than 2 orders of magnitude, the dry dispersion methods consistently gave higher INA results than the wet suspension methods at a given temperature (DeMott et al., 2018; Hiranuma et al., 2015, 2019), which is potentially due to modification of the sample particles' surface when in suspension leading to a reduction in INA. An intercomparison of different instruments measuring ambient INP concentrations at Puy de Dôme, France by Lacher et al. (2024) also showed that the method of sample collection can lead to differences in measurement results, for example using impactors to prevent the sampling of larger

aerosol particles can result in a lower INP concentration measurement. The results from these various intercomparison studies shows that different measurement methods may not always give similar results, particularly when the sample is treated in different ways prior to measurements. Therefore, care should be taken when comparing INA results of different samples measured using different methods.

## **1.6 The portable ice nucleation experiment chamber**

The Portable Ice Nucleation Experiment (PINE) (Möhler et al., 2021) is a portable cloud expansion chamber which operates using similar principles to the AIDA chamber. A schematic of the PINE-1B, a prototype version used for measurements in this thesis, is shown in Figure 2.1. The PINE can repeatedly perform autonomous expansions by cycling through three modes of operation known respectively as the flush, expansion and refill modes. First, the sample is pumped into a 7 to 10 L (depending on the version of PINE) chamber. Second, the chamber inlet is sealed, and air is pumped out of the chamber via the outlet which causes an expansion to occur in the chamber, as the pressure and temperature inside the chamber decrease, the RH inside the chamber increases and aerosol particles inside the chamber can activate to liquid droplets which can potentially freeze. An OPC at the chamber outlet measures any particles exiting the chamber and ice crystals can be distinguished from liquid droplets and aerosol particles based upon their size, the same method of ice detection as is commonly used in CFDCs. After the expansion ends, the third mode begins in which the chamber is refilled to ambient pressure using a flow of filtered air, once the chamber is repressurised the cycle repeats. The temperature of the chamber walls is controlled by a cooling system, which is typically a chilled fluid flowing through pipes wrapped around the outside of the chamber, and the chamber wall temperature controls the temperature of the gas inside the chamber before the start of an expansion. Thermocouples are positioned along the vertical length of both the chamber wall and the centre of the chamber to respectively measure the wall and internal gas temperature throughout the chamber. During operation, there is a temperature gradient through the vertical length of the chamber due to the incoming air from the inlet not being cooled, this can result in a measured temperature difference of up to 5 °C between top and bottom gas thermocouples at a chiller temperature of approximately -30 °C (Möhler et al., 2021). In previous studies, the lowest measured gas temperature has been used as the representative temperature of the measurements (Adams, 2020; Brasseur et al., 2022;

Lacher et al., 2024), based upon the assumption that the lowest temperature in the chamber is controlling the ice nucleation inside the chamber (Möhler et al., 2021).

The first fully operational PINE instruments were the PINE-1A and -1B, which have a 7 L chamber volume and an approximate temperature measurement range of -10 to -40 °C. Subsequently, a commercial version of PINE (shown in Figure 1.11), with a 10 L chamber volume and temperature measurement range of -10 to -60 °C, was developed, and continuous development is ongoing to further improve the instrument. The PINE has several advantages as an instrument for measuring ice nucleation. It is portable and so can be transported to field locations to make measurements of ambient INP concentrations around the world, provided there is a suitable power source. It is an online instrument capable of making measurements with a ~10-minute time resolution, allowing it to capture short term changes in INP concentrations such as diurnal cycles. It can be operated autonomously for long periods, with field studies demonstrating its capability to run continuously for up to 60 days (Brasseur et al., 2022; Lacher et al., 2024; Möhler et



**Figure 1.11:** Photograph of a commercial PINE instrument making continuous INP measurements in Oklahoma. Side panels are removed to show the internal workings of the PINE. Figure A7 from Möhler et al. (2021).

al., 2021) with minimal manpower needed, making it a simple and easy to use instrument. Unlike CFCDs, the PINE does not need to be preconditioned to achieve the temperature and RH conditions needed for ice nucleation and can be operated without background ice concentrations, furthering the ease of use of the PINE.

## 1.7 Thesis objectives and outline

The overarching goal of the research detailed in this thesis is to improve our understanding of high-latitude dusts and volcanic ashes as ice-nucleating particles through laboratory experiments. To achieve this, the following three objectives are addressed:

1. *The use and development of tools and methods for measuring ice nucleation.*

The PINE is a relatively new instrument with many advantages, but the temperature gradient across the chamber leads to an uncertainty in its measurements. To improve the accuracy of measurements made with PINE, the temperature inside the PINE-1B is characterised based upon phase changes that can be observed with the OPC during expansions. A new method for determining the temperature representative of measurements made with the PINE-1B is developed and used to help achieve the two subsequent objectives.

2. *Use PINE to characterise the ice-nucleating activity of high-latitude mineral dusts across a range of temperatures relevant for mixed-phase clouds.*

High-latitude mineral dusts are thought to be an important INP source for global climate (Murray et al., 2021), but most measurements of the INAs of high-latitude dusts (HLDs) have used methods which only characterise the activity down to  $\sim -25$  °C. By using the PINE, the INAs of HLD samples from two contrasting locations are measured at temperatures down to  $-35$  °C and these measurements are combined with results from previous studies to produce a parameterisation that represents the INA of HLDs across the temperature range relevant for mixed-phase clouds.

3. *Use PINE to characterise the ice-nucleating activity of volcanic ash and the effect of aging processes.*

Previous studies measuring the INA of volcanic ash and the effects of ageing have used cold stage methods to make measurements down to  $\sim -25$  °C. By using the PINE, the INA of these ash samples can be measured at lower temperatures down to  $\sim -35$  °C and can be compared to the results from the previous studies to extend the temperature range of measurements of the INA of volcanic ash.

## 1.8 Publication strategy

The results reported in this thesis could be published in two different scientific publications. The results in chapters 2 and 3 of this thesis would each be reported in individual publications and the results in chapter 4 could be reported in another publication if more supporting measurements are made.

The results in chapter 2 of this thesis would be published as methods paper in a journal such as Atmospheric Measurement Techniques. This publication would allow for the knowledge of the PINE instrument's temperature measurement weaknesses and the alternative method of calculating the adiabatic temperature to become more widespread and other PINE users could use the publication as a reference point to test the temperature measurements of their own PINE instruments. This publication could also be used as a reference in future papers which report PINE measurements using the adiabatic temperature.

The results in chapter 3 of this thesis would be published as a results paper in a journal such as Atmospheric Chemistry and Physics. This publication would enhance the existing knowledge of the INA of HLD and the parameterisation provided may be used or modified by those doing modelling studies.

The results in chapter 4 of this thesis could be published in a results paper if more PINE measurements of volcanic ashes are made. In particular, measurements of the INA of unaged and aged volcanic ashes across the full temperature measurement range of the PINE would help improve the knowledge of the effects of ageing on the INA of volcanic ashes across the full range of temperatures relevant for mixed-phase clouds.

## 1.9 Other work – Ponsonby oil paper

Aside from the work covered in this thesis, throughout my PhD I also contributed to other pieces of work. Of particular note is the study by Ponsonby et al. (2024) which used the PINE-1B to measure the temperature and RH conditions under which aerosolised jet aircraft lubrication oil droplets could activate to cloud droplets and subsequently freeze. The study was led by Joel Ponsonby to whom I provided training for use of the PINE-1B, I also provided support and advice on the experimental work, data analysis and interpretation throughout the study. The PINE-1B measurement and data analysis methods used by Ponsonby et al. (2024) were those developed as part of the first objective in this thesis, and so my work developing these methods allowed the study by Ponsonby et al. (2024) to take place and the results be published.

To summarise the study, Ponsonby et al. (2024) used the PINE-1B to measure the temperature and RH conditions under which  $\sim 100$  nm diameter droplets of an oil representative of oils used for lubrication in jet aircrafts could activate to cloud droplets and freeze. The formation and properties of contrail clouds from aircraft emissions is generally controlled by the soot particles emitted from the burning of fuel (Kärcher and Yu, 2009), but as aircrafts transition to cleaner fuels in the future, the relative impact of soot on contrails may decrease and other particles emitted from aircraft, such as oil particles used in the engines, may become more important. Before the study by Ponsonby et al. (2024), the impact of jet lubrication oils on contrail formation had not been investigated. The measurements by Ponsonby et al. (2024) found that the oil droplets activated to cloud droplets at RH  $\sim 10$  % higher than water saturation (shown in Figure 1.12), which was consistent with what would be expected for a wettable, insoluble aerosol (Petters and Kreidenweis, 2007), and the activated droplets homogeneously froze at temperatures below  $\sim -38$  °C. The results from these measurements demonstrated the capability of these oil droplets to act as condensation nuclei in contrail conditions and therefore highlighted the need to characterise and account for these droplets when considering contrail formation in soot-poor conditions.

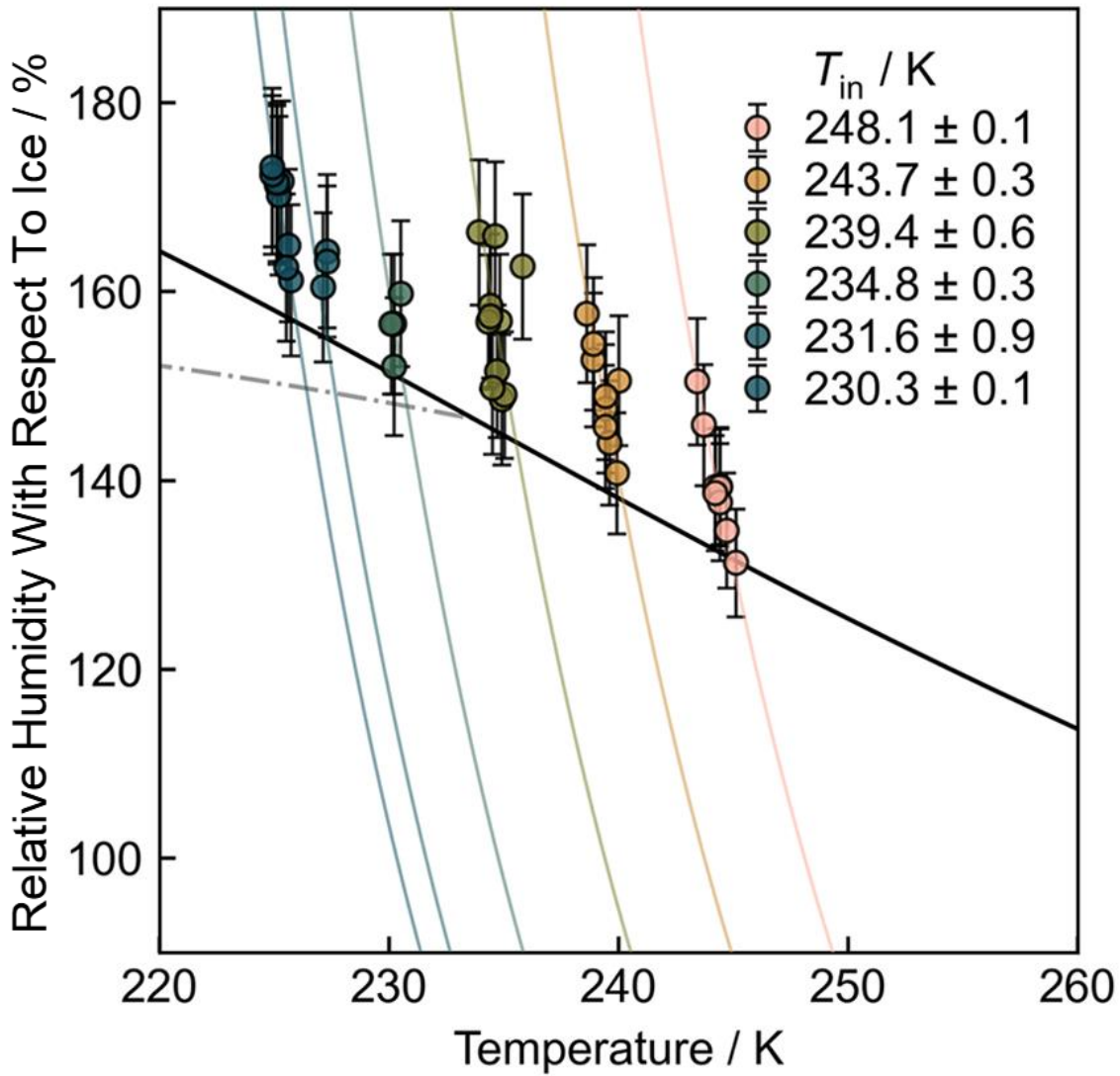


**Figure 1.12:** Plot showing the temperature and relative humidity with respect to ice conditions under which  $\sim 100$  nm diameter jet lubrication oil droplets activated to cloud droplets measured using the PINE-1B.  $T_{in}$  is the average initial temperature at the start of expansions for each set of measurements. Adapted from Figure 4 (a) from Ponsonby et al. (2024).

## 1.10 References

Adams, M. P.: Measurement and characterisation of atmospheric ice-nucleating particles, University of Leeds., 2020.

Adams, M. P., Atanasova, N. S., Sofieva, S., Ravantti, J., Heikkinen, A., Brasseur, Z., Duplissy, J., Bamford, D. H. and Murray, B. J.: Ice nucleation by viruses and their potential for cloud glaciation, *Biogeosciences*, 18(14), 4431–4444, doi:10.5194/bg-18-4431-2021, 2021.

Amino, T., Iizuka, Y., Matoba, S., Shimada, R., Oshima, N., Suzuki, T., Ando, T., Aoki, T. and Fujita, K.: Increasing dust emission from ice free terrain in southeastern Greenland since 2000, *Polar Sci.*, 27, 100599, doi:10.1016/j.polar.2020.100599, 2021.

Ansmann, A., Tesche, M., Althausen, D., Müller, D., Seifert, P., Freudenthaler, V., Heese, B., Wiegner, M., Pisani, G., Knippertz, P. and Dubovik, O.: Influence of Saharan dust on cloud glaciation in southern Morocco during the Saharan Mineral Dust Experiment, *J. Geophys. Res. Atmos.*, 113(4), doi:10.1029/2007JD008785, 2008.

Ansmann, A., Tesche, M., Seifert, P., Althausen, D., Engelmann, R., Fruntke, J., Wandinger, U., Mattis, I. and Müller, D.: Evolution of the ice phase in tropical altocumulus: SAMUM lidar observations over Cape Verde, *J. Geophys. Res. Atmos.*, 114(17), doi:10.1029/2008JD011659, 2009.

Atkinson, J. D., Murray, B. J., Woodhouse, M. T., Whale, T. F., Baustian, K. J., Carslaw, K. S., Dobbie, S., O’Sullivan, D. and Malkin, T. L.: The importance of feldspar for ice nucleation by mineral dust in mixed-phase clouds, *Nature*, 498(7454), 355–358, doi:10.1038/nature12278, 2013.

Benz, S., Megahed, K., Möhler, O., Saathoff, H., Wagner, R. and Schurath, U.: T-dependent rate measurements of homogeneous ice nucleation in cloud droplets using a large atmospheric simulation chamber, *J. Photochem. Photobiol. A Chem.*, 176(1-3 SPEC. ISS.), 208–217, doi:10.1016/j.jphotochem.2005.08.026, 2005.

De Boer, G., Morrison, H., Shupe, M. D. and Hildner, R.: Evidence of liquid dependent ice nucleation in high-latitude stratiform clouds from surface remote sensors, *Geophys. Res. Lett.*, 38(1), doi:10.1029/2010GL046016, 2011.

Brasseur, Z., Castarède, D., Thomson, E. S., Adams, M. P., Drossaert Van Dusseldorp, S., Heikkilä, P., Korhonen, K., Lampilahti, J., Paramonov, M., Schneider, J., Vogel, F., Wu,

Y., Abbatt, J. P. D., Atanasova, N. S., Bamford, D. H., Bertozzi, B., Boyer, M., Brus, D., Daily, M. I., Fösig, R., Gute, E., Harrison, A. D., Hietala, P., Höhler, K., Kanji, Z. A., Keskinen, J., Lacher, L., Lampimäki, M., Levula, J., Manninen, A., Nadolny, J., Peltola, M., Porter, G. C. E., Poutanen, P., Proske, U., Schorr, T., Silas Umo, N., Stenszky, J., Virtanen, A., Moisseev, D., Kulmala, M., Murray, B. J., Petäjä, T., Möhler, O. and Duplissy, J.: Measurement report: Introduction to the HyICE-2018 campaign for measurements of ice-nucleating particles and instrument inter-comparison in the Hyytiälä boreal forest, *Atmos. Chem. Phys.*, 22(8), 5117–5145, doi:10.5194/acp-22-5117-2022, 2022.

Broadley, S. L., Murray, B. J., Herbert, R. J., Atkinson, J. D., Dobbie, S., Malkin, T. L., Condliffe, E. and Neve, L.: Immersion mode heterogeneous ice nucleation by an illite rich powder representative of atmospheric mineral dust, *Atmos. Chem. Phys.*, 12(1), 287–307, doi:10.5194/acp-12-287-2012, 2012.

Bruns, E. A., Krapf, M., Orasche, J., Huang, Y., Zimmermann, R., Drinovec, L., Močnik, G., El-Haddad, I., Slowik, J. G., Dommen, J., Baltensperger, U. and Prévôt, A. S. H.: Characterization of primary and secondary wood combustion products generated under different burner loads, *Atmos. Chem. Phys.*, 15(5), 2825–2841, doi:10.5194/acp-15-2825-2015, 2015.

Bullard, J. E. and Mockford, T.: Seasonal and decadal variability of dust observations in the Kangerlussuaq area, west Greenland, Arctic, *Antarct. Alp. Res.*, 50(1), doi:10.1080/15230430.2017.1415854, 2018.

Bullard, J. E., Baddock, M., Bradwell, T., Crusius, J., Darlington, E., Gaiero, D., Gassó, S., Gisladottir, G., Hodgkins, R., McCulloch, R., McKenna-Neuman, C., Mockford, T., Stewart, H. and Thorsteinsson, T.: High-latitude dust in the Earth system, *Rev. Geophys.*, 54(2), 447–485, doi:10.1002/2016RG000518, 2016.

Campbell, J. M. and Christenson, H. K.: Nucleation- and Emergence-Limited Growth of Ice from Pores, *Phys. Rev. Lett.*, 120(16), doi:10.1103/PhysRevLett.120.165701, 2018.

Carnahan, E., Wolfenbarger, N. S., Jordan, J. S. and Hesse, M. A.: New insights into temperature-dependent ice properties and their effect on ice shell convection for icy ocean worlds, *Earth Planet. Sci. Lett.*, 563, doi:10.1016/j.epsl.2021.116886, 2021.

Castarède, D., Brasseur, Z., Wu, Y., Kanji, Z. A., Hartmann, M., Ahonen, L., Bilde, M., Kulmala, M., Petäjä, T., Pettersson, J. B. C., Sierau, B., Stetzer, O., Stratmann, F.,

- Svenningsson, B., Swietlicki, E., Thu Nguyen, Q., Duplissy, J. and Thomson, E. S.: Development and characterization of the Portable Ice Nucleation Chamber 2 (PINCii), *Atmos. Meas. Tech.*, 16(16), 3881–3899, doi:10.5194/amt-16-3881-2023, 2023.
- Chen, J., Wu, Z., Augustin-Bauditz, S., Grawe, S., Hartmann, M., Pei, X., Liu, Z., Ji, D. and Wex, H.: Ice-nucleating particle concentrations unaffected by urban air pollution in Beijing, China, *Atmos. Chem. Phys.*, 18(5), 3523–3539, doi:10.5194/acp-18-3523-2018, 2018.
- Chen, T., Rossow, W. B. and Zhang, Y.: Radiative effects of cloud-type variations, *J. Clim.*, 13(1), 264–286, doi:10.1175/1520-0442(2000)013<0264:REOCTV>2.0.CO;2, 2000.
- Chou, C.: Investigation of Ice Nucleation Properties onto Soot, Bioaerosol and Mineral Dust during Different Measurement Campaigns, ETH ZURICH., 2011.
- Creamean, J. M., Suski, K. J., Rosenfeld, D., Cazorla, A., DeMott, P. J., Sullivan, R. C., White, A. B., Ralph, F. M., Minnis, P., Comstock, J. M., Tomlinson, J. M. and Prather, K. A.: Dust and biological aerosols from the Sahara and Asia influence precipitation in the Western U.S, *Science (80-. )*, 340(6127), 1572–1578, doi:10.1126/science.1227279, 2013.
- Crusius, J., Schroth, A. W., Gassó, S., Moy, C. M., Levy, R. C. and Gatica, M.: Glacial flour dust storms in the Gulf of Alaska: Hydrologic and meteorological controls and their importance as a source of bioavailable iron, *Geophys. Res. Lett.*, 38(6), doi:10.1029/2010GL046573, 2011.
- Cziczo, D. J., Froyd, K. D., Hoose, C., Jensen, E. J., Diao, M., Zondlo, M. A., Smith, J. B., Twohy, C. H. and Murphy, D. M.: Clarifying the dominant sources and mechanisms of cirrus cloud formation, *Science (80-. )*, 340(6138), 1320–1324, doi:10.1126/science.1234145, 2013.
- Daily, M. I., Tarn, M. D., Whale, T. F. and Murray, B. J.: An evaluation of the heat test for the ice-nucleating ability of minerals and biological material, *Atmos. Meas. Tech.*, 15(8), 2635–2665, doi:10.5194/amt-15-2635-2022, 2022.
- David, R. O., Marcolli, C., Fahrni, J., Qiu, Y., Perez Sirkin, Y. A., Molinero, V., Mahrt, F., Brühwiler, D., Lohmann, U. and Kanji, Z. A.: Pore condensation and freezing is responsible for ice formation below water saturation for porous particles, *Proc. Natl. Acad. Sci.*, 116(17), 8184–8189, doi:10.1073/pnas.1813647116, 2019.

David, R. O., Fahrni, J., Marcolli, C., Mahrt, F., Brühwiler, D. and Kanji, Z. A.: The role of contact angle and pore width on pore condensation and freezing, *Atmos. Chem. Phys.*, 20(15), 9419–9440, doi:10.5194/acp-20-9419-2020, 2020.

Delmelle, P., Lambert, M., Dufrêne, Y., Gerin, P. and Óskarsson, N.: Gas/aerosol-ash interaction in volcanic plumes: New insights from surface analyses of fine ash particles, *Earth Planet. Sci. Lett.*, 259(1–2), 159–170, doi:10.1016/j.epsl.2007.04.052, 2007.

Delort, A. M., Väitilingom, M., Amato, P., Sancelme, M., Parazols, M., Mailhot, G., Laj, P. and Deguillaume, L.: A short overview of the microbial population in clouds: Potential roles in atmospheric chemistry and nucleation processes, *Atmos. Res.*, 98(2–4), 249–260, doi:10.1016/j.atmosres.2010.07.004, 2010.

Demott, P. J. and Rogers, D. C.: Freezing nucleation rates of dilute solution droplets measured between  $-30^{\circ}$  and  $-40^{\circ}\text{C}$  in laboratory simulations of natural clouds, *J. Atmos. Sci.*, 47(9), 1056–1064, doi:10.1175/1520-0469(1990)047<1056:FNRODS>2.0.CO;2, 1990.

DeMott, P. J., Möhler, O., Cziczo, D. J., Hiranuma, N., Petters, M. D., Petters, S. S., Belosi, F., Bingemer, H. G., Brooks, S. D., Budke, C., Burkert-Kohn, M., Collier, K. N., Danielczok, A., Eppers, O., Felgitsch, L., Garimella, S., Grothe, H., Herenz, P., Hill, T. C. J., Höhler, K., Kanji, Z. A., Kiselev, A., Koop, T., Kristensen, T. B., Krüger, K., Kulkarni, G., Levin, E. J. T., Murray, B. J., Nicosia, A., O’Sullivan, D., Peckhaus, A., Polen, M. J., Price, H. C., Reicher, N., Rothenberg, D. A., Rudich, Y., Santachiara, G., Schiebel, T., Schrod, J., Seifried, T. M., Stratmann, F., Sullivan, R. C., Suski, K. J., Szakáll, M., Taylor, H. P., Ullrich, R., Vergara-Temprado, J., Wagner, R., Whale, T. F., Weber, D., Welti, A., Wilson, T. W., Wolf, M. J. and Zenker, J.: The Fifth International Workshop on Ice Nucleation phase 2 (FIN-02): Laboratory intercomparison of ice nucleation measurements, *Atmos. Meas. Tech.*, 11(11), 6231–6257, doi:10.5194/amt-11-6231-2018, 2018.

Dentener, F., Kinne, S., Bond, T., Boucher, O., Cofala, J., Generoso, S., Ginoux, P., Gong, S., Hoelzemann, J. J., Ito, A., Marelli, L., Penner, J. E., Putaud, J. P., Textor, C., Schulz, M., Van Der Werf, G. R. and Wilson, J.: Emissions of primary aerosol and precursor gases in the years 2000 and 1750 prescribed data-sets for AeroCom, *Atmos. Chem. Phys.*, 6(12), 4321–4344, doi:10.5194/acp-6-4321-2006, 2006.

Després, V. R., Alex Huffman, J., Burrows, S. M., Hoose, C., Safatov, A. S., Buryak, G., Fröhlich-Nowoisky, J., Elbert, W., Andreae, M. O., Pöschl, U. and Jaenicke, R.: Primary biological aerosol particles in the atmosphere: A review, *Tellus, Ser. B Chem. Phys. Meteorol.*, 64(1), doi:10.3402/tellusb.v64i0.15598, 2012.

Duan, P., Hu, W., Wu, Z., Bi, K., Zhu, J. and Fu, P.: Ice nucleation activity of airborne pollen: A short review of results from laboratory experiments, *Atmos. Res.*, 285, doi:10.1016/j.atmosres.2023.106659, 2023.

Durant, A. J., Shaw, R. A., Rose, W. I., Mi, Y. and Ernst, G. G. J.: Ice nucleation and overseeding of ice in volcanic clouds, *J. Geophys. Res. Atmos.*, 113(9), 9206, doi:10.1029/2007JD009064, 2008.

Durant, A. J., Bonadonna, C. and Horwell, C. J.: Atmospheric and environmental impacts of volcanic particulates, *Elements*, 6(4), 235–240, doi:10.2113/gselements.6.4.235, 2010.

Engelstaedter, S., Tegen, I. and Washington, R.: North African dust emissions and transport, *Earth-Science Rev.*, 79(1–2), 73–100, doi:10.1016/j.earscirev.2006.06.004, 2006.

Engwell, S. and Eychenne, J.: Contribution of Fine Ash to the Atmosphere From Plumes Associated With Pyroclastic Density Currents, in *Volcanic Ash: Hazard Observation*, pp. 68–85, Elsevier., 2016.

Fahy, W. D., Maters, E. C., Giese Miranda, R., Adams, M. P., Jahn, L. G., Sullivan, R. C. and Murray, B. J.: Volcanic ash ice nucleation activity is variably reduced by aging in water and sulfuric acid: the effects of leaching, dissolution, and precipitation, *Environ. Sci. Atmos.*, 2(1), 85–99, doi:10.1039/D1EA00071C, 2022.

Forster, P., Storelvmo, T., Armour, K., Collins, W., Dufresne, J. L., Frame, D., Lunt, D. J., Mauritsen, T., Palmer, M. D., Watanabe, M., Wild, M. and Zhang, H.: The Earth's Energy Budget, Climate Feedbacks and Climate Sensitivity, in *Climate Change 2021 – The Physical Science Basis Contribution of Working Group I to the Sixth Assessment Report of the Intergovernmental Panel on Climate Change*, pp. 923–1054., 2023.

Friedman, B., Kulkarni, G., Beránek, J., Zelenyuk, A., Thornton, J. A. and Cziczo, D. J.: Ice nucleation and droplet formation by bare and coated soot particles, *J. Geophys. Res. Atmos.*, 116(17), doi:10.1029/2011JD015999, 2011.

Garimella, S., Kristensen, T. B., Ignatius, K., Welti, A., Voigtländer, J., Kulkarni, G. R., Sagan, F., Kok, G. L., Dorsey, J., Nichman, L., Rothenberg, D. A., Rösch, M., Kirchgäßner, A. C. R., Ladkin, R., Wex, H., Wilson, T. W., Ladino, L. A., Abbatt, J. P. D., Stetzer, O., Lohmann, U., Stratmann, F. and Cziczo, D. J.: The Spectrometer for Ice Nuclei (SPIN): an instrument to investigate ice nucleation, *Atmos. Meas. Tech.*, 9(7), 2781–2795, doi:10.5194/amt-9-2781-2016, 2016.

Groot Zwaafink, C. D., Grythe, H., Skov, H. and Stohl, A.: Substantial contribution of northern high-latitude sources to mineral dust in the Arctic, *J. Geophys. Res.*, 121(22), 13,678–13,697, doi:10.1002/2016JD025482, 2016.

Hammer, S. E., Mertes, S., Schneider, J., Ebert, M., Kandler, K. and Weinbruch, S.: Composition of ice particle residuals in mixed-phase clouds at Jungfraujoch (Switzerland): Enrichment and depletion of particle groups relative to total aerosol, *Atmos. Chem. Phys.*, 18(19), 13987–14003, doi:10.5194/acp-18-13987-2018, 2018.

Harrison, A. D., Lever, K., Sanchez-Marroquin, A., Holden, M. A., Whale, T. F., Tarn, M. D., McQuaid, J. B. and Murray, B. J.: The ice-nucleating ability of quartz immersed in water and its atmospheric importance compared to K-feldspar, *Atmos. Chem. Phys. Discuss.*, 1–23, doi:10.5194/acp-2019-288, 2019.

Hartmann, D. L., Ockert-Bell, M. E. and Michelsen, M. L.: The Effect of Cloud Type on Earth's Energy Balance: Global Analysis, *J. Clim.*, 5(11), 1281–1304, doi:10.1175/1520-0442(1992)005<1281:teocto>2.0.co;2, 1992.

Heneghan, A. F., Wilson, P. W. and Haymet, A. D. J.: Heterogeneous nucleation of supercooled water, and the effect of an added catalyst, *Proc. Natl. Acad. Sci. U. S. A.*, 99(15), 9631–9634, doi:10.1073/pnas.152253399, 2002.

Herbert, R. J., Murray, B. J., Dobbie, S. J. and Koop, T.: Sensitivity of liquid clouds to homogenous freezing parameterizations, *Geophys. Res. Lett.*, 42(5), 1599–1605, doi:10.1002/2014GL062729, 2015.

Hiranuma, N., Augustin-Bauditz, S., Bingemer, H., Budke, C., Curtius, J., Danielczok, A., Diehl, K., Dreischmeier, K., Ebert, M., Frank, F., Hoffmann, N., Kandler, K., Kiselev, A., Koop, T., Leisner, T., Möhler, O., Nillius, B., Peckhaus, A., Rose, D., Weinbruch, S., Wex, H., Boose, Y., Demott, P. J., Hader, J. D., Hill, T. C. J., Kanji, Z. A., Kulkarni, G., Levin, E. J. T., McCluskey, C. S., Murakami, M., Murray, B. J., Niedermeier, D., Petters, M. D., O'Sullivan, D., Saito, A., Schill, G. P., Tajiri, T., Tolbert, M. A., Welti, A., Whale,

T. F., Wright, T. P. and Yamashita, K.: A comprehensive laboratory study on the immersion freezing behavior of illite NX particles: A comparison of 17 ice nucleation measurement techniques, *Atmos. Chem. Phys.*, 15(5), doi:10.5194/acp-15-2489-2015, 2015.

Hiranuma, N., Adachi, K., Bell, D., Belosi, F., Beydoun, H., Bhaduri, B., Bingemer, H., Budke, C., Clemen, H. C., Conen, F., Cory, K., Curtius, J., Demott, P., Eppers, O., Grawe, S., Hartmann, S., Hoffmann, N., Höhler, K., Jantsch, E., Kiselev, A., Koop, T., Kulkarni, G., Mayer, A., Murakami, M., Murray, B., Nicosia, A., Petters, M., Piazza, M., Polen, M., Reicher, N., Rudich, Y., Saito, A., Santachiara, G., Schiebel, T., Schill, G., Schneider, J., Segev, L., Stopelli, E., Sullivan, R., Suski, K., Szakall, M., Tajiri, T., Taylor, H., Tobo, Y., Ullrich, R., Weber, D., Wex, H., Whale, T., Whiteside, C., Yamashita, K., Zelenyuk, A. and Möhler, O.: A comprehensive characterization of ice nucleation by three different types of cellulose particles immersed in water, *Atmos. Chem. Phys.*, 19(7), 4823–4849, doi:10.5194/acp-19-4823-2019, 2019.

Hobbs, P. V., Fullerton, C. M. and Bluhm, G. C.: Ice Nucleus Storms in Hawaii, *Nat. Phys. Sci.*, 230(12), 90–91, doi:10.1038/physci230090a0, 1971.

Holden, M. A., Whale, T. F., Tarn, M. D., O’Sullivan, D., Walshaw, R. D., Murray, B. J., Meldrum, F. C. and Christenson, H. K.: High-speed imaging of ice nucleation in water proves the existence of active sites, *Sci. Adv.*, 5(2), doi:10.1126/sciadv.aav4316, 2019.

Hoose, C., Kristjánsson, J. E., Chen, J. P. and Hazra, A.: A classical-theory-based parameterization of heterogeneous ice nucleation by mineral dust, soot, and biological particles in a global climate model, *J. Atmos. Sci.*, 67(8), 2483–2503, doi:10.1175/2010JAS3425.1, 2010.

Ickes, L., Welti, A., Hoose, C. and Lohmanna, U.: Classical Nucleation Theory of homogeneous freezing of water: Thermodynamic and kinetic parameters, *Phys. Chem. Chem. Phys.*, 17(8), 5514–5537, doi:10.1039/c4cp04184d, 2015.

Ickes, L., Porter, G. C. E., Wagner, R., Adams, M. P., Bierbauer, S., Bertram, A. K., Bilde, M., Christiansen, S., Ekman, A. M. L., Gorokhova, E., Höhler, K., Kiselev, A. A., Leck, C., Möhler, O., Murray, B. J., Schiebel, T., Ullrich, R. and Salter, M. E.: The ice-nucleating activity of Arctic sea surface microlayer samples and marine algal cultures, *Atmos. Chem. Phys.*, 20(18), 11089–11117, doi:10.5194/acp-20-11089-2020, 2020.

Isono, K., Komabayasi, M. and Ono, A.: Volcanoes as a source of atmospheric ice nuclei, *Nature*, 183(4657), 317–318, doi:10.1038/183317a0, 1959.

- Jaenicke, R.: Abundance of cellular material and proteins in the atmosphere, *Science* (80-. ), 308(5718), 73, doi:10.1126/science.1106335, 2005.
- Jaenicke, R., Matthias-Maser, S. and Gruber, S.: Omnipresence of biological material in the atmosphere, *Environ. Chem.*, 4(4), 217–220, doi:10.1071/EN07021, 2007.
- Jahn, L. G., Fahy, W. D., Williams, D. B. and Sullivan, R. C.: Role of Feldspar and Pyroxene Minerals in the Ice Nucleating Ability of Three Volcanic Ashes, *ACS Earth Sp. Chem.*, 3(4), 626–636, doi:10.1021/acsearthspacechem.9b00004, 2019.
- Jones, A. M. and Harrison, R. M.: The effects of meteorological factors on atmospheric bioaerosol concentrations – A review, *Sci. Total Environ.*, 326(1–3), 151–180, doi:10.1016/j.scitotenv.2003.11.021, 2004.
- Jones, H. M., Flynn, M. J., DeMott, P. J. and Möhler, O.: Manchester Ice Nucleus Counter (MINC) measurements from the 2007 International workshop on Comparing Ice nucleation Measuring Systems (ICIS-2007), *Atmos. Chem. Phys.*, 11(1), 53–65, doi:10.5194/acp-11-53-2011, 2011.
- Kamphus, M., Ettner-Mahl, M., Klimach, T., Drewnick, F., Keller, L., Cziczo, D. J., Mertes, S., Borrmann, S. and Curtius, J.: Chemical composition of ambient aerosol, ice residues and cloud droplet residues in mixed-phase clouds: Single particle analysis during the cloud and aerosol characterization experiment (CLACE 6), *Atmos. Chem. Phys.*, 10(16), 8077–8095, doi:10.5194/acp-10-8077-2010, 2010.
- Kanji, Z. A. and Abbatt, J. P. D.: The University of Toronto Continuous Flow Diffusion Chamber (UT-CFDC): A Simple Design for Ice Nucleation Studies, *Aerosol Sci. Technol.*, 43(7), 730–738, doi:10.1080/02786820902889861, 2009.
- Kanji, Z. A., Ladino, L. A., Wex, H., Boose, Y., Burkert-Kohn, M., Cziczo, D. J. and Krämer, M.: Overview of Ice Nucleating Particles, *Meteorol. Monogr.*, 58, 1.1-1.33, doi:10.1175/amsmonographs-d-16-0006.1, 2017.
- Kärcher, B. and Yu, F.: Role of aircraft soot emissions in contrail formation, *Geophys. Res. Lett.*, 36(1), doi:10.1029/2008GL036649, 2009.
- Kieft, T. L.: Ice Nucleation Activity in Lichens, *Appl. Environ. Microbiol.*, 54(7), 1678–1681, doi:10.1128/aem.54.7.1678-1681.1988, 1988.

Kohn, M., Lohmann, U., Welti, A. and Kanji, Z. A.: Immersion mode ice nucleation measurements with the new Portable Immersion Mode Cooling chamber (PIMCA), *J. Geophys. Res.*, 121(9), 4713–4733, doi:10.1002/2016JD024761, 2016.

Koop, T., Luo, B., Tsias, A. and Peter, T.: Water activity as the determinant for homogeneous ice nucleation in aqueous solutions, *Nature*, 406(6796), 611–614, doi:10.1038/35020537, 2000.

Kulkarni, G., Hiranuma, N., Möhler, O., Höhler, K., China, S., Cziczo, D. J. and Demott, P. J.: A new method for operating a continuous-flow diffusion chamber to investigate immersion freezing: Assessment and performance study, *Atmos. Meas. Tech.*, 13(12), 6631–6643, doi:10.5194/amt-13-6631-2020, 2020.

Lacher, L., Lohmann, U., Boose, Y., Zipori, A., Herrmann, E., Bukowiecki, N., Steinbacher, M. and Kanji, Z. A.: The Horizontal Ice Nucleation Chamber (HINC): INP measurements at conditions relevant for mixed-phase clouds at the High Altitude Research Station Jungfraujoch, *Atmos. Chem. Phys.*, 17(24), 15199–15224, doi:10.5194/acp-17-15199-2017, 2017.

Lacher, L., Adams, M. P., Barry, K., Bertozzi, B., Bingemer, H., Boffo, C., Bras, Y., Büttner, N., Castarede, D., Cziczo, D. J., DeMott, P. J., Fösig, R., Goodell, M., Höhler, K., Hill, T. C. J., Jentzsch, C., Ladino, L. A., Levin, E. J. T., Mertes, S., Möhler, O., Moore, K. A., Murray, B. J., Nadolny, J., Pfeuffer, T., Picard, D., Ramírez-Romero, C., Ribeiro, M., Richter, S., Schrod, J., Sellegri, K., Stratmann, F., Swanson, B. E., Thomson, E. S., Wex, H., Wolf, M. J. and Freney, E.: The Puy de Dôme Ice Nucleation Intercomparison Campaign (PICNIC): comparison between online and offline methods in ambient air, *Atmos. Chem. Phys.*, 24(4), 2651–2678, doi:10.5194/acp-24-2651-2024, 2024.

Levin, E. J. T., Mcmeeking, G. R., Demott, P. J., Mccluskey, C. S., Stockwell, C. E., Yokelson, R. J. and Kreidenweis, S. M.: A new method to determine the number concentrations of refractory black carbon ice nucleating particles, *Aerosol Sci. Technol.*, 48(12), 1264–1275, doi:10.1080/02786826.2014.977843, 2014.

Loeb, N. G., Wielicki, B. A., Doelling, D. R., Smith, G. L., Keyes, D. F., Kato, S., Manalo-Smith, N. and Wong, T.: Toward optimal closure of the Earth's top-of-atmosphere radiation budget, *J. Clim.*, 22(3), 748–766, doi:10.1175/2008JCLI2637.1, 2009.

Lohmann, U. and Feichter, J.: Global indirect aerosol effects: a review, *Atmos. Chem. Phys.*, 5(3), 715–737, doi:10.5194/acp-5-715-2005, 2005.

Lohmann, U., Lüönd, F. and Mahrt, F.: An introduction to clouds: From the microscale to climate., 2016.

Mahrt, F., Marcolli, C., David, R. O., Grönquist, P., Barthazy Meier, E. J., Lohmann, U. and Kanji, Z. A.: Ice nucleation abilities of soot particles determined with the Horizontal Ice Nucleation Chamber, *Atmos. Chem. Phys.*, 18(18), 13363–13392, doi:10.5194/acp-18-13363-2018, 2018.

Mangan, T. P., Atkinson, J. D., Neuberger, J. W., O’Sullivan, D., Wilson, T. W., Whale, T. F., Neve, L., Umo, N. S., Malkin, T. L. and Murray, B. J.: Heterogeneous Ice nucleation by Soufriere hills volcanic ash immersed in water droplets, *PloS One*, 12(1), e0169720, doi:10.1371/journal.pone.0169720, 2017.

Marcolli, C.: Deposition nucleation viewed as homogeneous or immersion freezing in pores and cavities, *Atmos. Chem. Phys.*, 14(4), 2071–2104, doi:10.5194/acp-14-2071-2014, 2014.

Marcolli, C., Gedamke, S., Peter, T. and Zobrist, B.: Efficiency of immersion mode ice nucleation on surrogates of mineral dust, *Atmos. Chem. Phys.*, 7(19), 5081–5091, doi:10.5194/acp-7-5081-2007, 2007.

Maters, E. C., Cimarelli, C., Casas, A. S., Dingwell, D. B. and Murray, B. J.: Volcanic ash ice-nucleating activity can be enhanced or depressed by ash-gas interaction in the eruption plume, *Earth Planet. Sci. Lett.*, 551, 116587, doi:10.1016/j.epsl.2020.116587, 2020.

Matthias-Maser, S. and Jaenicke, R.: The size distribution of primary biological aerosol particles with radii  $> 0.2 \mu\text{m}$  in an urban/rural influenced region, *Atmos. Res.*, 39(4), 279–286, doi:10.1016/0169-8095(95)00017-8, 1995.

Meinander, O., Dagsson-Waldhauserova, P., Amosov, P., Aseyeva, E., Atkins, C., Baklanov, A., Baldo, C., Barr, S. L., Barzycka, B., Benning, L. G., Cvetkovic, B., Enchilik, P., Frolov, D., Gassó, S., Kandler, K., Kasimov, N., Kavan, J., King, J., Koroleva, T., Krupskaya, V., Kulmala, M., Kusiak, M., Lappalainen, H. K., Laska, M., Lasne, J., Lewandowski, M., Luks, B., McQuaid, J. B., Moroni, B., Murray, B., Möhler, O., Nawrot, A., Nickovic, S., O’Neill, N. T., Pejanovic, G., Popovicheva, O., Ranjbar, K., Romanias, M., Samonova, O., Sanchez-Marroquin, A., Schepanski, K., Semenov, I., Sharapova, A., Shevnina, E., Shi, Z., Sofiev, M., Thevenet, F., Thorsteinsson, T., Timofeev, M., Umo, N. S., Uppstu, A., Urupina, D., Varga, G., Werner, T., Arnalds, O. and Vukovic Vimic, A.:

- Newly identified climatically and environmentally significant high-latitude dust sources, *Atmos. Chem. Phys.*, 22(17), 11889–11930, doi:10.5194/acp-22-11889-2022, 2022.
- Möhler, O., Georgakopoulos, D. G., Morris, C. E., Benz, S., Ebert, V., Hunsmann, S., Saathoff, H., Schnaiter, M. and Wagner, R.: Heterogeneous ice nucleation activity of bacteria: New laboratory experiments at simulated cloud conditions, *Biogeosciences*, 5(5), 1425–1435, doi:10.5194/bg-5-1425-2008, 2008.
- Möhler, O., Adams, M., Lacher, L., Vogel, F., Nadolny, J., Ullrich, R., Boffo, C., Pfeuffer, T., Hobl, A., Weiß, M., Vepuri, H. S. K., Hiranuma, N. and Murray, B. J.: The Portable Ice Nucleation Experiment (PINE): A new online instrument for laboratory studies and automated long-term field observations of ice-nucleating particles, *Atmos. Meas. Tech.*, 14(2), 1143–1166, doi:10.5194/amt-14-1143-2021, 2021.
- Morris, C. E., Georgakopoulos, D. G. and Sands, D. C.: Ice nucleation active bacteria and their potential role in precipitation, *J. Phys. IV JP*, 121, 87–103, doi:10.1051/jp4:2004121004, 2004.
- Murphy, D. M. and Koop, T.: Review of the vapour pressures of ice and supercooled water for atmospheric applications, *Q. J. R. Meteorol. Soc.*, 131(608), 1539–1565, doi:10.1256/qj.04.94, 2005.
- Murray, B. J., Broadley, S. L., Wilson, T. W., Bull, S. J., Wills, R. H., Christenson, H. K. and Murray, E. J.: Kinetics of the homogeneous freezing of water, *Phys. Chem. Chem. Phys.*, 12(35), 10380–10387, doi:10.1039/c003297b, 2010.
- Murray, B. J., Broadley, S. L., Wilson, T. W., Atkinson, J. D. and Wills, R. H.: Heterogeneous freezing of water droplets containing kaolinite particles, *Atmos. Chem. Phys.*, 11(9), 4191–4207, doi:10.5194/acp-11-4191-2011, 2011.
- Murray, B. J., O’Sullivan, D., Atkinson, J. D. and Webb, M. E.: Ice nucleation by particles immersed in supercooled cloud droplets, *Chem. Soc. Rev.*, 41(19), 6519, doi:10.1039/c2cs35200a, 2012.
- Murray, B. J., Carslaw, K. S. and Field, P. R.: Opinion: Cloud-phase climate feedback and the importance of ice-nucleating particles, *Atmos. Chem. Phys.*, 21(2), 665–679, doi:10.5194/acp-21-665-2021, 2021.

Nakagawa, M. and Ohba, T.: Minerals in Volcanic Ash 1: Primary Minerals and Volcanic Glass, *Glob. Environ. Res.*, 6(October), 41–51 [online] Available from: <http://www.airies.or.jp/publication/ger/pdf/06-2-06.pdf>, 2003.

Nichman, L., Wolf, M., Davidovits, P., Onasch, T. B., Zhang, Y., Worsnop, D. R., Bhandari, J., Mazzoleni, C. and Cziczo, D. J.: Laboratory study of the heterogeneous ice nucleation on black-carbon-containing aerosol, *Atmos. Chem. Phys.*, 19(19), 12175–12194, doi:10.5194/acp-19-12175-2019, 2019.

O’Sullivan, D., Murray, B. J., Malkin, T. L., Whale, T. F., Umo, N. S., Atkinson, J. D., Price, H. C., Baustian, K. J., Browse, J. and Webb, M. E.: Ice nucleation by fertile soil dusts: Relative importance of mineral and biogenic components, *Atmos. Chem. Phys.*, 14(4), 1853–1867, doi:10.5194/acp-14-1853-2014, 2014.

Pandey, R., Usui, K., Livingstone, R. A., Fischer, S. A., Pfaendtner, J., Backus, E. H. G., Nagata, Y., Fröhlich-Nowoisky, J., Schmäser, L., Mauri, S., Scheel, J. F., Knopf, D. A., Pöschl, U., Bonn, M. and Weidner, T.: Ice-nucleating bacteria control the order and dynamics of interfacial water, *Sci. Adv.*, 2(4), e1501630, doi:10.1126/sciadv.1501630, 2016.

Petters, M. D. and Kreidenweis, S. M.: A single parameter representation of hygroscopic growth and cloud condensation nucleus activity, *Atmos. Chem. Phys.*, 7(8), 1961–1971, doi:10.5194/acp-7-1961-2007, 2007.

Piaggi, P. M., Weis, J., Panagiotopoulos, A. Z., Debenedetti, P. G. and Car, R.: Homogeneous ice nucleation in an ab initio machine-learning model of water, *Proc. Natl. Acad. Sci. U. S. A.*, 119(33), doi:10.1073/pnas.2207294119, 2022.

Ponsonby, J., King, L., Murray, B. J. and Stettler, M. E. J.: Jet aircraft lubrication oil droplets as contrail ice-forming particles, *Atmos. Chem. Phys.*, 24(3), 2045–2058, doi:10.5194/acp-24-2045-2024, 2024.

Pouleur, S., Richard, C., Martin, J. and Antoun, H.: Ice nucleation activity in *Fusarium acuminatum* and *Fusarium avenaceum*, *Appl. Environ. Microbiol.*, 58(9), 2960–2964, doi:10.1128/aem.58.9.2960-2964.1992, 1992.

Pratt, K. A., Demott, P. J., French, J. R., Wang, Z., Westphal, D. L., Heymsfield, A. J., Twohy, C. H., Prenni, A. J. and Prather, K. A.: In situ detection of biological particles in cloud ice-crystals, *Nat. Geosci.*, 2(6), 398–401, doi:10.1038/ngeo521, 2009.

Prospero, J. M., Ginoux, P., Torres, O., Nicholson, S. E. and Gill, T. E.: Environmental characterization of global sources of atmospheric soil dust identified with the Nimbus 7 Total Ozone Mapping Spectrometer (TOMS) absorbing aerosol product, *Rev. Geophys.*, 40(1), 2-1-2–31, doi:10.1029/2000RG000095, 2002.

Ramanathan, V., Cess, R. D., Harrison, E. F., Minnis, P., Barkstrom, B. R., Ahmad, E. and Hartmann, D.: Cloud-radiative forcing and climate: Results from the earth radiation budget experiment, *Science (80-. )*, 243(4887), 57–63, doi:10.1126/science.243.4887.57, 1989.

Rasmussen, D. H.: Thermodynamics and nucleation phenomena – A set of experimental observations, *J. Cryst. Growth*, 56(1), 56–66, doi:10.1016/0022-0248(82)90012-4, 1982.

Reicher, N., Segev, L. and Rudich, Y.: The Weizmann Supercooled Droplets Observation on a Microarray (WISDOM) and application for ambient dust, *Atmos. Meas. Tech.*, 11(1), 233–248, doi:10.5194/amt-11-233-2018, 2018.

Richardson, M. S., DeMott, P. J., Kreidenweis, S. M., Cziczo, D. J., Dunlea, E. J., Jimenez, J. L., Thomson, D. S., Ashbaugh, L. L., Borys, R. D., Westphal, D. L., Casuccio, G. S. and Lersch, T. L.: Measurements of heterogeneous ice nuclei in the western United States in springtime and their relation to aerosol characteristics, *J. Geophys. Res. Atmos.*, 112(2), doi:10.1029/2006JD007500, 2007.

Rogers, D. C.: Development of a continuous flow thermal gradient diffusion chamber for ice nucleation studies, *Atmos. Res.*, 22(2), 149–181, doi:10.1016/0169-8095(88)90005-1, 1988.

Rossow, W. B. and Schiffer, R. A.: Advances in Understanding Clouds from ISCCP, *Bull. Am. Meteorol. Soc.*, 80(11), 2261–2287, doi:10.1175/1520-0477(1999)080<2261:AIUCFI>2.0.CO;2, 1999.

Saathoff, H., Möhler, O., Schurath, U., Kamm, S., Dippel, B. and Mihelcic, D.: The AIDA soot aerosol characterisation campaign 1999, *J. Aerosol Sci.*, 34(10), 1277–1296, doi:10.1016/S0021-8502(03)00363-X, 2003.

Schneider, S. H.: Cloudiness as a Global Climatic Feedback Mechanism: The Effects on the Radiation Balance and Surface Temperature of Variations in Cloudiness, *J. Atmos. Sci.*, 29(8), 1413–1422, doi:10.1175/1520-0469(1972)029<1413:caagcf>2.0.co;2, 1972.

- Schwidetzky, R., de Almeida Ribeiro, I., Bothen, N., Backes, A. T., DeVries, A. L., Bonn, M., Fröhlich-Nowoisky, J., Molinero, V. and Meister, K.: Functional aggregation of cell-free proteins enables fungal ice nucleation, *Proc. Natl. Acad. Sci. U. S. A.*, 120(46), e2303243120, doi:10.1073/pnas.2303243120, 2023.
- Steinke, I., Möhler, O., Kiselev, A., Niemand, M., Saathoff, H., Schnaiter, M., Skrotzki, J., Hoose, C. and Leisner, T.: Ice nucleation properties of fine ash particles from the Eyjafjallajökull eruption in April 2010, *Atmos. Chem. Phys.*, 11(24), 12945–12958, doi:10.5194/acp-11-12945-2011, 2011.
- Stetzer, O., Baschek, B., Lüönd, F. and Lohmann, U.: The Zurich Ice Nucleation Chamber (ZINC)-A New Instrument to Investigate Atmospheric Ice Formation, *Aerosol Sci. Technol.*, 42(1), 64–74, doi:10.1080/02786820701787944, 2008.
- Tarn, M. D., Sikora, S. N. F., Porter, G. C. E., Wyld, B. V., Alayof, M., Reicher, N., Harrison, A. D., Rudich, Y., Shim, J. U. and Murray, B. J.: On-chip analysis of atmospheric ice-nucleating particles in continuous flow, *Lab Chip*, 20(16), 2889–2910, doi:10.1039/d0lc00251h, 2020.
- Tegen, I. and Fung, I.: Contribution to the atmospheric mineral aerosol load from land surface modification, *J. Geophys. Res.*, 100(D9), doi:10.1029/95jd02051, 1995.
- Twohy, C. H., DeMott, P. J., Pratt, K. A., Subramanian, R., Kok, G. L., Murphy, S. M., Lersch, T., Heymsfield, A. J., Wang, Z., Prather, K. A. and Seinfeld, J. H.: Relationships of biomass-burning aerosols to ice in orographic wave clouds, *J. Atmos. Sci.*, 67(8), 2437–2450, doi:10.1175/2010JAS3310.1, 2010.
- Umo, N. S., Murray, B. J., Baeza-Romero, M. T., Jones, J. M., Lea-Langton, A. R., Malkin, T. L., O’Sullivan, D., Neve, L., Plane, J. M. C. and Williams, A.: Ice nucleation by combustion ash particles at conditions relevant to mixed-phase clouds, *Atmos. Chem. Phys.*, 15(9), 5195–5210, doi:10.5194/acp-15-5195-2015, 2015.
- Umo, N. S., Wagner, R., Ullrich, R., Kiselev, A., Saathoff, H., Weidler, P. G., Cziczo, D. J., Leisner, T. and Möhler, O.: Enhanced ice nucleation activity of coal fly ash aerosol particles initiated by ice-filled pores, *Atmos. Chem. Phys.*, 19(13), 8783–8800, doi:10.5194/acp-19-8783-2019, 2019.
- Vali, G.: Freezing Rate Due to Heterogeneous Nucleation, *J. Atmos. Sci.*, 51(13), 1843–1856, doi:10.1175/1520-0469(1994)051<1843:frdthn>2.0.co;2, 1994.

- Vali, G.: Repeatability and randomness in heterogeneous freezing nucleation, *Atmos. Chem. Phys.*, 8(16), 5017–5031, doi:10.5194/acp-8-5017-2008, 2008.
- Vali, G. and Stansbury, E. J.: TIME-DEPENDENT CHARACTERISTICS OF THE HETEROGENEOUS NUCLEATION OF ICE, *Can. J. Phys.*, 44(3), 477–502, doi:10.1139/p66-044, 1966.
- Vergara-Temprado, J., Holden, M. A., Orton, T. R., O’Sullivan, D., Umo, N. S., Browse, J., Reddington, C., Baeza-Romero, M. T., Jones, J. M., Lea-Langton, A., Williams, A., Carslaw, K. S. and Murray, B. J.: Is Black Carbon an Unimportant Ice-Nucleating Particle in Mixed-Phase Clouds?, *J. Geophys. Res. Atmos.*, 123(8), 4273–4283, doi:10.1002/2017JD027831, 2018.
- Vernier, J. P., Fairlie, T. D., Deshler, T., Natarajan, M., Knepp, T., Foster, K., Wienhold, F. G., Bedka, K. M., Thomason, L. and Trepte, C.: In situ and space-based observations of the Kelud volcanic plume: The persistence of ash in the lower stratosphere, *J. Geophys. Res.*, 121(18), 11,104–11,118, doi:10.1002/2016JD025344, 2016.
- Vial, J., Dufresne, J. L. and Bony, S.: On the interpretation of inter-model spread in CMIP5 climate sensitivity estimates, *Clim. Dyn.*, 41(11–12), 3339–3362, doi:10.1007/s00382-013-1725-9, 2013.
- Vonnegut, B. and Baldwin, M.: Repeated Nucleation of a Supercooled Water Sample that Contains Silver Iodide Particles, *J. Clim. Appl. Meteorol.*, 23(3), 486–490, doi:10.1175/1520-0450(1984)023<0486:RNOASW>2.0.CO;2, 1984.
- Wagner, R., Linke, C., Naumann, K.-H., Schnaiter, M., Vragel, M., Gangl, M. and Horvath, H.: A review of optical measurements at the aerosol and cloud chamber AIDA, *J. Quant. Spectrosc. Radiat. Transf.*, 110(11), 930–949, doi:10.1016/j.jqsrt.2009.01.026, 2009.
- Westbrook, C. D. and Illingworth, A. J.: Evidence that ice forms primarily in supercooled liquid clouds at temperatures  $>-27^{\circ}\text{C}$ , *Geophys. Res. Lett.*, 38(14), doi:10.1029/2011GL048021, 2011.
- Wex, H., Augustin-Bauditz, S., Boose, Y., Budke, C., Curtius, J., Diehl, K., Dreyer, A., Frank, F., Hartmann, S., Hiranuma, N., Jantsch, E., Kanji, Z. A., Kiselev, A., Koop, T., Möhler, O., Niedermeier, D., Nillius, B., Rösch, M., Rose, D., Schmidt, C., Steinke, I. and Stratmann, F.: Intercomparing different devices for the investigation of ice nucleating

particles using Snomax® as test substance, *Atmos. Chem. Phys.*, 15(3), 1463–1485, doi:10.5194/acp-15-1463-2015, 2015.

Whale, T. F., Murray, B. J., O’Sullivan, D., Wilson, T. W., Umo, N. S., Baustian, K. J., Atkinson, J. D., Workneh, D. A. and Morris, G. J.: A technique for quantifying heterogeneous ice nucleation in microlitre supercooled water droplets, *Atmos. Meas. Tech.*, 8(6), 2437–2447, doi:10.5194/amt-8-2437-2015, 2015.

Williams, S. N. and Self, S.: The October 1902 plinian eruption of Santa Maria volcano, Guatemala, *J. Volcanol. Geotherm. Res.*, 16(1–2), 33–56, doi:10.1016/0377-0273(83)90083-5, 1983.

WMO, W. M. O.: *International Cloud Atlas: Manual on the Observation of Clouds and Other Meteors.*, World Meteorol. Organ. [online] Available from: <https://cloudatlas.wmo.int/en/home.html>, 2017.

Xu, M., Yu, D., Yao, H., Liu, X. and Qiao, Y.: Coal combustion-generated aerosols: Formation and properties, *Proc. Combust. Inst.*, 33(1), 1681–1697, doi:10.1016/j.proci.2010.09.014, 2011.

Yoshimori, M., Hugo Lambert, F., Webb, M. J. and Andrews, T.: Fixed anvil temperature feedback: Positive, zero, or negative?, *J. Clim.*, 33(7), 2719–2739, doi:10.1175/JCLI-D-19-0108.1, 2020.

Zender, C. S., Miller, R. L. and Tegen, I.: Quantifying mineral dust mass budgets: Terminology, constraints, and current estimates, *Eos (Washington. DC.)*, 85(48), doi:10.1029/2004EO480002, 2004.

Zenker, J., Collier, K. N., Xu, G., Yang, P., Levin, E. J. T., Suski, K. J., DeMott, P. J. and Brooks, S. D.: Using depolarization to quantify ice nucleating particle concentrations: a new method, *Atmos. Meas. Tech.*, 10(12), 4639–4657, doi:10.5194/amt-10-4639-2017, 2017. Adams, M. P.: Measurement and characterisation of atmospheric ice-nucleating particles, University of Leeds., 2020.

Adams, M. P., Atanasova, N. S., Sofieva, S., Ravantti, J., Heikkinen, A., Brasseur, Z., Duplissy, J., Bamford, D. H. and Murray, B. J.: Ice nucleation by viruses and their potential for cloud glaciation, *Biogeosciences*, 18(14), 4431–4444, doi:10.5194/bg-18-4431-2021, 2021.

Amino, T., Iizuka, Y., Matoba, S., Shimada, R., Oshima, N., Suzuki, T., Ando, T., Aoki,

T. and Fujita, K.: Increasing dust emission from ice free terrain in southeastern Greenland since 2000, *Polar Sci.*, 27, 100599, doi:10.1016/j.polar.2020.100599, 2021.

Ansmann, A., Tesche, M., Althausen, D., Müller, D., Seifert, P., Freudenthaler, V., Heese, B., Wiegner, M., Pisani, G., Knippertz, P. and Dubovik, O.: Influence of Saharan dust on cloud glaciation in southern Morocco during the Saharan Mineral Dust Experiment, *J. Geophys. Res. Atmos.*, 113(4), doi:10.1029/2007JD008785, 2008.

Ansmann, A., Tesche, M., Seifert, P., Althausen, D., Engelmann, R., Fruntke, J., Wandinger, U., Mattis, I. and Müller, D.: Evolution of the ice phase in tropical altocumulus: SAMUM lidar observations over Cape Verde, *J. Geophys. Res. Atmos.*, 114(17), doi:10.1029/2008JD011659, 2009.

Atkinson, J. D., Murray, B. J., Woodhouse, M. T., Whale, T. F., Baustian, K. J., Carslaw, K. S., Dobbie, S., O'Sullivan, D. and Malkin, T. L.: The importance of feldspar for ice nucleation by mineral dust in mixed-phase clouds, *Nature*, 498(7454), 355–358, doi:10.1038/nature12278, 2013.

Bakhshaii, A. and Stull, R.: Saturated pseudoadiabats-A noniterative approximation, *J. Appl. Meteorol. Climatol.*, 52(1), 5–15, doi:10.1175/JAMC-D-12-062.1, 2013.

Barr, S. L., Wyld, B., McQuaid, J. B., Neely, R. R. and Murray, B. J.: Southern Alaska as a source of atmospheric mineral dust and ice-nucleating particles, *Sci. Adv.*, 9(33), eadg3708, doi:10.1126/sciadv.adg3708, 2023.

Benz, S., Megahed, K., Möhler, O., Saathoff, H., Wagner, R. and Schurath, U.: T-dependent rate measurements of homogeneous ice nucleation in cloud droplets using a large atmospheric simulation chamber, *J. Photochem. Photobiol. A Chem.*, 176(1-3 SPEC. ISS.), 208–217, doi:10.1016/j.jphotochem.2005.08.026, 2005.

De Boer, G., Morrison, H., Shupe, M. D. and Hildner, R.: Evidence of liquid dependent ice nucleation in high-latitude stratiform clouds from surface remote sensors, *Geophys. Res. Lett.*, 38(1), doi:10.1029/2010GL046016, 2011.

Brabets, T. P.: *Geomorphology of the lower Copper River, Alaska.*, 1997.

Brasseur, Z., Castarède, D., Thomson, E. S., Adams, M. P., Drossaert Van Dusseldorp, S., Heikkilä, P., Korhonen, K., Lampilahti, J., Paramonov, M., Schneider, J., Vogel, F., Wu, Y., Abbatt, J. P. D., Atanasova, N. S., Bamford, D. H., Bertozzi, B., Boyer, M., Brus, D., Daily, M. I., Fösig, R., Gute, E., Harrison, A. D., Hietala, P., Höhler, K., Kanji, Z. A.,

Keskinen, J., Lacher, L., Lampimäki, M., Levula, J., Manninen, A., Nadolny, J., Peltola, M., Porter, G. C. E., Poutanen, P., Proske, U., Schorr, T., Silas Umo, N., Stenszky, J., Virtanen, A., Moisseev, D., Kulmala, M., Murray, B. J., Petäjä, T., Möhler, O. and Duplissy, J.: Measurement report: Introduction to the HyICE-2018 campaign for measurements of ice-nucleating particles and instrument inter-comparison in the Hyytiälä boreal forest, *Atmos. Chem. Phys.*, 22(8), 5117–5145, doi:10.5194/acp-22-5117-2022, 2022.

Broadley, S. L., Murray, B. J., Herbert, R. J., Atkinson, J. D., Dobbie, S., Malkin, T. L., Condliffe, E. and Neve, L.: Immersion mode heterogeneous ice nucleation by an illite rich powder representative of atmospheric mineral dust, *Atmos. Chem. Phys.*, 12(1), 287–307, doi:10.5194/acp-12-287-2012, 2012.

Bruns, E. A., Krapf, M., Orasche, J., Huang, Y., Zimmermann, R., Drinovec, L., Močnik, G., El-Haddad, I., Slowik, J. G., Dommen, J., Baltensperger, U. and Prévôt, A. S. H.: Characterization of primary and secondary wood combustion products generated under different burner loads, *Atmos. Chem. Phys.*, 15(5), 2825–2841, doi:10.5194/acp-15-2825-2015, 2015.

Budke, C. and Koop, T.: BINARY: An optical freezing array for assessing temperature and time dependence of heterogeneous ice nucleation, *Atmos. Meas. Tech.*, 8(2), 689–703, doi:10.5194/amt-8-689-2015, 2015.

Bullard, J. E. and Mockford, T.: Seasonal and decadal variability of dust observations in the Kangerlussuaq area, west Greenland, Arctic, *Antarct. Alp. Res.*, 50(1), doi:10.1080/15230430.2017.1415854, 2018.

Bullard, J. E., Baddock, M., Bradwell, T., Crusius, J., Darlington, E., Gaiero, D., Gassó, S., Gisláttir, G., Hodgkins, R., McCulloch, R., McKenna-Neuman, C., Mockford, T., Stewart, H. and Thorsteinsson, T.: High-latitude dust in the Earth system, *Rev. Geophys.*, 54(2), 447–485, doi:10.1002/2016RG000518, 2016.

Bullard, J. E., Prater, C., Baddock, M. C. and Anderson, N. J.: Diurnal and seasonal source-proximal dust concentrations in complex terrain, West Greenland, *Earth Surf. Process. Landforms*, 48(14), 2808–2827, doi:10.1002/esp.5661, 2023.

Burrows, S. M., McCluskey, C. S., Cornwell, G., Steinke, I., Zhang, K., Zhao, B., Zawadowicz, M., Raman, A., Kulkarni, G., China, S., Zelenyuk, A. and DeMott, P. J.: Ice-Nucleating Particles That Impact Clouds and Climate: Observational and Modeling

Research Needs, *Rev. Geophys.*, 60(2), e2021RG000745, doi:10.1029/2021RG000745, 2022.

Campbell, J. M. and Christenson, H. K.: Nucleation- and Emergence-Limited Growth of Ice from Pores, *Phys. Rev. Lett.*, 120(16), doi:10.1103/PhysRevLett.120.165701, 2018.

Carnahan, E., Wolfenbarger, N. S., Jordan, J. S. and Hesse, M. A.: New insights into temperature-dependent ice properties and their effect on ice shell convection for icy ocean worlds, *Earth Planet. Sci. Lett.*, 563, doi:10.1016/j.epsl.2021.116886, 2021.

Castarède, D., Brasseur, Z., Wu, Y., Kanji, Z. A., Hartmann, M., Ahonen, L., Bilde, M., Kulmala, M., Petäjä, T., Pettersson, J. B. C., Sierau, B., Stetzer, O., Stratmann, F., Svenningsson, B., Swietlicki, E., Thu Nguyen, Q., Duplissy, J. and Thomson, E. S.: Development and characterization of the Portable Ice Nucleation Chamber 2 (PINCii), *Atmos. Meas. Tech.*, 16(16), 3881–3899, doi:10.5194/amt-16-3881-2023, 2023.

Chen, J., Wu, Z., Augustin-Bauditz, S., Grawe, S., Hartmann, M., Pei, X., Liu, Z., Ji, D. and Wex, H.: Ice-nucleating particle concentrations unaffected by urban air pollution in Beijing, China, *Atmos. Chem. Phys.*, 18(5), 3523–3539, doi:10.5194/acp-18-3523-2018, 2018.

Chen, T., Rossow, W. B. and Zhang, Y.: Radiative effects of cloud-type variations, *J. Clim.*, 13(1), 264–286, doi:10.1175/1520-0442(2000)013<0264:REOCTV>2.0.CO;2, 2000.

Chou, C.: Investigation of Ice Nucleation Properties onto Soot, Bioaerosol and Mineral Dust during Different Measurement Campaigns, ETH ZURICH., 2011.

Christner, B. C., Morris, C. E., Foreman, C. M., Cai, R. and Sands, D. C.: Ubiquity of biological ice nucleators in snowfall, *Science* (80-. ), 319(5867), 1214, doi:10.1126/science.1149757, 2008.

Connolly, P. J., Möhler, O., Field, P. R., Saathoff, H., Burgess, R., Choularton, T. and Gallagher, M.: Studies of heterogeneous freezing by three different desert dust samples, *Atmos. Chem. Phys.*, 9(8), 2805–2824, doi:10.5194/acp-9-2805-2009, 2009.

Creamean, J. M., Suski, K. J., Rosenfeld, D., Cazorla, A., DeMott, P. J., Sullivan, R. C., White, A. B., Ralph, F. M., Minnis, P., Comstock, J. M., Tomlinson, J. M. and Prather, K. A.: Dust and biological aerosols from the Sahara and Asia influence precipitation in the Western U.S, *Science* (80-. ), 340(6127), 1572–1578, doi:10.1126/science.1227279,

2013.

Crusius, J., Schroth, A. W., Gassó, S., Moy, C. M., Levy, R. C. and Gatica, M.: Glacial flour dust storms in the Gulf of Alaska: Hydrologic and meteorological controls and their importance as a source of bioavailable iron, *Geophys. Res. Lett.*, 38(6), doi:10.1029/2010GL046573, 2011.

Cziczo, D. J., Murphy, D. M., Hudson, P. K. and Thomson, D. S.: Single particle measurements of the chemical composition of cirrus ice residue during CRYSTAL-FACE, *J. Geophys. Res. Atmos.*, 109(4), doi:10.1029/2003jd004032, 2004.

Cziczo, D. J., Froyd, K. D., Hoose, C., Jensen, E. J., Diao, M., Zondlo, M. A., Smith, J. B., Twohy, C. H. and Murphy, D. M.: Clarifying the dominant sources and mechanisms of cirrus cloud formation, *Science* (80-. ), 340(6138), 1320–1324, doi:10.1126/science.1234145, 2013.

Daily, M. I., Tarn, M. D., Whale, T. F. and Murray, B. J.: An evaluation of the heat test for the ice-nucleating ability of minerals and biological material, *Atmos. Meas. Tech.*, 15(8), 2635–2665, doi:10.5194/amt-15-2635-2022, 2022.

David, R. O., Marcolli, C., Fahrni, J., Qiu, Y., Perez Sirkin, Y. A., Molinero, V., Mahrt, F., Brühwiler, D., Lohmann, U. and Kanji, Z. A.: Pore condensation and freezing is responsible for ice formation below water saturation for porous particles, *Proc. Natl. Acad. Sci.*, 116(17), 8184–8189, doi:10.1073/pnas.1813647116, 2019.

David, R. O., Fahrni, J., Marcolli, C., Mahrt, F., Brühwiler, D. and Kanji, Z. A.: The role of contact angle and pore width on pore condensation and freezing, *Atmos. Chem. Phys.*, 20(15), 9419–9440, doi:10.5194/acp-20-9419-2020, 2020.

Delmelle, P., Lambert, M., Dufrêne, Y., Gerin, P. and Óskarsson, N.: Gas/aerosol-ash interaction in volcanic plumes: New insights from surface analyses of fine ash particles, *Earth Planet. Sci. Lett.*, 259(1–2), 159–170, doi:10.1016/j.epsl.2007.04.052, 2007.

Delort, A. M., Vaïtilingom, M., Amato, P., Sancelme, M., Parazols, M., Mailhot, G., Laj, P. and Deguillaume, L.: A short overview of the microbial population in clouds: Potential roles in atmospheric chemistry and nucleation processes, *Atmos. Res.*, 98(2–4), 249–260, doi:10.1016/j.atmosres.2010.07.004, 2010.

Demott, P. J. and Rogers, D. C.: Freezing nucleation rates of dilute solution droplets measured between  $-30^{\circ}$  and  $-40^{\circ}\text{C}$  in laboratory simulations of natural clouds, *J. Atmos.*

Sci., 47(9), 1056–1064, doi:10.1175/1520-0469(1990)047<1056:FNRODS>2.0.CO;2, 1990.

DeMott, P. J., Sassen, K., Poellot, M. R., Baumgardner, D., Rogers, D. C., Brooks, S. D., Prenni, A. J. and Kreidenweis, S. M.: African dust aerosols as atmospheric ice nuclei, *Geophys. Res. Lett.*, 30(14), doi:10.1029/2003GL017410, 2003.

DeMott, P. J., Möhler, O., Cziczo, D. J., Hiranuma, N., Petters, M. D., Petters, S. S., Belosi, F., Bingemer, H. G., Brooks, S. D., Budke, C., Burkert-Kohn, M., Collier, K. N., Danielczok, A., Eppers, O., Felgitsch, L., Garimella, S., Grothe, H., Herenz, P., Hill, T. C. J., Höhler, K., Kanji, Z. A., Kiselev, A., Koop, T., Kristensen, T. B., Krüger, K., Kulkarni, G., Levin, E. J. T., Murray, B. J., Nicosia, A., O’Sullivan, D., Peckhaus, A., Polen, M. J., Price, H. C., Reicher, N., Rothenberg, D. A., Rudich, Y., Santachiara, G., Schiebel, T., Schrod, J., Seifried, T. M., Stratmann, F., Sullivan, R. C., Suski, K. J., Szakáll, M., Taylor, H. P., Ullrich, R., Vergara-Temprado, J., Wagner, R., Whale, T. F., Weber, D., Welti, A., Wilson, T. W., Wolf, M. J. and Zenker, J.: The Fifth International Workshop on Ice Nucleation phase 2 (FIN-02): Laboratory intercomparison of ice nucleation measurements, *Atmos. Meas. Tech.*, 11(11), 6231–6257, doi:10.5194/amt-11-6231-2018, 2018.

Dentener, F., Kinne, S., Bond, T., Boucher, O., Cofala, J., Generoso, S., Ginoux, P., Gong, S., Hoelzemann, J. J., Ito, A., Marelli, L., Penner, J. E., Putaud, J. P., Textor, C., Schulz, M., Van Der Werf, G. R. and Wilson, J.: Emissions of primary aerosol and precursor gases in the years 2000 and 1750 prescribed data-sets for AeroCom, *Atmos. Chem. Phys.*, 6(12), 4321–4344, doi:10.5194/acp-6-4321-2006, 2006.

Després, V. R., Alex Huffman, J., Burrows, S. M., Hoose, C., Safatov, A. S., Buryak, G., Fröhlich-Nowoisky, J., Elbert, W., Andreae, M. O., Pöschl, U. and Jaenicke, R.: Primary biological aerosol particles in the atmosphere: A review, *Tellus, Ser. B Chem. Phys. Meteorol.*, 64(1), doi:10.3402/tellusb.v64i0.15598, 2012.

Duan, P., Hu, W., Wu, Z., Bi, K., Zhu, J. and Fu, P.: Ice nucleation activity of airborne pollen: A short review of results from laboratory experiments, *Atmos. Res.*, 285, doi:10.1016/j.atmosres.2023.106659, 2023.

Durant, A. J., Shaw, R. A., Rose, W. I., Mi, Y. and Ernst, G. G. J.: Ice nucleation and overseeding of ice in volcanic clouds, *J. Geophys. Res. Atmos.*, 113(9), 9206, doi:10.1029/2007JD009064, 2008.

- Durant, A. J., Bonadonna, C. and Horwell, C. J.: Atmospheric and environmental impacts of volcanic particulates, *Elements*, 6(4), 235–240, doi:10.2113/gselements.6.4.235, 2010.
- Engelstaedter, S., Tegen, I. and Washington, R.: North African dust emissions and transport, *Earth-Science Rev.*, 79(1–2), 73–100, doi:10.1016/j.earscirev.2006.06.004, 2006.
- Engwell, S. and Eychenne, J.: Contribution of Fine Ash to the Atmosphere From Plumes Associated With Pyroclastic Density Currents, in *Volcanic Ash: Hazard Observation*, pp. 68–85, Elsevier., 2016.
- Espinosa, J. R., Navarro, C., Sanz, E., Valeriani, C. and Vega, C.: On the time required to freeze water, *J. Chem. Phys.*, 145(21), 211922, doi:10.1063/1.4965427, 2016.
- Fahy, W. D., Maters, E. C., Giese Miranda, R., Adams, M. P., Jahn, L. G., Sullivan, R. C. and Murray, B. J.: Volcanic ash ice nucleation activity is variably reduced by aging in water and sulfuric acid: the effects of leaching, dissolution, and precipitation, *Environ. Sci. Atmos.*, 2(1), 85–99, doi:10.1039/D1EA00071C, 2022.
- Forster, P., Storelvmo, T., Armour, K., Collins, W., Dufresne, J. L., Frame, D., Lunt, D. J., Mauritsen, T., Palmer, M. D., Watanabe, M., Wild, M. and Zhang, H.: The Earth's Energy Budget, Climate Feedbacks and Climate Sensitivity, in *Climate Change 2021 – The Physical Science Basis Contribution of Working Group I to the Sixth Assessment Report of the Intergovernmental Panel on Climate Change*, pp. 923–1054., 2023.
- Friedman, B., Kulkarni, G., Beránek, J., Zelenyuk, A., Thornton, J. A. and Cziczo, D. J.: Ice nucleation and droplet formation by bare and coated soot particles, *J. Geophys. Res. Atmos.*, 116(17), doi:10.1029/2011JD015999, 2011.
- Garimella, S., Kristensen, T. B., Ignatius, K., Welti, A., Voigtländer, J., Kulkarni, G. R., Sagan, F., Kok, G. L., Dorsey, J., Nichman, L., Rothenberg, D. A., Rösch, M., Kirchgäßner, A. C. R., Ladkin, R., Wex, H., Wilson, T. W., Ladino, L. A., Abbatt, J. P. D., Stetzer, O., Lohmann, U., Stratmann, F. and Cziczo, D. J.: The SPectrometer for Ice Nuclei (SPIN): an instrument to investigate ice nucleation, *Atmos. Meas. Tech.*, 9(7), 2781–2795, doi:10.5194/amt-9-2781-2016, 2016.
- Genareau, K., Cloer, S. M., Primm, K., Tolbert, M. A. and Woods, T. W.: Compositional and mineralogical effects on ice nucleation activity of volcanic ash, *Atmosphere (Basel)*, 9(7), 238, doi:10.3390/atmos9070238, 2018.

Glaze, L. S., Baloga, S. M. and Wilson, L.: Transport of atmospheric water vapor by volcanic eruption columns, *J. Geophys. Res. Atmos.*, 102(5), 6099–6108, doi:10.1029/96jd03125, 1997.

Grawe, S., Augustin-Bauditz, S., Clemen, H. C., Ebert, M., Eriksen Hammer, S., Lubitz, J., Reicher, N., Rudich, Y., Schneider, J., Staacke, R., Stratmann, F., Welti, A. and Wex, H.: Coal fly ash: Linking immersion freezing behavior and physicochemical particle properties, *Atmos. Chem. Phys.*, 18(19), 13903–13923, doi:10.5194/acp-18-13903-2018, 2018.

Groot Zwaafink, C. D., Grythe, H., Skov, H. and Stohl, A.: Substantial contribution of northern high-latitude sources to mineral dust in the Arctic, *J. Geophys. Res.*, 121(22), 13,678–13,697, doi:10.1002/2016JD025482, 2016.

Groot Zwaafink, C. D., Arnalds, Ó., Dagsson-Waldhauserova, P., Eckhardt, S., Prospero, J. M. and Stohl, A.: Temporal and spatial variability of Icelandic dust emissions and atmospheric transport, *Atmos. Chem. Phys.*, 17(17), 10865–10878, doi:10.5194/acp-17-10865-2017, 2017.

Hama, K. and Ito, K.: Freezing of supercooled water-droplets (II), *Pap. Meteorol. Geophys.*, 7(2), 99–106, doi:10.2467/mripapers1950.7.2\_99, 1956.

Hammer, S. E., Mertes, S., Schneider, J., Ebert, M., Kandler, K. and Weinbruch, S.: Composition of ice particle residuals in mixed-phase clouds at Jungfraujoch (Switzerland): Enrichment and depletion of particle groups relative to total aerosol, *Atmos. Chem. Phys.*, 18(19), 13987–14003, doi:10.5194/acp-18-13987-2018, 2018.

Harrison, A. D., Lever, K., Sanchez-Marroquin, A., Holden, M. A., Whale, T. F., Tarn, M. D., McQuaid, J. B. and Murray, B. J.: The ice-nucleating ability of quartz immersed in water and its atmospheric importance compared to K-feldspar, *Atmos. Chem. Phys. Discuss.*, 1–23, doi:10.5194/acp-2019-288, 2019.

Hartmann, D. L., Ockert-Bell, M. E. and Michelsen, M. L.: The Effect of Cloud Type on Earth's Energy Balance: Global Analysis, *J. Clim.*, 5(11), 1281–1304, doi:10.1175/1520-0442(1992)005<1281:teocto>2.0.co;2, 1992.

Herbert, R. J., Murray, B. J., Whale, T. F., Dobbie, S. J. and Atkinson, J. D.: Representing time-dependent freezing behaviour in immersion mode ice nucleation, *Atmos. Chem. Phys.*, 14(16), 8501–8520, doi:10.5194/acp-14-8501-2014, 2014.

Herbert, R. J., Murray, B. J., Dobbie, S. J. and Koop, T.: Sensitivity of liquid clouds to homogenous freezing parameterizations, *Geophys. Res. Lett.*, 42(5), 1599–1605, doi:10.1002/2014GL062729, 2015.

Herzog, M., Graf, H. F., Textor, C. and Oberhuber, J. M.: The effect of phase changes of water on the development of volcanic plumes, *J. Volcanol. Geotherm. Res.*, 87(1–4), 55–74, doi:10.1016/S0377-0273(98)00100-0, 1998.

Hiranuma, N., Augustin-Bauditz, S., Bingemer, H., Budke, C., Curtius, J., Danielczok, A., Diehl, K., Dreischmeier, K., Ebert, M., Frank, F., Hoffmann, N., Kandler, K., Kiselev, A., Koop, T., Leisner, T., Möhler, O., Nillius, B., Peckhaus, A., Rose, D., Weinbruch, S., Wex, H., Boose, Y., Demott, P. J., Hader, J. D., Hill, T. C. J., Kanji, Z. A., Kulkarni, G., Levin, E. J. T., McCluskey, C. S., Murakami, M., Murray, B. J., Niedermeier, D., Petters, M. D., O’Sullivan, D., Saito, A., Schill, G. P., Tajiri, T., Tolbert, M. A., Welti, A., Whale, T. F., Wright, T. P. and Yamashita, K.: A comprehensive laboratory study on the immersion freezing behavior of illite NX particles: A comparison of 17 ice nucleation measurement techniques, *Atmos. Chem. Phys.*, 15(5), doi:10.5194/acp-15-2489-2015, 2015.

Hiranuma, N., Adachi, K., Bell, D., Belosi, F., Beydoun, H., Bhaduri, B., Bingemer, H., Budke, C., Clemen, H. C., Conen, F., Cory, K., Curtius, J., Demott, P., Eppers, O., Grawe, S., Hartmann, S., Hoffmann, N., Höhler, K., Jantsch, E., Kiselev, A., Koop, T., Kulkarni, G., Mayer, A., Murakami, M., Murray, B., Nicosia, A., Petters, M., Piazza, M., Polen, M., Reicher, N., Rudich, Y., Saito, A., Santachiara, G., Schiebel, T., Schill, G., Schneider, J., Segev, L., Stopelli, E., Sullivan, R., Suski, K., Szakall, M., Tajiri, T., Taylor, H., Tobo, Y., Ullrich, R., Weber, D., Wex, H., Whale, T., Whiteside, C., Yamashita, K., Zelenyuk, A. and Möhler, O.: A comprehensive characterization of ice nucleation by three different types of cellulose particles immersed in water, *Atmos. Chem. Phys.*, 19(7), 4823–4849, doi:10.5194/acp-19-4823-2019, 2019.

Hobbs, P. V., Fullerton, C. M. and Bluhm, G. C.: Ice Nucleus Storms in Hawaii, *Nat. Phys. Sci.*, 230(12), 90–91, doi:10.1038/physci230090a0, 1971.

Hobbs, W. H.: Loess, Pebble Bands, and Boulders from Glacial Outwash of the Greenland Continental Glacier, *J. Geol.*, 39(4), 381–385, doi:10.1086/623849, 1931.

Holden, M. A., Whale, T. F., Tarn, M. D., O’Sullivan, D., Walshaw, R. D., Murray, B. J., Meldrum, F. C. and Christenson, H. K.: High-speed imaging of ice nucleation in water

- proves the existence of active sites, *Sci. Adv.*, 5(2), doi:10.1126/sciadv.aav4316, 2019.
- Hoose, C., Kristjánsson, J. E., Chen, J. P. and Hazra, A.: A classical-theory-based parameterization of heterogeneous ice nucleation by mineral dust, soot, and biological particles in a global climate model, *J. Atmos. Sci.*, 67(8), 2483–2503, doi:10.1175/2010JAS3425.1, 2010.
- Hoyle, C. R., Pinti, V., Welti, A., Zobrist, B., Marcolli, C., Luo, B., Höskuldsson, Á., Mattsson, H. B., Stetzer, O., Thorsteinsson, T., Larsen, G. and Peter, T.: Ice nucleation properties of volcanic ash from Eyjafjallajökull, *Atmos. Chem. Phys.*, 11(18), 9911–9926, doi:10.5194/acp-11-9911-2011, 2011.
- Huang, J. and Bartell, L. S.: Kinetics of Homogeneous Nucleation in the Freezing of Large Water Clusters Water clusters of 4000-6000 molecules were produced by condensation of vapor in supersonic flow and cooled by evaporation until they froze at about 200 K. Rates of nucleation up to. [online] Available from: <https://pubs.acs.org/sharingguidelines> (Accessed 12 June 2020), 1995.
- Ickes, L., Welti, A., Hoose, C. and Lohmann, U.: Classical Nucleation Theory of homogeneous freezing of water: Thermodynamic and kinetic parameters, *Phys. Chem. Chem. Phys.*, 17(8), 5514–5537, doi:10.1039/c4cp04184d, 2015.
- Ickes, L., Porter, G. C. E., Wagner, R., Adams, M. P., Bierbauer, S., Bertram, A. K., Bilde, M., Christiansen, S., Ekman, A. M. L., Gorokhova, E., Höhler, K., Kiselev, A. A., Leck, C., Möhler, O., Murray, B. J., Schiebel, T., Ullrich, R. and Salter, M. E.: The ice-nucleating activity of Arctic sea surface microlayer samples and marine algal cultures, *Atmos. Chem. Phys.*, 20(18), 11089–11117, doi:10.5194/acp-20-11089-2020, 2020.
- Isono, K., Komabayasi, M. and Ono, A.: Volcanoes as a source of atmospheric ice nuclei, *Nature*, 183(4657), 317–318, doi:10.1038/183317a0, 1959.
- Jaeger, J. M., Nittrouer, C. A., Scott, N. D. and Milliman, J. D.: Sediment accumulation along a glacially impacted mountainous coastline: north-east Gulf of Alaska, *Basin Res.*, 10(1), 155–173, doi:10.1046/j.1365-2117.1998.00059.x, 1998.
- Jaenicke, R.: Abundance of cellular material and proteins in the atmosphere, *Science* (80-. ), 308(5718), 73, doi:10.1126/science.1106335, 2005.
- Jaenicke, R., Matthias-Maser, S. and Gruber, S.: Omnipresence of biological material in the atmosphere, *Environ. Chem.*, 4(4), 217–220, doi:10.1071/EN07021, 2007.

Jahn, L. G., Fahy, W. D., Williams, D. B. and Sullivan, R. C.: Role of Feldspar and Pyroxene Minerals in the Ice Nucleating Ability of Three Volcanic Ashes, *ACS Earth Sp. Chem.*, 3(4), 626–636, doi:10.1021/acsearthspacechem.9b00004, 2019.

Jones, A. M. and Harrison, R. M.: The effects of meteorological factors on atmospheric bioaerosol concentrations - A review, *Sci. Total Environ.*, 326(1–3), 151–180, doi:10.1016/j.scitotenv.2003.11.021, 2004.

Jones, H. M., Flynn, M. J., DeMott, P. J. and Möhler, O.: Manchester Ice Nucleus Counter (MINC) measurements from the 2007 International workshop on Comparing Ice nucleation Measuring Systems (ICIS-2007), *Atmos. Chem. Phys.*, 11(1), 53–65, doi:10.5194/acp-11-53-2011, 2011.

Kamphus, M., Ettner-Mahl, M., Klimach, T., Drewnick, F., Keller, L., Cziczo, D. J., Mertes, S., Borrmann, S. and Curtius, J.: Chemical composition of ambient aerosol, ice residues and cloud droplet residues in mixed-phase clouds: Single particle analysis during the cloud and aerosol characterization experiment (CLACE 6), *Atmos. Chem. Phys.*, 10(16), 8077–8095, doi:10.5194/acp-10-8077-2010, 2010.

Kanji, Z. A. and Abbatt, J. P. D.: The University of Toronto Continuous Flow Diffusion Chamber (UT-CFDC): A Simple Design for Ice Nucleation Studies, *Aerosol Sci. Technol.*, 43(7), 730–738, doi:10.1080/02786820902889861, 2009.

Kanji, Z. A., Ladino, L. A., Wex, H., Boose, Y., Burkert-Kohn, M., Cziczo, D. J. and Krämer, M.: Overview of Ice Nucleating Particles, *Meteorol. Monogr.*, 58, 1.1-1.33, doi:10.1175/amsmonographs-d-16-0006.1, 2017.

Kanji, Z. A., Welti, A., Corbin, J. C. and Mensah, A. A.: Black Carbon Particles Do Not Matter for Immersion Mode Ice Nucleation, *Geophys. Res. Lett.*, 47(11), doi:10.1029/2019GL086764, 2020.

Kärcher, B. and Yu, F.: Role of aircraft soot emissions in contrail formation, *Geophys. Res. Lett.*, 36(1), doi:10.1029/2008GL036649, 2009.

Kieft, T. L.: Ice Nucleation Activity in Lichens, *Appl. Environ. Microbiol.*, 54(7), 1678–1681, doi:10.1128/aem.54.7.1678-1681.1988, 1988.

Kjær, H. A., Zens, P., Black, S., Lund, K. H., Svensson, A. and Vallelonga, P.: Canadian forest fires, Icelandic volcanoes and increased local dust observed in six shallow Greenland firn cores, *Clim. Past*, 18(10), 2211–2230, doi:10.5194/cp-18-2211-2022,

2022.

Kohn, M., Lohmann, U., Welti, A. and Kanji, Z. A.: Immersion mode ice nucleation measurements with the new Portable Immersion Mode Cooling chamber (PIMCA), *J. Geophys. Res.*, 121(9), 4713–4733, doi:10.1002/2016JD024761, 2016.

Koop, T. and Murray, B. J.: A physically constrained classical description of the homogeneous nucleation of ice in water, *J. Chem. Phys.*, 145(21), 211915, doi:10.1063/1.4962355, 2016.

Koop, T., Luo, B., Tsias, A. and Peter, T.: Water activity as the determinant for homogeneous ice nucleation in aqueous solutions, *Nature*, 406(6796), 611–614, doi:10.1038/35020537, 2000.

Kulkarni, G., Hiranuma, N., Möhler, O., Höhler, K., China, S., Cziczo, D. J. and Demott, P. J.: A new method for operating a continuous-flow diffusion chamber to investigate immersion freezing: Assessment and performance study, *Atmos. Meas. Tech.*, 13(12), 6631–6643, doi:10.5194/amt-13-6631-2020, 2020.

Kumar, A., Marcolli, C. and Peter, T.: Ice nucleation activity of silicates and aluminosilicates in pure water and aqueous solutions-Part 3: Aluminosilicates, *Atmos. Chem. Phys.*, 19(9), 6059–6084, doi:10.5194/acp-19-6059-2019, 2019.

Lacher, L., Lohmann, U., Boose, Y., Zipori, A., Herrmann, E., Bukowiecki, N., Steinbacher, M. and Kanji, Z. A.: The Horizontal Ice Nucleation Chamber (HINC): INP measurements at conditions relevant for mixed-phase clouds at the High Altitude Research Station Jungfraujoch, *Atmos. Chem. Phys.*, 17(24), 15199–15224, doi:10.5194/acp-17-15199-2017, 2017.

Lacher, L., Adams, M. P., Barry, K., Bertozzi, B., Bingemer, H., Boffo, C., Bras, Y., Büttner, N., Castarede, D., Cziczo, D. J., DeMott, P. J., Fösig, R., Goodell, M., Höhler, K., Hill, T. C. J., Jentzsch, C., Ladino, L. A., Levin, E. J. T., Mertes, S., Möhler, O., Moore, K. A., Murray, B. J., Nadolny, J., Pfeuffer, T., Picard, D., Ramírez-Romero, C., Ribeiro, M., Richter, S., Schrod, J., Sellegri, K., Stratmann, F., Swanson, B. E., Thomson, E. S., Wex, H., Wolf, M. J. and Freney, E.: The Puy de Dôme ICe Nucleation Intercomparison Campaign (PICNIC): comparison between online and offline methods in ambient air, *Atmos. Chem. Phys.*, 24(4), 2651–2678, doi:10.5194/acp-24-2651-2024, 2024.

Levin, E. J. T., Mcmeeking, G. R., Demott, P. J., Mccluskey, C. S., Stockwell, C. E.,

Yokelson, R. J. and Kreidenweis, S. M.: A new method to determine the number concentrations of refractory black carbon ice nucleating particles, *Aerosol Sci. Technol.*, 48(12), 1264–1275, doi:10.1080/02786826.2014.977843, 2014.

Loeb, N. G., Wielicki, B. A., Doelling, D. R., Smith, G. L., Keyes, D. F., Kato, S., Manalo-Smith, N. and Wong, T.: Toward optimal closure of the Earth's top-of-atmosphere radiation budget, *J. Clim.*, 22(3), 748–766, doi:10.1175/2008JCLI2637.1, 2009.

Lohmann, U. and Feichter, J.: Global indirect aerosol effects: a review, *Atmos. Chem. Phys.*, 5(3), 715–737, doi:10.5194/acp-5-715-2005, 2005.

Lohmann, U., Lüönd, F. and Mahrt, F.: An introduction to clouds: From the microscale to climate., 2016.

Mahrt, F., Marcolli, C., David, R. O., Grönquist, P., Barthazy Meier, E. J., Lohmann, U. and Kanji, Z. A.: Ice nucleation abilities of soot particles determined with the Horizontal Ice Nucleation Chamber, *Atmos. Chem. Phys.*, 18(18), 13363–13392, doi:10.5194/acp-18-13363-2018, 2018.

Le Maitre, R. W., Bateman, P., Dudek, A., Keller, J., Lameyre, J., Le Bas, M. J., Sabine, P. A., Schmit, R., Sorensen, H., Streckeisen, A., Woolley, A. R. and Zanettin, B.: A classification of Igneous rocks and glossary of terms: recommendations of the International Union of Geological Sciences subcommission on the systematic of igneous rocks, Oxford Blackwell Sci., 193, 1989.

Mangan, T. P., Atkinson, J. D., Neuberg, J. W., O'Sullivan, D., Wilson, T. W., Whale, T. F., Neve, L., Umo, N. S., Malkin, T. L. and Murray, B. J.: Heterogeneous Ice nucleation by soufriere hills volcanic ash immersed in water droplets, *PLoS One*, 12(1), e0169720, doi:10.1371/journal.pone.0169720, 2017.

Marcolli, C.: Deposition nucleation viewed as homogeneous or immersion freezing in pores and cavities, *Atmos. Chem. Phys.*, 14(4), 2071–2104, doi:10.5194/acp-14-2071-2014, 2014.

Marcolli, C., Gedamke, S., Peter, T. and Zobrist, B.: Efficiency of immersion mode ice nucleation on surrogates of mineral dust, *Atmos. Chem. Phys.*, 7(19), 5081–5091, doi:10.5194/acp-7-5081-2007, 2007.

Marcolli, C., Mahrt, F. and Kärcher, B.: Soot PCF: Pore condensation and freezing

framework for soot aggregates, *Atmos. Chem. Phys.*, 21(10), 7791–7843, doi:10.5194/acp-21-7791-2021, 2021.

Maters, E. C., Dingwell, D. B., Cimarelli, C., Müller, D., Whale, T. F. and Murray, B. J.: The importance of crystalline phases in ice nucleation by volcanic ash, *Atmos. Chem. Phys.*, 19(8), 5451–5465, doi:10.5194/acp-19-5451-2019, 2019.

Maters, E. C., Cimarelli, C., Casas, A. S., Dingwell, D. B. and Murray, B. J.: Volcanic ash ice-nucleating activity can be enhanced or depressed by ash-gas interaction in the eruption plume, *Earth Planet. Sci. Lett.*, 551, 116587, doi:10.1016/j.epsl.2020.116587, 2020.

Matthias-Maser, S. and Jaenicke, R.: The size distribution of primary biological aerosol particles with radii  $> 0.2 \mu\text{m}$  in an urban/rural influenced region, *Atmos. Res.*, 39(4), 279–286, doi:10.1016/0169-8095(95)00017-8, 1995.

Meinander, O., Dagsson-Waldhauserova, P., Amosov, P., Aseyeva, E., Atkins, C., Baklanov, A., Baldo, C., Barr, S. L., Barzycka, B., Benning, L. G., Cvetkovic, B., Enchilik, P., Frolov, D., Gassó, S., Kandler, K., Kasimov, N., Kavan, J., King, J., Koroleva, T., Krupskaya, V., Kulmala, M., Kusiak, M., Lappalainen, H. K., Laska, M., Lasne, J., Lewandowski, M., Luks, B., McQuaid, J. B., Moroni, B., Murray, B., Möhler, O., Nawrot, A., Nickovic, S., O'Neill, N. T., Pejanovic, G., Popovicheva, O., Ranjbar, K., Romanias, M., Samonova, O., Sanchez-Marroquin, A., Schepanski, K., Semenov, I., Sharapova, A., Shevnina, E., Shi, Z., Sofiev, M., Thevenet, F., Thorsteinsson, T., Timofeev, M., Umo, N. S., Uppstu, A., Urupina, D., Varga, G., Werner, T., Arnalds, O. and Vukovic Vimic, A.: Newly identified climatically and environmentally significant high-latitude dust sources, *Atmos. Chem. Phys.*, 22(17), 11889–11930, doi:10.5194/acp-22-11889-2022, 2022.

Möhler, O., Georgakopoulos, D. G., Morris, C. E., Benz, S., Ebert, V., Hunsmann, S., Saathoff, H., Schnaiter, M. and Wagner, R.: Heterogeneous ice nucleation activity of bacteria: New laboratory experiments at simulated cloud conditions, *Biogeosciences*, 5(5), 1425–1435, doi:10.5194/bg-5-1425-2008, 2008a.

Möhler, O., Benz, S., Saathoff, H., Schnaiter, M., Wagner, R., Schneider, J., Walter, S., Ebert, V. and Wagner, S.: The effect of organic coating on the heterogeneous ice nucleation efficiency of mineral dust aerosols, *Environ. Res. Lett.*, 3(2), 025007, doi:10.1088/1748-9326/3/2/025007, 2008b.

Möhler, O., Adams, M., Lacher, L., Vogel, F., Nadolny, J., Ullrich, R., Boffo, C., Pfeuffer, T., Hobl, A., Weiß, M., Vepuri, H. S. K., Hiranuma, N. and Murray, B. J.: The Portable Ice Nucleation Experiment (PINE): A new online instrument for laboratory studies and automated long-term field observations of ice-nucleating particles, *Atmos. Meas. Tech.*, 14(2), 1143–1166, doi:10.5194/amt-14-1143-2021, 2021.

Morris, C. E., Georgakopoulos, D. G. and Sands, D. C.: Ice nucleation active bacteria and their potential role in precipitation, *J. Phys. IV JP*, 121, 87–103, doi:10.1051/jp4:2004121004, 2004.

Murphy, D. M. and Koop, T.: Review of the vapour pressures of ice and supercooled water for atmospheric applications, *Q. J. R. Meteorol. Soc.*, 131(608), 1539–1565, doi:10.1256/qj.04.94, 2005.

Murray, B. J.: Inhibition of ice crystallisation in highly viscous aqueous organic acid droplets, *Atmos. Chem. Phys.*, 8(17), 5423–5433, doi:10.5194/acp-8-5423-2008, 2008.

Murray, B. J., Wilson, T. W., Dobbie, S., Cui, Z., Al-Jumur, S. M. R. K., Möhler, O., Schnaiter, M., Wagner, R., Benz, S., Niemand, M., Saathoff, H., Ebert, V., Wagner, S. and Kärcher, B.: Heterogeneous nucleation of ice particles on glassy aerosols under cirrus conditions, *Nat. Geosci.*, 3(4), 233–237, doi:10.1038/ngeo817, 2010a.

Murray, B. J., Broadley, S. L., Wilson, T. W., Bull, S. J., Wills, R. H., Christenson, H. K. and Murray, E. J.: Kinetics of the homogeneous freezing of water, *Phys. Chem. Chem. Phys.*, 12(35), 10380–10387, doi:10.1039/c003297b, 2010b.

Murray, B. J., Broadley, S. L., Wilson, T. W., Atkinson, J. D. and Wills, R. H.: Heterogeneous freezing of water droplets containing kaolinite particles, *Atmos. Chem. Phys.*, 11(9), 4191–4207, doi:10.5194/acp-11-4191-2011, 2011.

Murray, B. J., O’Sullivan, D., Atkinson, J. D. and Webb, M. E.: Ice nucleation by particles immersed in supercooled cloud droplets, *Chem. Soc. Rev.*, 41(19), 6519, doi:10.1039/c2cs35200a, 2012.

Murray, B. J., Carslaw, K. S. and Field, P. R.: Opinion: Cloud-phase climate feedback and the importance of ice-nucleating particles, *Atmos. Chem. Phys.*, 21(2), 665–679, doi:10.5194/acp-21-665-2021, 2021.

Nakagawa, M. and Ohba, T.: Minerals in Volcanic Ash 1: Primary Minerals and Volcanic Glass, *Glob. Environ. Res.*, 6(October), 41–51 [online] Available from:

<http://www.airies.or.jp/publication/ger/pdf/06-2-06.pdf>, 2003.

Nichman, L., Wolf, M., Davidovits, P., Onasch, T. B., Zhang, Y., Worsnop, D. R., Bhandari, J., Mazzoleni, C. and Cziczo, D. J.: Laboratory study of the heterogeneous ice nucleation on black-carbon-containing aerosol, *Atmos. Chem. Phys.*, 19(19), 12175–12194, doi:10.5194/acp-19-12175-2019, 2019.

Niemand, M., Möhler, O., Vogel, B., Vogel, H., Hoose, C., Connolly, P., Klein, H., Bingemer, H., Demott, P., Skrotzki, J. and Leisner, T.: A particle-surface-area-based parameterization of immersion freezing on desert dust particles, *J. Atmos. Sci.*, 69(10), 3077–3092, doi:10.1175/JAS-D-11-0249.1, 2012.

O’Sullivan, D., Murray, B. J., Malkin, T. L., Whale, T. F., Umo, N. S., Atkinson, J. D., Price, H. C., Baustian, K. J., Browse, J. and Webb, M. E.: Ice nucleation by fertile soil dusts: Relative importance of mineral and biogenic components, *Atmos. Chem. Phys.*, 14(4), 1853–1867, doi:10.5194/acp-14-1853-2014, 2014.

Pandey, R., Usui, K., Livingstone, R. A., Fischer, S. A., Pfaendtner, J., Backus, E. H. G., Nagata, Y., Fröhlich-Nowoisky, J., Schmöser, L., Mauri, S., Scheel, J. F., Knopf, D. A., Pöschl, U., Bonn, M. and Weidner, T.: Ice-nucleating bacteria control the order and dynamics of interfacial water, *Sci. Adv.*, 2(4), e1501630, doi:10.1126/sciadv.1501630, 2016.

Paramonov, M., David, R. O., Kretzschmar, R. and Kanji, Z. A.: A laboratory investigation of the ice nucleation efficiency of three types of mineral and soil dust, *Atmos. Chem. Phys.*, 18(22), 16515–16536, doi:10.5194/acp-18-16515-2018, 2018.

Peckhaus, A., Kiselev, A., Hiron, T., Ebert, M. and Leisner, T.: A comparative study of K-rich and Na/Ca-rich feldspar ice-nucleating particles in a nanoliter droplet freezing assay, *Atmos. Chem. Phys.*, 16(18), 11477–11496, doi:10.5194/acp-16-11477-2016, 2016.

Petters, M. D. and Kreidenweis, S. M.: A single parameter representation of hygroscopic growth and cloud condensation nucleus activity, *Atmos. Chem. Phys.*, 7(8), 1961–1971, doi:10.5194/acp-7-1961-2007, 2007.

Piaggi, P. M., Weis, J., Panagiotopoulos, A. Z., Debenedetti, P. G. and Car, R.: Homogeneous ice nucleation in an ab initio machine-learning model of water, *Proc. Natl. Acad. Sci. U. S. A.*, 119(33), doi:10.1073/pnas.2207294119, 2022.

Ponsonby, J., King, L., Murray, B. J. and Stettler, M. E. J.: Jet aircraft lubrication oil droplets as contrail ice-forming particles, *Atmos. Chem. Phys.*, 24(3), 2045–2058, doi:10.5194/acp-24-2045-2024, 2024.

Porter, G. C. E., Sikora, S. N. F., Adams, M. P., Proske, U., Harrison, A. D., Tarn, M. D., Brooks, I. M. and Murray, B. J.: Resolving the size of ice-nucleating particles with a balloon deployable aerosol sampler: the SHARK, *Atmos. Meas. Tech.*, 13(6), 2905–2921, doi:10.5194/amt-13-2905-2020, 2020.

Pouleur, S., Richard, C., Martin, J. and Antoun, H.: Ice nucleation activity in *Fusarium acuminatum* and *Fusarium avenaceum*, *Appl. Environ. Microbiol.*, 58(9), 2960–2964, doi:10.1128/aem.58.9.2960-2964.1992, 1992.

Pratt, K. A., Demott, P. J., French, J. R., Wang, Z., Westphal, D. L., Heymsfield, A. J., Twohy, C. H., Prenni, A. J. and Prather, K. A.: In situ detection of biological particles in cloud ice-crystals, *Nat. Geosci.*, 2(6), 398–401, doi:10.1038/ngeo521, 2009.

Prospero, J. M., Ginoux, P., Torres, O., Nicholson, S. E. and Gill, T. E.: Environmental characterization of global sources of atmospheric soil dust identified with the Nimbus 7 Total Ozone Mapping Spectrometer (TOMS) absorbing aerosol product, *Rev. Geophys.*, 40(1), 2-1-2–31, doi:10.1029/2000RG000095, 2002.

Prospero, J. M., Bullard, J. E. and Hodgkins, R.: High-latitude dust over the North Atlantic: Inputs from Icelandic proglacial dust storms, *Science (80-. )*, 335(6072), 1078–1082, doi:10.1126/science.1217447, 2012.

Ramanathan, V., Cess, R. D., Harrison, E. F., Minnis, P., Barkstrom, B. R., Ahmad, E. and Hartmann, D.: Cloud-radiative forcing and climate: Results from the earth radiation budget experiment, *Science (80-. )*, 243(4887), 57–63, doi:10.1126/science.243.4887.57, 1989.

Rasmussen, D. H.: Thermodynamics and nucleation phenomena - A set of experimental observations, *J. Cryst. Growth*, 56(1), 56–66, doi:10.1016/0022-0248(82)90012-4, 1982.

Reicher, N., Segev, L. and Rudich, Y.: The Weizmann Supercooled Droplets Observation on a Microarray (WISDOM) and application for ambient dust, *Atmos. Meas. Tech.*, 11(1), 233–248, doi:10.5194/amt-11-233-2018, 2018.

Richardson, M. S., DeMott, P. J., Kreidenweis, S. M., Cziczo, D. J., Dunlea, E. J., Jimenez, J. L., Thomson, D. S., Ashbaugh, L. L., Borys, R. D., Westphal, D. L., Casuccio, G. S.

and Lersch, T. L.: Measurements of heterogeneous ice nuclei in the western United States in springtime and their relation to aerosol characteristics, *J. Geophys. Res. Atmos.*, 112(2), doi:10.1029/2006JD007500, 2007.

Rogers, D. C.: Development of a continuous flow thermal gradient diffusion chamber for ice nucleation studies, *Atmos. Res.*, 22(2), 149–181, doi:10.1016/0169-8095(88)90005-1, 1988.

Rosenfeld, D. and Woodley, W. L.: Deep convective clouds with sustained supercooled liquid water down to - 37.5 °C, *Nature*, 405(6785), 440–442, doi:10.1038/35013030, 2000.

Rossow, W. B. and Schiffer, R. A.: Advances in Understanding Clouds from ISCCP, *Bull. Am. Meteorol. Soc.*, 80(11), 2261–2287, doi:10.1175/1520-0477(1999)080<2261:AIUCFI>2.0.CO;2, 1999.

Saathoff, H., Moehler, O., Schurath, U., Kamm, S., Dippel, B. and Mihelcic, D.: The AIDA soot aerosol characterisation campaign 1999, *J. Aerosol Sci.*, 34(10), 1277–1296, doi:10.1016/S0021-8502(03)00363-X, 2003.

Sanchez-Marroquin, A., Arnalds, O., Baustian-Dorsi, K. J., Browse, J., Dagsson-Waldhauserova, P., Harrison, A. D., Maters, E. C., Pringle, K. J., Vergara-Temprado, J., Burke, I. T., McQuaid, J. B., Carslaw, K. S. and Murray, B. J.: Iceland is an episodic source of atmospheric ice-nucleating particles relevant for mixed-phase clouds, *Sci. Adv.*, 6(26), 8137–8161, doi:10.1126/sciadv.aba8137, 2020.

Sassen, K., DeMott, P. J., Prospero, J. M. and Poellot, M. R.: Saharan dust storms and indirect aerosol effects on clouds: CRYSTAL-FACE results, *Geophys. Res. Lett.*, 30(12), doi:10.1029/2003GL017371, 2003.

Schill, G. P., Genareau, K. and Tolbert, M. A.: Deposition and immersion-mode nucleation of ice by three distinct samples of volcanic ash, *Atmos. Chem. Phys.*, 15(13), 7523–7536, doi:10.5194/acp-15-7523-2015, 2015.

Schneider, S. H.: Cloudiness as a Global Climatic Feedback Mechanism: The Effects on the Radiation Balance and Surface Temperature of Variations in Cloudiness, *J. Atmos. Sci.*, 29(8), 1413–1422, doi:10.1175/1520-0469(1972)029<1413:caagcf>2.0.co;2, 1972.

Schroth, A. W., Crusius, J., Gassó, S., Moy, C. M., Buck, N. J., Resing, J. A. and Campbell, R. W.: Atmospheric deposition of glacial iron in the Gulf of Alaska impacted

by the position of the Aleutian Low, *Geophys. Res. Lett.*, 44(10), 5053–5061, doi:10.1002/2017GL073565, 2017.

Schwidetzky, R., de Almeida Ribeiro, I., Bothen, N., Backes, A. T., DeVries, A. L., Bonn, M., Fröhlich-Nowoisky, J., Molinero, V. and Meister, K.: Functional aggregation of cell-free proteins enables fungal ice nucleation, *Proc. Natl. Acad. Sci. U. S. A.*, 120(46), e2303243120, doi:10.1073/pnas.2303243120, 2023.

Seifert, P., Ansmann, A., Groß, S., Freudenthaler, V., Heinold, B., Hiebsch, A., Mattis, I., Schmidt, J., Schnell, F., Tesche, M., Wandinger, U. and Wiegner, M.: Ice formation in ash-influenced clouds after the eruption of the Eyjafjallajökull volcano in April 2010, *J. Geophys. Res. Atmos.*, 116(18), doi:10.1029/2011JD015702, 2011.

Shi, Y., Liu, X., Wu, M., Zhao, X., Ke, Z. and Brown, H.: Relative importance of high-latitude local and long-range-transported dust for Arctic ice-nucleating particles and impacts on Arctic mixed-phase clouds, *Atmos. Chem. Phys.*, 22(4), 2909–2935, doi:10.5194/acp-22-2909-2022, 2022.

Sparks, R. S. J.: The dimensions and dynamics of volcanic eruption columns, *Bull. Volcanol.*, 48(1), 3–15, doi:10.1007/BF01073509, 1986.

Steinke, I., Möhler, O., Kiselev, A., Niemand, M., Saathoff, H., Schnaiter, M., Skrotzki, J., Hoose, C. and Leisner, T.: Ice nucleation properties of fine ash particles from the Eyjafjallajökull eruption in April 2010, *Atmos. Chem. Phys.*, 11(24), 12945–12958, doi:10.5194/acp-11-12945-2011, 2011.

Stetzer, O., Baschek, B., Lüönd, F. and Lohmann, U.: The Zurich Ice Nucleation Chamber (ZINC)-A New Instrument to Investigate Atmospheric Ice Formation, *Aerosol Sci. Technol.*, 42(1), 64–74, doi:10.1080/02786820701787944, 2008.

Stohl, A.: Characteristics of atmospheric transport into the Arctic troposphere, *J. Geophys. Res. Atmos.*, 111(D11), doi:10.1029/2005JD006888, 2006.

Tarn, M. D., Sikora, S. N. F., Porter, G. C. E., Wyld, B. V., Alayof, M., Reicher, N., Harrison, A. D., Rudich, Y., Shim, J. U. and Murray, B. J.: On-chip analysis of atmospheric ice-nucleating particles in continuous flow, *Lab Chip*, 20(16), 2889–2910, doi:10.1039/d0lc00251h, 2020.

Tarn, M. D., Sikora, S. N. F., Porter, G. C. E., Shim, J. U. and Murray, B. J.: Homogeneous freezing of water using microfluidics, *Micromachines*, 12(2), 1–23,

doi:10.3390/mi12020223, 2021.

Tegen, I. and Fung, I.: Contribution to the atmospheric mineral aerosol load from land surface modification, *J. Geophys. Res.*, 100(D9), doi:10.1029/95jd02051, 1995.

Textor, C., Graf, H. F., Herzog, M. and Oberhuber, J. M.: Injection of gases into the stratosphere by explosive volcanic eruptions, *J. Geophys. Res. Atmos.*, 108(19), doi:10.1029/2002jd002987, 2003.

Tobo, Y.: An improved approach for measuring immersion freezing in large droplets over a wide temperature range, *Sci. Rep.*, 6, doi:10.1038/srep32930, 2016.

Tobo, Y., Prenni, A. J., Demott, P. J., Huffman, J. A., McCluskey, C. S., Tian, G., Pöhlker, C., Pöschl, U. and Kreidenweis, S. M.: Biological aerosol particles as a key determinant of ice nuclei populations in a forest ecosystem, *J. Geophys. Res. Atmos.*, 118(17), 10,100–10,110, doi:10.1002/jgrd.50801, 2013.

Tobo, Y., Adachi, K., DeMott, P. J., Hill, T. C. J., Hamilton, D. S., Mahowald, N. M., Nagatsuka, N., Ohata, S., Uetake, J., Kondo, Y. and Koike, M.: Glacially sourced dust as a potentially significant source of ice nucleating particles, *Nat. Geosci.*, 12(4), 253–258, doi:10.1038/s41561-019-0314-x, 2019.

TSI: Model 390069 Data Merge Software Module for Merging and Fitting of SMPS and APS Data Files User's Guide, 2011.

Twohy, C. H., DeMott, P. J., Pratt, K. A., Subramanian, R., Kok, G. L., Murphy, S. M., Lersch, T., Heymsfield, A. J., Wang, Z., Prather, K. A. and Seinfeld, J. H.: Relationships of biomass-burning aerosols to ice in orographic wave clouds, *J. Atmos. Sci.*, 67(8), 2437–2450, doi:10.1175/2010JAS3310.1, 2010.

Ullrich, R., Hoose, C., Möhler, O., Niemand, M., Wagner, R., Höhler, K., Hiranuma, N., Saathoff, H. and Leisner, T.: A new ice nucleation active site parameterization for desert dust and soot, *J. Atmos. Sci.*, 74(3), 699–717, doi:10.1175/JAS-D-16-0074.1, 2017.

Umo, N. S., Murray, B. J., Baeza-Romero, M. T., Jones, J. M., Lea-Langton, A. R., Malkin, T. L., O'Sullivan, D., Neve, L., Plane, J. M. C. and Williams, A.: Ice nucleation by combustion ash particles at conditions relevant to mixed-phase clouds, *Atmos. Chem. Phys.*, 15(9), 5195–5210, doi:10.5194/acp-15-5195-2015, 2015.

Umo, N. S., Wagner, R., Ullrich, R., Kiselev, A., Saathoff, H., Weidler, P. G., Cziczo, D. J., Leisner, T. and Möhler, O.: Enhanced ice nucleation activity of coal fly ash aerosol

particles initiated by ice-filled pores, *Atmos. Chem. Phys.*, 19(13), 8783–8800, doi:10.5194/acp-19-8783-2019, 2019.

Vali, G.: Freezing Rate Due to Heterogeneous Nucleation, *J. Atmos. Sci.*, 51(13), 1843–1856, doi:10.1175/1520-0469(1994)051<1843:frdthn>2.0.co;2, 1994.

Vali, G.: Repeatability and randomness in heterogeneous freezing nucleation, *Atmos. Chem. Phys.*, 8(16), 5017–5031, doi:10.5194/acp-8-5017-2008, 2008.

Vali, G. and Stansbury, E. J.: TIME-DEPENDENT CHARACTERISTICS OF THE HETEROGENEOUS NUCLEATION OF ICE, *Can. J. Phys.*, 44(3), 477–502, doi:10.1139/p66-044, 1966.

Vergara-Temprado, J., Murray, B. J., Wilson, T. W., O’Sullivan, D., Browse, J., Pringle, K. J., Ardon-Dryer, K., Bertram, A. K., Burrows, S. M., Ceburnis, D., Demott, P. J., Mason, R. H., O’Dowd, C. D., Rinaldi, M. and Carslaw, K. S.: Contribution of feldspar and marine organic aerosols to global ice nucleating particle concentrations, *Atmos. Chem. Phys.*, 17(5), 3637–3658, doi:10.5194/acp-17-3637-2017, 2017.

Vergara-Temprado, J., Holden, M. A., Orton, T. R., O’Sullivan, D., Umo, N. S., Browse, J., Reddington, C., Baeza-Romero, M. T., Jones, J. M., Lea-Langton, A., Williams, A., Carslaw, K. S. and Murray, B. J.: Is Black Carbon an Unimportant Ice-Nucleating Particle in Mixed-Phase Clouds?, *J. Geophys. Res. Atmos.*, 123(8), 4273–4283, doi:10.1002/2017JD027831, 2018.

Vernier, J. P., Fairlie, T. D., Deshler, T., Natarajan, M., Knepp, T., Foster, K., Wienhold, F. G., Bedka, K. M., Thomason, L. and Trepte, C.: In situ and space-based observations of the Kelud volcanic plume: The persistence of ash in the lower stratosphere, *J. Geophys. Res.*, 121(18), 11,104–11,118, doi:10.1002/2016JD025344, 2016.

Vial, J., Dufresne, J. L. and Bony, S.: On the interpretation of inter-model spread in CMIP5 climate sensitivity estimates, *Clim. Dyn.*, 41(11–12), 3339–3362, doi:10.1007/s00382-013-1725-9, 2013.

Vogel, F., Lacher, L., Nadolny, J., Saathoff, H., Leisner, T. and Möhler, O.: Development and validation of a new cloud simulation experiment for lab-based aerosol-cloud studies, *Rev. Sci. Instrum.*, 93(9), 095106, doi:10.1063/5.0098777, 2022.

Vonnegut, B. and Baldwin, M.: Repeated Nucleation of a Supercooled Water Sample that Contains Silver Iodide Particles, *J. Clim. Appl. Meteorol.*, 23(3), 486–490,

doi:10.1175/1520-0450(1984)023<0486:RNOASW>2.0.CO;2, 1984.

Wagner, F., Bortoli, D., Pereira, S., Costa, M. J., Silva, A. M., Weinzierl, B., Esselborn, M., Petzold, A., Rasp, K., Heinold, B. and Tegen, I.: Properties of dust aerosol particles transported to Portugal from the Sahara desert, *Tellus, Ser. B Chem. Phys. Meteorol.*, 61(1), 297–306, doi:10.1111/j.1600-0889.2008.00393.x, 2009a.

Wagner, R., Linke, C., Naumann, K.-H., Schnaiter, M., Vragel, M., Gangl, M. and Horvath, H.: A review of optical measurements at the aerosol and cloud chamber AIDA, *J. Quant. Spectrosc. Radiat. Transf.*, 110(11), 930–949, doi:10.1016/j.jqsrt.2009.01.026, 2009b.

Westbrook, C. D. and Illingworth, A. J.: Evidence that ice forms primarily in supercooled liquid clouds at temperatures  $>-27^{\circ}\text{C}$ , *Geophys. Res. Lett.*, 38(14), doi:10.1029/2011GL048021, 2011.

Wex, H., Augustin-Bauditz, S., Boose, Y., Budke, C., Curtius, J., Diehl, K., Dreyer, A., Frank, F., Hartmann, S., Hiranuma, N., Jantsch, E., Kanji, Z. A., Kiselev, A., Koop, T., Möhler, O., Niedermeier, D., Nillius, B., Rösch, M., Rose, D., Schmidt, C., Steinke, I. and Stratmann, F.: Intercomparing different devices for the investigation of ice nucleating particles using Snomax® as test substance, *Atmos. Chem. Phys.*, 15(3), 1463–1485, doi:10.5194/acp-15-1463-2015, 2015.

Wex, H., Huang, L., Zhang, W., Hung, H., Traversi, R., Becagli, S., Sheesley, R. J., Moffett, C. E., Barrett, T. E., Bossi, R., Skov, H., Hünerbein, A., Lubitz, J., Löffler, M., Linke, O., Hartmann, M., Herenz, P. and Stratmann, F.: Annual variability of ice-nucleating particle concentrations at different Arctic locations, *Atmos. Chem. Phys.*, 19(7), 5293–5311, doi:10.5194/acp-19-5293-2019, 2019.

Whale, T. F., Murray, B. J., O’Sullivan, D., Wilson, T. W., Umo, N. S., Baustian, K. J., Atkinson, J. D., Workneh, D. A. and Morris, G. J.: A technique for quantifying heterogeneous ice nucleation in microlitre supercooled water droplets, *Atmos. Meas. Tech.*, 8(6), 2437–2447, doi:10.5194/amt-8-2437-2015, 2015.

Williams, S. N. and Self, S.: The October 1902 plinian eruption of Santa Maria volcano, Guatemala, *J. Volcanol. Geotherm. Res.*, 16(1–2), 33–56, doi:10.1016/0377-0273(83)90083-5, 1983.

Wilson, T. W., Murray, B. J., Wagner, R., Möhler, O., Saathoff, H., Schnaiter, M., Skrotzki, J., Price, H. C., Malkin, T. L., Dobbie, S. and Al-Jumur, S. M. R. K.: Glassy

aerosols with a range of compositions nucleate ice heterogeneously at cirrus temperatures, *Atmos. Chem. Phys.*, 12(18), 8611–8632, doi:10.5194/acp-12-8611-2012, 2012.

Wilson, T. W., Ladino, L. A., Alpert, P. A., Breckels, M. N., Brooks, I. M., Browse, J., Burrows, S. M., Carslaw, K. S., Huffman, J. A., Judd, C., Kilhau, W. P., Mason, R. H., McFiggans, G., Miller, L. A., Najera, J. J., Polishchuk, E., Rae, S., Schiller, C. L., Si, M., Temprado, J. V., Whale, T. F., Wong, J. P. S., Wurl, O., Yakobi-Hancock, J. D., Abbatt, J. P. D., Aller, J. Y., Bertram, A. K., Knopf, D. A. and Murray, B. J.: A marine biogenic source of atmospheric ice-nucleating particles, *Nature*, 525(7568), 234–238, doi:10.1038/nature14986, 2015.

WMO, W. M. O.: International Cloud Atlas: Manual on the Observation of Clouds and Other Meteors., World Meteorol. Organ. [online] Available from: <https://cloudatlas.wmo.int/en/home.html>, 2017.

Woods, A. W.: Moist convection and the injection of volcanic ash into the atmosphere, *J. Geophys. Res.*, 98(B10), doi:10.1029/93jb00718, 1993.

Wright, H. M. N., Cashman, K. V., Mothes, P. A., Hall, M. L., Ruiz, A. G. and Le Pennec, J. L.: Estimating rates of decompression from textures of erupted ash particles produced by 1999-2006 eruptions of Tungurahua volcano, Ecuador, *Geology*, 40(7), 619–622, doi:10.1130/G32948.1, 2012.

Wright, T. P. and Petters, M. D.: The role of time in heterogeneous freezing nucleation, *J. Geophys. Res. Atmos.*, 118(9), 3731–3743, doi:10.1002/jgrd.50365, 2013.

Xi, Y., Xu, C., Downey, A., Stevens, R., Bachelder, J. O., King, J., Hayes, P. L. and Bertram, A. K.: Ice nucleating properties of airborne dust from an actively retreating glacier in Yukon, Canada, *Environ. Sci. Atmos.*, 2(4), 714–726, doi:10.1039/d1ea00101a, 2022.

Xu, M., Yu, D., Yao, H., Liu, X. and Qiao, Y.: Coal combustion-generated aerosols: Formation and properties, *Proc. Combust. Inst.*, 33(1), 1681–1697, doi:10.1016/j.proci.2010.09.014, 2011.

Yoshimori, M., Hugo Lambert, F., Webb, M. J. and Andrews, T.: Fixed anvil temperature feedback: Positive, zero, or negative?, *J. Clim.*, 33(7), 2719–2739, doi:10.1175/JCLI-D-19-0108.1, 2020.

Zender, C. S., Miller, R. L. and Tegen, I.: Quantifying mineral dust mass budgets :

Terminology, constraints, and current estimates, *Eos* (Washington. DC)., 85(48), doi:10.1029/2004EO480002, 2004.

Zenker, J., Collier, K. N., Xu, G., Yang, P., Levin, E. J. T., Suski, K. J., DeMott, P. J. and Brooks, S. D.: Using depolarization to quantify ice nucleating particle concentrations: a new method, *Atmos. Meas. Tech.*, 10(12), 4639–4657, doi:10.5194/amt-10-4639-2017, 2017.

Zhou, X., Liu, D., Bu, H., Deng, L., Liu, H., Yuan, P., Du, P. and Song, H.: XRD-based quantitative analysis of clay minerals using reference intensity ratios, mineral intensity factors, Rietveld, and full pattern summation methods: A critical review, *Solid Earth Sci.*, 3(1), 16–29, doi:10.1016/j.sesci.2017.12.002, 2018.

## **2 Characterising temperature in a portable cloud expansion chamber designed for counting ice-nucleating particles**

### **2.1 Background**

There are different pathways via which an INP can nucleate ice and various different INP types that can carry out these processes. Immersion nucleation is when the INP is first immersed in a liquid droplet, usually by acting as a cloud condensation nuclei, and then the droplet freezes upon cooling to a temperature at which the INP is active (Murray et al., 2012). Aerosol types known to be important for immersion nucleation include mineral dusts, particularly K-feldspar (Atkinson et al., 2013), sea spray (Vergara-Temprado et al., 2017; Wilson et al., 2015) and bioaerosols (Adams et al., 2021; Christner et al., 2008; Morris et al., 2004). PCF nucleation is the formation of an ice crystal without a liquid droplet, water condenses into pores on the INP's surface and when it freezes the ice grows out of the pore to form an ice crystal, this can occur below water saturation via the reverse Kelvin effect. Mineral dusts and BC aerosols have been shown to have ice-nucleating activities below water saturation related to their porosities (David et al., 2019; Mahrt et al., 2018; Marcolli et al., 2021). The key difference between immersion freezing of cloud droplets and PCF nucleation is the RH at which the ice crystal forms; for immersion freezing of cloud droplets to occur it must be at or above water saturation in order for the liquid droplet to form, whilst PCF can occur below water saturation, without the formation of a liquid droplet.

The PINE is a new instrument for measuring INP concentrations (Möhler et al., 2021). PINE is a portable cloud expansion chamber capable of running autonomously over long periods of time; this along with its low backgrounds and high time resolution (5 to 10 minutes per measurement) make it a useful instrument for measuring ambient INP concentrations across the globe. PINE has been used in several field campaigns (Brasseur et al., 2022; Lacher et al., 2024; Möhler et al., 2021), in which it has successfully made continuous measurements of INP concentrations. A PINE has also been used to investigate the contrail particle forming potential of hydrophobic jet lubrication oils (Ponsonby et al., 2024). There are multiple different models of PINE, the PINE-1A and -1B are prototypes, and subsequent models have been developed and are sold commercially, but the key operating principles are the same between different models.

To quantify the INA of an aerosol, an accurate measure of the temperature that the aerosol and hydrometeors experience is needed. Temperature measurements inside the PINE

chamber are made by multiple thermocouples through the length of the chamber, these thermocouples show a strong temperature gradient across the chamber, with the top of the chamber being the warmest and the bottom of the chamber being the coldest. This temperature gradient results in the measurement being sensitive to the exact position of the thermocouple in the chamber and so introduces an uncertainty in the measurement of the temperature that is experienced by the particles in the PINE chamber ( $T_{\text{exp}}$ ). An uncertainty of  $\pm 1$  °C in temperature results in an uncertainty of approximately  $\pm 10$  % relative humidity with respect to ice ( $\text{RH}_i$ ) at an expansion starting temperature of  $-10$  °C and  $\pm 15$  %  $\text{RH}_i$  at an expansion starting temperature of  $-30$  °C. This shows that even a small uncertainty in temperature can produce a large uncertainty in derived values. Given that altering the thermocouple position to iteratively find the coldest region of the chamber is impractical due to the design of the chamber, and that the thermocouple may move with repeated expansions and transport of the chamber, we set about finding an alternative way of determining temperature in the chamber.

In this study we explore a way of quantifying the temperature in the chamber that does not rely on accurate thermocouple measurements. This involves using the measured pressure during expansion to derive temperature according to the first law of thermodynamics, assuming adiabatic conditions (i.e. that the heat influx from the walls can be neglected). We present evidence that shows that if the cooling rate is sufficiently rapid then the adiabatic temperature is consistent with well-defined phase changes in the chamber. These phase changes include the activation of cloud condensation nuclei to cloud droplets and the homogeneous freezing of cloud droplets as well as the heterogeneous nucleation and freezing of droplets containing K-feldspar.

## 2.2 Methods

In this study we measured the ice nucleation of test aerosols in a controlled laboratory setting. The test material was aerosolised into an aerosol chamber from which aerosol was sampled, size distribution instruments were used in parallel to the PINE, which measures the nucleation of ice. Further detail on each part of the methodology follows.

### 2.2.1 Test aerosol preparation and size distributions

Test aerosols were aerosolised into a container, labelled “Sample Input” in Figure 2.1, and fed into a 0.73 m<sup>3</sup> (90 x 90 x 90 cm) aerosol chamber by a flow of air from an air compressor (Titan Precision, model TT-25L-SILENT) which was first filtered using a carbon capsule filter (PALL Life Sciences) and HEPA-CAP filter (Whatman). Citric acid aerosol was produced from a 0.01 weight % solution of citric acid in milli-Q water (18.2 MΩ) and aerosolised using a pocket nebuliser (Omron MicroAir U22). Smoke aerosol was produced by lighting a Swan Vesta safety match and extinguishing so that it smouldered and produced smoke. K-feldspar aerosol was produced from a milled sample of BSC 376 K-feldspar (Bureau of Analysed Samples Ltd) and aerosolised using a GRIMM X78502 Dust Tower. The flow rate of test aerosol into the aerosol chamber was controlled using Sierra mass flow controllers (C100L-DD-3-OV1-SV1-PV2-V1-S0) (MFCs). For citric acid and smoke aerosols, the flow rate was 2 slpm (standard litres per minute) and a second MFC was used to balance the input flow into the aerosol chamber

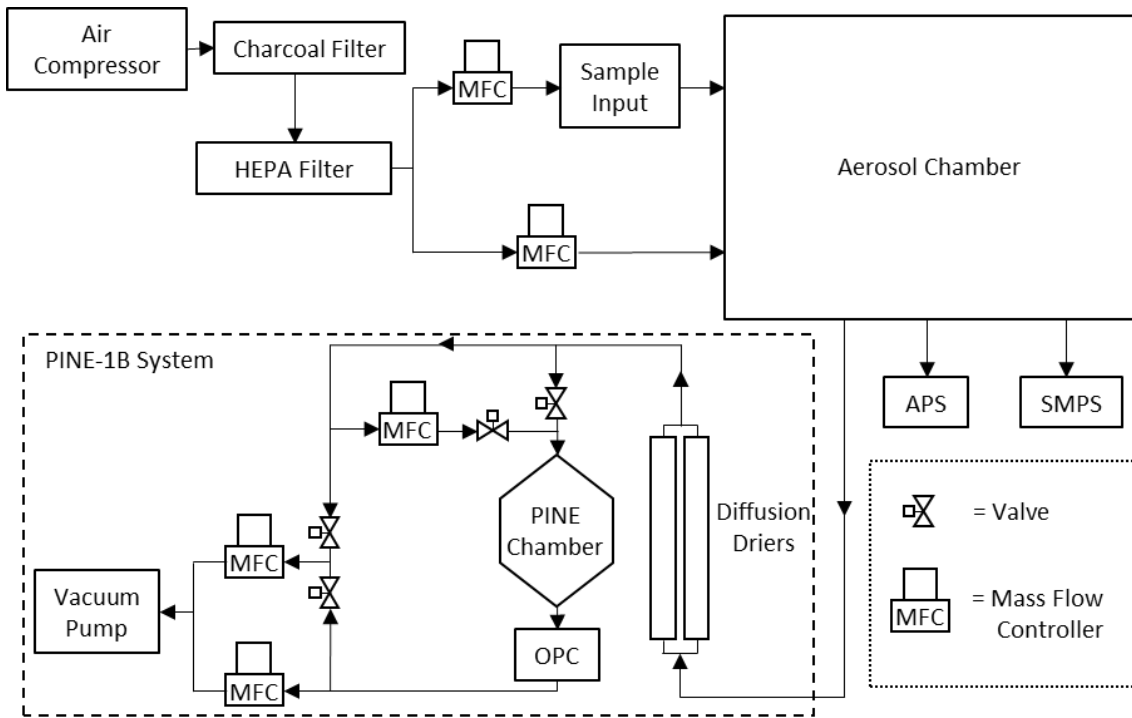


**Figure 2.1:** Schematic of the experimental setup used for measurements in this study. Compressed air was used to fill a 0.73 m<sup>3</sup> aerosol chamber with sample. The size distribution of the aerosol sample in the chamber from 0.01 to 20 μm was measured by combining measurements from a TSI model 3938 SMPS and a TSI model 3321 APS. The PINE-1B system measured INP concentrations in the chamber as described in the text. Valves and MFCs were used to control the direction and rate of the various flows through the system.

with the output flow to the aerosol size distribution instruments and the PINE-1B (as detailed later). For K-feldspar aerosol the flow rate through the “Sample Input” was set to be equal to the output flow from the aerosol chamber, so no flow was passed through the second MFC.

The size distribution and concentration of test aerosol in the aerosol chamber was continuously measured using a TSI model 3938 Scanning Mobility Particle Sizer (SMPS) measuring 0.01 – 0.6  $\mu\text{m}$  diameter particles and a TSI model 3321 Aerodynamic Particle Sizer (APS) measuring 0.5 – 20  $\mu\text{m}$  diameter particles. The SMPS measures mobility-equivalent particle diameter and the APS measures aerodynamic diameter, to compare and combine their measurements into a full aerosol size distribution their measured diameters were converted into volume-equivalent sphere diameters (Möhler et al., 2008b). Figure 2.2 shows example size distributions of the citric acid and K-feldspar aerosols, the size distribution of the smoke aerosol was not measured due to the APS and SMPS instruments being unavailable during the experiments using the smoke test aerosol. For the diameter conversion calculations, the citric acid particles were assumed to have a density of 1.0  $\text{g cm}^{-3}$  and a shape factor of 1.0 due to the particles being 0.01 weight % concentration solution droplets. The K-feldspar particles were assumed to have a density of 2.6  $\text{g cm}^{-3}$  due to that being the typical density of mineral dusts (Wagner et al., 2009a) and the shape factor was assumed to be 1.1 (Möhler et al., 2008b). In the size range over which the distribution measurements overlap, the smallest two APS size bins were discounted from further analysis due to inefficiencies in the lower size bins of the APS as stated by TSI literature (TSI, 2011). The SMPS measurements at sizes greater than the 3<sup>rd</sup> smallest APS size bin were then also discounted from further analysis, resulting in a diameter of  $\sim 0.6 \mu\text{m}$  for the citric acid aerosol and  $\sim 0.4 \mu\text{m}$  for the K-feldspar aerosol below which the SMPS measurements were used, and above which the APS measurements were used.

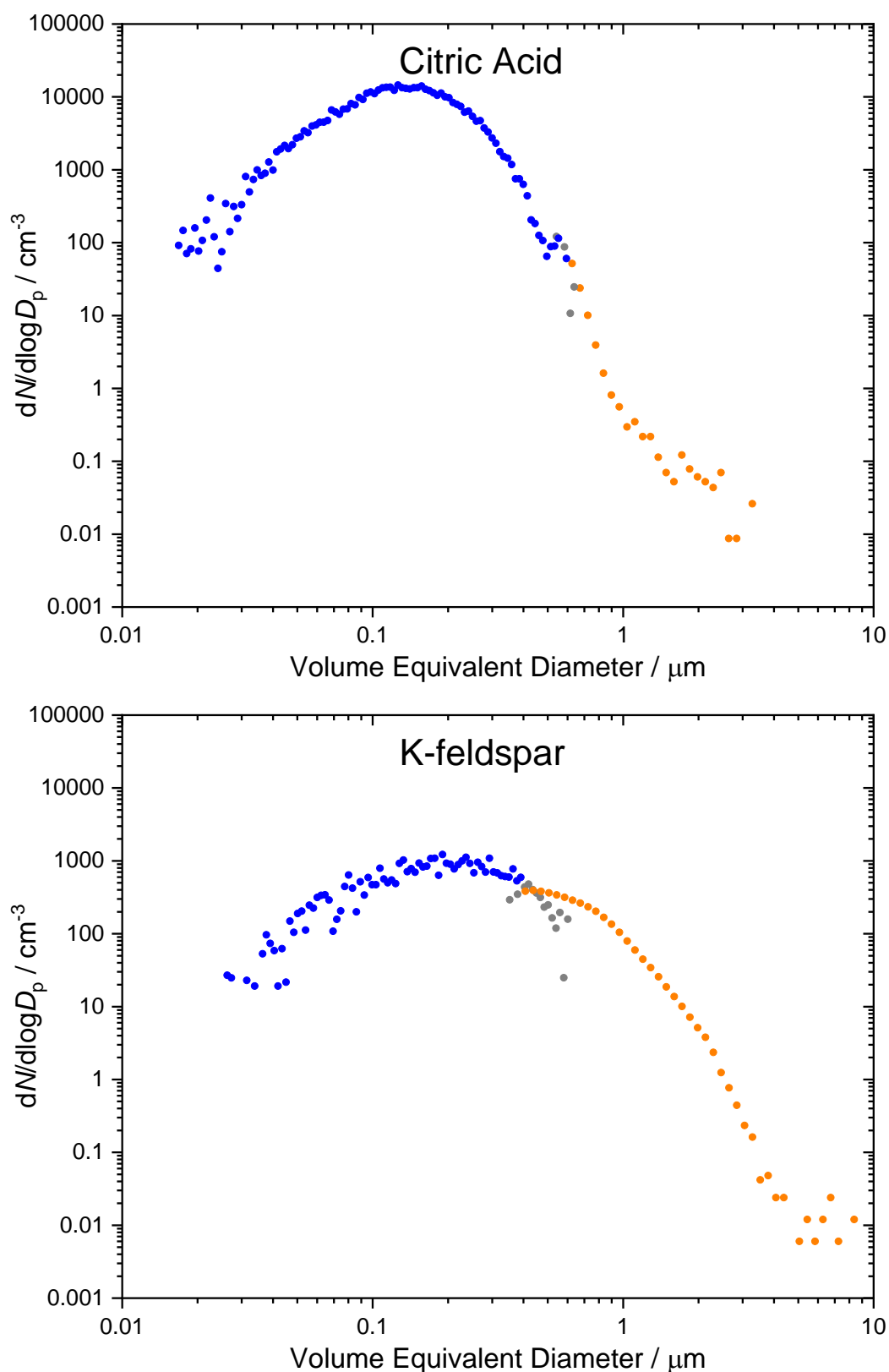


**Figure 2.2:** Examples of aerosol size distributions measured by APS and SMPS of citric acid and K-feldspar test aerosols. APS and SMPS measured diameters were converted into volume equivalent sphere diameters as in Möhler et al, (2008) in order to compare the two different instruments. Grey points show the measurements which were not used in further analysis due to the overlap between the APS and SMPS size ranges.

### 2.2.2 Portable Ice Nucleation Experiment (PINE)

This study uses PINE-1B, a prototype version of the commercially available PINE instrument, a basic schematic is shown in Figure 2.1 and further details about the development and operation of the PINE are given in Möhler et al. (2021). Below is a description of the aspects of the PINE most relevant for this study.

The PINE is a portable cloud expansion chamber that can measure the concentration of INPs in a sample by simulating the formation of a cloud via the principle of adiabatic expansion. The expansion chamber of PINE-1B has a volume of 7 L. Experiments are carried out by cycling through three distinct modes of operation, which are achieved by opening and closing the various valves and altering flow rates through the system using MFCs. First, in the flush mode air from the aerosol chamber is passed through the chamber to fill the chamber with the test aerosol, this is done for 5 minutes at a rate of 4 slpm to replace the volume in the chamber several times over. Next, in the expansion mode the chamber inlet is sealed but a flow is maintained through the outlet, resulting in a decrease in pressure in the chamber, and therefore a decrease in temperature due to the expansion of the gas. During this expansion mode, liquid droplets and ice crystals are produced in the chamber as it undergoes an expansion. After the expansion, the refill mode begins, during which the chamber is slowly refilled with filtered air, once the chamber is close to the sample pressure, the system returns to flush mode and a new cycle begins.

A Palas Welas 2500 OPC at the chamber outlet along with a Promo 2000 control unit are used to count and measure the size of particles exiting the chamber. During an expansion, ice crystals can be distinguished from non-ice particles by their larger size, and the INP concentration is calculated from the number of ice crystals detected by the OPC. The OPC was set to measure different nominal particle size ranges for different experiments; a 0.6 to 40  $\mu\text{m}$  range was used to measure the smallest particles forming at the start of expansions while a 2 to 105  $\mu\text{m}$  range was used to measure the larger ice crystals that formed throughout the expansion. Although the OPC output gives a size for each measured particle in micrometres, the absolute size measurements may be inaccurate because the different particle types that are simultaneously measured interact with light in different ways. Therefore, the OPC size measurements are instead used qualitatively where relative shifts in size distribution indicate a phase change.

The temperature of the chamber walls is controlled by an external flow of chilled liquid ethanol from a refrigerated circulator (LAUDA-Brinkmann, Proline RP 890) and continuous temperature measurements are made by three pairs of thermocouples that record the chamber wall and gas temperatures at the top, middle and bottom of the chamber. The chiller can cool the chamber walls down to approximately -50 °C. During the flush mode the temperature of gas inside the chamber equilibrates to the same temperature as the chamber walls, meaning the temperature of the walls is the temperature at which the expansions start. Two parallel gas drying columns (Perma Pure, MD-700-24S-1) reduce the humidity of the air that enters the chamber which, along with the deposition of water vapour onto the inner chamber walls as ice, allows the  $RH_i$  within the chamber to equilibrate to 100 % during the flush phase.

The flow rates through the MFCs can be changed to control the rate of pressure and temperature decrease during an expansion; the duration of expansions can also be changed by changing the pressure at which the expansion mode ends. The flow through the driers must be between 2 and 5 slpm to maintain drying efficiency whilst minimising particle losses; based upon this, a flush and expansion flow rate of 4 slpm is used for all experiments performed for this study unless otherwise stated. Similarly, a minimum expansion pressure of 800 mbar was used unless otherwise stated, this was chosen because when going to lower minimum pressures the concentration of liquid droplets and ice crystals produced during the expansion becomes higher than the detector's maximum detection limit which results in the OPC undercounting particles.

### **2.2.3 Adiabatic temperature calculation**

In previous studies using PINE instruments, the coldest measuring thermocouple was used to represent the temperature measurement within the chamber, this is based upon the assumption that the nucleation processes in the chamber are primarily driven by the coldest temperature in the chamber (Möhler et al., 2021). The coldest thermocouple is always the one closest to the chamber outlet and therefore the OPC, which is also indicative of it being the thermocouple most representative of what is being measured by the OPC.

Here, we explore the conditions under which it is appropriate to assume that the expansion in some volume of the centre of the PINE chamber is adiabatic. When the RH in the chamber (calculation detailed in next subsection) was below water saturation, the dry adiabatic temperature was calculated using the following equation:

$$T = T_0 \times \left( \frac{P}{P_0} \right)^{\frac{R_d}{c_p}} \quad (\text{Eq. 2.1})$$

Where  $T$  is the adiabatic temperature,  $T_0$  is the temperature at the start of the expansion as measured by the thermocouple,  $P$  is the pressure measured in the PINE and  $P_0$  is the pressure measurement at the start of the expansion.  $R_d$  is the gas constant for dry air ( $= 287 \text{ J K}^{-1} \text{ kg}^{-1}$ ) and  $c_p$  is the specific heat capacity of dry air in  $\text{J K}^{-1} \text{ kg}^{-1}$ .

Once the RH in the chamber reached and increased beyond water saturation during each expansion, the wet adiabatic temperature was calculated using the MetPy python function “moist\_lapse” which uses equation 8 from Bakhshaii and Stull (2013), shown below as equation 2.2. The inputs for this function are pressure, for which the pressure measurement was used, a starting temperature, for which the dry adiabatic temperature at water saturation was used, and a starting pressure, for which the pressure measurement at water saturation was used.

$$\frac{\partial T}{\partial P} = \left( \frac{b}{P} \right) \frac{R_d T + L_v r_s}{C_{pd} + \frac{L_v^2 r_s \varepsilon b}{R_d T^2}} \quad (\text{Eq. 2.2})$$

Where  $L_v$  is the latent heat of vaporization of water,  $C_{pd}$  is the specific heat for dry air at constant pressure,  $r_s$  is the saturated water vapor mixing ratio,  $\varepsilon$  is the ratio of the ideal gas constants of dry air and water vapor ( $R_d/R_v = 0.622 \text{ kg}_{\text{watervapor}} \text{ kg}^{-1}_{\text{dryair}}$ ) and  $b$  is a dimensionless factor which describes how the specific heat and gas constant change with humidity (Bakhshaii and Stull, 2013).

#### 2.2.4 Relative humidity calculation

Due to the lack of a direct measurement of water vapour within the PINE chamber, the RH in the chamber must be inferred.  $RH_i$  can be calculated from the temperature and pressure measurements in the PINE using the following equation:

$$RH_i = \frac{p_{ice}(T_0) \times \frac{P}{P_0}}{p_{ice}(T)} \times 100$$

(Eq. 2.3)

Where  $RH_i$  is the relative humidity with respect to ice inside the PINE chamber,  $p_{ice}(T)$  is the saturation vapour pressure of ice and is calculated based upon the temperature,  $T$ , in the chamber using equation 7 from Murphy and Koop (2005) and  $p_{ice}(T_0)$  is the saturation vapour pressure of ice at the start of the expansion. The  $RH_i$  in the chamber is assumed to come to 100 % during the flush phase via the deposition of excess water vapour onto the internal walls of the PINE as ice, therefore  $p_{ice}(T_0)$  is assumed to be equal to the vapour pressure of ice in the chamber at the start of an expansion.  $\frac{P}{P_0}$  is the ratio of the pressure in the chamber,  $P$ , to the pressure at the start of the expansions,  $P_0$ , which accounts for the removal of water vapour via the pumping out of air during an expansion. The use of Equation 2.3 to calculate  $RH_i$  in the PINE chamber is only valid up until the onset of liquid droplet or ice crystal formation, at which point the formation and growth of these hydrometeors will begin to take up water vapour from the air in the PINE chamber.

#### 2.2.5 Active site density

The temperature dependant active site density ( $n_s(T)$ ) of a material is a measure of the number of active sites capable of triggering heterogeneous ice nucleation per unit surface area at temperature  $T$ .  $n_s(T)$  is a commonly used quantity for comparing the INA of different materials between different studies since it is independent of the sample concentrations used for different measurement techniques (Murray et al., 2012).

The quantity of  $n_s(T)$  to represent immersion mode INA was first used by Connolly et al. (2009), they used modelling to calculate the surface area of mineral dusts in contact with water droplets during AIDA measurements which allowed for the change in aerosol particle and droplet number concentration over the course of a measurement to be accounted for. Niemand et al. (2012) used a simplified method of calculating  $n_s(T)$ , which was to divide the concentration of ice crystals measured during an AIDA experiment by

the surface area concentration of the sample calculated from the size distribution measurements. To avoid significantly increased complications, both of these formulations assumed that for a given sample  $n_s(T)$  did not vary with particle size.

In this study,  $n_s(T)$  is calculated using a similar method to Niemand et al. (2012) with the following equation:

$$n_s(T) = \frac{N_{\text{ice}}}{s} \quad (\text{Eq. 2.4})$$

Where  $N_{\text{ice}}$  is the number concentration of ice crystals measured by the PINE per  $\text{cm}^3$  and  $s$  is the surface area of sample per  $\text{cm}^3$ , measured by the SMPS and APS. This equation assumes that each ice crystal measured by the PINE-1B contains a single sample particle which has a single site active at the measured temperature.

For the calculation of the surface area concentrations from the SMPS and APS measurements of aerosol number concentration, the particles were assumed to be spheres and the surface area concentrations ( $ds$ ) calculated for each size bin were summed to give a total surface area concentration of the test aerosol. Measurements of the transmission efficiency of particles from the aerosol chamber to the PINE were made by using the APS to measure the size distribution of K-feldspar aerosol in the aerosol chamber and then moving the APS to measure the aerosol size distribution after the diffusion dryers in the PINE-1B system. These measurements showed that the transmissions efficiency was approximately 100 % for particles with volume equivalent diameters of up to approximately 3.5  $\mu\text{m}$ , a plot of the measured transmission efficiency as a function of volume equivalent diameter is shown in Figure 2.10 in the appendix. For calculations of  $n_s(T)$ , it was assumed that the concentration and size distribution of the aerosol sample in the PINE chamber was equivalent to the aerosol size distribution measured in the aerosol chamber. To test the accuracy of this assumption and determine the potential impact of the loss of particles larger than 3.5  $\mu\text{m}$  in diameter, the surface area concentration of K-feldspar aerosol was calculated without any of the particles larger than 3.5  $\mu\text{m}$  in diameter. The result of this calculation was a decrease in the surface area concentration of approximately 0.7 % at most, which in turn would lead to an increase in  $n_s(T)$  of 0.7 %. The typical uncertainty calculated for  $n_s(T)$  of K-feldspar was on the order of  $\sim 7$  % (as shown in Figure 2.9), an order of magnitude greater than the uncertainty caused by potential particle losses. Based upon this small change in the values of  $n_s(T)$  compared to

the uncertainty, the assumption that the aerosol sample size distribution in PINE was equivalent to that measured in the aerosol chamber was considered appropriate.

## 2.3 Results & Discussion

To test the assumption that a portion of the PINE chamber experiences adiabatic conditions, we use well-defined phase transformations where the temperature and RH conditions are known. In the first set of experiments, we use soluble aerosol particles where the activation of cloud droplets at water saturation and the homogeneous freezing of haze droplets below  $\sim -35$  °C are both well defined. In the second set of experiments, we examine the homogeneous freezing of cloud droplets, the rate of which has been extensively characterised in laboratory studies. In addition, we explore the heterogeneous nucleation of K-feldspar, quantifying the active site density and compare this to literature data. But first we illustrate the challenge of accurately measuring the temperature in the chamber.

### 2.3.1 Comparison of the measured and dry adiabatic temperatures

In Figure 2.3 we present the thermocouple temperature measurements alongside the temperature derived according to the adiabatic assumption during a typical expansion with K-feldspar aerosol. This figure shows that there is a large difference between the temperatures measured in the chamber (solid red, orange and yellow lines) and the theoretical adiabatic temperature (dashed red line). At cloud droplet onset, we see that the coldest thermocouple in this case is about 3 °C warmer than that derived assuming adiabatic expansion. We also show the derived  $RH_i$  according to both the measured and the adiabatic temperatures. We see that when calculating  $RH_i$  using the coldest thermocouple measurement the droplet onset is barely above 100 %  $RH_i$ , whereas with the adiabatic assumption the onset is well above 100 % (we come back to the absolute determination of onset  $RH_i$  below).

There are multiple factors that may cause this discrepancy between measured and adiabatic temperature, including heat influx from the chamber walls heating the gas during expansions, the thermocouples responding too slowly to measure the true temperature change during expansions, and our assumptions about RH at the start of each expansion being incorrect.

To test the response rate of the PINE thermocouples, we performed experiments in which an additional faster-response thermocouple, one with a thinner wire (0.5 mm diameter) than those used in the PINE-1B, was inserted into the PINE chamber to compare the response rate of the two different thermocouples to temperature changes during expansions (see Figure 2.11 and associated text). The PINE-1B thermocouple had a maximum temperature change rate of  $-0.09 \pm 0.01 \text{ }^\circ\text{C s}^{-1}$  at an expansion rate of 2.0 slpm and  $-0.16 \pm 0.01 \text{ }^\circ\text{C s}^{-1}$  at an expansion rate of 4.0 slpm. The thinner thermocouple had a maximum temperature change rate of  $-0.08 \pm 0.01 \text{ }^\circ\text{C s}^{-1}$  at an expansion rate of 2.0 slpm and  $-0.17 \pm 0.02 \text{ }^\circ\text{C s}^{-1}$  at an expansion rate of 4.0 slpm. The PINE thermocouple responded to temperature changes at rates consistent with the thinner wire thermocouple,

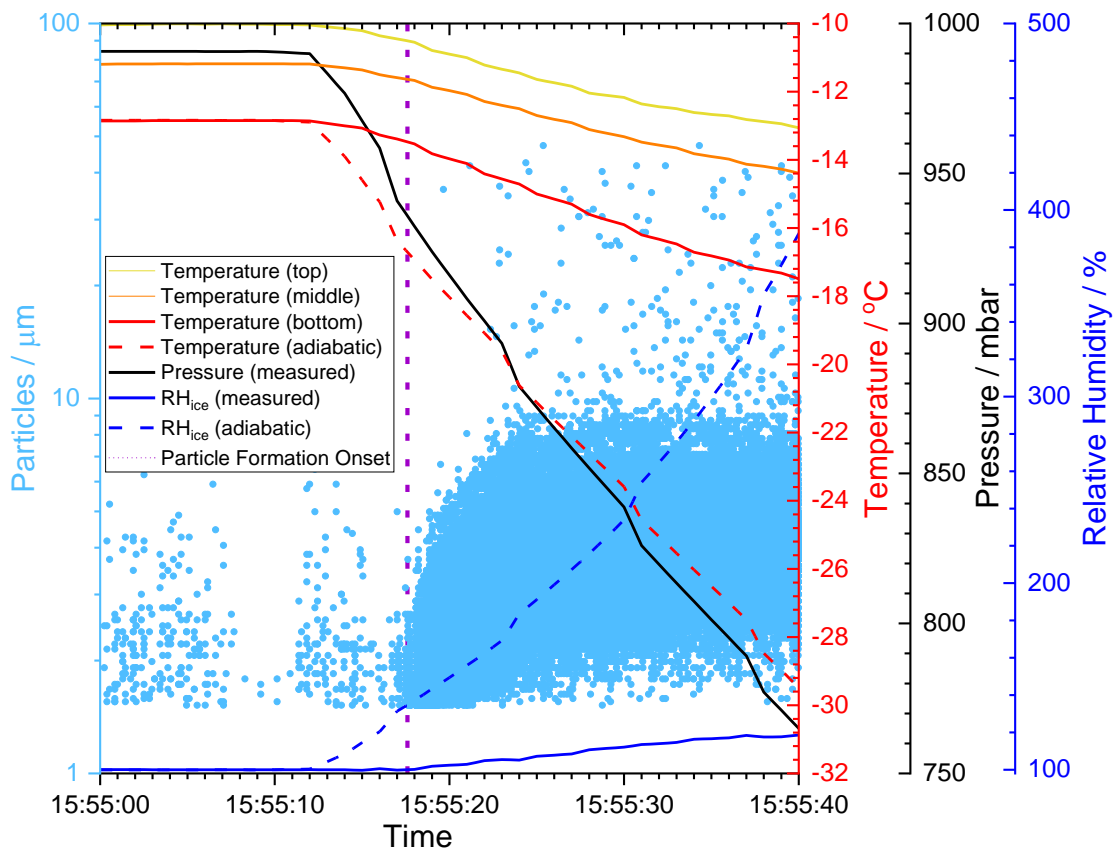


**Figure 2.3:** Plot of an expansion using K-Feldspar aerosol to illustrate the operation of PINE and show the difference between the measured and calculated adiabatic temperatures. Dashed lines show the conditions calculated according to an adiabatic expansion while solid lines show the conditions measured in the case of temperature and pressure and calculated from these measurements in the case of  $\text{RH}_i$ . Top, middle and bottom temperature lines refer to the positions of the thermocouples inside the PINE chamber. Blue points represent individual particles measured by the OPC. Vertical dotted line indicates the time at which cloud particles are first measured by the OPC, referred to as the onset.

and therefore we concluded that the PINE-1B thermocouples were able to respond fast enough to accurately measure temperature changes in the PINE chamber during expansions.

To test the validity of our assumption that the PINE chamber equilibrates to 100 % RH<sub>i</sub> during the flush phase, we performed experiments in which we added a “pause phase” between the flush and expansion phases to give more time for water vapour to diffuse from the centre of the PINE chamber to the walls and therefore the chamber to come to equilibrium before expansions. We used a range of pause times from 1 to 60 minutes, however our experiments showed no systematic effect when including a pause phase (see Figure 2.12 and associated text). Therefore, we concluded that our assumption of reaching 100 % RH<sub>i</sub> during the flush phase is accurate.

As well as the discrepancy between the adiabatic and measured temperatures, there is a temperature gradient from the top to the bottom of the chamber, with the bottom thermocouple measuring roughly 3 °C colder than the top thermocouple, and the gradient increasing during expansions. This temperature gradient highlights that the temperature measurement of each thermocouple is sensitive to its position inside the chamber. Based upon experimental evidence using different PINE models, the coldest measuring thermocouple has previously been assumed to be representing the coldest temperature inside the chamber (Möhler et al., 2021), however it is possible that there are areas inside the chamber that are at colder temperatures than those being measured.

Considering that different PINE models may have their thermocouples positioned in slightly different places, there is uncertainty associated comparing thermocouple measurement between different PINES. Moving the thermocouples inside an already built PINE would be a long and difficult process involving removing the detector assembly, removing insulation, taking apart the sealed PINE chamber, moving the thermocouples and testing for leaks on rebuilding it before testing the temperature measurements. This would likely need to be done many times and is therefore impractical, so having an alternative method for accurately determining the temperature in the PINE chamber that could be used with consistency between different PINE models is preferable. Hence, we set out a series of test to determine whether the derived adiabatic temperature can be used as an accurate alternative to the thermocouple measured temperature for representing  $T_{\text{exp}}$ .

### 2.3.2 Onset of cloud particle formation using non-ice-nucleating aerosol

To test the accuracy of the adiabatic and measured temperatures in the PINE during expansions, we used the activation of cloud droplets and the homogeneous freezing of haze droplets as observable phase transitions. These phase transitions occur at well-defined conditions and so allow for the adiabatic and measured temperatures (and  $RH_i$  calculated from them) to be compared to theoretically expected values.

Citric acid and soot were used as test aerosols to observe these phase transitions. Citric acid is known to not nucleate ice heterogeneously when in the liquid solution state (Murray et al., 2010a; Wilson et al., 2012) and soot aerosol has been shown to be non-ice-nucleating at temperatures warmer than  $\sim -38$  °C (Kanji et al., 2020; Mahrt et al., 2018). In addition, citric acid is known to form a very viscous or glassy solution at low humidity, rather than effloresce (Murray, 2008). Efflorescence would be a problem for these experiments because the crystalline citric acid may nucleate heterogeneously. Therefore, at temperatures above  $-38$  °C, the first phase transition expected to be seen in the PINE during expansions using citric acid and soot aerosols is the activation of liquid cloud droplets at water saturation. At temperatures below  $\sim -38$  °C, soot has been shown to be capable of nucleating ice via PCF (Mahrt et al., 2018; Marcolli et al., 2021; Nichman et al., 2019), therefore expansions using soot aerosol were limited to  $> -35$  °C in order to avoid PCF from occurring. Citric acid has only been shown to be capable of heterogeneously nucleating ice when in the glassy state, which only occurs at much lower temperatures (Murray et al., 2010a; Wilson et al., 2012). Therefore expansions using citric acid aerosol at temperatures lower than  $-35$  °C were performed to observe the homogeneous freezing of haze droplets, the conditions for which are defined in Koop et al. (2000).

To observe these phase transitions in the PINE-1B and quantitatively compare the measured and adiabatic conditions with those theoretically expected, the experiments were specifically tailored to capture the onset of the phase transition, referred to herein simply as the “onset”. The OPC size range was set to measure particles  $0.6 - 40$   $\mu\text{m}$  in diameter (rather than the typical  $2 - 105$   $\mu\text{m}$ , used in Figure 2.3) so as to measure the cloud droplets as early as possible while they were growing, expansion flow rate was set to 4.0 slpm. The onset was defined as the earliest point in the expansion at which the measured particle concentration in the PINE chamber reached a factor of 10 above the background concentration of test aerosol, the adiabatic and measured temperature and  $RH_i$  conditions were defined at this point of onset.

Figure 2.4 shows the  $RH_i$  and temperature conditions at which the onsets were observed in the PINE-1B. Each point represents a single expansion, and the error bars cover the conditions at  $\pm 0.5$  seconds from the onset time, which was used to represent the uncertainty of the onset conditions due to the measurement of the onset occurring over roughly a 1 second period rather than it being instantaneous. The citric acid measurements shown here have been published by Ponsonby et al. (2024) as part of the first publication using the experimental methods described in this chapter. The citric acid measurements were included in Ponsonby et al. (2024) to support the use of the method, but the citric

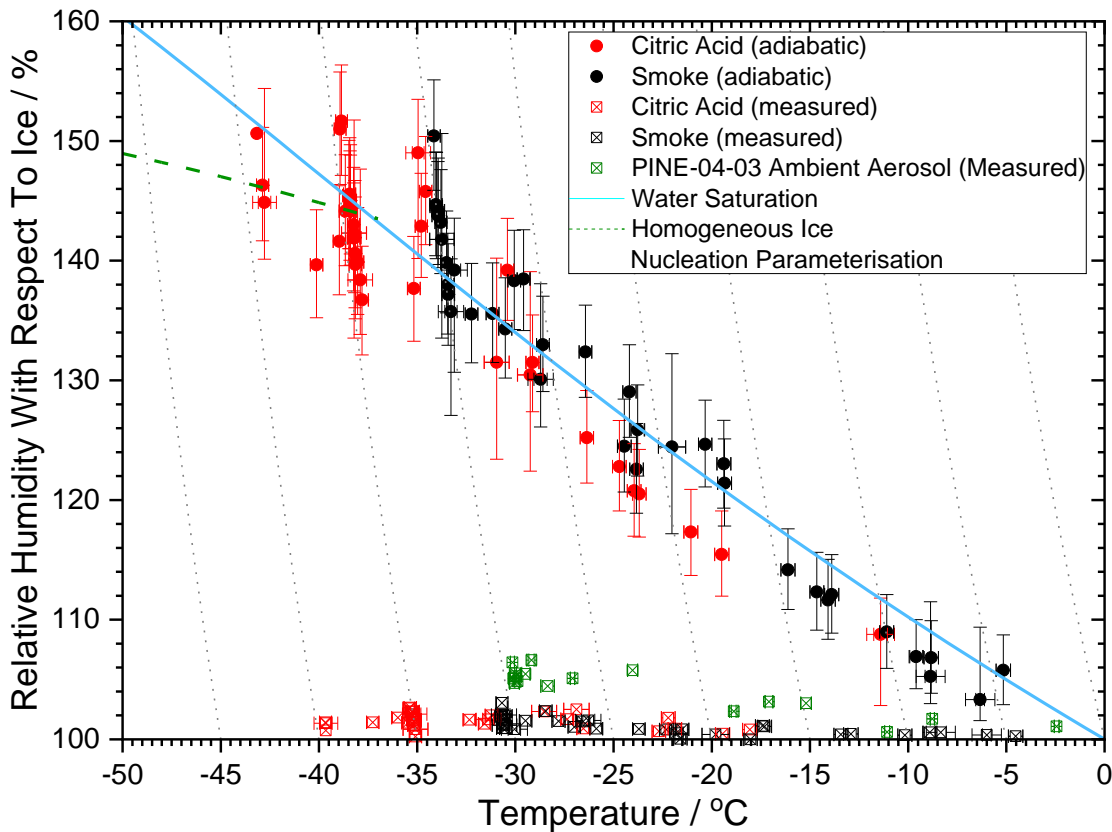


**Figure 2.4:** Plot showing the  $RH_i$  and temperature conditions under which cloud particle formation onset is observed. Each individual point represents a single expansion at 4.0 slpm such as the one shown in Figure 2.3. Solid circles represent conditions calculated according to a dry adiabatic expansion while crossed squares represents conditions calculated from temperature and pressure measurements in the chamber. Red points represent citric acid aerosol while black points represent smoke aerosol, green points represent ambient aerosol measured by the PINE-04-03. Solid blue line represents water saturation (100 %  $RH_w$ ) conditions, dashed green line represents parameterisation of homogeneous ice nucleation according to Koop et al. (2000). Error bars represent conditions at  $\pm 0.5$  seconds from the time at which onset is observed. Grey dotted lines represent calculated dry adiabatic conditions through expansions.

acid measurements were performed by myself. At temperatures above  $-35\text{ }^{\circ}\text{C}$ , the onsets according to the measured temperature occurred at  $\text{RH}_i$  just above 100 %, which is far below water saturation (shown by the solid blue line) where the onset is expected to occur. Conversely, the adiabatic onset conditions were close to water saturation, with most expansion onsets overlapping with water saturation conditions within their uncertainty.

The same pattern was seen at temperatures approximately  $-35\text{ }^{\circ}\text{C}$  and below, at which the first phase transition for citric acid solution droplets is expected to be homogeneous freezing according to the parameterisation from Koop et al. (2000) (shown by the dashed green line in Figure 2.4). Again, the onsets according to measured temperature occurred at  $\text{RH}_i$  just above 100 %, well below expected conditions, while the adiabatic onsets occurred at the expected conditions within uncertainty.

The fact that the onset  $\text{RH}_i$  calculated from the thermocouple-measured temperature was always far below water saturation indicates that this temperature measurement is warmer than  $T_{\text{exp}}$  in the PINE-1B chamber. On the other hand, the fact that the onset  $\text{RH}_i$  calculated from the adiabatic temperature was consistent with the expected conditions indicates that the adiabatic temperature is an accurate representation of  $T_{\text{exp}}$  up until at least the onset and when using an expansion flow rate of 4.0 slpm. The accuracy of the adiabatic temperature along with the poor representativity of the thermocouple-measured temperature suggests that there is a volume within the chamber where there is minimal heat influx from the chamber walls such that this region can undergo a temperature decrease approximated by adiabatic expansion up until at least the onset.

To test whether the poor representativity of the thermocouples was a potential issue for other PINE instruments, onset conditions in the PINE-04-03, a more recently developed model than the PINE-1B, were investigated. The onset conditions for ambient aerosol measured in the PINE-04-03 are shown as green points in Figure 2.4, these points show that, similar to the PINE-1B, the coldest measuring thermocouple in the PINE-04-03 does not accurately represent the conditions of water droplet formation. Adiabatic conditions for the PINE-04-03 have not been calculated for this study, but the poor representativity of the measured thermocouple highlights that this issue may be present in other PINE models. Similarly, Vogel et al. (2022) also observed evidence of  $T_{\text{exp}}$  being colder than their measured temperature in the AIDAm, an expansion chamber similar to the PINE in size and functionality. When comparing homogeneous freezing onsets between the AIDAm to the  $84\text{ m}^3$  AIDA expansion chamber, they find that the AIDAm onsets occurred at approximately  $1.5\text{ }^{\circ}\text{C}$  warmer than those in the AIDA.

### 2.3.3 The optimal expansion flow rate

While it is shown above that the adiabatic temperature is an accurate representation of  $T_{\text{exp}}$  when performing expansions at 4.0 slpm, we anticipate that heat influx from the walls will become increasingly important for slower expansions. Therefore, we performed further onset measurements of cloud droplet activation using citric acid at different expansion flow rates to determine at what flow rates the adiabatic temperature remains accurate.

Figure 2.5 shows the results of these measurements at two different expansion starting temperatures in the form of the ratio of the adiabatic onset  $\text{RH}_i$  to the  $\text{RH}_i$  of water saturation calculated according to an adiabatic expansion. A ratio of 1 indicates the onset occurred at adiabatic water saturation and therefore that the expansion was adiabatic. Expansions at flow rates between 1 and 2 slpm had their onsets at  $\text{RH}_i$  above what would

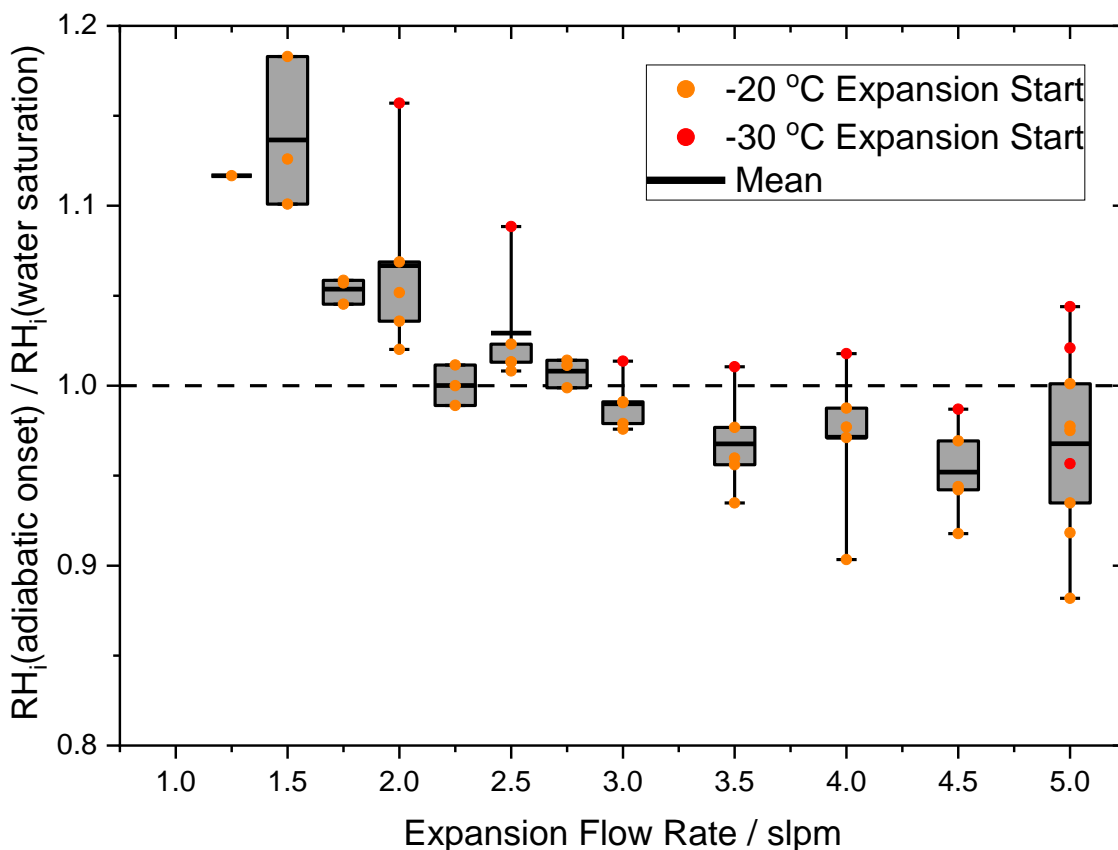


**Figure 2.5:** Plot showing the adiabatic  $\text{RH}_i$  at the onset of cloud droplet activation of citric acid aerosol relative to water saturation  $\text{RH}_i$  for different expansion flow rates. The black dotted line represents a ratio of 1.0. Coloured points represent individual expansions. Box and whisker plots include all expansions at a given flow rate, grey shaded box area represents 25 to 75 %, horizontal black line represents mean value, and whiskers span 5 to 95 %.

be expected as water saturation for an adiabatic expansion, at flow rates between 2 and 3 slpm, the onsets mostly occur close to water saturation, at flow rates between 3 and 5 slpm, the onsets occur either close to or below water saturation. The expansions with starting temperatures of -30 °C generally had onsets at higher relative  $RH_i$  than their same-flow-rate counterparts at expansion starting temperatures of -20 °C.

The low bias in  $RH_i$  at expansion flow rates greater than 3 slpm was also seen in Figure 2.4, particularly for the citric acid measurements. It is not clear why there was a low bias at these flow rates, but one possibility is that hygroscopic growth below water saturation was misinterpreted as the droplet onset. In Figure 2.4 the onsets for soot particles generally occurred at slightly higher RH than citric acid particles, which supports the hygroscopic growth explanation since soot is less hygroscopic than citric acid. Nevertheless, even with this low bias, the measured onsets are generally consistent with expected onsets within uncertainty.

The results in Figure 2.5 indicate that at expansion flow rates of 2 slpm and lower, the expansions occurred too slowly to conform to adiabatic conditions. This was most likely caused by heat influx from the PINE chamber walls during these expansions increasing the temperature inside the chamber relative to the theoretical adiabatic expansion, causing cloud droplet onset to occur later into the expansion. At expansion flow rates above 2 slpm, the heat influx from the walls does not affect the expansions, at least up until water saturation since the onsets consistently occur near water saturation.

Based upon these measurements using different expansion flow rates, when using the adiabatic temperature to represent  $T_{exp}$ , it is best to use flow rates between 2.5 and 4.0 slpm to ensure the expansion is meeting adiabatic conditions up until water saturation is reached. However, when using PINE to measure immersion mode INPs, expansions must go beyond water saturation to produce and measure ice crystals. Therefore, we recommend an expansion flow rate of 4.0 slpm to maintain adiabatic expansion conditions beyond water saturation. Flow rates higher than 4.0 slpm were not used because the ice crystals also needed time to grow to be detected during expansions. At faster flow rates there would be less time for crystal growth and therefore greater risk of undercounting ice concentration due to the crystals not being large enough to be detected as ice.

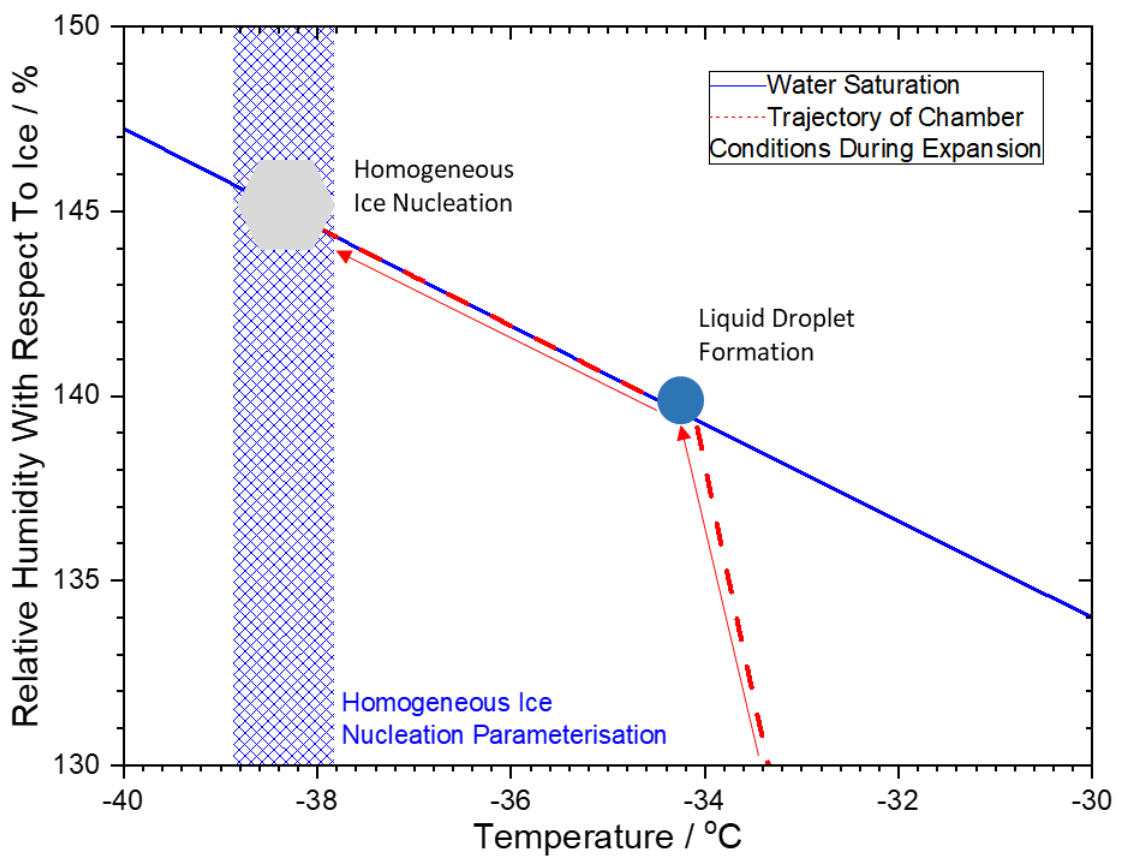
### 2.3.4 Homogeneous ice nucleation in cloud droplets

We used the homogeneous freezing of cloud droplets as another phase change observable in the PINE chamber to test the accuracy of the adiabatic and measured temperatures in the PINE-1B during expansions. There are several parameterisations that have been derived from model calculations and experimental measurements to represent this process (Espinosa et al., 2016; Koop and Murray, 2016; Tarn et al., 2021). An advantage of looking at homogeneous freezing of cloud droplets is that this phase transformation occurs much deeper into an expansion and therefore provided a test of the adiabatic assumption at greater differences between the initial and adiabatic temperatures.

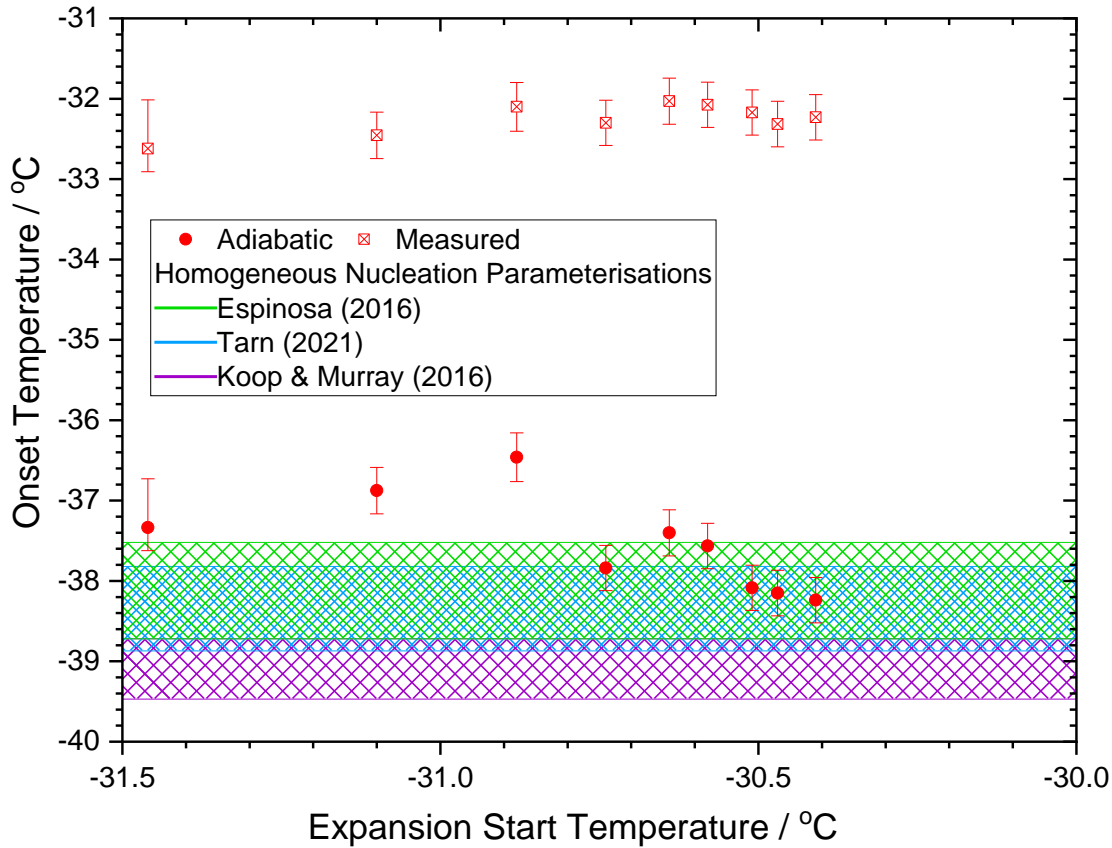
To observe the onset of homogeneous freezing in the PINE chamber, the OPC was set to measure 2 to 105  $\mu\text{m}$  diameter particles, this meant that the liquid droplets were too small to be measured until they froze and grew into the detectable range as ice crystals, allowing the onset of particle observation with the OPC to be identified as homogeneous ice nucleation (defined in the same way as the previous liquid droplet activation experiments). We know that the liquid droplets formed first because we observe them when the OPC size range is set at 0.6 to 40  $\mu\text{m}$ , as shown in Figure 2.4 in separate experiments (it is not possible to change the size range settings of the Welas OPC part way through an expansion). Expansion starting temperatures of -30.0 to -31.5  $^{\circ}\text{C}$  were used to ensure that, during expansions, the citric acid aerosol first activated to cloud droplets at water saturation that then homogeneously froze when reaching a cold enough temperature, as illustrated in Figure 2.6. An expansion flow rate of 4.0 slpm was used to match the previous liquid droplet activation experiments.

Figure 2.7 shows the homogeneous ice nucleation onset temperatures for citric acid aerosol, the expected temperature range of homogeneous ice nucleation onset (shaded coloured areas) was calculated from three different parameterisations for homogeneous ice nucleation (Espinosa et al., 2016; Koop and Murray, 2016; Tarn et al., 2021), the ranges cover 0.1 to 50 % of the total population of liquid droplets undergoing homogeneous ice nucleation and assume a cloud droplet diameter of 2  $\mu\text{m}$  since this was the lower size measurement limit the OPC was set to for these experiments. The onsets according to the thermocouple measured temperature occur at roughly 5  $^{\circ}\text{C}$  warmer than the expected temperature range for homogeneous nucleation. On the other hand, when using the adiabatic temperature, the onsets occur mostly within the expected range, with only 2 expansions occurring roughly 1  $^{\circ}\text{C}$  warmer than expected.

These results show that the thermocouple temperature measurement is warmer than  $T_{\text{exp}}$  at the point of homogeneous ice nucleation in PINE-1B, and that the calculated adiabatic temperature provides a more accurate representation of  $T_{\text{exp}}$  at this point in expansions. As with the onsets for liquid droplets in Figure 2.4, this indicates that the adiabatic temperature is a more appropriate representation of  $T_{\text{exp}}$  in the PINE-1B chamber during expansions under the conditions used for these measurements than the temperatures measured by the thermocouples.



**Figure 2.6:** Illustration showing the conditions in the PINE chamber during the expansions measuring the homogeneous ice nucleation of citric acid aerosol. Solid blue line represents water saturation (100 %  $RH_w$ ) conditions, dashed red line represents the trajectory of the conditions through the expansion, with arrows indicating the direction with time. Blue shaded area represents the temperature range in which homogeneous ice nucleation is expected (defined as 0.1 to 50 % of droplets frozen) to occur based upon the parameterisation from Tarn et al. (2021), assuming liquid particles with a diameter of 2  $\mu\text{m}$ . Blue circle represents expected conditions for the formation of liquid droplets and grey hexagon for homogeneous ice nucleation.



**Figure 2.7:** Plot showing the homogeneous ice nucleation onset temperatures for citric acid aerosol. Solid circle points represent conditions calculated according to an adiabatic expansion while crossed square points represents conditions calculated from temperature and pressure measurements in the chamber. Coloured shaded areas represent the temperature range in which homogeneous ice nucleation is expected to occur (defined as 0.1 to 50 % of droplets frozen) based upon three different parameterisations for homogeneous ice nucleation (Espinosa et al., 2016; Koop and Murray, 2016; Tarn et al., 2021), assuming liquid particles with a diameter of 2  $\mu\text{m}$ .

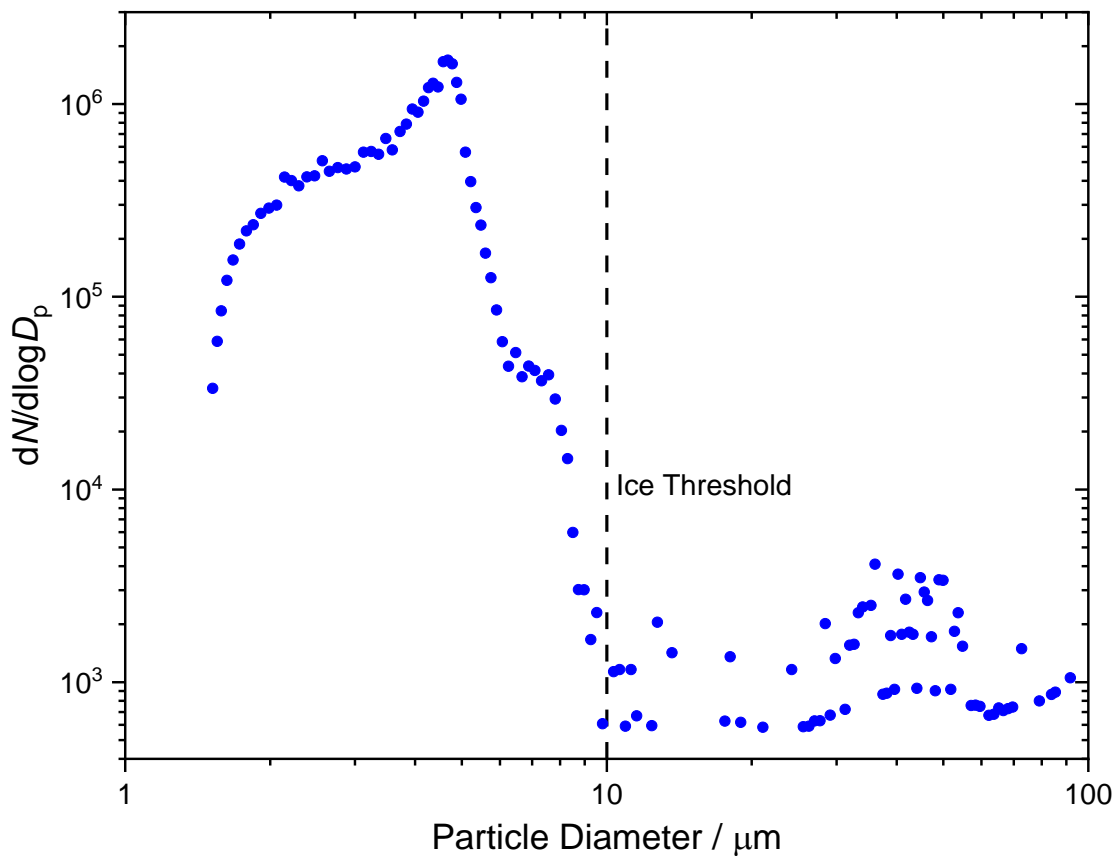
### 2.3.5 Heterogeneous ice nucleation of K-feldspar

The PINE is an instrument primarily designed for measuring INP concentrations, therefore, we used K-feldspar dust to test the accuracy of the adiabatic temperature when measuring INP concentrations during expansions. K-feldspar is a mineral dust known for its high INA (Atkinson et al., 2013) and has been used as a material for comparing different INP measurement methods (DeMott et al., 2018).

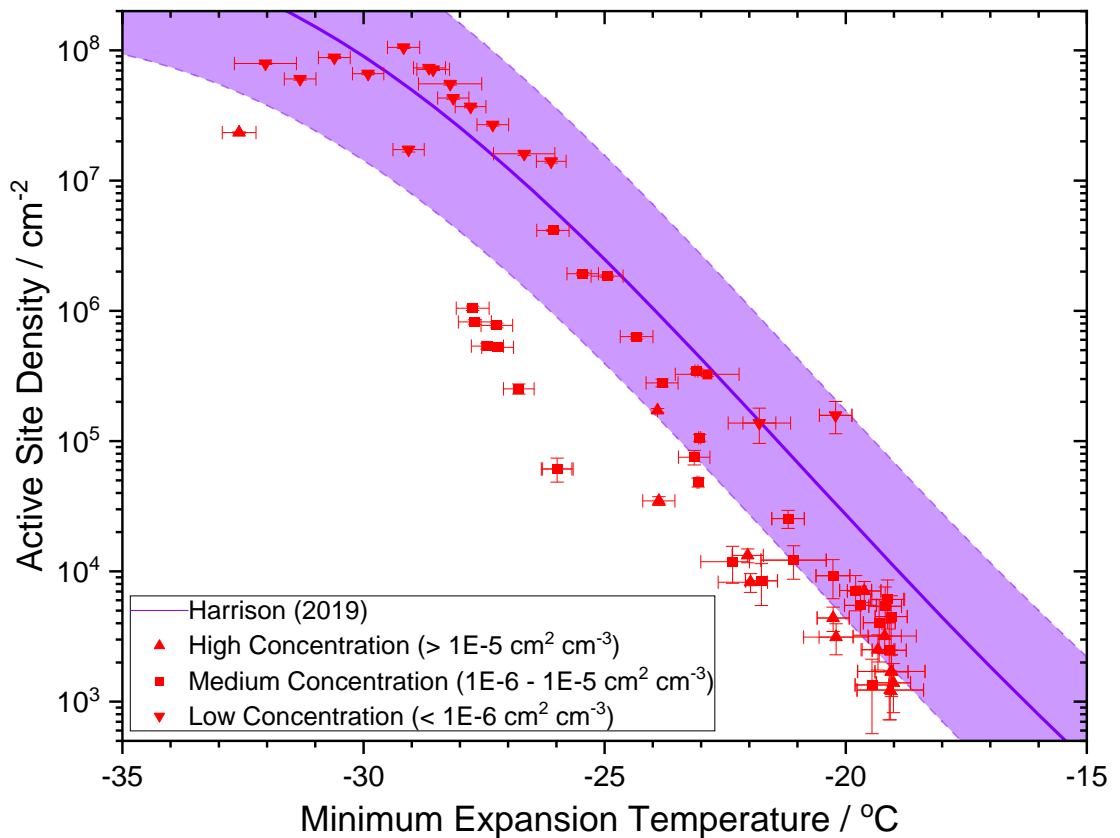
A sample of BSC 376 K-feldspar was aerosolised using a GRIMM X78502 Dust Tower to produce different test aerosol concentrations in the aerosol chamber. The different concentrations allowed measurements to be made across a range of temperatures between -15 and -35 °C since at warmer temperatures a higher concentration of test aerosol was needed to observe enough ice crystals while at colder temperatures a lower concentration of test aerosol was needed to avoid producing too many ice crystals that the OPC went above the upper limit of detection. Expansions were performed at a flow rate of 4.0 slpm to match the other work in this study and were stopped at a pressure of 800 mbar inside the PINE chamber. For the calculation of ice crystal concentration, only the first 100 mbar was used to ensure that the use of adiabatic temperature was accurate. Ice crystals were defined as particles measured by the OPC with a diameter larger than 10 µm, this was based upon the cloud size distributions measured by the OPC during expansions, which showed a peak of liquid cloud droplets at 5 µm which ended at 10 µm as shown in Figure 2.8. This assumption that only particles larger than 10 µm in diameter were ice crystals may have resulted in an undercounting of ice crystals, therefore the INP concentrations from this study and the active site density calculated may be biased low.

Figure 2.9 shows the active site density as a function of temperature, a measure of INA, for K-feldspar measured by the PINE-1B during this study using the calculated adiabatic temperature. A parameterisation from Harrison et al. (2019) is plotted to compare to previous studies of K-feldspar. The parameterisation from Harrison et al. (2019) is derived from multiple different K-feldspar samples from different studies using different measurement techniques, therefore the range in the parameterisation represents the variability found between different samples and instruments. The INA of K-feldspar measured in this study compared well with previous studies when using the adiabatic temperature with most points overlapping with the parameterisation range. There is variability in the derived INA values, particularly at temperatures between -26 and -28 °C, and there is a low bias at temperatures warmer than -28 °C. This low bias is similar to that seen in Figure 2.4 and Figure 2.5, however unlike that case, the low bias seen in Figure

**2.9** cannot be due to hygroscopic growth since that would not affect the INA. Instead, the low bias seen in the INAs at temperatures warmer than  $-28\text{ }^{\circ}\text{C}$  may be due to an undercounting of ice crystals, at warmer temperatures ice crystal growth will be slower due to a lower  $\text{RH}_i$  and therefore there may be a higher fraction of the total ice crystal population that is smaller than the ice threshold and therefore not counted as ice. However, despite this low bias in INA at warmer temperatures, there is generally overlap between our measurements and the range in literature values. This agreement is further evidence in favour of the accuracy of the adiabatic temperature as a representation of  $T_{\text{exp}}$  during the first 100 mbar of expansions.



**Figure 2.8:** Size distribution of particles measured by the Welas OPC during an expansion using K-feldspar test aerosol at expansion starting temperature of  $-13\text{ }^{\circ}\text{C}$  and flow rate of 4.0 slpm. Black dashed line indicates the ice diameter threshold; all particles larger than this threshold were considered ice crystals and all particles smaller than this threshold were considered not ice crystals.



**Figure 2.9:** Plot showing the surface area density of active sites as a function of adiabatic temperature for K-Feldspar aerosol. Each point represents a measurement from a single expansion. The different shapes for the red points represent different surface area concentrations of K-Feldspar aerosol in the aerosol chamber during measurements. Purple line represents a parameterisation for K-feldspar by Harrison et al. (2019) and purple shaded area represents standard deviation of the parameterisation. The temperature (x-axis) uncertainty for adiabatic points represents adiabatic temperatures at  $\pm 0.5$  seconds from the minimum expansion temperature. Uncertainty for active site density (y-axis) is calculated from the uncertainty associated with the counting statistics of ice particles during expansions.

## 2.4 Conclusions

In this study we have tested using the adiabatic-derived temperature as a way of quantifying temperature in the PINE-1B chamber during expansions via three different experiments. We show that the adiabatic temperature can be used to accurately represent the conditions of liquid droplet formation as well as homogeneous freezing of supercooled water droplets. We also demonstrate that the ice-nucleating ability of K-feldspar measured by the PINE-1B compares well with previous studies when using the adiabatic temperature. The use of the adiabatic temperature to represent the temperature inside the PINE-1B chamber during expansions allows for an accurate measure of temperature without relying on the thermocouples, which can be sensitive to their positioning within the chamber.

However, the accuracy of the adiabatic temperature is dependent on the conditions of the expansion, at an expansion flow rate of 2.0 slpm and below the adiabatic temperature is no longer an accurate representation of  $T_{\text{exp}}$  for the activation of cloud droplets. Also, when deriving ice particle concentration and active site density for K-feldspar in this study, we only quantitatively used measurements from the first 100 mbar into expansions. When expanding to lower pressures the adiabatic temperature is expected to become less accurate as the influx of heat from the walls becomes a greater factor. Nevertheless, we showed that the first 100 mbar of expansions is enough to measure the INP concentration of a known active INP across a temperature range of -15 to -35 °C whilst the adiabatic temperature was still accurate.

The method outlined in this study of using the adiabatic-derived temperature was used by Ponsonby et al. (2024) in their study investigating the viability of jet engine lubrication oil droplets at nucleating ice in contrail clouds. The study used the PINE-1B and the analytical methods detailed in this study to show that the oil droplets activated to form water droplets at conditions  $\sim 10\%$  RH<sub>i</sub> above water saturation, consistent with what would be expected for a wettable, insoluble aerosol (Petters and Kreidenweis, 2007). These droplets then froze homogeneously below -38 °C. The study by Ponsonby et al. (2024) is a successful case of the adiabatic temperature in PINE being used to measure the ice nucleation of material not previously studied.

Like in the PINE-1B, we show that the newer PINE model PINE-04-03 also poorly represents the conditions of liquid droplet formation with its thermocouple measurements. This highlights a need for other PINE models to be tested using methods similar to those

in this study to characterise their temperature measurements. In the longer term, improved temperature measurements within future PINE models should be implemented, for example, a continuous measurement of temperature across the full vertical length of the chamber would allow the coldest temperature to always be measured during an expansion.

In this study we also show that the RH calculated from the adiabatic temperature provides a good approximation for the RH at which liquid droplets form in the PINE chamber. This knowledge can be used in future studies to investigate the temperature and RH conditions of liquid droplet or ice crystal formation in the PINE using different aerosols. It would be particularly interesting to try and observe heterogeneous ice nucleation below water saturation, potentially through the mechanism of PCF. A limitation of the calculated RH value is that it will only be accurate up until the formation of liquid droplets or ice crystals in the chamber; after this these hydrometeors will uptake the water vapour to grow, adding significant complexity and uncertainty to the calculation of RH. An independent measure of water vapour content in future PINE models would allow RH to be calculated throughout the whole expansion and with less uncertainty, allowing RH to be known during phase changes that occur after the initial onset.

The ability to accurately quantify the temperature and RH conditions at onset and further into the expansion using the PINE would allow PINE to be used to characterise the INA of different materials using an experimental method similar to what occurs within clouds. This can be used in both a controlled laboratory setting to improve the understanding of how different materials nucleate ice and also in field measurements looking at the aerosol naturally found in different areas around the world.

## **2.5 Appendix**

### **2.5.1 Aerosol particle transmission efficiency**

To test the transmission efficiency of particles from the aerosol chamber to the PINE, the APS was used to measure the size distribution of K-feldspar aerosol both in the aerosol chamber and in the PINE-1B system line between the diffusion driers and the inlet to the PINE chamber. Figure 2.10 shows the measured particle concentrations as a function of volume equivalent diameter in panel a, and the calculated transmission efficiencies as a function of volume equivalent diameter in panel b. The values shown in panel b are the mean of multiple measurements in which the APS sampling location was repeatedly

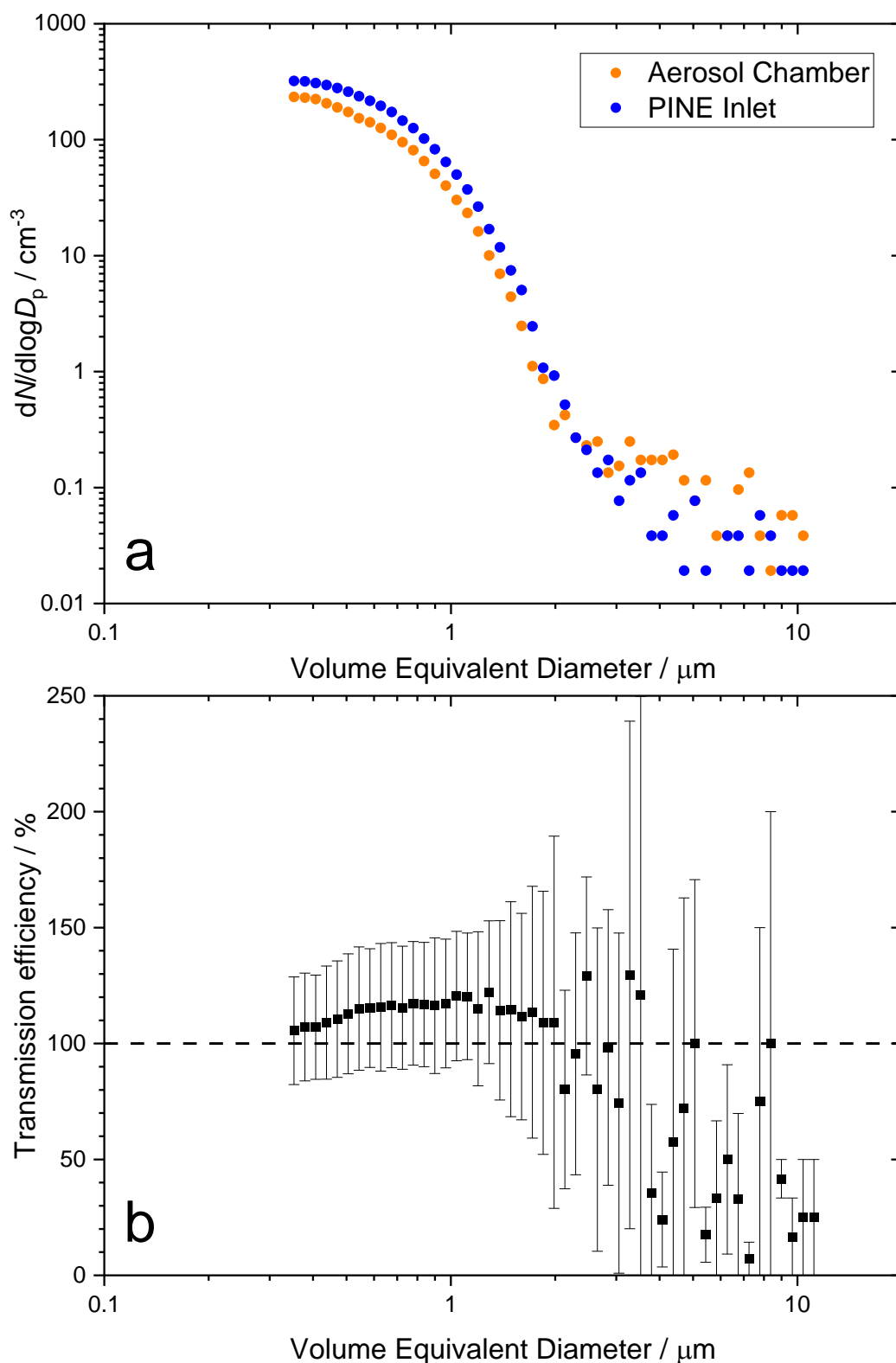


**Figure 2.10:** Plot showing **a)** aerosol size distribution of K-feldspar aerosol measured by the APS from the aerosol chamber and between the diffusion driers and the PINE chamber inlet. **b)** Transmission efficiency of particles from the aerosol chamber to the PINE chamber as a function of the volume equivalent diameter, measured using the APS. Horizontal dashed line shows a 100 % transmission efficiency where no particles are lost.

swapped between the aerosol chamber and after the diffusion driers, the error bars in panel b are the standard deviation of the multiple measurements. At diameters up to approximately 2  $\mu\text{m}$  the transmission efficiency is consistent with 100 % within the uncertainty, but at diameters greater than 2  $\mu\text{m}$  the uncertainty increases and there is more variability in the transmission efficiency values due to the aerosol concentrations decreasing at these sizes and approaching the lower limit of detection for the APS. At diameters greater than 3.5  $\mu\text{m}$  the transmission efficiency values are consistently below 100 %, but the low concentrations result in large uncertainties which cover a range of over 100 % in some cases. The measurements shown in Figure 2.10 indicate that particle losses from the aerosol chamber to the PINE chamber are close to 0 at particle diameters smaller than  $\sim 3.5 \mu\text{m}$ .

### 2.5.2 Thermocouple response time

A potential reason for the PINE-1B's measured temperature not being an accurate representation of  $T_{\text{exp}}$  is due to the response time of the thermocouples used to measure the temperature. The thermocouples in the PINE-1B may be too thick so that the time required for the thermocouple itself to change temperature could be greater than the timescale of temperature change of the gas in the PINE chamber during expansion. This hypothesis was tested by comparing the change in temperature of the coldest PINE-1B thermocouple with a thinner wire thermocouple; if the PINE-1B thermocouple was not able to keep up with temperature changes it would be expected that the thinner thermocouple would be faster to respond since it has less thermal mass needed to undergo temperature change.

Figure 2.11 panel a shows a comparison between the temperatures measured during a sequence of expansions by the PINE-1B's bottom gas thermocouple, the thermocouple used to represent the temperature measured in the PINE chamber, and an additional thermocouple inserted into the bottom of the PINE chamber as close to the PINE-1B's bottom gas thermocouple as possible so that they are both measuring similar areas in the chamber. The first two expansions were done at a flow rate of 2.0 slpm and the second two at 4.0 slpm. Panel b shows the rate of temperature change for each thermocouple averaged over 10 seconds.

There is a consistent offset between the two thermocouples, with the thinner thermocouple measuring approximately 1  $^{\circ}\text{C}$  colder than the PINE, this is because the thermocouples were not in exactly the same position due to the difficulty of precisely

placing the extra thermocouple at a specific location. During the 2.0 slpm expansions, the PINE thermocouple reached a maximum temperature change rate of  $-0.09 \pm 0.01 \text{ } ^\circ\text{C s}^{-1}$  and the thinner wire thermocouple  $-0.08 \pm 0.01 \text{ } ^\circ\text{C s}^{-1}$ . During the 4.0 slpm expansions, the PINE thermocouple reached a maximum temperature change rate of  $-0.16 \pm 0.01 \text{ } ^\circ\text{C s}^{-1}$  and the thinner wire thermocouple  $-0.17 \pm 0.02 \text{ } ^\circ\text{C s}^{-1}$ . The temperature change rates for both thermocouples during expansion cooling are consistent with each other at the same expansion flow rates. The warming that occurs after each expansion during the refill phase occurs at a faster rate than the cooling during expansions, 0.25 to  $0.50 \text{ } ^\circ\text{C s}^{-1}$  depending on expansion flow rate, but the temperature measurements during this refill phase are not used for any quantitative analysis and therefore do not need to be accurate. The fact that both thermocouples cool at close to identical rates to one another during expansions indicates that the PINE thermocouple is not struggling to measure rapid changes in temperature during expansions, and therefore thermocouple response is not a factor in the inaccuracy of the thermocouple measurements.

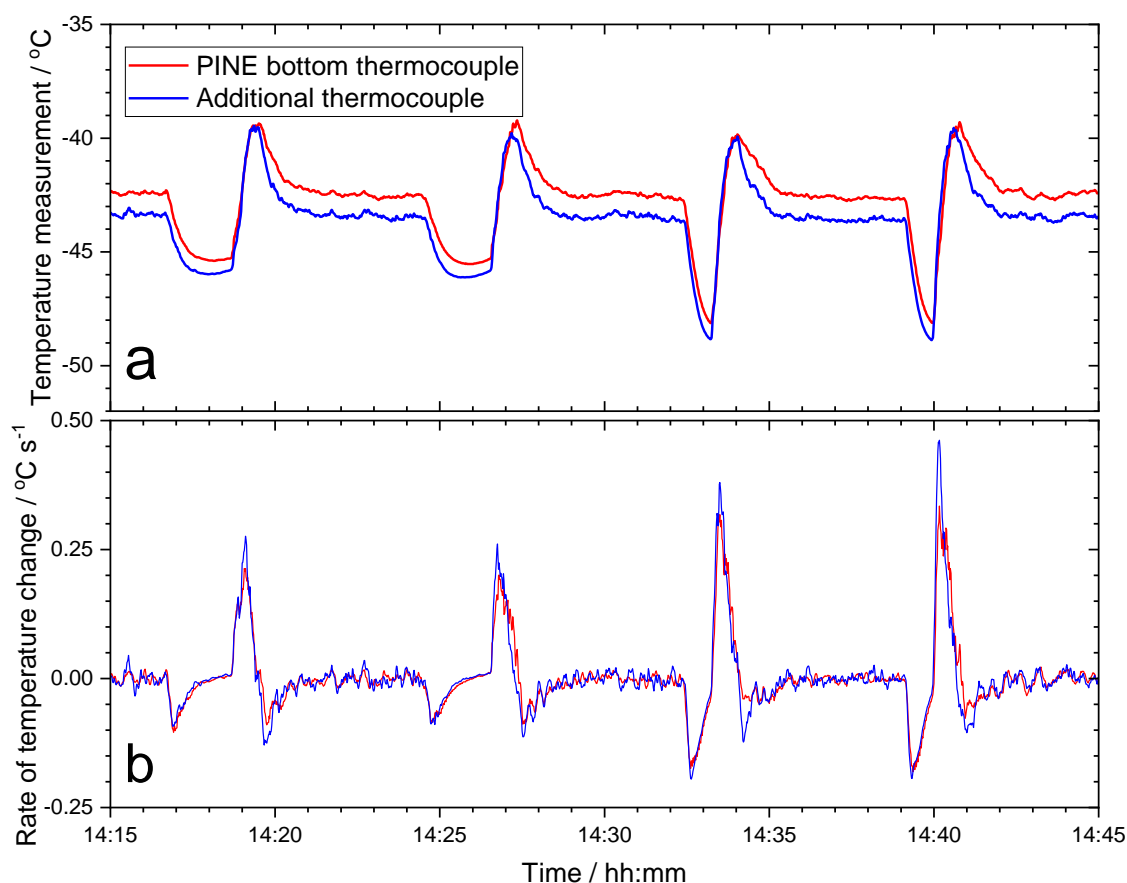


**Figure 2.11:** a) Comparison between the temperature measurements from the bottom PINE-1B gas thermocouple and an additional wire thermocouple inserted into the bottom of the PINE chamber during 4 expansions. The first two expansions were performed at a flow rate of 2.0 slpm and the second two at 4.0 slpm. b) Rate of temperature change for the two thermocouples averaged over 10 seconds.

### 2.5.3 Relative humidity at the start of expansions

One of the key assumptions made when calculating the  $RH_i$  in the PINE chamber is that the chamber is at 100 %  $RH_i$  at the start of the expansion, this assumes that during the flush phase the  $RH_i$  in the chamber reaches equilibrium by depositing excess water vapour onto the inner walls of the chamber as ice. To test this assumption, a series of expansions were performed in which a pause period was introduced in between the flush and the expansion phases, during this pause the top of the chamber was sealed and all flows were set to zero to allow the air in the chamber to hold steady and be given more time to come to equilibrium with the chamber walls.

Expansions using citric acid test aerosol were performed with a range of pause lengths up to 60 minutes to investigate the potential relationship between the pause length and the  $RH_i$  at which the onset is observed. If it were the case that the chamber does not come to equilibrium without a pause, the calculated onset  $RH_i$  would be too low, and increasing pause length would increase onset  $RH_i$  until equilibrium is reached. An expansion starting temperature of  $-40\text{ }^\circ\text{C}$  was used as at colder temperatures more water vapour is required to deposit as ice to reach 100 %  $RH_i$ . An expansion flow rate of 2.0 slpm was used.

Figure 2.12 shows the relationship between the pause length and the  $RH_i$ , calculated from the measured temperature, at which the onset of homogeneous freezing of citric acid haze droplets (see section 2.3.2 for details). The standard deviation of the onset RH values from the measurements with a 0-minute pause length is equal to 0.75 %, which indicates the natural variability in the measurements and is shown by the error bars. The majority of the expansions with  $>0$  pause length had onsets within the range of values at 0 minutes, with one expansion with a 1.5-minute pause length being at lower  $RH_i$  and one with a 60-minute pause length being at higher  $RH_i$ , but even for these two measurements the uncertainties overlap with those at 0 minutes. The fact that there was no clear correlation between the pause length and the onset  $RH_i$  indicates that the chamber was already at equilibrium before a pause, and therefore the assumption that the chamber is at 100 %  $RH_i$  at the start of an expansion is accurate.

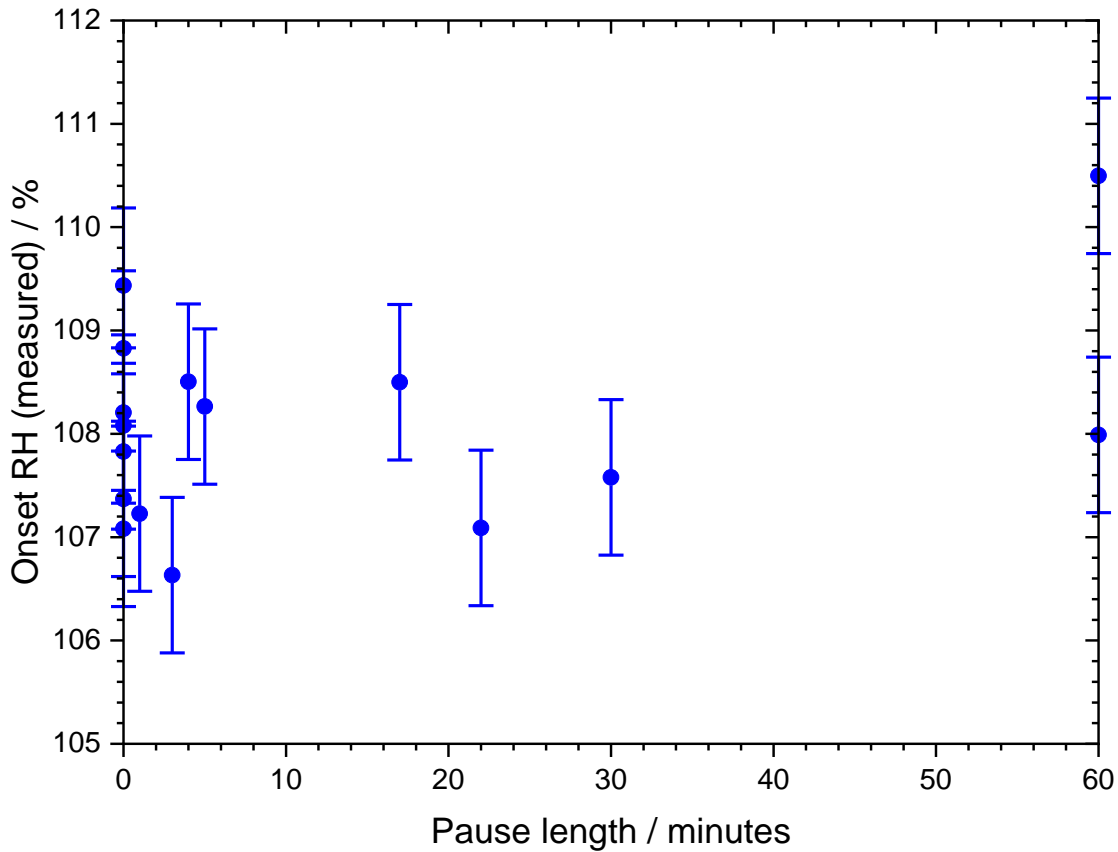


**Figure 2.12:** Plot showing the effect of introducing a pause before expansions has on the onset RH<sub>i</sub> of homogeneous freezing of citric acid haze droplets, calculated from temperature and pressure measurements in the PINE-1B chamber. Each point represents a single expansion with a starting temperature of -40 °C and an expansion flow rate of 2.0 slpm. Error bars represent the standard deviation of the results at 0 minutes, equal to  $\pm 0.75\%$  RH.

## 2.6 References

Adams, M. P., Atanasova, N. S., Sofieva, S., Ravantti, J., Heikkinen, A., Brasseur, Z., Duplissy, J., Bamford, D. H. and Murray, B. J.: Ice nucleation by viruses and their potential for cloud glaciation, *Biogeosciences*, 18(14), 4431–4444, doi:10.5194/bg-18-4431-2021, 2021.

Atkinson, J. D., Murray, B. J., Woodhouse, M. T., Whale, T. F., Baustian, K. J., Carslaw, K. S., Dobbie, S., O’Sullivan, D. and Malkin, T. L.: The importance of feldspar for ice nucleation by mineral dust in mixed-phase clouds, *Nature*, 498(7454), 355–358, doi:10.1038/nature12278, 2013.

Bakhshaii, A. and Stull, R.: Saturated pseudoadiabats-A noniterative approximation, *J. Appl. Meteorol. Climatol.*, 52(1), 5–15, doi:10.1175/JAMC-D-12-062.1, 2013.

Brasseur, Z., Castarède, D., Thomson, E. S., Adams, M. P., Drossaert Van Dusseldorp, S., Heikkilä, P., Korhonen, K., Lampilahti, J., Paramonov, M., Schneider, J., Vogel, F., Wu, Y., Abbatt, J. P. D., Atanasova, N. S., Bamford, D. H., Bertozzi, B., Boyer, M., Brus, D., Daily, M. I., Fösig, R., Gute, E., Harrison, A. D., Hietala, P., Höhler, K., Kanji, Z. A., Keskinen, J., Lacher, L., Lampimäki, M., Levula, J., Manninen, A., Nadolny, J., Peltola, M., Porter, G. C. E., Poutanen, P., Proske, U., Schorr, T., Silas Umo, N., Stenszky, J., Virtanen, A., Moisseev, D., Kulmala, M., Murray, B. J., Petäjä, T., Möhler, O. and Duplissy, J.: Measurement report: Introduction to the HyICE-2018 campaign for measurements of ice-nucleating particles and instrument inter-comparison in the Hyytiälä boreal forest, *Atmos. Chem. Phys.*, 22(8), 5117–5145, doi:10.5194/acp-22-5117-2022, 2022.

Christner, B. C., Morris, C. E., Foreman, C. M., Cai, R. and Sands, D. C.: Ubiquity of biological ice nucleators in snowfall, *Science* (80-. ), 319(5867), 1214, doi:10.1126/science.1149757, 2008.

David, R. O., Marcolli, C., Fahrni, J., Qiu, Y., Perez Sirkin, Y. A., Molinero, V., Mahrt, F., Brühwiler, D., Lohmann, U. and Kanji, Z. A.: Pore condensation and freezing is responsible for ice formation below water saturation for porous particles, *Proc. Natl. Acad. Sci.*, 116(17), 8184–8189, doi:10.1073/pnas.1813647116, 2019.

DeMott, P. J., Möhler, O., Cziczo, D. J., Hiranuma, N., Petters, M. D., Petters, S. S., Belosi, F., Bingemer, H. G., Brooks, S. D., Budke, C., Burkert-Kohn, M., Collier, K. N., Danielczok, A., Eppers, O., Felgitsch, L., Garimella, S., Grothe, H., Herenz, P., Hill, T. C.

J., Höhler, K., Kanji, Z. A., Kiselev, A., Koop, T., Kristensen, T. B., Krüger, K., Kulkarni, G., Levin, E. J. T., Murray, B. J., Nicosia, A., O'Sullivan, D., Peckhaus, A., Polen, M. J., Price, H. C., Reicher, N., Rothenberg, D. A., Rudich, Y., Santachiara, G., Schiebel, T., Schrod, J., Seifried, T. M., Stratmann, F., Sullivan, R. C., Suski, K. J., Szakáll, M., Taylor, H. P., Ullrich, R., Vergara-Temprado, J., Wagner, R., Whale, T. F., Weber, D., Welti, A., Wilson, T. W., Wolf, M. J. and Zenker, J.: The Fifth International Workshop on Ice Nucleation phase 2 (FIN-02): Laboratory intercomparison of ice nucleation measurements, *Atmos. Meas. Tech.*, 11(11), 6231–6257, doi:10.5194/amt-11-6231-2018, 2018.

Espinosa, J. R., Navarro, C., Sanz, E., Valeriani, C. and Vega, C.: On the time required to freeze water, *J. Chem. Phys.*, 145(21), 211922, doi:10.1063/1.4965427, 2016.

Harrison, A. D., Lever, K., Sanchez-Marroquin, A., Holden, M. A., Whale, T. F., Tarn, M. D., McQuaid, J. B. and Murray, B. J.: The ice-nucleating ability of quartz immersed in water and its atmospheric importance compared to K-feldspar, *Atmos. Chem. Phys. Discuss.*, 1–23, doi:10.5194/acp-2019-288, 2019.

Herbert, R. J., Murray, B. J., Dobbie, S. J. and Koop, T.: Sensitivity of liquid clouds to homogenous freezing parameterizations, *Geophys. Res. Lett.*, 42(5), 1599–1605, doi:10.1002/2014GL062729, 2015.

Kanji, Z. A., Ladino, L. A., Wex, H., Boose, Y., Burkert-Kohn, M., Cziczo, D. J. and Krämer, M.: Overview of Ice Nucleating Particles, *Meteorol. Monogr.*, 58, 1.1-1.33, doi:10.1175/amsmonographs-d-16-0006.1, 2017.

Koop, T. and Murray, B. J.: A physically constrained classical description of the homogeneous nucleation of ice in water, *J. Chem. Phys.*, 145(21), 211915, doi:10.1063/1.4962355, 2016.

Koop, T., Luo, B., Tsias, A. and Peter, T.: Water activity as the determinant for homogeneous ice nucleation in aqueous solutions, *Nature*, 406(6796), 611–614, doi:10.1038/35020537, 2000.

Lacher, L., Adams, M. P., Barry, K., Bertozzi, B., Bingemer, H., Boffo, C., Bras, Y., Büttner, N., Castarede, D., Cziczo, D. J., DeMott, P. J., Fösig, R., Goodell, M., Höhler, K., Hill, T. C. J., Jentsch, C., Ladino, L. A., Levin, E. J. T., Mertes, S., Möhler, O., Moore, K. A., Murray, B. J., Nadolny, J., Pfeuffer, T., Picard, D., Ramírez-Romero, C., Ribeiro, M., Richter, S., Schrod, J., Sellegri, K., Stratmann, F., Swanson, B. E., Thomson, E. S.,

Wex, H., Wolf, M. J. and Freney, E.: The Puy de Dôme Ice Nucleation Intercomparison Campaign (PICNIC): comparison between online and offline methods in ambient air, *Atmos. Chem. Phys.*, 24(4), 2651–2678, doi:10.5194/acp-24-2651-2024, 2024.

Lohmann, U. and Feichter, J.: Global indirect aerosol effects: a review, *Atmos. Chem. Phys.*, 5(3), 715–737, doi:10.5194/acp-5-715-2005, 2005.

Mahrt, F., Marcolli, C., David, R. O., Grönquist, P., Barthazy Meier, E. J., Lohmann, U. and Kanji, Z. A.: Ice nucleation abilities of soot particles determined with the Horizontal Ice Nucleation Chamber, *Atmos. Chem. Phys.*, 18(18), 13363–13392, doi:10.5194/acp-18-13363-2018, 2018.

Marcolli, C., Mahrt, F. and Kärcher, B.: Soot PCF: Pore condensation and freezing framework for soot aggregates, *Atmos. Chem. Phys.*, 21(10), 7791–7843, doi:10.5194/acp-21-7791-2021, 2021.

Möhler, O., Benz, S., Saathoff, H., Schnaiter, M., Wagner, R., Schneider, J., Walter, S., Ebert, V. and Wagner, S.: The effect of organic coating on the heterogeneous ice nucleation efficiency of mineral dust aerosols, *Environ. Res. Lett.*, 3(2), 025007, doi:10.1088/1748-9326/3/2/025007, 2008.

Möhler, O., Adams, M., Lacher, L., Vogel, F., Nadolny, J., Ullrich, R., Boffo, C., Pfeuffer, T., Hobl, A., Weiß, M., Vepuri, H. S. K., Hiranuma, N. and Murray, B. J.: The Portable Ice Nucleation Experiment (PINE): A new online instrument for laboratory studies and automated long-term field observations of ice-nucleating particles, *Atmos. Meas. Tech.*, 14(2), 1143–1166, doi:10.5194/amt-14-1143-2021, 2021.

Morris, C. E., Georgakopoulos, D. G. and Sands, D. C.: Ice nucleation active bacteria and their potential role in precipitation, *J. Phys. IV JP*, 121, 87–103, doi:10.1051/jp4:2004121004, 2004.

Murphy, D. M. and Koop, T.: Review of the vapour pressures of ice and supercooled water for atmospheric applications, *Q. J. R. Meteorol. Soc.*, 131(608), 1539–1565, doi:10.1256/qj.04.94, 2005.

Murray, B. J.: Inhibition of ice crystallisation in highly viscous aqueous organic acid droplets, *Atmos. Chem. Phys.*, 8(17), 5423–5433, doi:10.5194/acp-8-5423-2008, 2008.

Murray, B. J., Wilson, T. W., Dobbie, S., Cui, Z., Al-Jumur, S. M. R. K., Möhler, O., Schnaiter, M., Wagner, R., Benz, S., Niemand, M., Saathoff, H., Ebert, V., Wagner, S. and

Kärcher, B.: Heterogeneous nucleation of ice particles on glassy aerosols under cirrus conditions, *Nat. Geosci.*, 3(4), 233–237, doi:10.1038/ngeo817, 2010.

Murray, B. J., O’Sullivan, D., Atkinson, J. D. and Webb, M. E.: Ice nucleation by particles immersed in supercooled cloud droplets, *Chem. Soc. Rev.*, 41(19), 6519, doi:10.1039/c2cs35200a, 2012.

Nichman, L., Wolf, M., Davidovits, P., Onasch, T. B., Zhang, Y., Worsnop, D. R., Bhandari, J., Mazzoleni, C. and Cziczo, D. J.: Laboratory study of the heterogeneous ice nucleation on black-carbon-containing aerosol, *Atmos. Chem. Phys.*, 19(19), 12175–12194, doi:10.5194/acp-19-12175-2019, 2019.

Petters, M. D. and Kreidenweis, S. M.: A single parameter representation of hygroscopic growth and cloud condensation nucleus activity, *Atmos. Chem. Phys.*, 7(8), 1961–1971, doi:10.5194/acp-7-1961-2007, 2007.

Ponsonby, J., King, L., Murray, B. J. and Stettler, M. E. J.: Jet aircraft lubrication oil droplets as contrail ice-forming particles, *Atmos. Chem. Phys.*, 24(3), 2045–2058, doi:10.5194/acp-24-2045-2024, 2024.

Rosenfeld, D. and Woodley, W. L.: Deep convective clouds with sustained supercooled liquid water down to  $-37.5$  °C, *Nature*, 405(6785), 440–442, doi:10.1038/35013030, 2000.

Tarn, M. D., Sikora, S. N. F., Porter, G. C. E., Shim, J. U. and Murray, B. J.: Homogeneous freezing of water using microfluidics, *Micromachines*, 12(2), 1–23, doi:10.3390/mi12020223, 2021.

TSI: Model 390069 Data Merge Software Module for Merging and Fitting of SMPS and APS Data Files User’s Guide, 2011.

Vergara-Temprado, J., Murray, B. J., Wilson, T. W., O’Sullivan, D., Browse, J., Pringle, K. J., Ardon-Dryer, K., Bertram, A. K., Burrows, S. M., Ceburnis, D., Demott, P. J., Mason, R. H., O’Dowd, C. D., Rinaldi, M. and Carslaw, K. S.: Contribution of feldspar and marine organic aerosols to global ice nucleating particle concentrations, *Atmos. Chem. Phys.*, 17(5), 3637–3658, doi:10.5194/acp-17-3637-2017, 2017.

Vogel, F., Lacher, L., Nadolny, J., Saathoff, H., Leisner, T. and Möhler, O.: Development and validation of a new cloud simulation experiment for lab-based aerosol-cloud studies, *Rev. Sci. Instrum.*, 93(9), 095106, doi:10.1063/5.0098777, 2022.

Wagner, F., Bortoli, D., Pereira, S., Costa, M. J., Silva, A. M., Weinzierl, B., Esselborn, M., Petzold, A., Rasp, K., Heinold, B. and Tegen, I.: Properties of dust aerosol particles transported to Portugal from the Sahara desert, *Tellus, Ser. B Chem. Phys. Meteorol.*, 61(1), 297–306, doi:10.1111/j.1600-0889.2008.00393.x, 2009.

Westbrook, C. D. and Illingworth, A. J.: Evidence that ice forms primarily in supercooled liquid clouds at temperatures  $>-27^{\circ}\text{C}$ , *Geophys. Res. Lett.*, 38(14), doi:10.1029/2011GL048021, 2011.

Wilson, T. W., Murray, B. J., Wagner, R., Möhler, O., Saathoff, H., Schnaiter, M., Skrotzki, J., Price, H. C., Malkin, T. L., Dobbie, S. and Al-Jumur, S. M. R. K.: Glassy aerosols with a range of compositions nucleate ice heterogeneously at cirrus temperatures, *Atmos. Chem. Phys.*, 12(18), 8611–8632, doi:10.5194/acp-12-8611-2012, 2012.

Wilson, T. W., Ladino, L. A., Alpert, P. A., Breckels, M. N., Brooks, I. M., Browse, J., Burrows, S. M., Carslaw, K. S., Huffman, J. A., Judd, C., Kilhau, W. P., Mason, R. H., McFiggans, G., Miller, L. A., Najera, J. J., Polishchuk, E., Rae, S., Schiller, C. L., Si, M., Temprado, J. V., Whale, T. F., Wong, J. P. S., Wurl, O., Yakobi-Hancock, J. D., Abbatt, J. P. D., Aller, J. Y., Bertram, A. K., Knopf, D. A. and Murray, B. J.: A marine biogenic source of atmospheric ice-nucleating particles, *Nature*, 525(7568), 234–238, doi:10.1038/nature14986, 2015.

### **3 Using a small cloud expansion chamber to characterise the ice-nucleating activity of northern high-latitude mineral dusts**

#### **3.1 Background**

HLD refers to dust emitted from locations  $\geq 50^{\circ}\text{N}$  and  $\geq 40^{\circ}\text{S}$  on the globe. It is estimated that approximately 1 % to 5 % of the Earth's total dust emissions are from high-latitude sources (Bullard et al., 2016; Meinander et al., 2022). Much of the HLD emitted into the atmosphere is thought to be from glacial outwash plains (Bullard et al., 2016); as glaciers melt during warmer months the meltwater carries with it fine sediment which is deposited onto floodplains, this sediment can then be exposed once the water level drops and entrained into the atmosphere by winds. Since this source of HLD is dependent on the regional temperature, the emission of HLD in the atmosphere is strongly seasonal and depends on local environmental conditions such as river discharge and snow and ice cover (Bullard and Mockford, 2018; Crusius et al., 2011). HLD emissions can occur all year-round, but the highest concentrations are typically seen in spring, summer or autumn months when temperatures are highest (Groot Zwaafink et al., 2017; Meinander et al., 2022; Prospero et al., 2012; Shi et al., 2022; Wex et al., 2019). This temperature dependence also means that in a warming climate, HLD emissions can be expected to increase due to glacial retreat exposing more sediment (Amino et al., 2021).

The capability of HLD to nucleate ice at conditions relevant for mixed-phase clouds has been demonstrated by measurement studies of dusts from northern high-latitude sources including Alaska (Barr et al., 2023), Canada (Xi et al., 2022), Greenland (Wyld et al., in prep), Iceland (Paramonov et al., 2018; Sanchez-Marroquin et al., 2020) and Svalbard (Porter et al., 2020; Tobo et al., 2019). A map of locations known to be sources of HLD is shown in Figure 3.1 (Meinander et al., 2022). At low- and mid-latitudes, mineral dusts from arid regions such as central Asia and the Sahara are known to be a major source of INPs in the ambient atmosphere (DeMott et al., 2003; Sassen et al., 2003), with measurements of ice crystal residuals over land typically showing mineral dust to be the most common type of INP (Cziczo et al., 2004; Pratt et al., 2009). Of the various minerals present in these dusts, K-feldspar is thought to have the highest INA and the INA of mineral dusts from arid regions can often be attributed primarily to the K-feldspar content (Atkinson et al., 2013; Harrison et al., 2019). For high-latitude dusts, the INA has been indicated to also be influenced by biological material, particularly at temperatures higher

than  $-15\text{ }^{\circ}\text{C}$ , based upon a decrease in activity after heat or chemical treatment of the samples (Barr et al., 2023; Tobo et al., 2019; Xi et al., 2022).

In the atmosphere of the Arctic, approximately 30 % of the total dust concentration is estimated to be from local, high-latitude sources, with the rest being transported from low-latitude sources, however these relative abundances have a strong altitude and seasonal dependence (Groot Zwaafink et al., 2016; Shi et al., 2022). Locally emitted dust is generally the highest contributor to Arctic dust concentrations in the lower troposphere ( $> 800\text{ hPa}$ ) but its contribution rapidly decreases at higher altitudes due to limited vertical transport (Sanchez-Marroquin et al., 2020; Shi et al., 2022). On the other hand, dust concentrations in the middle and upper troposphere are often dominated by low-latitude dust (LLD) due to it being uplifted as it travels to the Arctic (Stohl, 2006). In summer months, when HLD emissions are at their highest, the HLD is generally too low in altitude to reach temperatures low enough to cause immersion nucleation (Shi et al., 2022). The strongest effect of HLD on mixed-phase clouds is seen in autumn, when local emissions are still high but temperatures are lower, at this time HLD is thought to contribute  $>20\%$  to the immersion freezing rate below  $500\text{ hPa}$  based upon a modelling study by Shi et al. (2022) who quantified the activity of HLD using parameterisations from Sanchez-Marroquin et al. (2020). Studies focusing specifically on dust from Iceland (Sanchez-Marroquin et al., 2020) and Alaska (Barr et al., 2023) have shown that for a few days after dust events, the contribution of local HLD to ambient INP concentrations can outcompete LLD at altitudes up to  $\sim 500\text{ hPa}$ . It is at these altitudes that supercooled

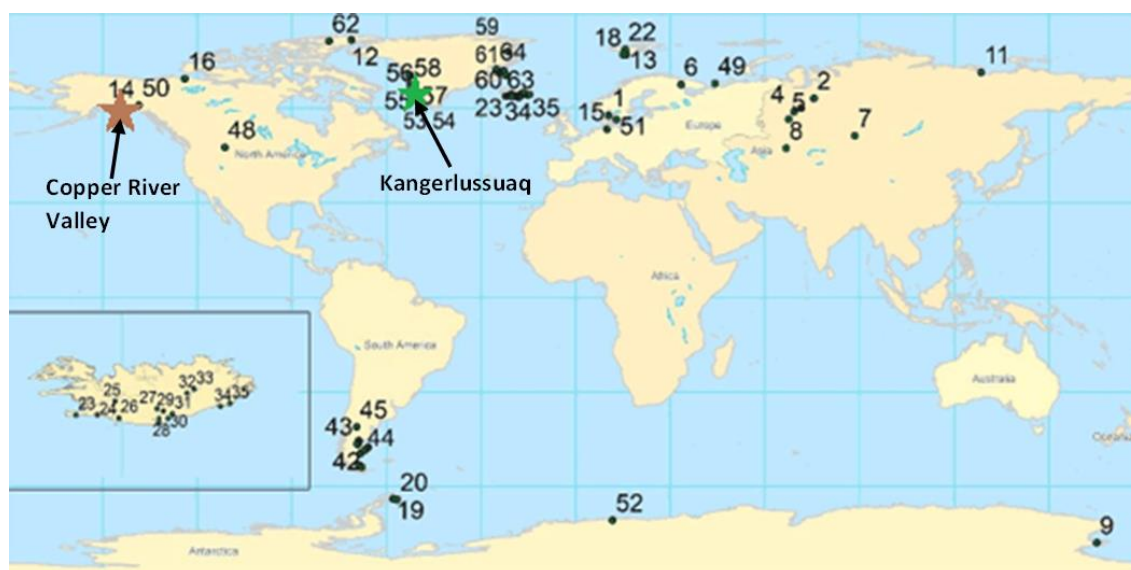


**Figure 3.1:** Map showing locations of known high-latitude dust sources. Brown and green stars highlight the Copper River Valley, Alaska, and Kangerlussuaq, Greenland, respectively. Adapted from figure 1 from Meinander et al. (2022)

shallow clouds can form from cold-air outbreaks, the properties of these clouds are particularly sensitive to INP concentrations (Murray et al., 2021) and so HLD INPs can influence the global climate via these clouds.

There are many locations in the Arctic that have been identified as HLD sources (Meinander et al., 2022) (Figure 3.1), in this study we focus on the Copper River valley in Alaska and the Kangerlussuaq valley in Greenland. These two sources were chosen based upon the following combination of factors: they are both known sources of HLD (Meinander et al., 2022); samples from both have previously been measured in terms of their INA and shown to be active at temperatures above  $-25\text{ }^{\circ}\text{C}$  which allows for comparisons with our measurements (Barr et al., 2023; Wyld et al., in prep); the two environments are different from one another in that much of the Copper River is in the vicinity of vegetation such as forests (Barr et al., 2023) while Kangerlussuaq has much less vegetation in comparison; samples from both sources were readily accessible for PINE-1B measurements to be made.

The Copper River, highlighted by the brown star in Figure 3.1, is a river in south-central Alaska which drains into the Gulf of Alaska. The coastline along the Gulf of Alaska is thought to be one of the largest sinks of sediments into the marine environment in North America (Jaeger et al., 1998). The Copper River transports roughly 69 million tons of sediment per year (Brabets, 1997), and is one of the main sources of sediment into the Gulf of Alaska (Jaeger et al., 1998). The sediment from the Copper River can be resuspended into the atmosphere by northerly/north-easterly winds in autumn and winter when river discharge is low so that there is dry, exposed sediment at the surface (Crusius et al., 2011; Schroth et al., 2017). When conditions are favourable, large dust events can occur, with single events being known to transport up to 80 kilotons of dust away from the Copper River and over the Gulf of Alaska (Crusius et al., 2011). The INA of ambient aerosol at the surface near the Copper River has been measured by Barr et al. (2023) using  $\mu\text{L}$ -NIPI droplet freezing assays of size-resolved aerosol collected using a cascade impactor. Their results showed that the dust from the Copper River was able to nucleate ice at temperatures between  $-10$  and  $-25\text{ }^{\circ}\text{C}$  and a decrease in activity seen after heat treatment indicated the presence of biological material influencing the INA. Barr et al. (2023) also used FLEXPART modelling to show that the Copper River dust could be transported to altitudes at which it could contribute to glaciation of mixed-phase clouds and potentially outcompete the contribution from low-latitude sources.

Kangerlussuaq is a settlement located at the head of a fjord of the same name in western Greenland, highlighted by the green star in Figure 3.1. Dust storms have been long known to occur in the ice-free areas of Greenland (Hobbs, 1931), and dust events at Kangerlussuaq have been recorded since 1942 using qualitative dust codes (Bullard and Mockford, 2018). Since approximately the year 2000, the magnitude of Greenland dust emissions has increased according to both dust code records (Bullard and Mockford, 2018) and ice/firn core measurements (Amino et al., 2021; Kjær et al., 2022), most likely as a result of decreasing ice cover over Greenland resulting in more exposed sediment. Similar to the Copper River, dust emissions from Kangerlussuaq are highest in autumn and spring when conditions are dry and river levels are low (Bullard and Mockford, 2018). The wind direction also needs to be in-line with the valley for dust to be resuspended into the atmosphere (Bullard et al., 2023), resulting in most of the emissions being transported southwest over the ocean, but sometimes winds in the opposite direction can transport dust onto the ice sheet which could reduce its albedo and increase melt rate (Bullard and Mockford, 2018). The INA of dust from Kangerlussuaq has been measured by Wyld et al. (in prep) using  $\mu\text{L-NIPI}$  droplet freezing assays of surface sediment filtered to particles  $<10\ \mu\text{m}$  in diameter. Their results were similar to those for the Copper River dust from Barr et al. (2023) in that the Kangerlussuaq dust showed heterogeneous activity at temperatures from  $-5$  to  $-25\ ^\circ\text{C}$  and this activity decreased upon heat treatment, indicating the presence of biological material influencing the INA at these temperatures.

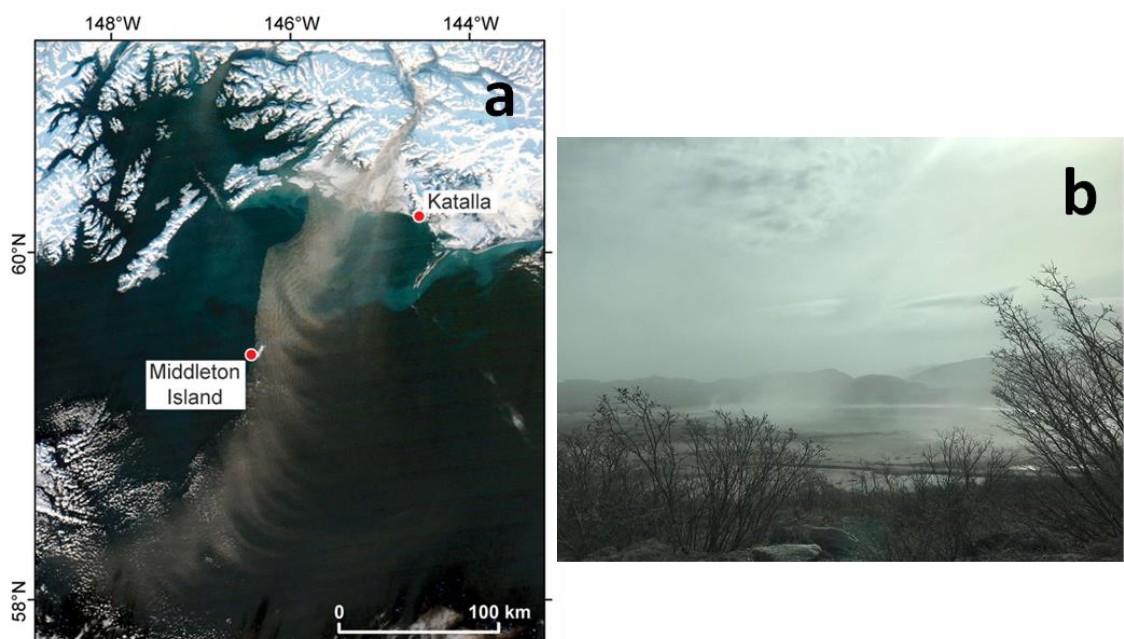


**Figure 3.2:** **a)** MODIS Aqua satellite image of dust plume from the Copper River valley on 04/10/2012, taken from figure 8 from Bullard et al. (2016). **b)** Photograph showing airborne dust at the surface at Kangerlussuaq, photograph taken by Bethany Wyld.

The  $\mu\text{L-NIPI}$  droplet freezing assay method used to previously measure these HLDs from the Copper River valley (Barr et al., 2023) and the Kangerlussuaq valley (Wyld et al., in prep) has a lower temperature measurement range of  $\sim -25$  °C. Also, previous intercomparison studies of different ice nucleation measurement techniques have showed that the results from cold stage methods often give lower INA values than those from online aerosol sampling methods when measuring mineral dusts (DeMott et al., 2018; Hiranuma et al., 2015). Therefore, in this study we use the PINE-1B to measure the INA of high-latitude mineral dust samples from the Copper River valley, Alaska, and Kangerlussuaq valley, Greenland, at temperatures between  $\sim -15$  and  $-36$  °C to extend the measurement range of the INAs of samples from these sources down to homogeneous freezing temperatures. The results from the PINE-1B agree closely to those from the  $\mu\text{L-NIPI}$  in their overlapping temperature measurement range of  $-15$  to  $-25$  °C. By combining the results from the PINE and the  $\mu\text{L-NIPI}$ , a parameterisation is developed to represent the INA of HLDs between  $-3.5$  and  $-37.5$  °C.

## **3.2 Materials and methods**

### **3.2.1 High-latitude dust sample collection**

Surface sediment samples were collected from two high-latitude locations shown in Figure 3.3. Sediment from the Copper River valley on the south coast of Alaska (Figure 3.3 panel a) was collected by Sarah Barr in October 2019, this sample was the same surface sediment sample used for X-ray diffraction (XRD) measurements by Barr et al. (2023). The sample was collected using a stainless-steel scoop from the driest area of the floodplain to obtain a dry sample containing a fraction of fine dust, which was then sieved to  $45\ \mu\text{m}$  and stored frozen in prerinsed containers (Barr et al., 2023).

Surface sediment from a glacial outwash plain in Kangerlussuaq on the east coast of Greenland (Figure 3.3 panel b) was collected by Sarah Barr on 24<sup>th</sup> August 2022. The sample was collected using a stainless-steel scoop from the driest area of the floodplain to obtain a dry sample containing a fraction of fine dust, which was stored in sealed sterile bags and frozen within 48 hours of collection. The sample was defrosted and vacuum dried in May 2023 prior to measurements.

### **3.2.2 Mineral composition of samples**

The mineral components of the HLD samples were measured using quantitative X-ray diffraction (QXRD) using a Bruker D8 X-ray diffractometer with a  $\text{Cu K}\alpha$  X-ray emission

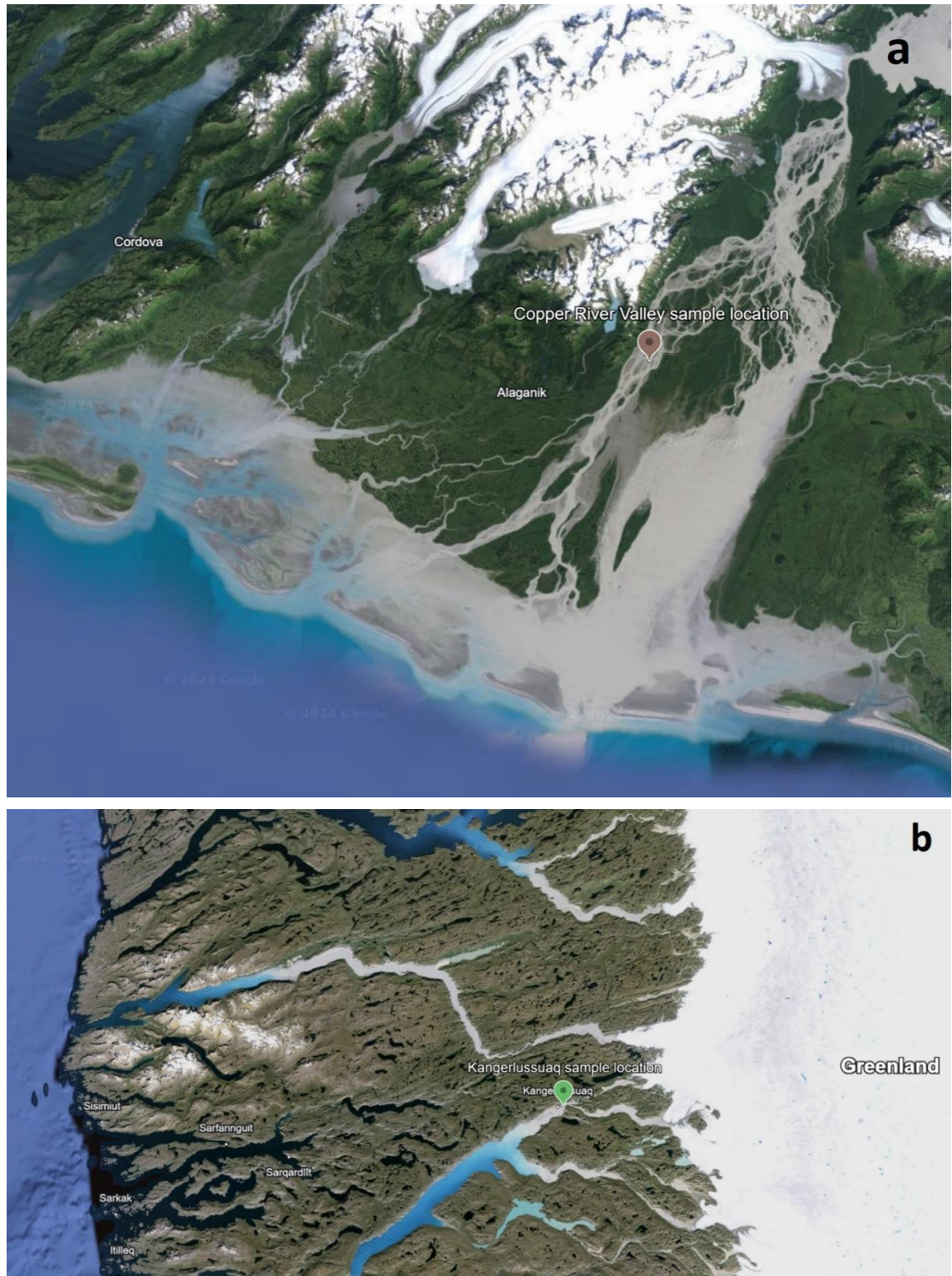


**Figure 3.3:** Sampling locations of the a) Copper River ( $60^{\circ}27'43''\text{N}$   $145^{\circ}02'26''\text{W}$ ) and b) Kangerlussuaq ( $67^{\circ}00'26''\text{N}$   $50^{\circ}40'53''\text{W}$ ) surface sediments used in this study. Satellite images taken from Google Earth on 26/02/2024, maps include data from CNES/Airbus, Landsat/Copernicus, Maxar Technologies, TerraMetrics, IBCAO, Airbus and U.S. Geological Survey.

tube (1.5418 Å wavelength). The Kangerlussuaq dust was sieved to 45 µm for the QXRD measurements to match the size of the Copper River dust. The compositions of the samples were quantified using a relative intensity ratio method with 20 % corundum as the internal standard to which other components were compared in order to calculate their percentage composition (Zhou et al., 2018). The QXRD measurements and analysis were performed by Lesley Neve.

### **3.2.3 Ice nucleation measurements**

Ice nucleation measurements were made using the PINE-1B expansion chamber, the measurement and analysis methods for the determination of HLD samples' ice-nucleating activities were the same as those detailed in chapter 2. An overview of the experimental methods is given here, see chapter 2 for further details and the development of these methods. A schematic of the experimental setup used for ice nucleation measurements is shown in Figure 2.1. The dust samples were aerosolised into a 0.73 m<sup>3</sup> (90 x 90 x 90 cm) aerosol chamber using a GRIMM X78502 Dust Tower, a TSI model 3938 SMPS and a TSI model 3321 APS were used to measure the size distribution of the aerosol in the aerosol chamber. In parallel to the SMPS and APS, the PINE-1B system also simultaneously sampled from the aerosol chamber. For the PINE-1B measurements, the sample was first dried using two parallel diffusion driers before entering the PINE chamber, the temperature of the PINE chamber was controlled using an external flow of chilled liquid ethanol from a refrigerated circulator (LAUDA-Brinkmann, Proline RP 890). The chamber then underwent an expansion by decreasing internal pressure and therefore temperature, the liquid droplets and ice crystals produced by this expansion were counted using a Palas Welas 2500 OPC at the PINE chamber outlet. This expansion process was repeated multiple times at different temperatures to measure the sample INA at a range of temperatures.

## **3.3 Sample characterisation**

### **3.3.1 Sample mineralogy**

The mineralogical compositions of the HLD samples as determined by QXRD are shown in Table 3.1. Both samples contained components which were not quantifiable due to analysis database not having calculation factors for the specific components, these components include amphiboles for both samples and other unidentified components in

the Kangerlussuaq sample. Both samples primarily consist of quartz and albite, but the Copper River dust has more variety in its composition than the Kangerlussuaq dust, including notable amounts of mica and chlorite. K-feldspar is expected to be a key factor in the INA of the dust samples due to the high INA of K-feldspar compared to other minerals (Atkinson et al., 2013). The K-feldspar content of the Kangerlussuaq dust (6.4 %) is roughly 50 % greater than that of the Copper River (4.2 %) dust, based upon this the Kangerlussuaq could be expected to have the higher INA of the two samples.

**Table 3.1:** Mineral composition of high-latitude dust samples from Copper River, Alaska and Kangerlussuaq, Greenland. Quantified using QRXD with relative intensity ratio using corundum reference. Samples were sieved to 45  $\mu\text{m}$  prior to analysis. The unknown % composition includes the minerals which were not able to be quantified, these unquantified minerals include amphiboles in both samples.

Sample	% Composition								
	Quartz	Albite	K-feldspar	Calcite	Dolomite	Mica	Illite-smectite	Chlorite	Unknown
Copper River	18.0	25.8	4.2	8.4	3.8	12.0	2.1	8.3	17.4
Kangerlussuaq	22.7	33.9	6.4	0.5	2.3	0.0	4.3	0.0	29.9

### 3.3.2 Aerosol size distributions

Different size fractions of ambient dust aerosol have been found to have different INAs, with larger sized aerosol generally having higher activity (Barr et al., 2023; Reicher et al., 2018), therefore knowledge of the aerosol size distribution of a sample is important when studying its INA. Examples of aerosol size distributions of the samples used for the PINE measurements of INA are shown in Figure 3.4, the mobility-equivalent particle diameters measured by the SMPS and the aerodynamic particle diameters measured by the APS were both converted into volume-equivalent sphere diameters using equations 1 and 2 from Möhler et al. (2008). For the diameter conversion calculations, the density of the particles was assumed to be  $2.6 \text{ g cm}^{-3}$  and the shape factor was assumed to be 1.1, the same as for the K-feldspar particles used in chapter 2. The SMPS and APS had overlapping measurements between 0.3 and 0.6  $\mu\text{m}$ , so when using these aerosol size distribution measurements in further analysis the SMPS measurements were used in favour of the APS, as recommended by the manufacturer of the instruments due to counting inefficiencies in the lower size bins of the APS (TSI, 2011). The Copper River

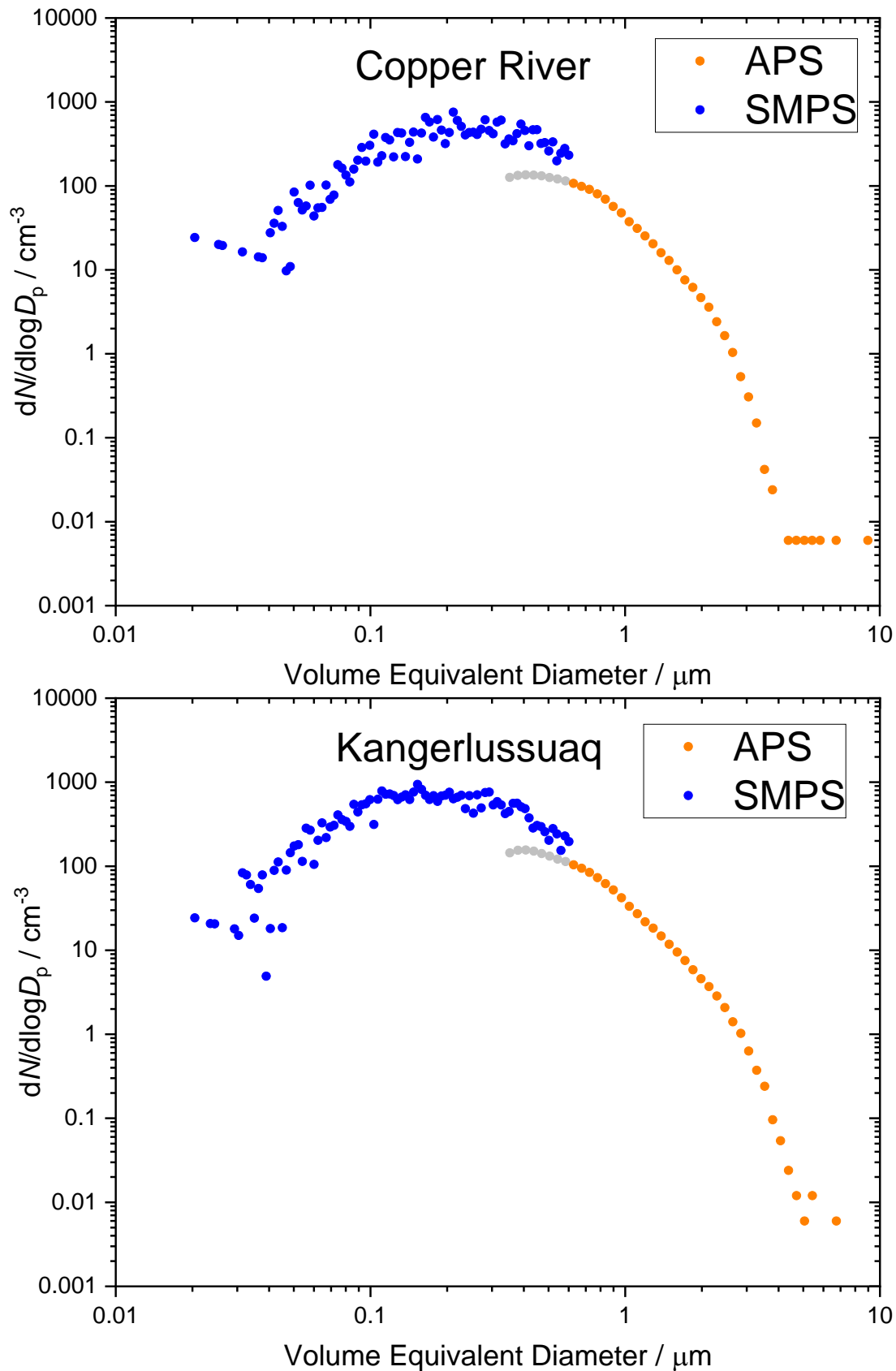


**Figure 3.4:** Example aerosol size distribution measurements of the Copper River and Kangerlussuaq dust samples in the aerosol chamber. The diameters measured by the SMPS and APS were converted to a volume-equivalent diameter to be merged (Möhler et al., 2008). Grey APS points are measurements which were not used in further analysis.

and Kangerlussuaq aerosols had similar aerosol size distributions, with peaks at around 0.2  $\mu\text{m}$  and an upper limit of around 5  $\mu\text{m}$  volume equivalent diameter. The mineralogical compositions given in Table 3.1 were for particles up to 45  $\mu\text{m}$  in diameter, and so the compositions of the aerosolised samples used for ice nucleation measurements may be different from those reported in Table 3.1.

## **3.4 Results & Discussion**

### **3.4.1 High-latitude dust ice-nucleating activities**

To obtain quantifiable information about the INA of a sample, a quantitative measure of ice crystal concentration is needed. For the PINE-1B, this measure of ice crystals is obtained by Welas OPC measurements of the particles exiting the PINE chamber during expansions, these OPC measurements include dust particles and liquid droplets which need to be distinguished from the ice crystals. The distinction between ice crystals and non-ice particles measured by the OPC is done based upon the diameter of the measured particles, as shown in Figure 2.8. To quantify the number of ice crystals in an expansion with confidence, there needs to be a clear distinction between the ice crystals and other particles, which requires the temperature and sample concentration to be within certain limits. Examples of different cloud size distribution scenarios measured by the Welas OPC during PINE-1B expansions using the HLD samples in this study are shown in Figure 3.5. Panel a shows an example in which the end of the liquid droplet distribution can be clearly seen at 10  $\mu\text{m}$  but very few ice crystals above this size are measured, resulting in a high error associated with the counting statistics of the crystals. This case occurs when the temperature in the PINE chamber is too high to produce a statistically significant number of detected ice crystals, which for the samples and aerosol concentrations used in this study was usually when the minimum adiabatic temperature reached during the expansion was  $>-20\text{ }^{\circ}\text{C}$ . To reduce the uncertainty of measurements at these temperatures, many repeated expansions can be done at the same temperature and the results can be averaged to give a result with lower uncertainty. Panel b shows an example in which the ice crystals can clearly be distinguished from the other particles, with the peak centred at 2 to 4  $\mu\text{m}$  being primarily liquid droplets and the smaller peak at  $>10\text{ } \mu\text{m}$  being ice crystals. Panel c shows an example in which a high ice crystal concentration results in the merging of the two peaks and so the ice crystals become difficult to unambiguously distinguish from droplets. This typically occurs when the

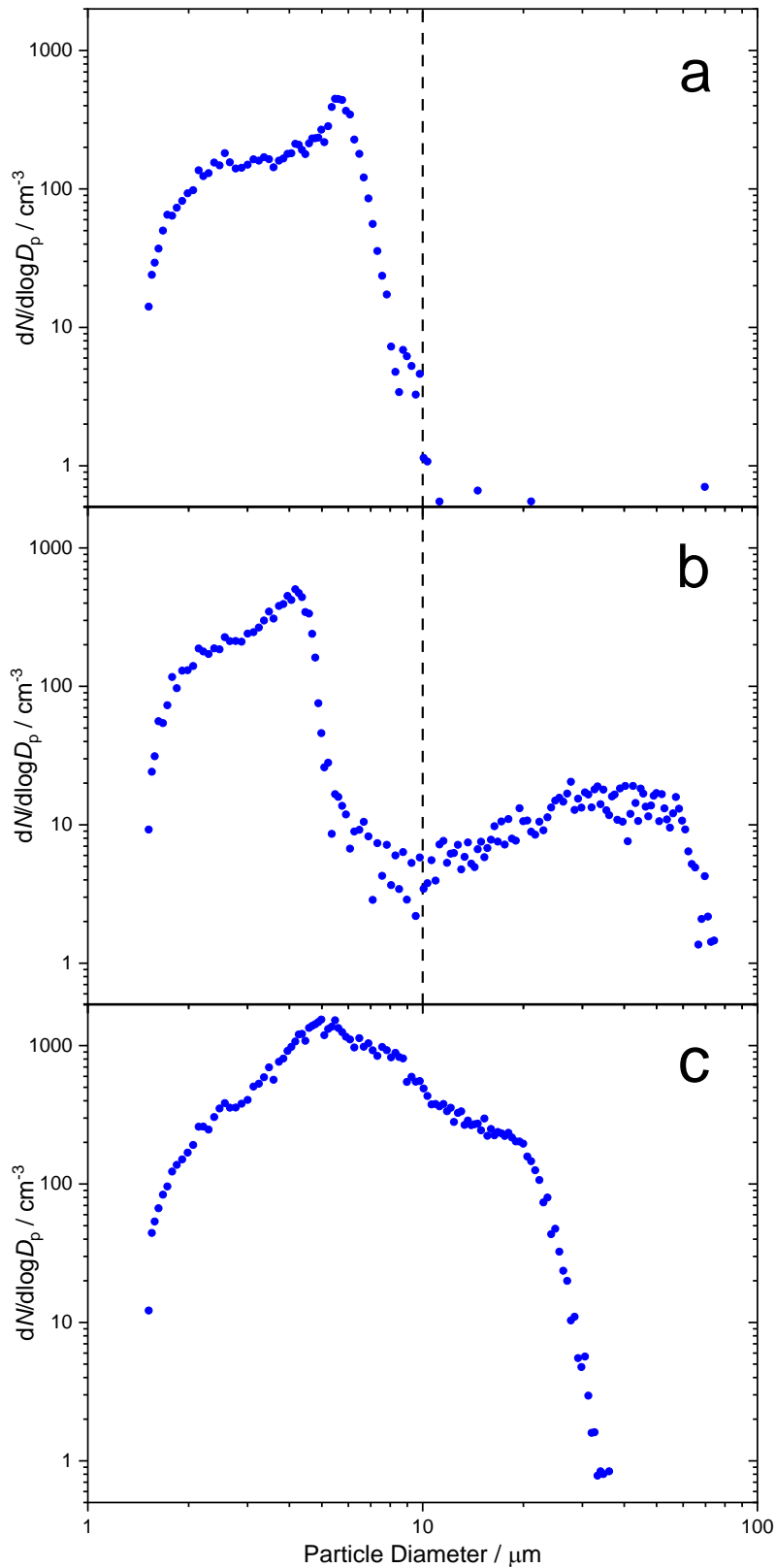


**Figure 3.5:** Cloud size distributions measured by the Welas OPC during PINE expansions with **a)** too few ice crystals, **b)** a balance of ice crystals and liquid droplets, **c)** too many ice crystals. Dashed black line indicates size threshold above which all particles are counted as ice crystals. **a)** and **b)** are from expansions using the Kangerlussuaq sample and **c)** is from an expansion using the Copper River sample.

adiabatic temperature is below  $-36\text{ }^{\circ}\text{C}$ , likely due to the liquid droplets beginning to freeze homogeneously at this temperature (Herbert et al., 2015; Rosenfeld and Woodley, 2000; Westbrook and Illingworth, 2011), and in extreme cases, all the liquid droplets would freeze and there would no longer be a preferential growth of ice crystals over liquid droplets. The cloud size distributions shown in Figure 3.5 highlight the temperature limitations of INP concentration measurements using the PINE with a Welas OPC, with  $-10$  to  $-36\text{ }^{\circ}\text{C}$  being the typical range in which accurate measurements can be made. For some expansions, the cloud size distribution consisted of two distinct peaks as in panel b despite the adiabatic temperature going below  $-36\text{ }^{\circ}\text{C}$  during the expansion. Although these cases could be interpreted as a liquid peak and an ice peak, it is also possible that both peaks are ice crystals and that during the expansion heterogeneous nucleation occurred first to produce the larger ice crystals and then once the temperature was low enough the remaining liquid droplets froze homogeneously and remained at their smaller size. Measurements of the homogeneous nucleation of citric acid droplets detailed in chapter 2 showed that homogeneous nucleation in the PINE-1B occurred at adiabatic temperatures between  $-36$  and  $-38\text{ }^{\circ}\text{C}$  (see Figure 2.7). Also, measurements of jet aircraft lubrication oil droplets using the PINE-1B by Ponsonby et al. (2024) showed that that homogeneous nucleation of liquid water droplets of  $\sim 3.4\text{ }\mu\text{m}$  occurred at an adiabatic temperature of  $\sim -38\text{ }^{\circ}\text{C}$ . Based upon these previous results for homogeneous freezing in the PINE-1B, any expansions in which the minimum adiabatic temperature was below  $-36\text{ }^{\circ}\text{C}$  were not included in further analysis to avoid the misinterpretation of homogeneous nucleation as heterogeneous nucleation.

A time series showing the key measurements made during a series of expansions of the Copper River sample is shown in Figure 3.6. The grey points indicate the expansions which were not included in further analysis due to the number concentration of ice crystals being too high or too low and therefore the number of ice crystals was not able to be determined with confidence. The trend in the concentration of ice crystals measured by PINE ( $N_{\text{ice}}$ ) (panel b) closely follows the adiabatic temperature in the PINE chamber (panel a), with lower temperatures resulting in higher  $N_{\text{ice}}$ . The sample aerosol surface area concentration measured by the SMPS and APS (panel c) varies by approximately 1 order of magnitude over the duration of measurements, which is small compared to the  $\sim 3$  orders of magnitude range in  $N_{\text{ice}}$ . Although a higher aerosol surface area concentration of a given sample would be expected to lead to a higher concentration of ice crystals, in Figure 3.6 the changes in aerosol surface area concentration are too small to result in

noticeable changes in  $N_{ice}$  when compared to the changes in temperature. The ice active site density ( $n_s$ ) (panel d) of the sample is a measure of the concentration of ice-nucleating active sites, which trigger heterogeneous ice nucleation, at the given temperature.  $n_s$  is calculated by dividing  $N_{ice}$  by the aerosol surface area, assuming that each ice crystal contains a single active site. Since  $n_s$  is normalised to the surface area concentration of the sample used, it can be used to compare the INAs of different samples and of

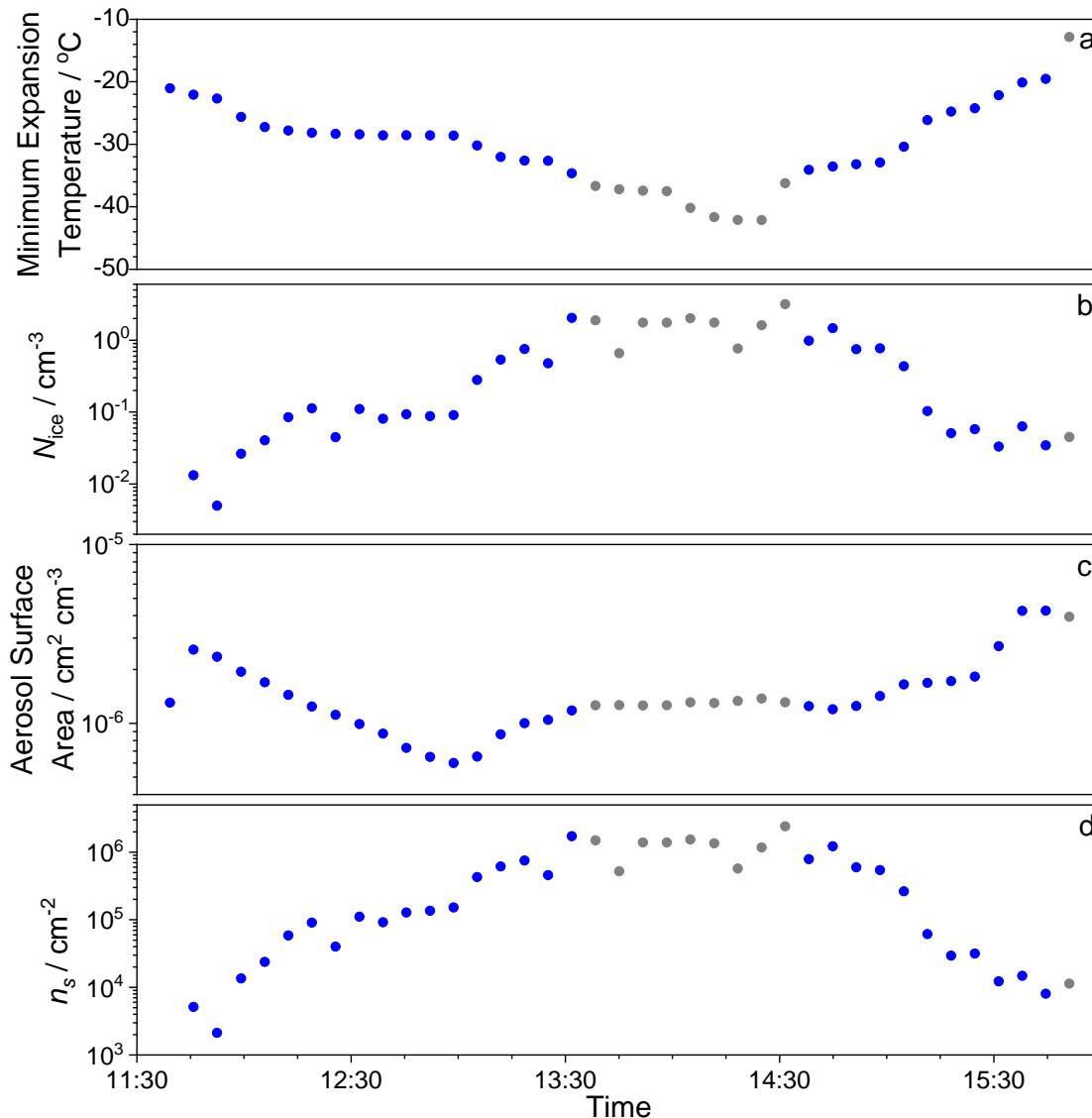


**Figure 3.6:** Time series of PINE expansion measurements of Copper River aerosol sample. Each point represents a single expansion. **a)** Minimum adiabatic temperature inside PINE chamber during expansion, **b)** concentration of ice particles measured by PINE during expansion, **c)** surface area concentration of sample in aerosol chamber measured by SMPS and APS, **d)** active site density, calculated by dividing  $N_{ice}$  by the aerosol surface area. Grey points indicate expansions which were not included in further analysis due to a lack of confidence in the measured number of ice crystals, explained further in main text.

measurements using different experimental methods. A table containing the key values for all expansions of HLD samples used in this study is given in the appendix (Table 3.3).

The INA of the Copper River and Kangerlussuaq aerosols measured by PINE are shown in Figure 3.7 alongside the K-feldspar measurements from chapter 2 and K-feldspar parameterisation from Harrison et al. (2019) for comparison. Each of the Copper River and K-feldspar points represent a single expansion, whereas some of the Kangerlussuaq points are an average of multiple expansions at similar temperatures. Averaging was done

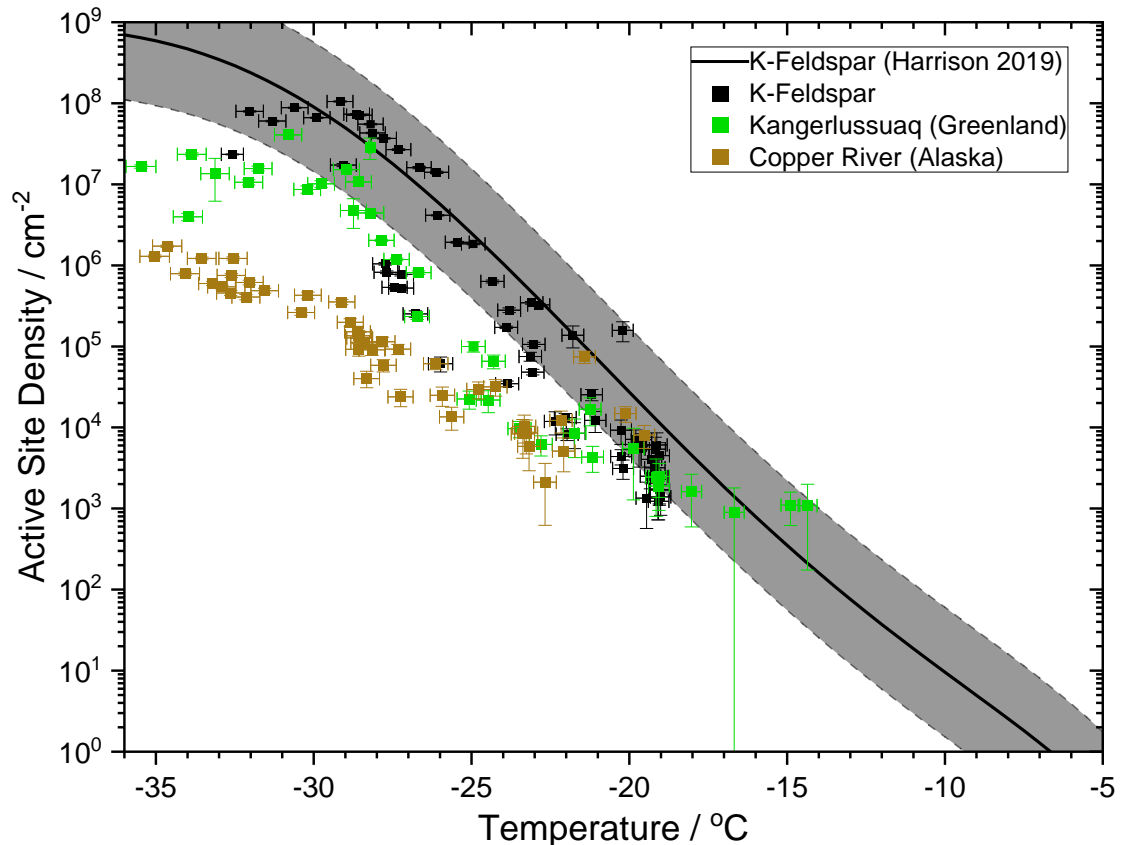


**Figure 3.7:** INAs of Copper River and Kangerlussuaq HLD samples as measured by the PINE-1B. K-feldspar measurements from chapter 2 and parameterisation from Harrison et al. (2019) are shown for comparison. Each point represents a single expansion, apart from Kangerlussuaq points above  $-20$  °C and at  $-33$ ,  $-29$  and  $-28$  °C which are averages of multiple expansions. Error bars represent the estimated value uncertainties. For individual expansions, the adiabatic temperature uncertainty is calculated by combining the fractional thermocouple measurements uncertainty ( $\pm 0.1$  °C) with the fractional pressure measurement uncertainty ( $\pm 0.5$  %). The active site density uncertainty is calculated from the Poisson error of the number of ice crystals measured. For averaged points, the adiabatic temperature uncertainty is calculated using the same method as for individual expansions and the active site density uncertainty is the standard deviation of the averaged values.

for the Kangerlussuaq measurements above  $-20\text{ }^{\circ}\text{C}$  to obtain INA values of higher confidence since the individual expansions at these temperatures produced low ice crystal numbers ( $\sim 0$  to 5) and therefore had high uncertainty. Averaging was also done for Kangerlussuaq expansions with temperatures that rounded to  $-33$ ,  $-29$  and  $-28\text{ }^{\circ}\text{C}$  to improve the readability of Figure 3.7 due to a high number of individual expansions at these temperatures. A version of Figure 3.7 without any averaging of datapoints is shown in Figure 3.15 in the appendix. Between  $-20$  and  $-25\text{ }^{\circ}\text{C}$  the two HLD samples have similar INAs to one another, they are also similar to some of the K-feldspar measurements in this range and lie roughly along the lower band of the K-feldspar parameterisation. Below  $-25\text{ }^{\circ}\text{C}$  the INAs begin to deviate from one another, with Kangerlussuaq mostly being slightly below the K-feldspar band and Copper River being 1 to 2 orders of magnitude lower than Kangerlussuaq.

Figure 3.8 shows the HLD INA measurements in comparison to parameterisations for K-feldspar, albite and quartz from Harrison et al. (2019) and NX-illite from Hiranuma et al. (2015), the parameterisations are scaled to the quantities of each mineral in the samples as determined by QXRD. The NX-illite parameterisation is not for pure illite, but for a sample containing 69 % illite and smaller quantities of feldspar, kaolinite, quartz and calcite/carbonate. Measurements of mica, calcite and chlorite made by Atkinson et al. (2013) showed that the INA of these materials is substantially lower than that of K-feldspar and quartz and so they are not expected to notably contribute to the INA of the samples. For the Copper River sample (panel a), the activity is most similar to that of albite at temperatures below  $-25\text{ }^{\circ}\text{C}$  but increases relative to albite above  $-25\text{ }^{\circ}\text{C}$  and is more active than all the minerals at temperatures above  $-22\text{ }^{\circ}\text{C}$ . For the Kangerlussuaq sample (panel b), the activity is most similar to K-feldspar at temperatures below  $-22\text{ }^{\circ}\text{C}$  and is more active than all the minerals at temperatures above  $-22\text{ }^{\circ}\text{C}$ . The fact that the Copper River sample's INA below  $-22\text{ }^{\circ}\text{C}$  is lower than expected based upon its most active mineral component (K-feldspar) may be due to the K-feldspar present in the Copper River sample being lower in activity than what is represented in the parameterisation, since different K-feldspar samples can have different INAs ranging over orders of magnitude (Harrison et al., 2019). Alternatively, the quantity of K-feldspar in the measured aerosol sample may be lower than what was quantified by QXRD, since the sample used for QXRD was sieved to  $45\text{ }\mu\text{m}$  whereas the sample for PINE measurements was aerosolised and consisted of particles between  $\sim 0.02$  and  $5.0\text{ }\mu\text{m}$  in diameter (Figure 3.4). These different sample size distributions may have different

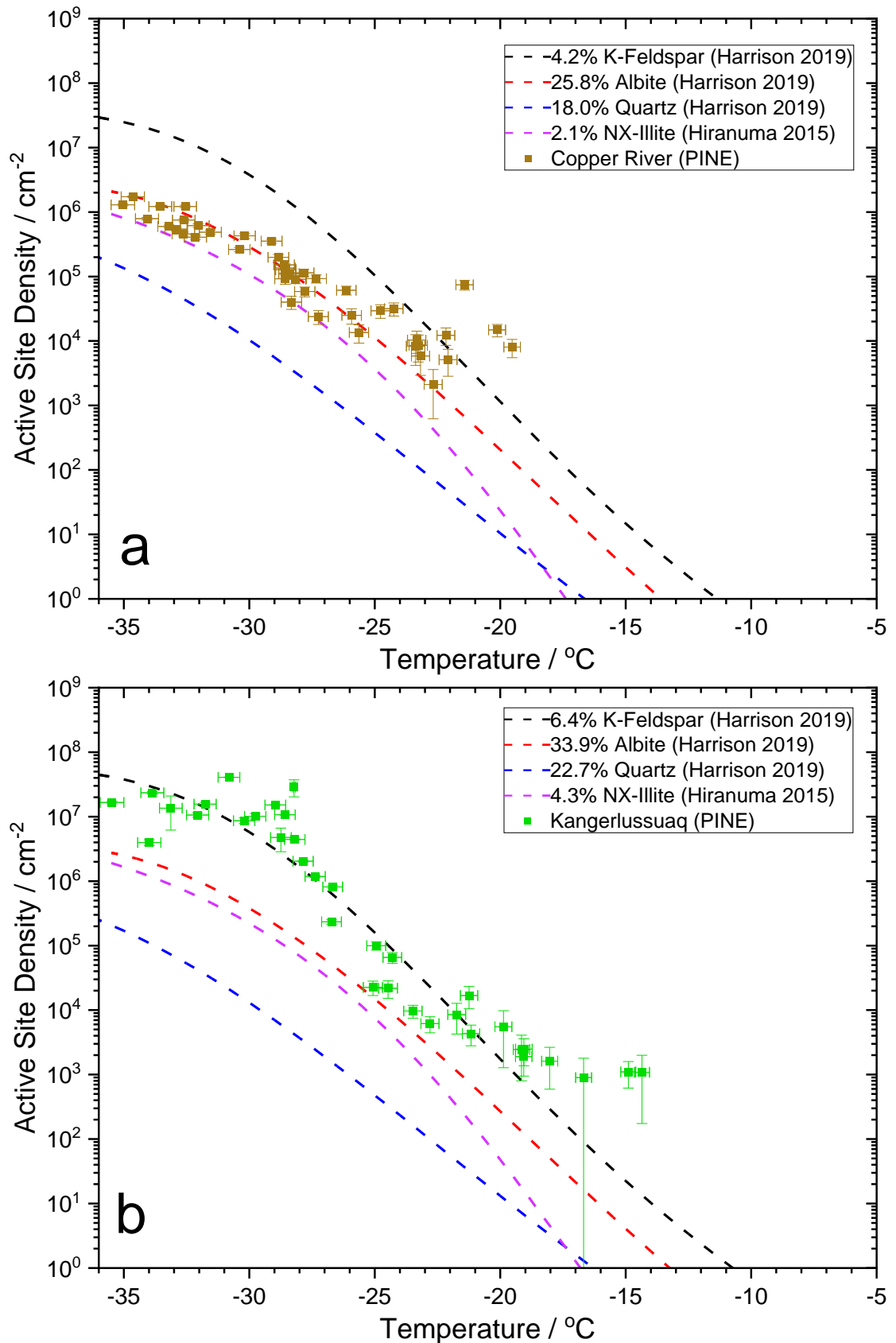


**Figure 3.8:** INAs of **a)** Copper River and **b)** Kangerlussuaq samples in comparison to parameterisations of the activities of the mineral components of the samples (Harrison et al., 2019; Hiranuma et al., 2015). Parameterisations are scaled according to the compositions determined by QXRD.

mineral compositions, and so the values in Table 3.1 may not be fully representative of the aerosolised compositions. The measurements shown in Figure 3.8 indicate that the INAs of the samples at temperatures below  $-22\text{ }^{\circ}\text{C}$  is primarily controlled by the mineral components, but above  $-22\text{ }^{\circ}\text{C}$  there is something else in the samples controlling the activity.

### 3.4.2 Comparison to cold stage measurements

The Copper River dust sample used in this study is the same surface sample used by Barr et al. (2023) for XRD measurements, it is different from the size-segregated aerosol samples used by Barr et al. (2023) for ice nucleation measurements. In the study by Barr et al. (2023), INA measurements of size segregated filters collected in the Copper River valley were made using the  $\mu\text{L-NIPI}$  cold stage instrument. Although the surface sample and filter samples may be different from one another, the samples were both taken from the same time and place and so are likely comparable to one another. The typical measurement range for the  $\mu\text{L-NIPI}$  is  $-5$  to  $-25\text{ }^{\circ}\text{C}$  and so it complements the PINE-1B by measuring at the higher temperatures, where the PINE-1B struggles with low ice production, while overlapping between  $\sim -15$  and  $-25\text{ }^{\circ}\text{C}$  to allow for comparison.

Figure 3.9 shows the INA measurements of Copper River dust using the PINE-1B from this study and the  $\mu\text{L-NIPI}$  from Barr et al. (2023). Panel a shows the  $\mu\text{L-NIPI}$  measurements for the individual size fractions while panel b shows the average across the size fractions, weighted to the surface area of sample in each size fraction. In both panels the  $\mu\text{L-NIPI}$  measurements are averaged across all measurement days and available measurements of heat-treated samples are shown. The PINE-1B and  $\mu\text{L-NIPI}$  measurements in Figure 3.9 agree with one another in the temperature range which they overlap. Overall, the INA of the Copper River samples is below that of 4.2 % K-feldspar at temperatures below  $-22\text{ }^{\circ}\text{C}$  but above that of 4.2 % K-feldspar at temperatures above  $-22\text{ }^{\circ}\text{C}$ . Again, this suggests that there is a component other than mineral dust controlling the INA at these higher temperatures. The decrease in INA after heat treatment is also indicative of the presence of biogenic components influencing the INA of the sample at the temperatures measured by the  $\mu\text{L-NIPI}$  (Barr et al., 2023).

The INA of HLD samples from Kangerlussuaq have also been measured using the  $\mu\text{L-NIPI}$  by Wyld et al. (in prep) and are shown alongside the PINE measurements of Kangerlussuaq dust from this study in Figure 3.10. The  $\mu\text{L-NIPI}$  data is split into 3 different samples, A, B and C, which were collected as surface sediment samples from

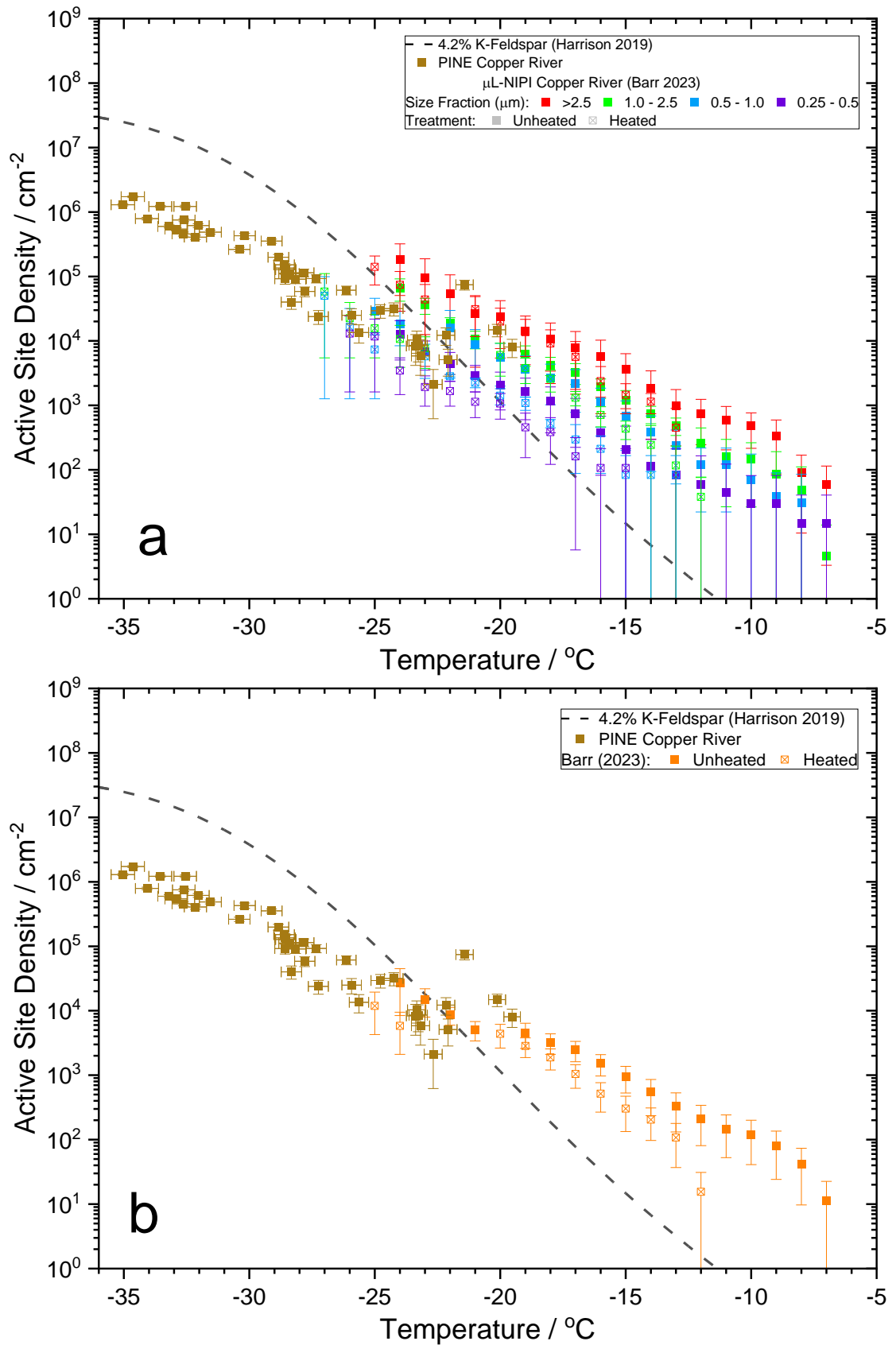


**Figure 3.9:** Comparison of the INA of Copper River dust measured in this study using the PINE and by Barr et al. (2023) using the  $\mu\text{L-NIPI}$ , including heat treated samples. **a)**  $\mu\text{L-NIPI}$  data separated into size segregated filter samples, **b)** average of all size fractions.

different locations along the Kangerlussuaq valley in August 2018. These dust samples were sieved to 50  $\mu\text{m}$  and the  $< 10 \mu\text{m}$  fraction was collected using Stokes' settling and used for INA measurements. Like the Copper River dust, the PINE and  $\mu\text{L-NIPI}$  measurements of the Kangerlussuaq dust INA are consistent with one another in the overlapping temperature range, with the best agreement being for samples B and C, and the INA goes above the K-feldspar parameterisation at temperatures above  $-22 \text{ }^\circ\text{C}$ . This along with the decrease in INA after heat-treatment indicates a biogenic component also being present in the Kangerlussuaq dust samples.

Figure 3.11 shows the Copper River and Kangerlussuaq INA measurements together along with the scaled K-feldspar parameterisation for each sample. The Copper River and Kangerlussuaq dusts have similar INAs to one another at temperatures above to  $-25 \text{ }^\circ\text{C}$ , but at temperatures below than  $-25 \text{ }^\circ\text{C}$  they begin to deviate with Copper River being lower in activity. The INA spectra of the Kangerlussuaq sample below  $-25 \text{ }^\circ\text{C}$  closely follows the 6.4 % K-feldspar parameterisation, while the Copper River sample is lower than 4.2 % K-feldspar but is approximately parallel below  $-25 \text{ }^\circ\text{C}$ . This shows that a scaled Harrison et al. (2019) could be used to represent the INA of these dusts at these

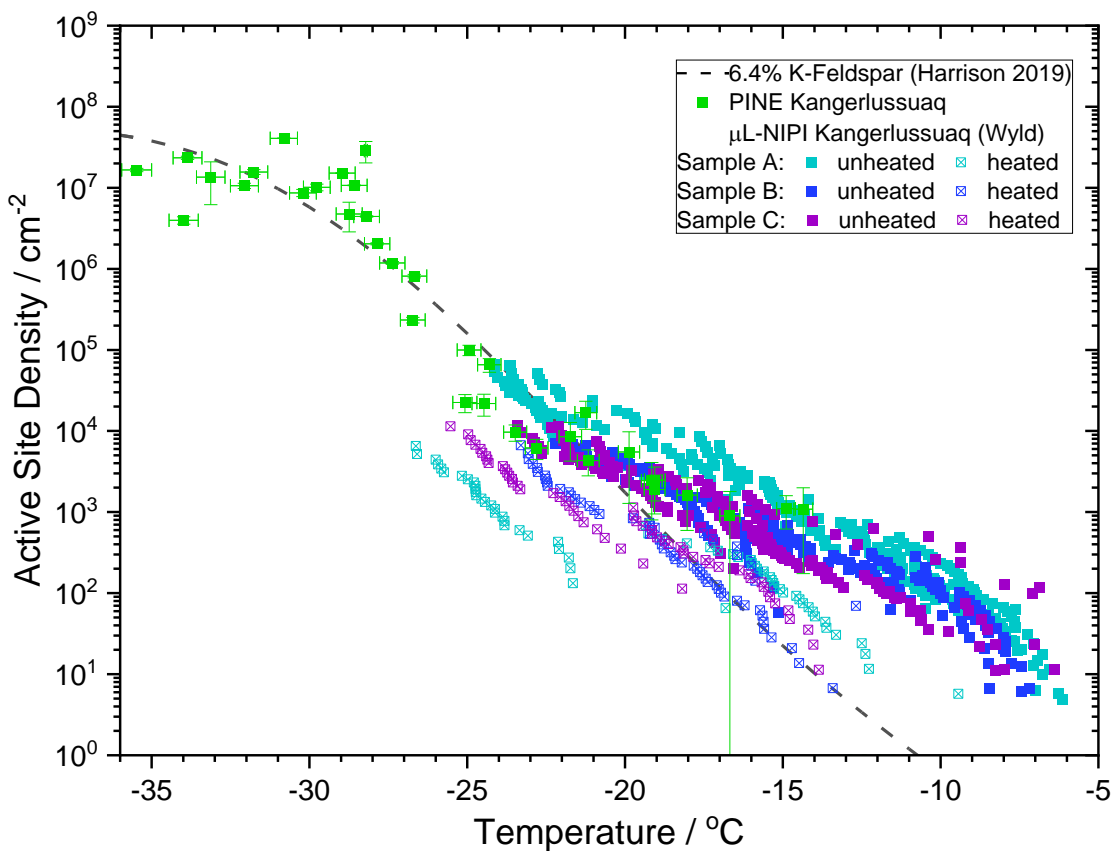


**Figure 3.10:** Comparison of the INA of Kangerlussuaq dust measured in this study using the PINE and by Wyld et al. (preprint) using the  $\mu\text{L-NIPI}$ , including heated samples.

temperatures. However, at temperatures above  $-22\text{ }^{\circ}\text{C}$  the HLD spectra are above the K-feldspar parameterisation and so a different parameterisation would be needed to represent the activity at these higher temperatures.

### 3.4.3 High-latitude dust ice-nucleating activity parameterisation

Ice nucleation parameterisations are used as a tool for representing ice nucleation in atmospheric models based upon conditions such as temperature and pressure and aerosol properties such as surface area. These parameterisations are built upon measurements of INPs in a laboratory or field setting and a single parameterisation will typically represent a specific type of INP or the ambient INPs found at a specific location (Burrows et al., 2022). Notable examples of parameterisations of mineral dusts include Niemand et al. (2012) who produced a parameterisation from AIDA measurements of arid desert dusts and Atkinson et al. (2013) who produced a parameterisation for K-feldspar from cold stage measurements. Parameterisations of biological INPs have also been developed, but these typically required additional measurements to quantify the biological aerosol such as fluorescence detection (Tobo et al., 2013).

To better represent the INAs of HLDs in atmospheric models, a parameterisation can be developed which captures both the mineral component influence at temperatures below  $-25\text{ }^{\circ}\text{C}$  as well as the contribution of other, likely biogenic components at temperatures above  $-25\text{ }^{\circ}\text{C}$ . The gradient in the data shown in Figure 3.11 decreases as the temperature decreases from  $-5$  to  $-20\text{ }^{\circ}\text{C}$ , this pattern can be described simply using a power law function (Equation 3.1). A power law function also fits with the expectation, based upon CNT, that the number of ice-nucleating active sites become increasingly rare as the temperature approaches  $0\text{ }^{\circ}\text{C}$  (Murray et al., 2012). Since a scaled form of the Harrison et al. (2019) K-feldspar parameterisation can be used to represent the INA of the mineral dust component, this can be added to the power law function to produce a parameterisation for HLD as given in Equation 3.2:

$$n_s = -T^{\alpha}k \tag{Eq. 3.1}$$

$$n_s = -T^{\alpha}k + n_{s,Kf}F_{Kf} \tag{Eq. 3.2}$$

$$\log(n_{s,Kf}) = -3.25 + (-0.793T) + (-6.91 \times 10^{-2}T^2) + (-4.17 \times 10^{-3}T^3) + (-1.05 \times 10^{-4}T^4) + (-9.08 \times 10^{-7}T^5)$$

(Eq. 3.3)

Where  $n_{s,Kf}$  is the active site density of K-feldspar in  $\text{cm}^{-2}$ ,  $k$  is a constant,  $\alpha$  is the power law exponent,  $T$  is the temperature in  $^{\circ}\text{C}$  and  $F_{Kf}$  is the fraction of K-feldspar, which is equal to the % composition of K-feldspar divided by 100. Since the Harrison et al. (2019) parameterisation is only valid between -3.5 and -37.5  $^{\circ}\text{C}$ , this new HLD parameterisation is also only valid between -3.5 and -37.5  $^{\circ}\text{C}$ .

As shown in Figure 3.11, HLDs can have a range of INAs at a given temperature, therefore the best fit of Equation 3.2 could be different for different samples. This is demonstrated in Figure 3.12, which shows the HLD parameterisation fit to only the Copper River data (panel a) and the Kangerlussuaq data (panel b). The individual power law and scaled K-feldspar parameterisation functions are also shown as dashed lines and

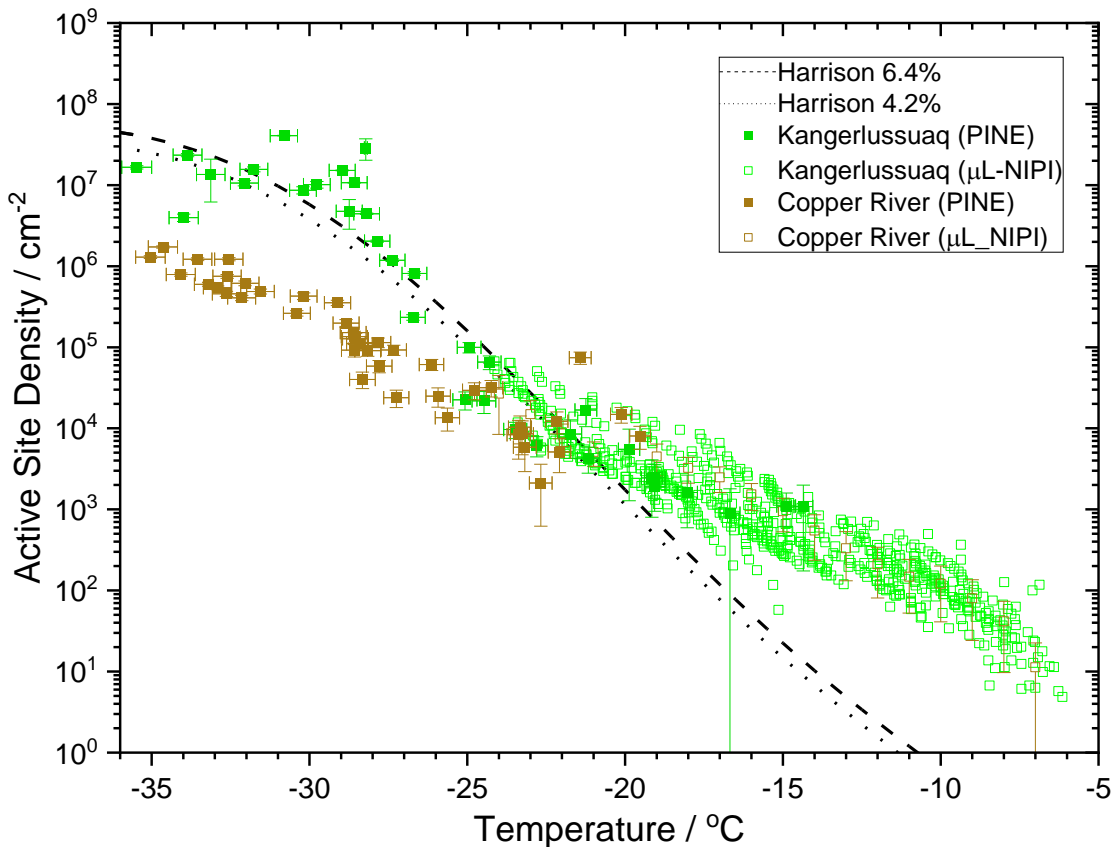


**Figure 3.11:** INAs of Copper River and Kangerlussuaq dusts measured by the PINE-1B and  $\mu\text{L-NIPI}$  (Barr et al., 2023; Wyld et al., preprint). Parameterisations of K-feldspar from Harrison et al. (2019) are scaled according to the quantities in each sample as determined by QXRD.

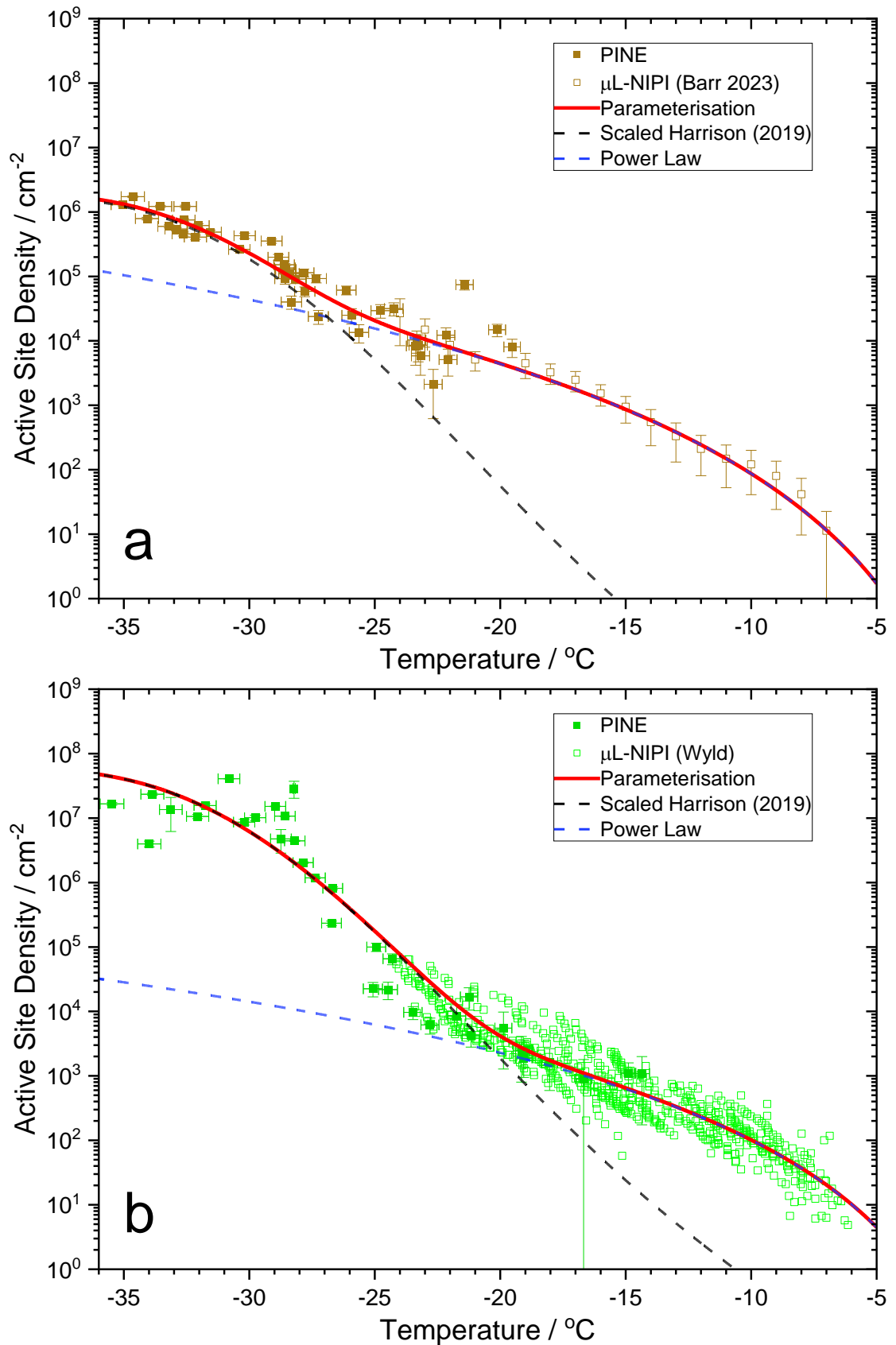


**Figure 3.12:** Best fits of Equation 3.2 to the data from **a)** Copper River, **b)** Kangerlussuaq. Red line shows the parameterisation which represents the INA of the HLD, and black and blue dashed lines show the two individual components which are added together produce the parameterisation.

the  $k$ ,  $\alpha$  and  $F_{Kf}$  values used for each fit are given in Table 3.2. The Kangerlussuaq parameterisation uses a  $F_{Kf}$  of 0.068 which is similar to the composition measured by QXRD, while the Copper River parameterisation uses 0.002 which is a factor of 20 lower than the measured composition. These  $F_{Kf}$  values do not necessarily represent the true quantity of K-feldspar in the samples but might reflect the INA of the mineral dust component of the aerosol in relation to K-feldspar. This order of magnitude difference between the two HLD samples highlights that there is a potentially large range of INAs for different HLD sources at temperatures below  $-25$  °C. The difference in the power law component of the parameterisation fits shown in Figure 3.12 is less pronounced than that of the  $F_{Kf}$  since the INAs are much more similar at temperatures above  $-20$  °C. Since the values of  $k$  and  $\alpha$  are not linked to any physical properties of the samples, they are simply empirical measures of the activity of the sample at these higher temperatures which quantify the importance of the INPs active at these temperatures.

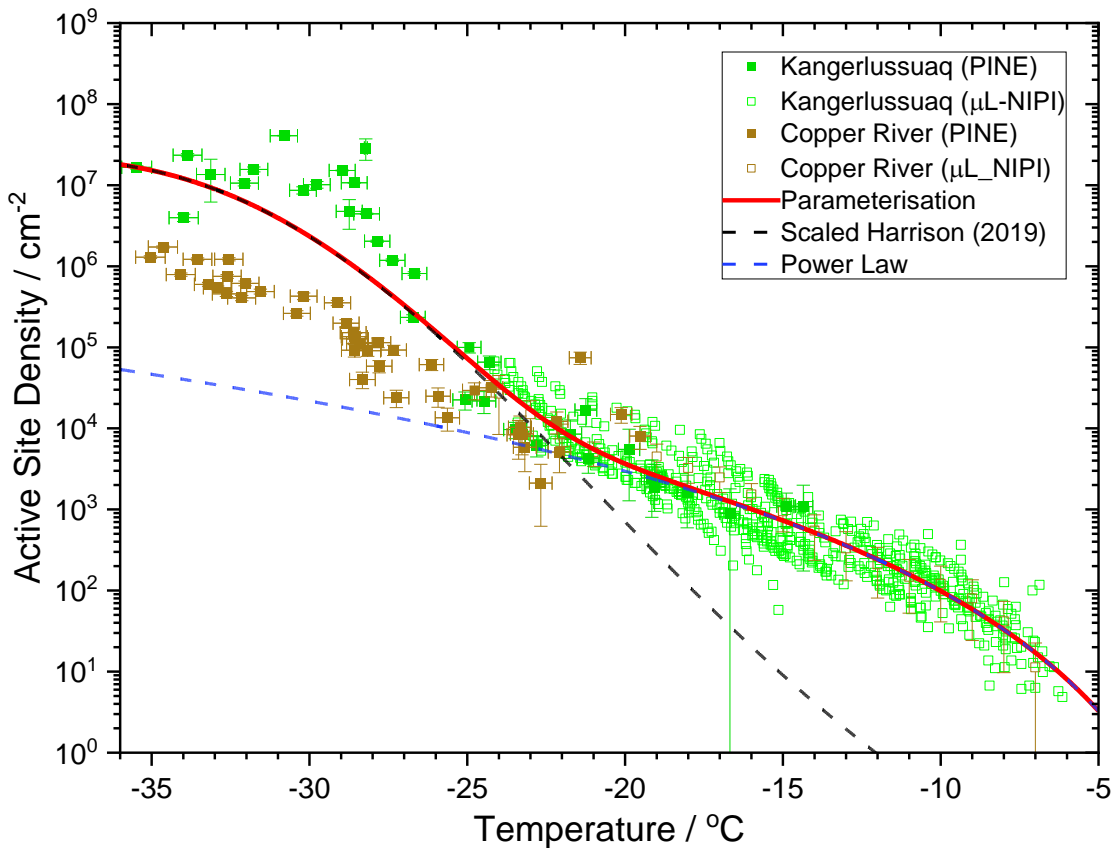


**Figure 3.13:** Parameterisation of the INA of HLDs (Equation 3.2) fit to the data shown. Black and blue dashed lines show the two individual components which are added together produce the parameterisation.

**Table 3.2:** Values used in Equation 3.2 to produce the parameterisation fits shown in Figure 3.12 and Figure 3.13.

Sample	$F_{Kf}$	$k$	$\alpha$
Copper River	0.002057	$1.907 \times 10^{-4}$	5.659
Kangerlussuaq	0.06840	$3.195 \times 10^{-3}$	4.500
Copper River & Kangerlussuaq	0.02575	$1.200 \times 10^{-3}$	4.914

The fit of Equation 3.2 to both the Copper River and Kangerlussuaq measurements is shown in Figure 3.13, with the fitted values also given in Table 3.2. The combined fit is between the two individual fits, with a  $F_{Kf}$  value of 0.026. Figure 3.14 shows further HLD INA measurements made in previous studies including Portable Ice Nucleation Chamber CFDC measurements of surface dust from the glacial river Múlavísl in Iceland by Paramonov et al. (2018), droplet freezing measurements of ambient aerosol collected in an aircraft over Iceland by Sanchez-Marroquin et al. (2020) and droplet freezing measurements of size resolved ambient aerosol from Longyearbyen, Svalbard by Porter et al. (2020). Panel a shows this data in comparison to the Kangerlussuaq and Copper River data used to produce the HLD parameterisation. The additional data from previous studies is within 1 to 2 orders of magnitude of that from Copper River and Kangerlussuaq, with the measurements from Svalbard being slightly higher in activity at temperatures above  $-20$  °C but become closer to the other measurements at lower temperatures. The INA measurements from Iceland mostly overlap with all the other measurements at temperatures above  $-25$  °C and are slightly lower INA than other measurements at  $-30$  and  $-35$  °C. The Iceland and Svalbard measurements show a variability of roughly 1 order of magnitude, which is similar to the variance seen in measurements of Copper River and Kangerlussuaq dust shown in Figure 3.9 and Figure 3.10. Panel b shows the parameterisation from this study alongside parameterisations for low-latitude desert dusts from Ullrich et al. (2017) and for Icelandic dust from Sanchez-Marroquin et al. (2020). These two parameterisations have previously been used in an INP modelling study to represent LLD and HLD respectively (Shi et al., 2022). The Sanchez-Marroquin et al. (2020) parameterisation is of similar magnitude to that from this study at temperatures of  $-15$  and  $-25$  °C but does not show the dip in INA seen in the parameterisation from this study, which may indicate that our parameterisation underestimates the INA of HLDs at temperatures between  $-15$  and  $-25$  °C. The Ullrich et al. (2017) parameterisation for LLDs is approximately 1 order of magnitude higher than the HLD parameterisations, which may

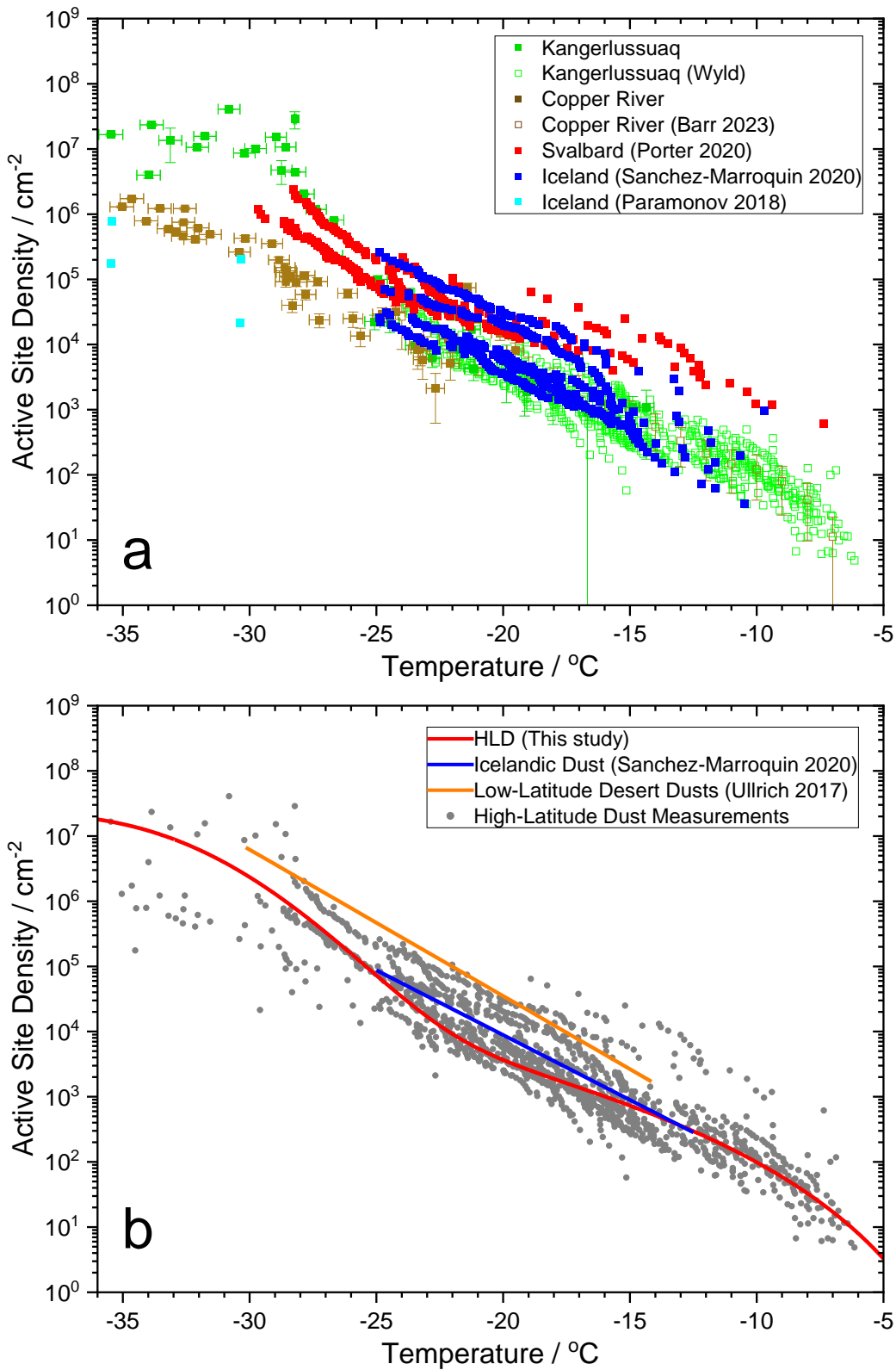


**Figure 3.14:** a) Comparison of HLD INA measurements from multiple locations (Paramonov et al., 2018; Porter et al., 2020; Sanchez-Marroquin et al., 2020). b) Comparison of data from panel a to the HLD parameterisation from this study (Equation 3.2) and previous parameterisations of HLD (Sanchez-Marroquin et al., 2020) and LLD (Ullrich et al., 2017).

indicate that LLDs are typically more active as INPs than HLDs. However the Ullrich et al. (2017) parameterisation still overlaps with some of the HLD measurements, suggesting that at the higher end some HLDs can have similar INA to LLDs.

The use of different fits for the HLD parameterisation (Equation 3.2) highlights that, in its current state, the parameterisation is meant to be used as a flexible tool to aid with the representation of the INA of HLDs. It can be fit to measurements from a single source region to capture the INA of the dust from that region or fit to data from many source regions to give a more average representation of HLDs. In this initial state, the power law function was chosen to represent the activity of the samples at temperatures above  $-20\text{ }^{\circ}\text{C}$  because it represents the trend in INA that is seen for these HLDs as well as fitting with the expected behaviour at higher temperatures from CNT that the INA should be equal to 0 at a temperature of  $0\text{ }^{\circ}\text{C}$  (Murray et al., 2012). For future developments of the parameterisation, functions other than a power law should be explored to see if they can be used to provide a better representation of the INA at these higher temperatures.

### **3.5 Conclusions**

In this study the PINE-1B was used to make measurements of the INA of northern high-latitude dusts from the Copper River valley in Alaska and Kangerlussuaq valley in Greenland. The INAs of the two samples were similar to one another at temperatures above  $-25\text{ }^{\circ}\text{C}$  but deviated below  $-25\text{ }^{\circ}\text{C}$ , where the Kangerlussuaq dust was more active by 1 to 2 orders of magnitude. These INA measurements from the PINE-1B compared well with  $\mu\text{L-NIPI}$  measurements of dust samples from the same regions, these two techniques have different temperature ranges over which they can make accurate measurements, and so combining results from the two instruments can produce broader spectra of INP measurements. The close agreement between the PINE-1B and  $\mu\text{L-NIPI}$  measurements highlights the strength of using different instruments and methods to compare and expand upon one another. When comparing this data to measurements of other HLDs from Svalbard and Iceland, the INAs of the various dusts are all similar at temperatures above  $-25\text{ }^{\circ}\text{C}$ , but below this temperature there is more variation. This variation in INA at lower temperatures is most likely due to variations in the mineralogical compositions of HLDs from different sources. Since K-feldspar is thought to be the dominant mineral in control of the INA at these temperatures, differences in either K-feldspar content or the types of K-feldspar present in each sample could lead to large

differences in INA between the samples. It is also possible that there are other minerals influencing the INA at temperatures below  $-25\text{ }^{\circ}\text{C}$  since not all the minerals known to be present in HLDs have been quantitatively measured for their INAs using modern experimental methods. For example, amphiboles are potentially a major component in both HLD samples investigated in this study, but the INA of amphiboles has not been quantitatively measured in recent years. A study by Hama and Ito (1956) showed that droplets containing amphibole suspended in silicon oil froze at  $-9.7\text{ }^{\circ}\text{C}$ , roughly  $5\text{ }^{\circ}\text{C}$  warmer than for distilled water droplets. While this indicates that amphiboles may be capable of acting as heterogeneous INPs, the freezing temperature for amphibole-containing droplets was lower than that for quartz-containing droplets, and so based upon the relative activity of the different minerals shown in Figure 3.8, the amphibole component of the HLD samples would not be expected to have a notable influence on the INA of the samples. The lack of any quantitative measurements of the INA of amphiboles over a range of temperatures using modern experimental methods highlights that more experiments are needed to characterise the INAs of all the different minerals commonly found in HLDs. By having quantifications of the INAs of these different minerals at temperatures from the melting point of ice to the homogeneous freezing temperature of cloud droplets, our understanding of the components controlling the INA of HLDs and our capability to predict the INA of these dusts from other measurable quantities would be improved.

The results from the PINE-1B and  $\mu\text{L-NIPI}$  measurements of the Copper River and Kangerlussuaq samples were used to produce a parameterisation to represent the INA of HLDs. The use of data from the two instruments in this case allowed a parameterisation to be produced from data over a wide range of temperatures ( $-6$  to  $-37.5\text{ }^{\circ}\text{C}$ ). This initial iteration of the parameterisation combines a power law function with the Harrison et al. (2019) K-feldspar parameterisation, the variables in the power law and the scale of the K-feldspar parameterisation can be changed to fit the parameterisation to different datasets. This allows the parameterisation to be used as a tool to explore the INA of HLDs from different regions and potentially give an average representation for all HLDs. Further developments of this parameterisation could include developing a function which represents the INA at temperatures above  $-20\text{ }^{\circ}\text{C}$  using physically measurable properties of a sample rather than using the purely empirical power law function. Since the INA of the samples measured in this study at temperatures above  $-20\text{ }^{\circ}\text{C}$  appears to be controlled

by biogenic material, the physical properties would likely be related to this biogenic component such as total organic carbon content in the sample.

Future studies could use a version of the parameterisation developed in this study in atmospheric models to investigate the influence HLDs may have on mixed-phase clouds both regionally at the sources and globally. Since the INA of HLDs at temperatures below  $-20\text{ }^{\circ}\text{C}$  is controlled primarily by the mineral dust components, its INA at these temperatures is similar to that of low-latitude desert dusts and so HLDs could have a comparable impact to LLDs if it is able to reach locations in the atmosphere where there are mixed-phase clouds. In a warming environment, HLD emissions are expected to increase (Amino et al., 2021), and so an understanding of the INAs and emissions of HLDs is needed to be able to accurately predict the cloud radiative effect in a future climate.

### 3.6 Appendix

**Table 3.3:** Key results for each expansion used in this study, each line represents a single expansion (a.k.a. run). Runs are not included if there was no distinguishable ice threshold or if the minimum adiabatic expansion temperature was below  $-36\text{ }^{\circ}\text{C}$  since the number of ice crystals could not be accurately determined (see Figure 3.5 and related text). Kan = Kangerlussuaq, CR = Copper River.

Experiment	Run	Expansion Start Temp. / $^{\circ}\text{C}$	Minimum Adiabatic Temp. / $^{\circ}\text{C}$	N $^{\circ}$ ice crystals measured	$N_{\text{ice}} / \text{cm}^{-3}$	Aerosol Surface Area / $\text{cm}^2 \text{cm}^{-3}$	$n_s / \text{cm}^{-2}$
Kan_1	1	-21.2	-28.1	3318	9.070	3.59E-07	2.53E+07
Kan_1	2	-21.2	-28.1	4230	11.968	3.47E-07	3.45E+07
Kan_1	3	-21.3	-28.3	3045	8.572	3.15E-07	2.72E+07
Kan_1	4	-21.2	-28.2	3694	9.935	2.60E-07	3.82E+07
Kan_1	5	-21.3	-28.2	3495	9.338	2.18E-07	4.28E+07
Kan_1	6	-21.3	-28.3	1889	5.272	2.13E-07	2.48E+07
Kan_1	7	-21.3	-28.3	2679	7.102	1.62E-07	4.38E+07
Kan_1	8	-21.3	-28.3	1054	2.811	1.50E-07	1.88E+07
Kan_1	9	-21.3	-28.2	3607	9.762	2.39E-07	4.08E+07
Kan_1	10	-21.3	-28.2	7796	21.095	8.39E-07	2.51E+07
Kan_1	11	-21.3	-28.2	8440	23.858	1.08E-06	2.22E+07

Kan_1	12	-21.2	-28.2	8155	22.677	1.03E-06	2.21E+07
Kan_1	13	-21.3	-28.2	7580	20.433	9.43E-07	2.17E+07
Kan_1	14	-21.2	-28.2	6493	17.270	9.29E-07	1.86E+07
Kan_1	15	-21.2	-28.2	7660	21.990	8.55E-07	2.57E+07
Kan_1	16	-23.9	-30.8	11484	30.847	7.56E-07	4.08E+07
Kan_1	40	-22.0	-29.0	11405	31.059	2.04E-06	1.52E+07
Kan_1	41	-21.6	-28.6	9118	25.683	2.40E-06	1.07E+07
Kan_2	2	-5.5	-11.7	0	0.000	7.30E-07	0.00E+00
Kan_2	3	-14.9	-21.7	4	0.010	1.19E-06	8.50E+03
Kan_2	4	-18.1	-25.1	16	0.039	1.74E-06	2.25E+04
Kan_2	5	-19.7	-26.7	159	0.411	1.76E-06	2.34E+05
Kan_2	6	-20.4	-27.4	702	1.912	1.61E-06	1.19E+06
Kan_2	7	-20.9	-27.9	1208	3.200	1.57E-06	2.04E+06
Kan_2	8	-21.2	-28.2	2386	6.636	1.49E-06	4.44E+06
Kan_2	9	-19.7	-26.7	412	1.137	1.40E-06	8.13E+05
Kan_2	10	-18.0	-24.9	47	0.131	1.32E-06	9.96E+04
Kan_2	11	-17.5	-24.5	11	0.029	1.34E-06	2.18E+04
Kan_2	12	-17.4	-24.3	27	0.086	1.31E-06	6.57E+04
Kan_2	13	-14.4	-21.2	7	0.023	1.36E-06	1.69E+04
Kan_2	14	-13.4	-20.2	6	0.016	1.40E-06	1.15E+04
Kan_2	15	-13.0	-19.8	1	0.003	1.48E-06	1.98E+03
Kan_2	16	-12.8	-19.6	2	0.005	1.76E-06	3.09E+03
Kan_2	17	-12.7	-19.5	4	0.010	2.05E-06	4.96E+03
Kan_2	18	-12.7	-19.4	4	0.011	2.24E-06	4.89E+03
Kan_2	19	-12.6	-19.3	1	0.003	2.28E-06	1.10E+03
Kan_2	20	-12.6	-19.3	2	0.005	2.26E-06	2.04E+03
Kan_2	21	-12.6	-19.2	2	0.005	2.31E-06	2.20E+03
Kan_2	22	-10.9	-17.6	3	0.008	2.59E-06	3.07E+03
Kan_2	23	-9.1	-15.8	0	0.000	2.89E-06	0.00E+00
Kan_2	24	-8.5	-15.0	1	0.003	2.93E-06	9.03E+02
Kan_2	25	-8.2	-14.7	1	0.003	2.84E-06	8.89E+02
Kan_2	26	-8.0	-14.5	3	0.008	2.65E-06	3.12E+03
Kan_2	27	-8.0	-14.4	1	0.003	2.69E-06	9.53E+02
Kan_2	28	-7.9	-14.5	1	0.004	2.64E-06	1.37E+03
Kan_2	29	-7.9	-14.4	2	0.008	3.02E-06	2.65E+03
Kan_2	30	-7.9	-14.4	0	0.000	3.14E-06	0.00E+00

Kan_2	31	-7.9	-14.4	0	0.000	3.18E-06	0.00E+00
Kan_2	32	-7.9	-14.4	1	0.003	3.49E-06	8.39E+02
Kan_2	33	-7.9	-14.4	0	0.000	3.56E-06	0.00E+00
Kan_2	34	-7.9	-14.4	2	0.005	3.66E-06	1.48E+03
Kan_2	35	-7.9	-14.3	2	0.005	4.33E-06	1.18E+03
Kan_2	36	-7.9	-14.3	2	0.005	4.14E-06	1.23E+03
Kan_2	37	-7.9	-14.2	1	0.002	3.66E-06	6.71E+02
Kan_2	38	-7.9	-14.3	0	0.000	3.26E-06	0.00E+00
Kan_2	39	-7.9	-14.3	1	0.003	2.93E-06	9.15E+02
Kan_2	40	-7.8	-14.3	2	0.005	2.81E-06	1.87E+03
Kan_2	41	-10.0	-16.7	1	0.003	2.93E-06	8.98E+02
Kan_2	42	-11.3	-18.1	1	0.003	3.30E-06	7.97E+02
Kan_2	43	-11.9	-18.6	1	0.003	4.17E-06	6.46E+02
Kan_2	44	-12.2	-18.8	2	0.006	4.63E-06	1.28E+03
Kan_2	45	-14.3	-21.2	8	0.022	5.00E-06	4.32E+03
Kan_2	46	-15.9	-22.8	13	0.032	5.25E-06	6.17E+03
Kan_2	47	-16.6	-23.5	19	0.048	4.96E-06	9.68E+03
Kan_2	48	-11.7	-18.4	2	0.004	4.37E-06	9.94E+02
Kan_2	49	-9.5	-16.2	0	0.000	3.81E-06	0.00E+00
Kan_2	50	-8.6	-15.1	1	0.002	3.54E-06	6.88E+02
Kan_2	51	-8.2	-14.8	2	0.007	3.43E-06	1.93E+03
Kan_2	52	-6.3	-12.6	0	0.000	3.28E-06	0.00E+00
Kan_3	2	-19.9	-26.9	31	0.080	6.92E-08	1.16E+06
Kan_3	15	-28.5	-35.5	448	1.125	6.78E-08	1.66E+07
Kan_3	16	-26.9	-33.9	531	1.390	5.93E-08	2.34E+07
Kan_3	17	-26.5	-33.4	373	0.948	5.56E-08	1.71E+07
Kan_3	18	-26.2	-33.1	373	0.920	4.91E-08	1.87E+07
Kan_3	19	-26.2	-33.1	383	1.000	5.12E-08	1.95E+07
Kan_3	20	-26.0	-33.0	225	0.563	4.25E-08	1.33E+07
Kan_3	21	-26.1	-33.1	310	0.774	3.79E-08	2.04E+07
Kan_3	22	-26.0	-33.0	298	0.783	3.10E-08	2.53E+07
Kan_3	23	-24.8	-31.8	207	0.520	3.31E-08	1.57E+07
Kan_3	24	-22.8	-29.8	112	0.293	2.88E-08	1.01E+07
Kan_3	25	-22.0	-29.0	88	0.229	2.55E-08	8.98E+06
Kan_3	26	-21.9	-28.8	82	0.212	3.12E-08	6.78E+06
Kan_3	27	-21.8	-28.7	45	0.114	3.08E-08	3.70E+06

Kan_3	28	-21.7	-28.7	48	0.125	2.47E-08	5.05E+06
Kan_3	29	-21.7	-28.6	30	0.079	2.99E-08	2.63E+06
Kan_3	30	-21.7	-28.8	34	0.089	2.34E-08	3.83E+06
Kan_3	31	-21.7	-28.7	31	0.081	1.69E-08	4.78E+06
Kan_3	32	-21.7	-28.7	41	0.106	1.87E-08	5.69E+06
Kan_3	33	-21.7	-28.7	34	0.085	3.21E-08	2.65E+06
Kan_3	34	-21.7	-28.7	48	0.127	3.73E-08	3.40E+06
Kan_3	35	-23.2	-30.2	97	0.254	2.93E-08	8.67E+06
Kan_3	36	-25.2	-32.1	181	0.470	4.44E-08	1.06E+07
Kan_3	37	-25.9	-32.9	114	0.281	5.34E-08	5.27E+06
Kan_3	38	-26.2	-33.1	135	0.340	5.75E-08	5.91E+06
Kan_3	39	-26.3	-33.2	100	0.250	5.28E-08	4.74E+06
Kan_3	40	-26.3	-33.3	129	0.323	6.37E-08	5.06E+06
Kan_3	41	-27.0	-34.0	92	0.231	5.82E-08	3.98E+06
Kan_4	29	-12.4	-19.9	4	0.011	5.59E-06	1.90E+03
Kan_4	30	-12.3	-19.9	5	0.014	5.46E-06	2.48E+03
CR_1	1	-16.4	-23.4	4	0.010	1.25E-06	8.35E+03
CR_1	2	-16.4	-23.3	7	0.018	1.78E-06	1.03E+04
CR_1	3	-16.3	-23.2	4	0.010	1.73E-06	5.85E+03
CR_1	4	-16.4	-23.3	5	0.014	1.59E-06	8.55E+03
CR_1	5	-19.0	-25.9	14	0.036	1.44E-06	2.49E+04
CR_1	6	-20.3	-27.3	48	0.126	1.36E-06	9.27E+04
CR_1	7	-20.8	-27.8	54	0.139	1.22E-06	1.14E+05
CR_1	8	-21.9	-28.8	88	0.223	1.12E-06	1.98E+05
CR_1	9	-24.6	-31.6	216	0.523	1.07E-06	4.88E+05
CR_1	10	-25.2	-32.2	179	0.423	1.04E-06	4.07E+05
CR_1	11	-25.6	-32.6	525	1.296	1.06E-06	1.22E+06
CR_1	12	-28.0	-35.0	594	1.426	1.10E-06	1.29E+06
CR_1	18	-22.1	-29.1	188	0.479	1.36E-06	3.53E+05
CR_1	19	-14.6	-21.4	33	0.089	1.20E-06	7.44E+04
CR_2	1	-14.2	-21.0	0	0.000	1.30E-06	0.00E+00
CR_2	2	-15.2	-22.1	5	0.013	2.58E-06	5.12E+03
CR_2	3	-15.8	-22.7	2	0.005	2.36E-06	2.12E+03
CR_2	4	-18.7	-25.6	10	0.026	1.94E-06	1.35E+04
CR_2	5	-20.3	-27.2	17	0.040	1.70E-06	2.38E+04
CR_2	6	-20.8	-27.8	33	0.085	1.44E-06	5.86E+04

CR_2	7	-21.2	-28.2	45	0.113	1.24E-06	9.09E+04
CR_2	8	-21.3	-28.3	19	0.045	1.11E-06	4.02E+04
CR_2	9	-21.4	-28.4	44	0.110	9.91E-07	1.11E+05
CR_2	10	-21.5	-28.6	33	0.081	8.76E-07	9.20E+04
CR_2	11	-21.6	-28.5	37	0.093	7.29E-07	1.28E+05
CR_2	12	-21.6	-28.6	36	0.088	6.48E-07	1.35E+05
CR_2	13	-21.6	-28.6	36	0.091	6.00E-07	1.51E+05
CR_2	14	-23.2	-30.2	113	0.278	6.51E-07	4.28E+05
CR_2	15	-25.1	-32.0	220	0.535	8.68E-07	6.16E+05
CR_2	16	-25.6	-32.6	319	0.750	1.00E-06	7.50E+05
CR_2	17	-25.8	-32.6	204	0.477	1.04E-06	4.56E+05
CR_2	18	-27.7	-34.6	865	2.034	1.18E-06	1.72E+06
CR_2	28	-27.2	-34.1	430	0.983	1.25E-06	7.88E+05
CR_2	29	-26.6	-33.5	611	1.464	1.20E-06	1.22E+06
CR_2	30	-26.2	-33.2	324	0.747	1.25E-06	5.98E+05
CR_2	31	-26.0	-32.9	333	0.771	1.42E-06	5.42E+05
CR_2	32	-23.4	-30.4	170	0.434	1.65E-06	2.63E+05
CR_2	33	-19.2	-26.1	41	0.103	1.68E-06	6.12E+04
CR_2	34	-17.8	-24.8	18	0.051	1.72E-06	2.95E+04
CR_2	35	-17.3	-24.2	19	0.058	1.82E-06	3.16E+04
CR_2	36	-15.3	-22.2	11	0.033	2.70E-06	1.23E+04
CR_2	37	-13.4	-20.1	21	0.063	4.25E-06	1.48E+04
CR_2	38	-12.7	-19.5	10	0.034	4.27E-06	8.05E+03

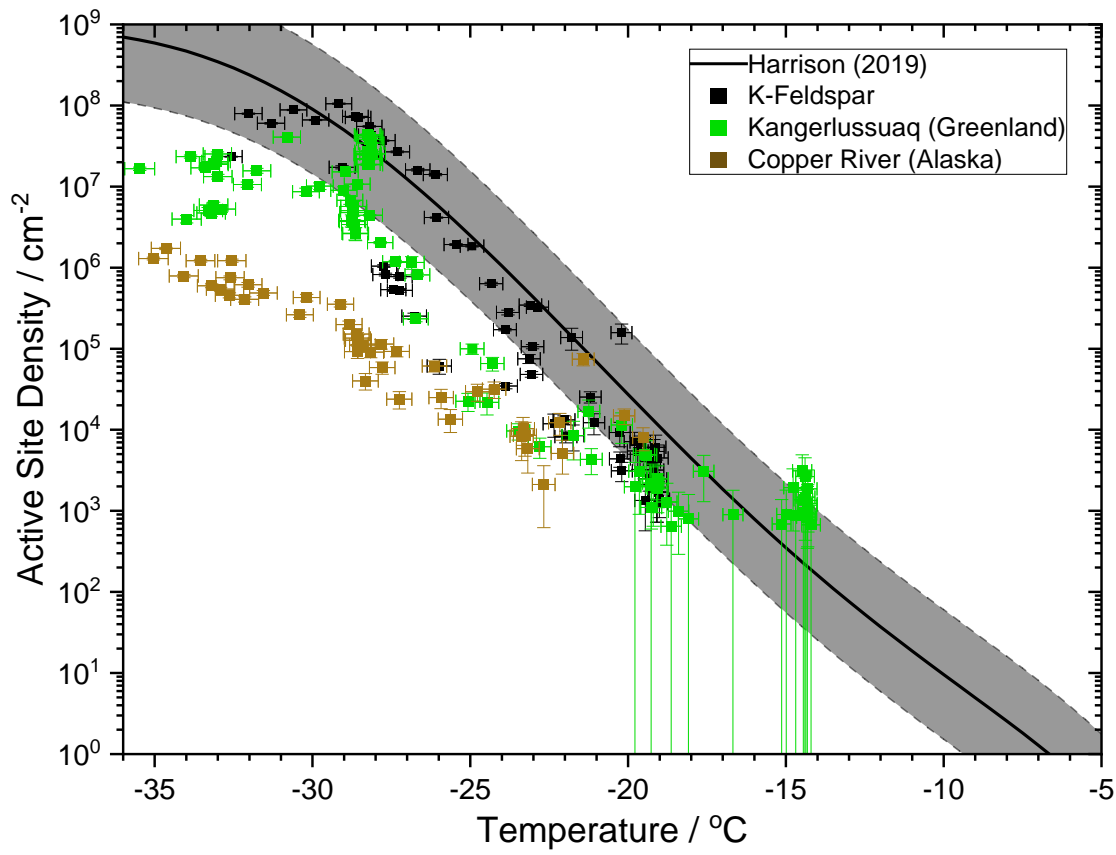


**Figure 3.15:** Duplicate of Figure 3.7 but without any averaging of data points.

### 3.7 References

Amino, T., Iizuka, Y., Matoba, S., Shimada, R., Oshima, N., Suzuki, T., Ando, T., Aoki, T. and Fujita, K.: Increasing dust emission from ice free terrain in southeastern Greenland since 2000, *Polar Sci.*, 27, 100599, doi:10.1016/j.polar.2020.100599, 2021.

Atkinson, J. D., Murray, B. J., Woodhouse, M. T., Whale, T. F., Baustian, K. J., Carslaw, K. S., Dobbie, S., O'Sullivan, D. and Malkin, T. L.: The importance of feldspar for ice nucleation by mineral dust in mixed-phase clouds, *Nature*, 498(7454), 355–358, doi:10.1038/nature12278, 2013.

Barr, S. L., Wyld, B., McQuaid, J. B., Neely, R. R. and Murray, B. J.: Southern Alaska as a source of atmospheric mineral dust and ice-nucleating particles, *Sci. Adv.*, 9(33), eadg3708, doi:10.1126/sciadv.adg3708, 2023.

Brabets, T. P.: *Geomorphology of the lower Copper River, Alaska.*, 1997.

Bullard, J. E. and Mockford, T.: Seasonal and decadal variability of dust observations in the Kangerlussuaq area, west Greenland, *Arctic, Antarct. Alp. Res.*, 50(1), doi:10.1080/15230430.2017.1415854, 2018.

Bullard, J. E., Baddock, M., Bradwell, T., Crusius, J., Darlington, E., Gaiero, D., Gassó, S., Gisladottir, G., Hodgkins, R., McCulloch, R., McKenna-Neuman, C., Mockford, T., Stewart, H. and Thorsteinsson, T.: High-latitude dust in the Earth system, *Rev. Geophys.*, 54(2), 447–485, doi:10.1002/2016RG000518, 2016.

Bullard, J. E., Prater, C., Baddock, M. C. and Anderson, N. J.: Diurnal and seasonal source - proximal dust concentrations in complex terrain, West Greenland, *Earth Surf. Process. Landforms*, 48(14), 2808–2827, doi:10.1002/esp.5661, 2023.

Crusius, J., Schroth, A. W., Gassó, S., Moy, C. M., Levy, R. C. and Gatica, M.: Glacial flour dust storms in the Gulf of Alaska: Hydrologic and meteorological controls and their importance as a source of bioavailable iron, *Geophys. Res. Lett.*, 38(6), doi:10.1029/2010GL046573, 2011.

Cziczo, D. J., Murphy, D. M., Hudson, P. K. and Thomson, D. S.: Single particle measurements of the chemical composition of cirrus ice residue during CRYSTAL-FACE, *J. Geophys. Res. Atmos.*, 109(4), doi:10.1029/2003jd004032, 2004.

DeMott, P. J., Sassen, K., Poellot, M. R., Baumgardner, D., Rogers, D. C., Brooks, S. D., Prenni, A. J. and Kreidenweis, S. M.: African dust aerosols as atmospheric ice nuclei, *Geophys. Res. Lett.*, 30(14), doi:10.1029/2003GL017410, 2003.

DeMott, P. J., Möhler, O., Cziczo, D. J., Hiranuma, N., Petters, M. D., Petters, S. S., Belosi, F., Bingemer, H. G., Brooks, S. D., Budke, C., Burkert-Kohn, M., Collier, K. N., Danielczok, A., Eppers, O., Felgitsch, L., Garimella, S., Grothe, H., Herenz, P., Hill, T. C. J., Höhler, K., Kanji, Z. A., Kiselev, A., Koop, T., Kristensen, T. B., Krüger, K., Kulkarni, G., Levin, E. J. T., Murray, B. J., Nicosia, A., O'Sullivan, D., Peckhaus, A., Polen, M. J., Price, H. C., Reicher, N., Rothenberg, D. A., Rudich, Y., Santachiara, G., Schiebel, T., Schrod, J., Seifried, T. M., Stratmann, F., Sullivan, R. C., Suski, K. J., Szakáll, M., Taylor, H. P., Ullrich, R., Vergara-Temprado, J., Wagner, R., Whale, T. F., Weber, D., Welti, A., Wilson, T. W., Wolf, M. J. and Zenker, J.: The Fifth International Workshop on Ice Nucleation phase 2 (FIN-02): Laboratory intercomparison of ice nucleation measurements, *Atmos. Meas. Tech.*, 11(11), 6231–6257, doi:10.5194/amt-11-6231-2018, 2018.

Groot Zwaafink, C. D., Grythe, H., Skov, H. and Stohl, A.: Substantial contribution of northern high-latitude sources to mineral dust in the Arctic, *J. Geophys. Res.*, 121(22), 13,678–13,697, doi:10.1002/2016JD025482, 2016.

Groot Zwaafink, C. D., Arnalds, Ó., Dagsson-Waldhauserova, P., Eckhardt, S., Prospero, J. M. and Stohl, A.: Temporal and spatial variability of Icelandic dust emissions and atmospheric transport, *Atmos. Chem. Phys.*, 17(17), 10865–10878, doi:10.5194/acp-17-10865-2017, 2017.

Hama, K. and Ito, K.: Freezing of supercooled water-droplets (II), *Pap. Meteorol. Geophys.*, 7(2), 99–106, doi:10.2467/mripapers1950.7.2\_99, 1956.

Harrison, A. D., Lever, K., Sanchez-Marroquin, A., Holden, M. A., Whale, T. F., Tarn, M. D., McQuaid, J. B. and Murray, B. J.: The ice-nucleating ability of quartz immersed in water and its atmospheric importance compared to K-feldspar, *Atmos. Chem. Phys. Discuss.*, 1–23, doi:10.5194/acp-2019-288, 2019.

Herbert, R. J., Murray, B. J., Dobbie, S. J. and Koop, T.: Sensitivity of liquid clouds to homogenous freezing parameterizations, *Geophys. Res. Lett.*, 42(5), 1599–1605, doi:10.1002/2014GL062729, 2015.

Hiranuma, N., Augustin-Bauditz, S., Bingemer, H., Budke, C., Curtius, J., Danielczok, A., Diehl, K., Dreischmeier, K., Ebert, M., Frank, F., Hoffmann, N., Kandler, K., Kiselev, A., Koop, T., Leisner, T., Möhler, O., Nillius, B., Peckhaus, A., Rose, D., Weinbruch, S., Wex, H., Boose, Y., Demott, P. J., Hader, J. D., Hill, T. C. J., Kanji, Z. A., Kulkarni, G., Levin, E. J. T., McCluskey, C. S., Murakami, M., Murray, B. J., Niedermeier, D., Petters, M. D., O'Sullivan, D., Saito, A., Schill, G. P., Tajiri, T., Tolbert, M. A., Welti, A., Whale, T. F., Wright, T. P. and Yamashita, K.: A comprehensive laboratory study on the immersion freezing behavior of illite NX particles: A comparison of 17 ice nucleation measurement techniques, *Atmos. Chem. Phys.*, 15(5), doi:10.5194/acp-15-2489-2015, 2015.

Hobbs, W. H.: Loess, Pebble Bands, and Boulders from Glacial Outwash of the Greenland Continental Glacier, *J. Geol.*, 39(4), 381–385, doi:10.1086/623849, 1931.

Jaeger, J. M., Nittrouer, C. A., Scott, N. D. and Milliman, J. D.: Sediment accumulation along a glacially impacted mountainous coastline: north-east Gulf of Alaska, *Basin Res.*, 10(1), 155–173, doi:10.1046/j.1365-2117.1998.00059.x, 1998.

Kjær, H. A., Zens, P., Black, S., Lund, K. H., Svensson, A. and Vallelonga, P.: Canadian forest fires, Icelandic volcanoes and increased local dust observed in six shallow Greenland firn cores, *Clim. Past*, 18(10), 2211–2230, doi:10.5194/cp-18-2211-2022, 2022.

Meinander, O., Dagsson-Waldhauserova, P., Amosov, P., Aseyeva, E., Atkins, C., Baklanov, A., Baldo, C., Barr, S. L., Barzycka, B., Benning, L. G., Cvetkovic, B., Enchilik, P., Frolov, D., Gassó, S., Kandler, K., Kasimov, N., Kavan, J., King, J., Koroleva, T., Krupskaya, V., Kulmala, M., Kusiak, M., Lappalainen, H. K., Laska, M., Lasne, J., Lewandowski, M., Luks, B., McQuaid, J. B., Moroni, B., Murray, B., Möhler, O., Nawrot, A., Nickovic, S., O'Neill, N. T., Pejanovic, G., Popovicheva, O., Ranjbar, K., Romanias, M., Samonova, O., Sanchez-Marroquin, A., Schepanski, K., Semenov, I., Sharapova, A., Shevnina, E., Shi, Z., Sofiev, M., Thevenet, F., Thorsteinsson, T., Timofeev, M., Umo, N. S., Uppstu, A., Urupina, D., Varga, G., Werner, T., Arnalds, O. and Vukovic Vimic, A.: Newly identified climatically and environmentally significant high-latitude dust sources, *Atmos. Chem. Phys.*, 22(17), 11889–11930, doi:10.5194/acp-22-11889-2022, 2022.

Möhler, O., Benz, S., Saathoff, H., Schnaiter, M., Wagner, R., Schneider, J., Walter, S., Ebert, V. and Wagner, S.: The effect of organic coating on the heterogeneous ice nucleation efficiency of mineral dust aerosols, *Environ. Res. Lett.*, 3(2), 025007, doi:10.1088/1748-9326/3/2/025007, 2008.

Murray, B. J., O'Sullivan, D., Atkinson, J. D. and Webb, M. E.: Ice nucleation by particles immersed in supercooled cloud droplets, *Chem. Soc. Rev.*, 41(19), 6519, doi:10.1039/c2cs35200a, 2012.

Murray, B. J., Carslaw, K. S. and Field, P. R.: Opinion: Cloud-phase climate feedback and the importance of ice-nucleating particles, *Atmos. Chem. Phys.*, 21(2), 665–679, doi:10.5194/acp-21-665-2021, 2021.

Paramonov, M., David, R. O., Kretzschmar, R. and Kanji, Z. A.: A laboratory investigation of the ice nucleation efficiency of three types of mineral and soil dust, *Atmos. Chem. Phys.*, 18(22), 16515–16536, doi:10.5194/acp-18-16515-2018, 2018.

Ponsonby, J., King, L., Murray, B. J. and Stettler, M. E. J.: Jet aircraft lubrication oil droplets as contrail ice-forming particles, *Atmos. Chem. Phys.*, 24(3), 2045–2058, doi:10.5194/acp-24-2045-2024, 2024.

Porter, G. C. E., Sikora, S. N. F., Adams, M. P., Proske, U., Harrison, A. D., Tarn, M. D., Brooks, I. M. and Murray, B. J.: Resolving the size of ice-nucleating particles with a balloon deployable aerosol sampler: the SHARK, *Atmos. Meas. Tech.*, 13(6), 2905–2921, doi:10.5194/amt-13-2905-2020, 2020.

Pratt, K. A., Demott, P. J., French, J. R., Wang, Z., Westphal, D. L., Heymsfield, A. J., Twohy, C. H., Prenni, A. J. and Prather, K. A.: In situ detection of biological particles in cloud ice-crystals, *Nat. Geosci.*, 2(6), 398–401, doi:10.1038/ngeo521, 2009.

Prospero, J. M., Bullard, J. E. and Hodgkins, R.: High-latitude dust over the North Atlantic: Inputs from Icelandic proglacial dust storms, *Science* (80-. ), 335(6072), 1078–1082, doi:10.1126/science.1217447, 2012.

Reicher, N., Segev, L. and Rudich, Y.: The Weizmann Supercooled Droplets Observation on a Microarray (WISDOM) and application for ambient dust, *Atmos. Meas. Tech.*, 11(1), 233–248, doi:10.5194/amt-11-233-2018, 2018.

Rosenfeld, D. and Woodley, W. L.: Deep convective clouds with sustained supercooled liquid water down to - 37.5 °C, *Nature*, 405(6785), 440–442, doi:10.1038/35013030, 2000.

Sanchez-Marroquin, A., Arnalds, O., Baustian-Dorsi, K. J., Browse, J., Dagsson-Waldhauserova, P., Harrison, A. D., Maters, E. C., Pringle, K. J., Vergara-Temprado, J., Burke, I. T., McQuaid, J. B., Carslaw, K. S. and Murray, B. J.: Iceland is an episodic

source of atmospheric ice-nucleating particles relevant for mixed-phase clouds, *Sci. Adv.*, 6(26), 8137–8161, doi:10.1126/sciadv.aba8137, 2020.

Sassen, K., DeMott, P. J., Prospero, J. M. and Poellot, M. R.: Saharan dust storms and indirect aerosol effects on clouds: CRYSTAL-FACE results, *Geophys. Res. Lett.*, 30(12), doi:10.1029/2003GL017371, 2003.

Schroth, A. W., Crusius, J., Gassó, S., Moy, C. M., Buck, N. J., Resing, J. A. and Campbell, R. W.: Atmospheric deposition of glacial iron in the Gulf of Alaska impacted by the position of the Aleutian Low, *Geophys. Res. Lett.*, 44(10), 5053–5061, doi:10.1002/2017GL073565, 2017.

Shi, Y., Liu, X., Wu, M., Zhao, X., Ke, Z. and Brown, H.: Relative importance of high-latitude local and long-range-transported dust for Arctic ice-nucleating particles and impacts on Arctic mixed-phase clouds, *Atmos. Chem. Phys.*, 22(4), 2909–2935, doi:10.5194/acp-22-2909-2022, 2022.

Stohl, A.: Characteristics of atmospheric transport into the Arctic troposphere, *J. Geophys. Res. Atmos.*, 111(D11), doi:10.1029/2005JD006888, 2006.

Tobo, Y., Adachi, K., DeMott, P. J., Hill, T. C. J., Hamilton, D. S., Mahowald, N. M., Nagatsuka, N., Ohata, S., Uetake, J., Kondo, Y. and Koike, M.: Glacially sourced dust as a potentially significant source of ice nucleating particles, *Nat. Geosci.*, 12(4), 253–258, doi:10.1038/s41561-019-0314-x, 2019.

TSI: Model 390069 Data Merge Software Module for Merging and Fitting of SMPS and APS Data Files User's Guide, 2011.

Westbrook, C. D. and Illingworth, A. J.: Evidence that ice forms primarily in supercooled liquid clouds at temperatures  $>-27^{\circ}\text{C}$ , *Geophys. Res. Lett.*, 38(14), doi:10.1029/2011GL048021, 2011.

Wex, H., Huang, L., Zhang, W., Hung, H., Traversi, R., Becagli, S., Sheesley, R. J., Moffett, C. E., Barrett, T. E., Bossi, R., Skov, H., Hünnerbein, A., Lubitz, J., Löffler, M., Linke, O., Hartmann, M., Herenz, P. and Stratmann, F.: Annual variability of ice-nucleating particle concentrations at different Arctic locations, *Atmos. Chem. Phys.*, 19(7), 5293–5311, doi:10.5194/acp-19-5293-2019, 2019.

Xi, Y., Xu, C., Downey, A., Stevens, R., Bachelder, J. O., King, J., Hayes, P. L. and Bertram, A. K.: Ice nucleating properties of airborne dust from an actively retreating

glacier in Yukon, Canada, *Environ. Sci. Atmos.*, 2(4), 714–726, doi:10.1039/d1ea00101a, 2022.

Zhou, X., Liu, D., Bu, H., Deng, L., Liu, H., Yuan, P., Du, P. and Song, H.: XRD-based quantitative analysis of clay minerals using reference intensity ratios, mineral intensity factors, Rietveld, and full pattern summation methods: A critical review, *Solid Earth Sci.*, 3(1), 16–29, doi:10.1016/j.sesci.2017.12.002, 2018.

## **4 Characterising the ice-nucleating activity of volcanic ash and the effects of water and acid aging**

### **4.1 Contributions statement**

The laboratory work in this chapter, specifically the volcanic ash sample collection, milling and ageing as well as the measurements using the SMPS, APS and PINE were done by William D. Fahy, Elena C. Maters, Michael P. Adams and Rona Giese Miranda. This was done in the summer of 2019, before I began my PhD. When the University of Leeds laboratories closed for several months during 2020, I took on the analysis of this dataset. The data processing, analysis, plotting, interpretation and write up for this chapter are all my own work.

### **4.2 Background**

Volcanic eruptions can release substantial quantities of ash into the atmosphere during a single event, for example it is thought that >20,000 Tg of ash was emitted from the 1902 eruption of Santa María, Guatemala (Williams and Self, 1983). As an eruption plume rises, it expands, causing the temperature to decrease, and the surrounding ambient air is entrained into the eruption column. If there is sufficient thermal energy from the eruption, the plume can rise to altitudes at which the water vapour in the entrained ambient air becomes saturated and so condensation of liquid water onto aerosol particles will occur (Woods, 1993). This water condensation then releases latent heat into the plume which increases the thermal energy and causes further convection in the plume of up to several kilometres (Herzog et al., 1998; Woods, 1993). The convection in an eruption plume can redistribute water vapour from the troposphere to the stratosphere (Glaze et al., 1997) and volcanic gases such as HCl and SO<sub>2</sub> can be scavenged by ash particles, liquid droplets and ice crystals in the plume which can also enter the stratosphere (Textor et al., 2003). When the eruption plume reaches a height at which it is no longer buoyant compared to the surrounding atmosphere, it begins to spread outwards to form an umbrella cloud (Sparks, 1986). A portion of the volcanic ash from eruptions can persist in the atmosphere for weeks or months and can be transported tens of thousands of kilometres from the source, potentially affecting regional and global climate (Durant et al., 2010; Engwell and Eychenne, 2016; Vernier et al., 2016).

Volcanic eruptions have historically been associated an increase in local INP concentrations (Hobbs et al., 1971; Isono et al., 1959), and previous laboratory studies have generally found that the immersion mode INA of volcanic ashes is comparable to other active mineral dusts (Durant et al., 2008; Jahn et al., 2019; Mangan et al., 2017; Steinke et al., 2011). Remote sensing measurements of the effect of volcanic ash from the 2010 eruption of Eyjafjallajkull by Seifert et al. (2011) showed that clouds over Europe influenced by the volcanic ash all contained ice at temperatures of  $-15\text{ }^{\circ}\text{C}$  and below, whereas under typical non-volcanic conditions this quantity of ice in clouds would only be seen at temperatures below  $-25\text{ }^{\circ}\text{C}$ , indicating that aerosol from the volcanic eruption caused heterogeneous ice nucleation in clouds at warmer temperatures than typical. Volcanic ash consists primarily of silicate material, the composition of the ash is a reflection of the composition of its source magma and so ashes from different volcanoes are often distinguishable by their compositions (Nakagawa and Ohba, 2003). Volcanic

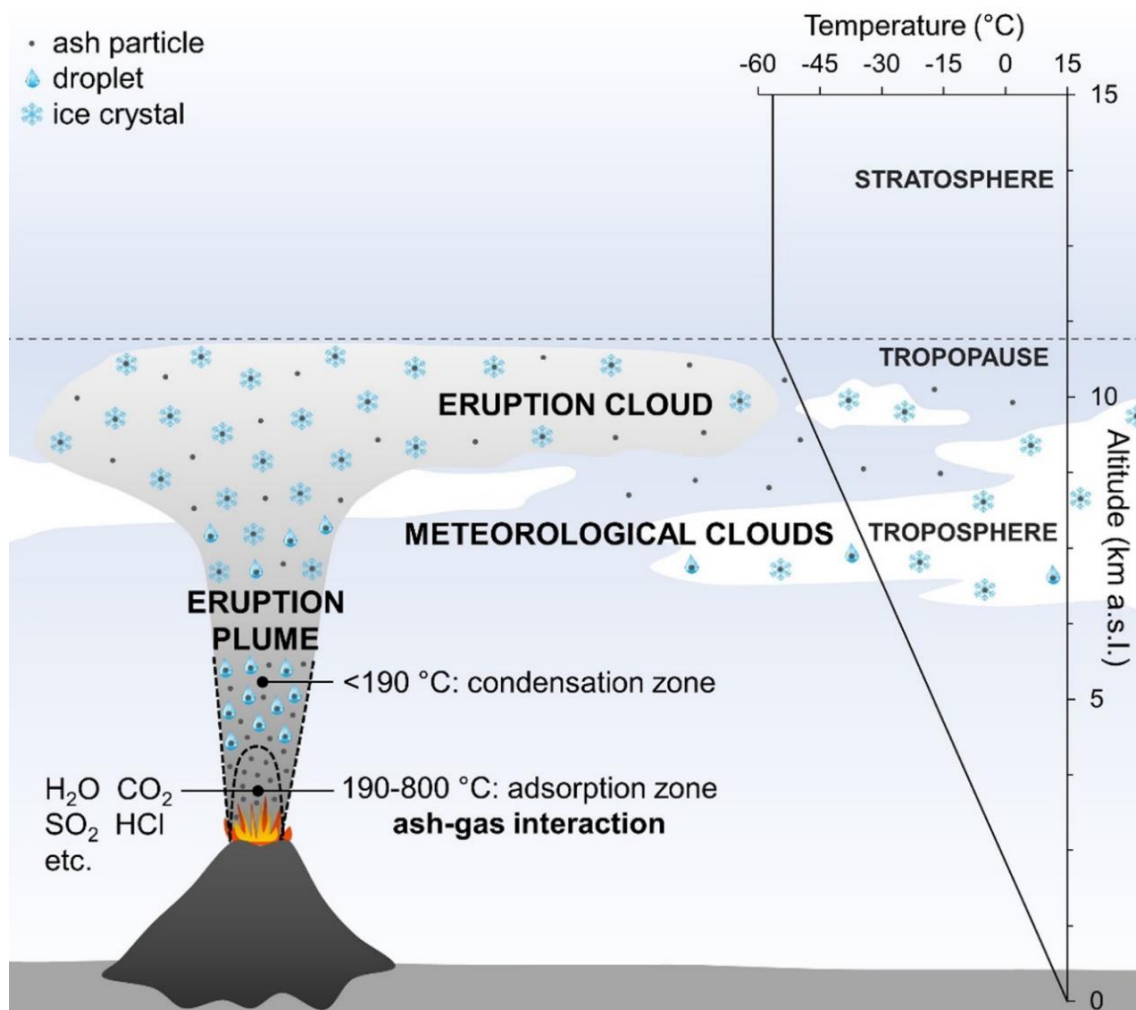


**Figure 4.1:** Schematic showing the presence of volcanic ash particles in the eruption plume, eruption cloud and meteorological clouds following a volcanic eruption. From Maters et al. (2020).

ashes can be categorised based upon their silica and alkali content, as shown in Figure 4.2. Studies comparing the INA of volcanic ashes from different sources have shown that mineralogical differences may lead to different INAs, however, studies attempting to find correlations between the mineralogy of volcanic ashes and their INAs have shown inconsistent results (Genareau et al., 2018; Schill et al., 2015). The crystallinity of volcanic ash also affects its INA, with glassy material having much lower activity than crystalline (Maters et al., 2019), most likely due to a link between crystallinity and active sites.

Ash from the 1974 eruption of Volcán de Fuego, Guatemala was studied for its immersion mode INA by Schill et al. (2015) using 1.3 pL – 0.7 nL droplets of 0.5, 1.0 and 2.0 wt% ash concentration. They found that the largest droplets with the highest concentration Fuego ash began freezing at -30 °C, but most did not nucleate ice above -35 °C, the temperature at which homogeneous freezing begins to be seen. A study by Jahn et al. (2019) also studied ash from Volcán de Fuego but from a later 2015 eruption, they found that 0.1 µL droplets of 0.1 wt% Fuego ash nucleated ice between -12 and -25 °C and that its INA was generally comparable to other volcanic ashes from previous studies. This

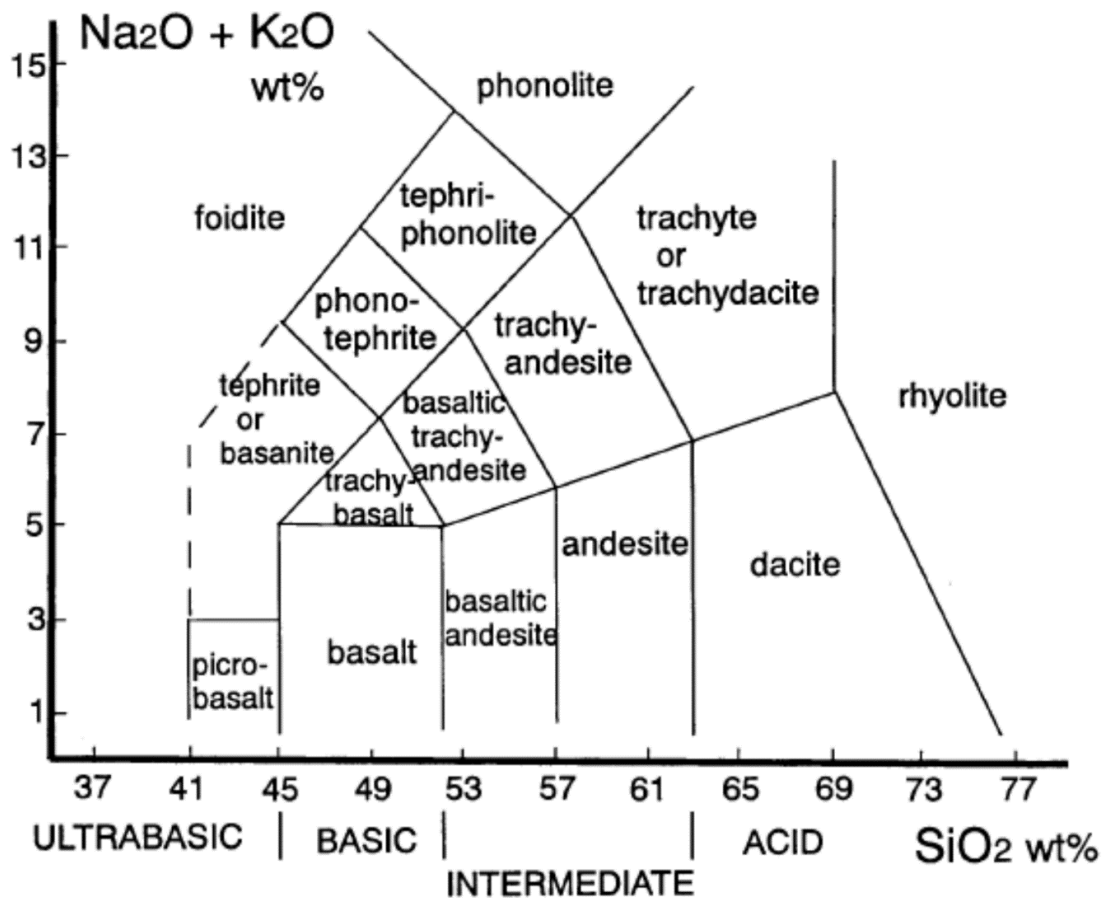


**Figure 4.2:** Diagram showing the different classifications of volcanic rock based upon their silica and alkali content. From Le Maitre et al. (1989)

difference between the two results may be due to the different sized droplets, but could also highlight that even ash from the same source volcano can have different INA between different eruptions, since it is known that different types of eruption can lead to differences in ash mineralogy and crystallinity (Wright et al., 2012). The immersion mode INA of ash from a 3.8 to 4.4 ka eruption of Astroni volcano, Italy was found to have high activity compared to other volcanic ashes in a study by Maters et al. (2019), with 1  $\mu\text{L}$  droplets of 1 wt% Astroni ash concentration nucleating ice between -3 and -13  $^{\circ}\text{C}$ . This high activity was attributed to its high alkali feldspar content compared to other ashes. Ash from the 2010 eruption of Eyjafjallajökull was studied by Hoyle et al. (2011) and Steinke et al. (2011), the immersion mode INA of the volcanic ash was measured by different techniques between the two studies. Hoyle et al. (2011) used the Zurich ice nucleation chamber CFDC and found the ash to only nucleate ice at temperatures below -33  $^{\circ}\text{C}$ , very close to homogeneous nucleation of liquid droplets. On the other hand, Steinke et al. (2011) used the AIDA cloud expansion chamber and found the ash to be immersion active at temperatures below -21  $^{\circ}\text{C}$  and have INA similar to other natural mineral dusts. When the results from these two studies of Eyjafjallajökull ash are normalised to the surface area of the particles used by each experimental method, the results are consistent with one another in terms of the INA of the Eyjafjallajökull ash (Herbert et al., 2014).

Alongside the solid ash particles, gases are also emitted during volcanic eruptions, including  $\text{H}_2\text{O}$ ,  $\text{SO}_2$  and  $\text{HCl}$ , which can interact with and alter the surface properties of the ash particles in the eruption plume (Delmelle et al., 2007). Maters et al. (2020) tested the effect of this interaction with volcanic gases on the INA of volcanic ashes by simulating the interaction in a gas reactor and measuring immersion nucleation using the  $\mu\text{L}$ -NIPI cold stage instrument. They found that in most cases, the INA of the ashes was decreased after treatment with gases, however certain volcanic ashes were found to increase in activity after treatment with a  $\text{H}_2\text{O}$  and  $\text{SO}_2$  gas mixture. The decreases in INA after treatment with volcanic gases were attributed to the destruction of active sites on the surface of the volcanic ash particles via chemical processing. The increase in INA was suggested to be due to the formation of anhydrous  $\text{CaSO}_4$  (anhydrite) deposits on the surface of the ash particles; anhydrite has also been shown to enhance the INA of coal fly ash (Grawe et al., 2018).

A study by Fahy et al. (2022) also investigated the effects of water and acid on the INA of volcanic ashes, but in the solution phase in order to simulate the ageing of coated

volcanic ash particles in the atmosphere. To measure INA, they used the  $\mu\text{L-NIPI}$  instrument, which has a lower temperature measurement limit of roughly  $-25\text{ }^{\circ}\text{C}$  due to background measurements of pure water droplets beginning to freeze at this temperature. Also, since the cold stage method involves suspending the sample in water and pipetting droplets onto the stage, there can be many particles per droplet and an uneven number of particles across each droplet, resulting in uncertainty in INA measurements. This lower experimental measurement limit of  $-25\text{ }^{\circ}\text{C}$  does not cover the full range of temperatures relevant for mixed phase clouds, which can persist down to homogeneous freezing temperatures of  $-33$  and below (Herbert et al., 2014).

To extend the temperature range of measurements of aged volcanic ash samples, we use the PINE-1B cloud expansion chamber to measure the INA of the same samples as measured by Fahy et al. (2022). Three volcanic ashes from the previously mentioned Fuego (FUE), Astroni (AST) and Eyjafjallajökull (EYJ) eruptions were measured both unaged and aged in acid or water. The PINE-1B measures ice nucleation directly in the aerosol phase and can make immersion nucleation measurements down to  $-35\text{ }^{\circ}\text{C}$ , providing a different method of ice-nucleation measurement than the  $\mu\text{L-NIPI}$  as well as being able to extend those measurements to lower temperatures. The results from the PINE-1B measurements are consistent with those from Fahy et al. (2022) in that the different ashes have different INAs pre-ageing, and that the effect of ageing depends on the ash, the ageing solution and the length of ageing.

## **4.3 Methods**

### **4.3.1 Volcanic ash samples and ageing process**

Ash samples from three different volcanic eruptions were used, the 3.8 – 4.4 ka eruption of Astroni (AST), Italy, the February 2015 eruption of Volcán de Fuego (FUE), Guatemala and the 2010 eruption of Eyjafjallajökull (EYJ), Iceland. The ash samples were milled using a zirconia ceramic ball mill to expose fresh surfaces which are more representative of the ash particle surfaces which would be emitted during volcanic eruptions (Fahy et al., 2022). Subsamples of each ash were taken and aged in MilliQ  $\text{H}_2\text{O}$  ( $18.2\text{ M}\Omega$ ) or  $\text{H}_2\text{SO}_4$  ( $0.01\text{ M}$ ) to simulate the effects of atmospheric ageing that the ashes may experience in volcanic plumes. This was done by suspending a 1 wt% concentration of

the ash in the respective ageing solution at room temperature with a constant 1 rpm rotation for 10 minutes, 1 hour, 4 hours or 24 hours (Fahy et al., 2022).

#### **4.3.2 PINE-1B ice nucleation measurements**

The volcanic ash samples were aerosolised into a 0.73 m<sup>3</sup> (90 x 90 x 90 cm) aerosol chamber. The INA of the aerosols was measured using the PINE-1B cloud expansion chamber for the measurement of ice crystals alongside a TSI model 3938 SMPS and a TSI model 3321 APS for the measurement of the aerosol size distribution.

This experimental setup was mostly the same as that used in chapters 2 and 3, however these measurements of volcanic ashes were performed prior to those in chapters 2 and 3 and so there were two notable differences to the setup. First, the volcanic ash samples were aerosolised into the aerosol chamber by putting the sample into a wash bottle, shaking the bottle, and then squeezing the resulting aerosol into one of the aerosol chamber inlets. This resulted in a single loading of the sample into the aerosol chamber which depleted over the course of a series of measurements, as can be seen in Figure 4.7 panel b. Second, the PINE-1B only had one diffusion drier in the line between the aerosol chamber and the PINE chamber. However, the drier was specifically tuned to allow water saturation to be reached, and therefore immersion freezing to occur, during expansions.

The PINE-1B is a 7 L volume cloud expansion chamber which measures INP concentrations by undergoing expansion cooling whilst containing sample aerosol. The aerosol is first flowed from the aerosol chamber into the PINE chamber, the pressure in the PINE chamber is then decreased to decrease the temperature and the formation of liquid droplets and ice crystals is measured by a Palas Welas 2500 OPC. Ice crystals are distinguished from liquid droplets and aerosol particles based upon their size as measured by the OPC. The adiabatic temperature inside the PINE chamber during expansions, calculated using thermocouple temperature measurements at the start of expansions and pressure measurements during expansions, was used as the representative measure of temperature for the PINE expansion measurements. Further details about the operating principles of the PINE and the data analysis methods and justifications are given in chapter 2.

#### **4.3.3 Droplet freezing assay measurements**

Results from  $\mu$ L-NIPI cold stage droplet freezing assay measurements of these volcanic ash samples from Fahy et al. (2022) are also discussed in this chapter and are compared

with the PINE-1B measurement results. MilliQ H<sub>2</sub>O suspensions containing 1, 0.2 and 0.04 wt% of each of the aged and unaged volcanic ash samples were made and for each sample arrays of 30 to 40 1  $\mu$ L droplets were pipetted onto the hydrophobic stage of the  $\mu$ L-NIPI. The freezing temperatures of the droplets were then measured by cooling the stage from 0 °C at a rate of -1 °C min<sup>-1</sup> until all the droplets were frozen.

## 4.4 Results & Discussion

### 4.4.1 Sample aerosol and expansion cloud size distributions

The PINE-1B measurements in this study were performed at a constant expansion starting temperature of -24 °C, which resulted in a minimum adiabatic temperature during expansions of  $\sim$ -31 °C after a decrease in pressure of  $\sim$ 100 mbar. Since the temperature was not varied, the primary experimental variable over the course of the series of expansions of each sample was the concentration of the sample aerosol in the aerosol chamber. The Fuego ash aged in acid for 24 hours was the sample measured for the longest time, these measurements took place over  $\sim$ 11 hours during which the aerosol surface area concentration in the aerosol chamber decreased by  $\sim$ 5 orders of magnitude. The change over time of the sample aerosol size distribution in the aerosol chamber is shown in Figure 4.3, the mobility-equivalent particle diameters measured by the SMPS and the aerodynamic particle diameters measured by the APS were converted into volume-equivalent sphere diameters using equations 1 and 2 from Möhler et al. (2008). For the same reasons as for the K-feldspar mineral dust test aerosol in chapter 2, the density of the particles was assumed to be 2.6 g cm<sup>-3</sup> and the shape factor was assumed to be 1.1. For the overlapping SMPS and APS measurements, a volume equivalent diameter of 0.4  $\mu$ m was chosen as the point below which the SMPS measurements were used and above which the APS measurements were used. At the start of the measurements, the 24-hour acid aged Fuego sample had a broad aerosol size distribution with particles up to  $\sim$ 15  $\mu$ m in diameter and a  $\sim$ 0.2  $\mu$ m peak. At diameters of 0.02  $\mu$ m and below the number concentration increased, indicating a possible second aerosol mode peaking at sizes below what was measured by the SMPS. After 4 hours, the number concentration of the aerosol decreased by  $\sim$ 2 orders of magnitude and the distribution narrowed to an upper size limit of 2  $\mu$ m, at diameters below 0.05  $\mu$ m the SMPS began to reach its lower limit of detection. After 7 hours, the number concentration decreased by a further  $\sim$ 1 order of magnitude and the distribution also narrowed further, however due to the SMPS being at its limit of detection across its full measurement range, the shape of the aerosol size

distribution below  $0.4 \mu\text{m}$  is no longer discernible. A composite plot of aerosol size distributions of all the samples used in this study is shown in Figure 4.4, with each aerosol size distribution corresponding to a surface area concentration of approximately  $1.0 \times 10^{-6} \text{ cm}^2 \text{ cm}^{-3}$ . The samples had similar aerosol size distributions, with peaks at  $\sim 0.2 \mu\text{m}$  and an upper size of  $\sim 2 \mu\text{m}$ , all the samples also showed an increase in particle numbers at diameters below  $0.02 \mu\text{m}$  as seen in Figure 4.3. For many of the aerosol size distributions shown in Figure 4.4, the SMPS and APS curves do not align at  $0.4 \mu\text{m}$ , with the APS number concentration measurements being lower by up to a factor of 4. This may be due to counting inefficiencies in the lower size measurements of the APS, which is mentioned TSI literature (TSI, 2011). The uncertainty associated with the potential

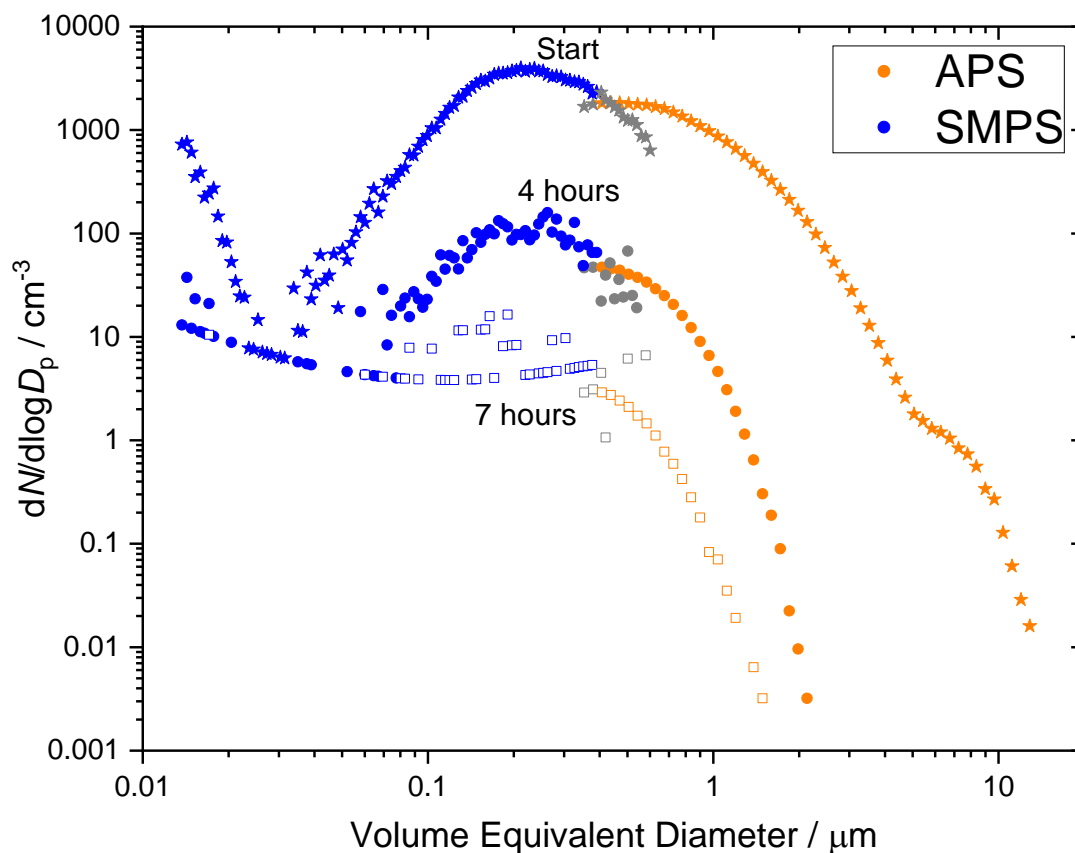


**Figure 4.3:** Aerosol size distribution measurements of the Fuego volcanic ash aged in acid for 24 hours, aerosolised in the aerosol chamber. Star points show the size distribution at the start of the measurements, when the sample is first aerosolised. Circle points show the size distribution after 4 hours of measurements. Hollow square points show the size distribution after 7 hours of measurements. The diameters measured by the SMPS and APS were converted to volume-equivalent diameters to be merged (Möhler et al., 2008). A diameter of  $0.4 \mu\text{m}$  was used below which only SMPS measurements were used and above which only APS measurements were used, as illustrated by the grey points which are the unused measurements.

undercounting of lower size measurements of the APS was quantified by adjusting the APS values to be consistent with the SMPS measurements and calculating increase in total aerosol surface area that results from this adjustment. Figure 4.5 shows an example aerosol surface area size distribution of the unaged Astroni volcanic ash sample, which was the sample in Figure 4.4 with the largest discrepancy between the SMPS and APS values. The blue points in Figure 4.5 are the SMPS and APS measurements and the hollow black circles are the adjusted APS values. When calculating the total surface area concentration by summing each of the individual points, the adjustment of the APS values increases the total surface area concentration from  $1.00 \times 10^{-6} \text{ cm}^2 \text{ cm}^{-3}$  to  $1.10 \times 10^{-6} \text{ cm}^2 \text{ cm}^{-3}$ , resulting in a 10 % increase in the total surface area concentration of the sample. The significance of this 10 % uncertainty is visualised below in Figure 4.7 panel b, which shows that the uncertainty is negligible compared to the variation in the aerosol surface area concentration over the course of experiments.

The cloud size distributions measured by the PINE-1B during expansions corresponding to the aerosol size distributions in Figure 4.3 are shown in Figure 4.6. For the expansion

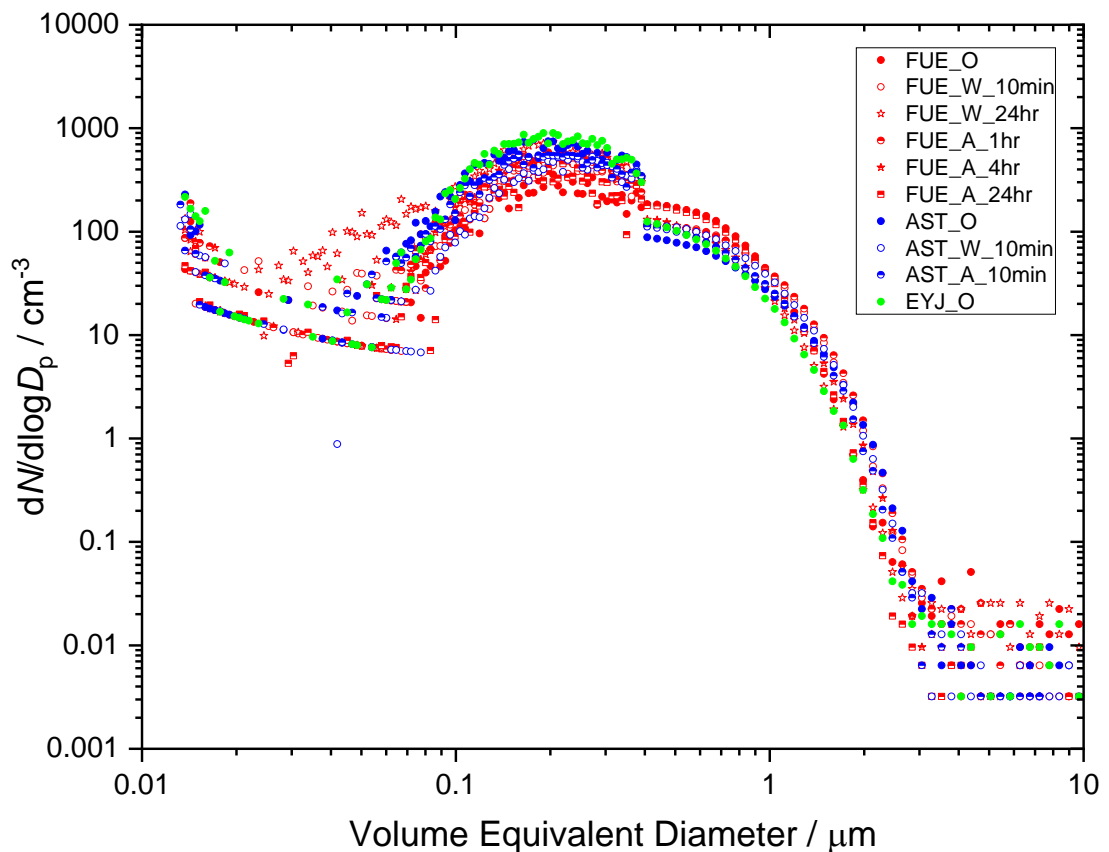


**Figure 4.4:** Aerosol size distributions measured by SMPS and APS for each volcanic ash sample used in this study from when the surface area concentration of the sample was approximately  $1.0 \times 10^{-6} \text{ cm}^2 \text{ cm}^{-3}$ . Sample names in the legend indicate type of ash, type of ageing and length of ageing.

at the start of measurements, there was a first peak at  $\sim 0.7$  to  $10 \mu\text{m}$  and a second peak at  $\sim 10$  to  $100 \mu\text{m}$ . Generally, for PINE measurements the first peak would be interpreted as being primarily liquid droplets and the second peak primarily ice crystals, however in this case at the start of measurements the aerosol sample had particles up to and above  $10 \mu\text{m}$  in diameter and so the first peak may have consisted of both aerosol particles and liquid droplets. The concentration of particles at diameters  $>10 \mu\text{m}$  in the starting cloud distribution shown in Figure 4.6 is  $17.47 \text{ cm}^{-3}$  while the concentration of particles at volume equivalent diameters  $>10 \mu\text{m}$  in the starting aerosol size distribution shown in Figure 4.3 is  $7.30 \times 10^{-3}$ . Assuming that the volume equivalent diameters of the aerosol size distributions are equivalent to the particle diameters of the cloud size distributions, up to 0.042 % of the particles measured at  $>10 \mu\text{m}$  in the cloud size distribution may be large aerosol particles as opposed to ice crystals. Although this is a very small fraction of the total number of ice crystals, it is not clear how consistent the aerosol size distribution volume equivalent diameters are with the cloud size distribution diameters. Since the cases in which the aerosol size distribution extends up to and above  $10 \mu\text{m}$  make up a minority of the total measurements, the ice concentration values from these cases were

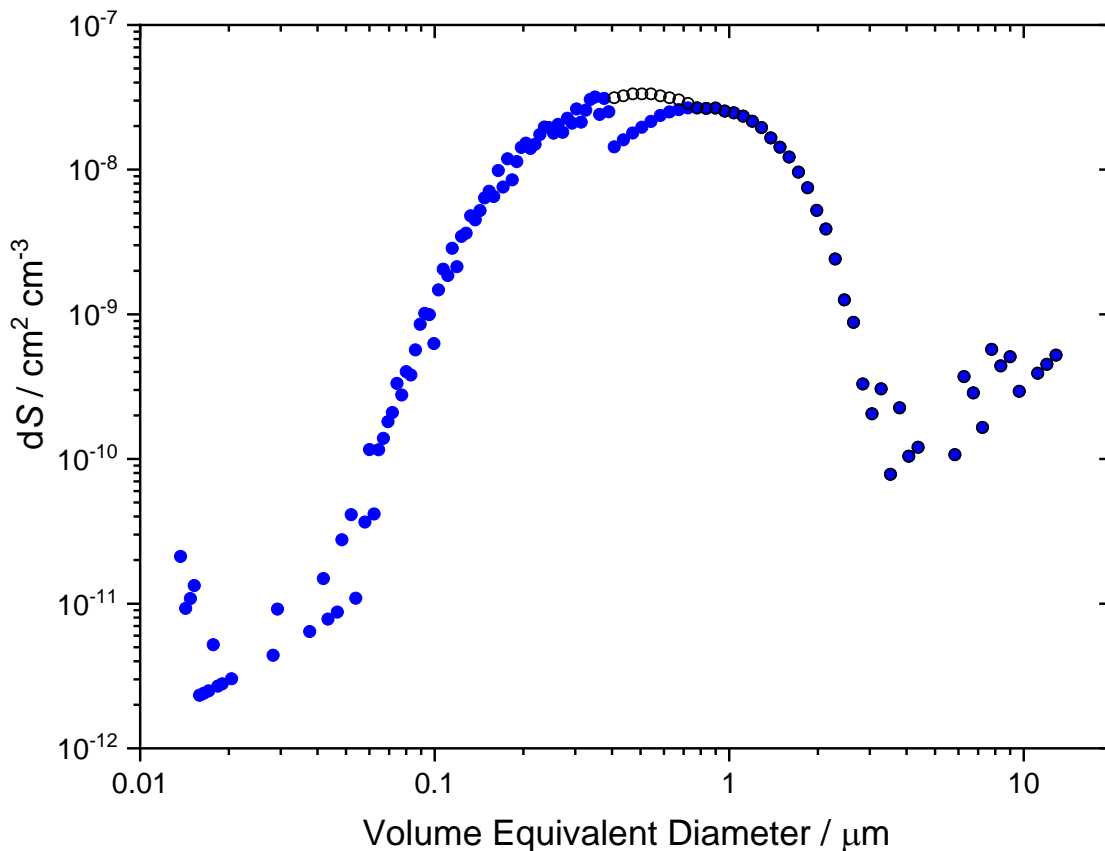


**Figure 4.5:** Aerosol surface area size distribution of unaged Astroni volcanic ash. Blue points are the values measured by the SMPS and APS and hollow black circles are the adjusted APS values.

not used when determining the INAs of the volcanic ash samples. The specific method used to determine which measurements should be used for INA determination is discussed in the next section. After 4 hours, the smaller peak in the cloud size distribution shifts to lower concentrations at sizes below  $4\ \mu\text{m}$  but has a higher and more prominent peak at  $6\ \mu\text{m}$ . This shift in the peak's shape is likely due to the decreased sample aerosol concentration and the reduction of the sample aerosol's upper size limit to  $\sim 2\ \mu\text{m}$  resulting in the peak consisting primarily of liquid droplets activated from the aerosol particles. The second peak in the 4-hour cloud size distribution also shifted to slightly higher sizes compared to the start due to the increased size of the liquid droplets, but the concentrations decreased by  $\sim 1$  order of magnitude. The cloud size distribution after 7 hours was similar to the 4-hour cloud size distribution, but at concentrations approximately 1 order of magnitude lower. As time went on and the aerosol sample number concentration decreased, the diameter of peak of the liquid droplet distribution

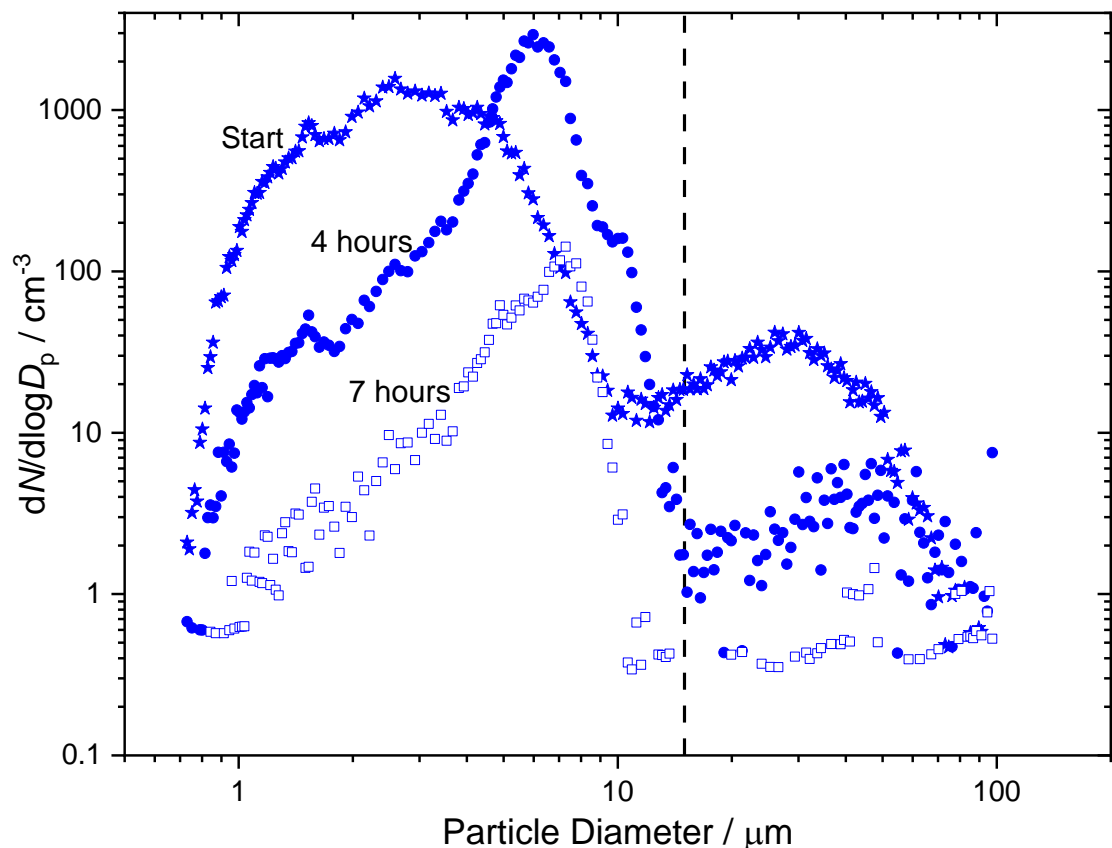


**Figure 4.6:** Cloud size distributions measured by the Welas OPC during PINE-1B expansions using 24-hour acid-aged Fuego volcanic ash sample aerosol. Star points show the size distribution at the start of the measurements, when the is first aerosolised. Circle points show the size distribution after 4 hours of measurements. Hollow square points show the size distribution after 7 hours of measurements. Dashed black line indicates size threshold above which all particles are counted as ice crystals.

shifted to larger diameters due to the available water vapour during expansions being shared between fewer particles and therefore individual droplets could grow to larger sizes during the expansions, which in turn resulted in larger ice crystals when the droplets froze.

#### 4.4.2 Determination of volcanic ash ice-nucleating activity

To be able to compare the INA of different samples measured at different concentrations, the concentration of ice crystals measured by the PINE-1B can be normalised to the surface area concentration of the aerosol sample to obtain a measure of the concentration of ice-nucleating active sites across the sample's surface, known as the active site density ( $n_s$ ). Figure 4.7 shows the full series of measurements made to determine the INA of the 24-hour acid-aged FUE ash sample, each blue point represents the data corresponding to a single expansion. Panel a shows the concentration of ice particles measured in the PINE during the expansion ( $N_{ice}$ ), panel b shows the surface area concentration of the ash aerosol as measured by the SMPS and APS and panel c shows the active site density ( $n_s$ ), calculated by dividing  $N_{ice}$  by the surface area concentration. The aerosol surface area concentration decreases by over 5 orders of magnitude over the course of the measurements due to the removal of particles via both gravitational settling and their intake into the measurement instruments, this decrease in ash aerosol results in a decrease in ice concentration over time as shown in panel a. The active site density of the ash shows an overall increase over the experiment, although there is a roughly 5-hour period between 14:10 and 19:00, outlined by the vertical lines in Figure 4.7, during which the active site density stays constant despite a change in  $N_{ice}$  and aerosol surface area concentration of over 2 orders of magnitude. Equivalent plots for the other samples are shown in the appendix Figure 4.11 through Figure 4.19, all the samples show the same trends as seen in Figure 4.7 but most are less pronounced due to having a smaller range of aerosol surface area concentrations.

The overall increase in active site density seen as the aerosol surface area concentration decreases indicates a change in the INA of the sample as the aerosol size distribution changes, issues with the PINE-1B measurements of ice crystals at certain concentrations, or a combination of both. The decrease in aerosol surface area concentration in Figure 4.7 occurs at a constant rate for the full length of the measurements, however the decrease in  $N_{ice}$  is not consistent with this. Between 14:10 and 19:00, the decrease in  $N_{ice}$  occurs at a constant rate, but before 14:10 the decrease in  $N_{ice}$  has a shallower gradient, and after 19:00  $N_{ice}$  does not decrease but has higher uncertainty and scatter between measurements.

The reason for the higher uncertainty in the  $N_{ice}$  measurements after 19:00 is due to the increased uncertainty associated with the counting statistics of the ice crystals in the PINE chamber, which in turn leads to an increased uncertainty in the active site density. The number of ice crystals measured during these expansions after 19:00 was 0 to 10, and so for these measurements the sample aerosol concentration was low enough that the PINE-1B was effectively at its lower measurement limit, resulting in the reported  $N_{ice}$  values not decreasing despite the decrease in the surface area concentration. This lack of change in the measured  $N_{ice}$  values while the surface area concentration still decreased

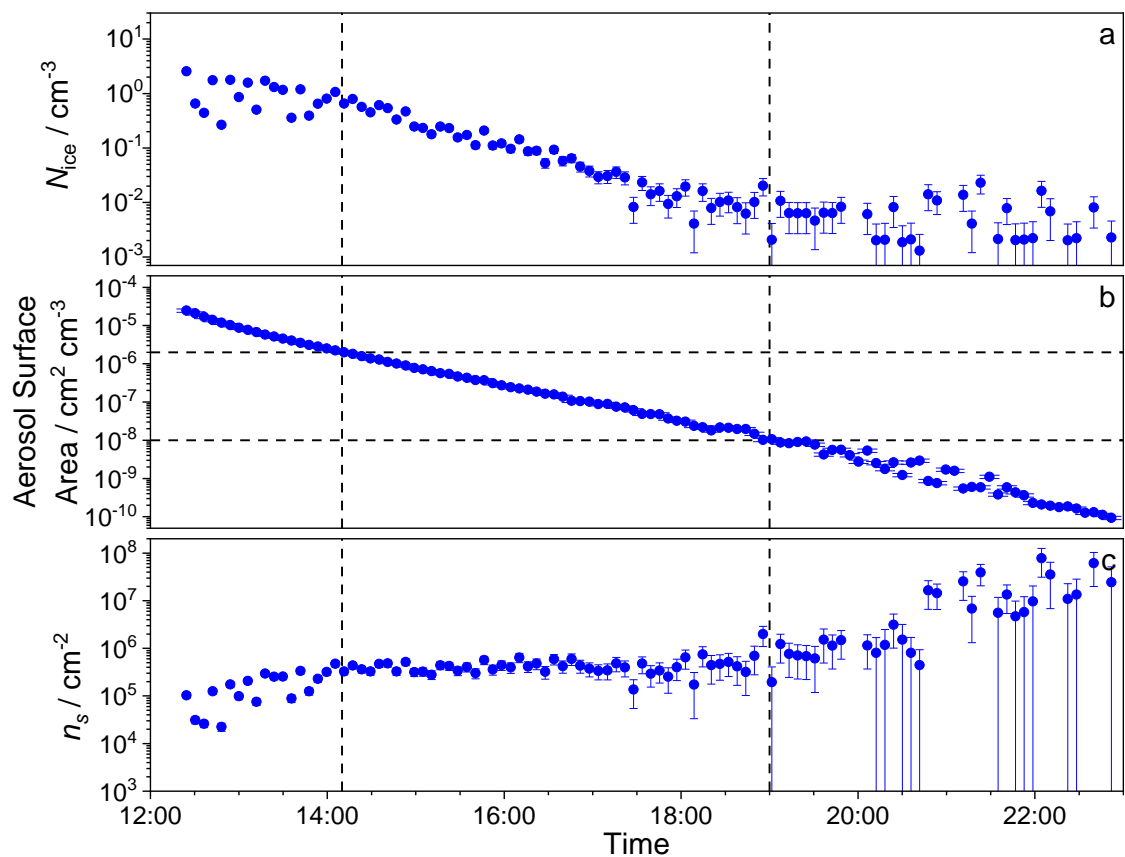


**Figure 4.7:** Series of expansion measurements of Fuego volcanic ash aged in acid for 24 hours, each blue point represents a single expansion. **a)** concentration of ice crystals measured by the PINE-1B, **b)** ash aerosol surface area concentration measured by SMPS and APS, **c)** active site density of the ash calculated by dividing a by b. Vertical dashed lines at 14:10 and 19:00 enclose the period during which the value of  $n_s$  remains constant. Horizontal dashed lines in panel b enclose the range of aerosol surface area concentration values during the constant period of  $n_s$  values ( $2 \times 10^{-6}$  to  $1 \times 10^{-8}$   $\text{cm}^2 \text{cm}^{-3}$ ). Error bars in panel a represent the uncertainty associated with the counting statistics of ice particles, error bars in panel b represent the 10 % uncertainty associated with the undercounting of particles by the APS, error bars in panel c represent the combination of the uncertainties in  $N_{ice}$  and aerosol surface area concentration.

resulted in the increase in the calculated active site density values after 19:00, but with a large uncertainty. At times before 14:10, the cloud size distributions are shifted to lower sizes compared to measurements at later times, as shown in Figure 4.6. If the size of the ice crystals produced in the PINE chamber is lower during measurements before 14:10, then the number of ice crystals would be undercounted compared to measurements after 14:10 due to the ice size threshold being constant at 15  $\mu\text{m}$  for all measurements. Although the ice threshold could be decreased for the measurements before 14:10 to account for the shift in the cloud size distribution, the presence of aerosol particles up to 10  $\mu\text{m}$  in diameter during these early measurements adds uncertainty to the identification of ice crystals based upon their measured diameter. Therefore, it is better to only consider the measurements where the active site density is constant while maintaining a constant ice threshold.

By comparing the measurements across all the volcanic ash samples, a sample aerosol surface area concentration range between  $2 \times 10^{-6}$  and  $1 \times 10^{-8} \text{ cm}^2 \text{ cm}^{-3}$  was found to result in stable active site density values for each sample, illustrated by the vertical dashed lines in panel b of Figure 4.7. Therefore, measurements outside of this concentration range were removed from further analysis of the INAs of the volcanic ash samples. This surface area concentration range is dependent on the temperature at which measurements are made, since at higher temperatures less ice crystals are likely to be produced during expansions and therefore the lower detection limit of the PINE-1B would be reached at higher sample concentrations. The range could also be dependent on the INA of the sample, since more active samples would produce higher  $N_{\text{ice}}$  and vice versa. The fact that a specific aerosol concentration range was required to produce consistent active site density values highlights that the PINE-1B can produce inaccurate results if sample concentrations are too high, due to potential interference with ice particle detection, or if sample concentrations are too low, due to the number of measured ice crystals being too low to produce a statistically accurate concentration.

#### 4.4.3 Effect of ageing on volcanic ash ice-nucleating ability

A comparison of the INAs of the unaged and aged volcanic ash samples is shown in Figure 4.8. Each box plot includes all expansions in which the minimum adiabatic temperature reached  $-31.2 \pm 0.5 \text{ }^\circ\text{C}$  (corresponding to an expansion starting temperature of  $-24 \text{ }^\circ\text{C}$ ) and the surface area concentration of the sample aerosol was between  $2 \times 10^{-6}$  and  $1 \times 10^{-8} \text{ cm}^2 \text{ cm}^{-3}$ . Of the unaged ashes, Fuego was the most active by over an order of magnitude, with a mean active site density of  $2.0 \times 10^6 \text{ cm}^{-2}$ . Comparatively, the INAs

of Astroni and Eyjafjallajökull were within uncertainty of one another. When considering the effects of ageing on Fuego ash, all cases of ageing decreased its INA, with water ageing resulting in a stronger decrease than acid ageing and longer periods of ageing resulted in an increase in INA compared to shorter periods. In contrast to Fuego, the INA of Astroni ash was not decreased by ageing but instead increased slightly, however the overlap between the box plots and their uncertainties may indicate that the INA did not change notably with ageing in the 10-minute time used for the Astroni samples.

The high INA of Fuego ash at  $-31.2\text{ }^{\circ}\text{C}$  compared to the other two indicates the presence of ice-active sites on the surface of Fuego ash particles that were not found on the other two ashes. The fact that upon ageing the INA of the Fuego ash was decreased to be closer

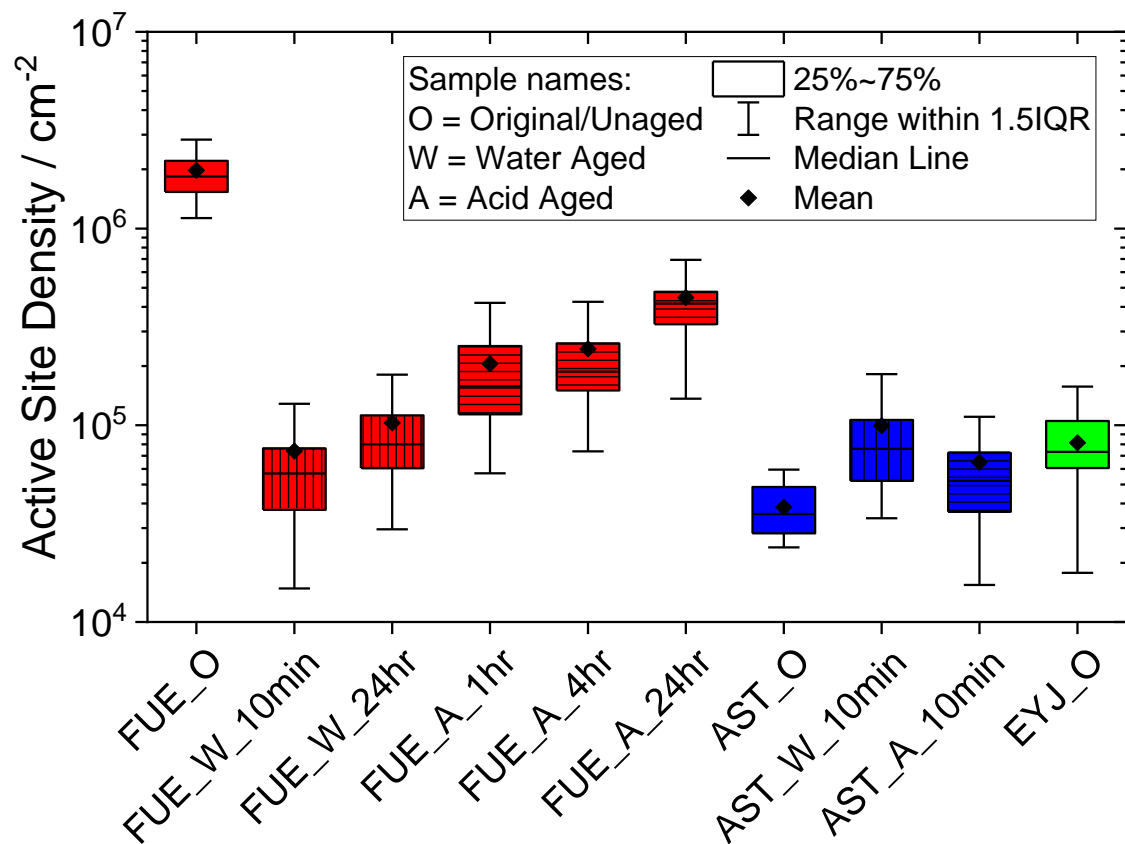


**Figure 4.8:** Comparison of ice-nucleating ability of Fuego (FUE) (red), Astroni (AST) (blue) and Eyjafjallajökull (EYJ) (green) volcanic ashes and the effects of ageing in  $\text{H}_2\text{O}$  and  $\text{H}_2\text{SO}_4$ . Each box plot consists of all expansions with a minimum adiabatic temperature of  $-31.2 \pm 0.5\text{ }^{\circ}\text{C}$  and ash sample surface area concentrations between  $2 \times 10^{-6}$  and  $1 \times 10^{-8}\text{ cm}^2\text{ cm}^{-3}$ . Black diamonds represent the mean active site density and horizontal lines represent the median active site density. Coloured boxes represent the interquartile range of active site density values and whiskers show the range of values which were within 1.5 times of the interquartile range. Sample names indicate type of ash, type of ageing and length of ageing.

to that of Astroni and Eyjafjallajökull suggests that the ageing process removed or decreased the efficacy these unique active sites. This decrease in active site efficacy could be caused by changes in the structure of the site, for example if the active site were made smaller by the ageing process the size of the critical ice cluster it could stabilise would be smaller and therefore a lower temperature would be needed for ice nucleation to occur. Since the greatest decrease in the INA of the Fuego ash was seen when aged in water for 10 minutes, the removal of active sites was a fast process, and longer ageing timescales seemed to increase INA as opposed to decrease. This increase in INA suggests that after the initial removal of active sites, longer periods of ageing may result in the reformation, exposure or creation of new active sites, such as the formation of anhydrite deposits as seen by Maters et al. (2020). However, for both the water and acid-aged Fuego samples, the INA increased by approximately a factor of 2 when going from the shortest ageing time to the longest, which was much smaller than the factor of 10 decrease in INA compared to the unaged ash. Compared to Fuego, the INA of Astroni ash was not changed significantly by ageing, indicating that the active sites on the Astroni aerosol were not altered by the ageing process. Although the mean active site density values for both water and acid aged Astroni were greater than that for unaged, the general overlap of the box plots suggests that the INA was not notably changed.

#### **4.4.4 Comparison between PINE-1B and $\mu$ L-NIPI measurements**

The PINE measurements of the volcanic ashes in this study were performed within approximately 1 month of the  $\mu$ L-NIPI cold stage measurements of the same samples reported by Fahy et al. (2022). The  $\mu$ L-NIPI measurements had a temperature range of -5 to -25 °C, and so the PINE-1B measurements at  $\sim$ -31 °C extend the measurement range of the INAs of these samples. Figure 4.9 shows the INAs of the unaged Fuego and Astroni ash samples measured by the PINE-1B compared to the INAs of the same samples measured by Fahy et al. (2022). Although the INA results from this study are too low in temperature to overlap with the  $\mu$ L-NIPI measurements shown in Figure 4.9, the results are consistent in that the Fuego sample had a higher INA than the Astroni ash at temperatures below -12 °C. The results from the  $\mu$ L-NIPI cannot be extrapolated to the PINE-1B measurement temperature because it cannot be predicted how the active site density will change as temperature decreases, other than that it cannot decrease since it is a cumulative quantity.

The effects of water and acid ageing on the INA activity of the Fuego and Astroni volcanic ash samples are shown in Figure 4.10, which compares the PINE-1B measurements with

those from the  $\mu\text{L-NIPI}$  by Fahy et al. (2022). To identify possible mechanisms for the changes in the INAs of the volcanic ash samples upon ageing, Fahy et al. (2022) also measured the concentrations of various elements dissolved in the ageing solutions and used correlation coefficients and predictive modelling to link changes in elemental compositions to the changes in INA. Panel a shows the effects of ageing on the Fuego ash, both the PINE-1B and the  $\mu\text{L-NIPI}$  measurements showed that 10-minute water-ageing resulted in the largest decrease in INA of  $\sim 1$  order of magnitude at  $-31\text{ }^\circ\text{C}$  as measured by the PINE-1B and  $\sim 3$  orders of magnitude as measured by the  $\mu\text{L-NIPI}$ . Fahy et al. (2022) attributed this deactivation to the leaching of cations from the ice-nucleating minerals at the ash's surface, which could cause a reduction in INA since the exchange of surface cations with protons in solution has been suggested to be important for the heterogeneous ice-nucleating activity of certain minerals (Kumar et al., 2019). The partial recovery of the INA of Fuego ash after ageing in water for 24 hours compared to 10 minutes is seen in the  $\mu\text{L-NIPI}$  measurements, with the INA increasing by  $\sim 1$  order of magnitude. For the PINE-1B measurements, a slight increase in the mean INA by  $\sim 40\%$  is seen from the 10-minute to 24-hour water-aged samples, but the

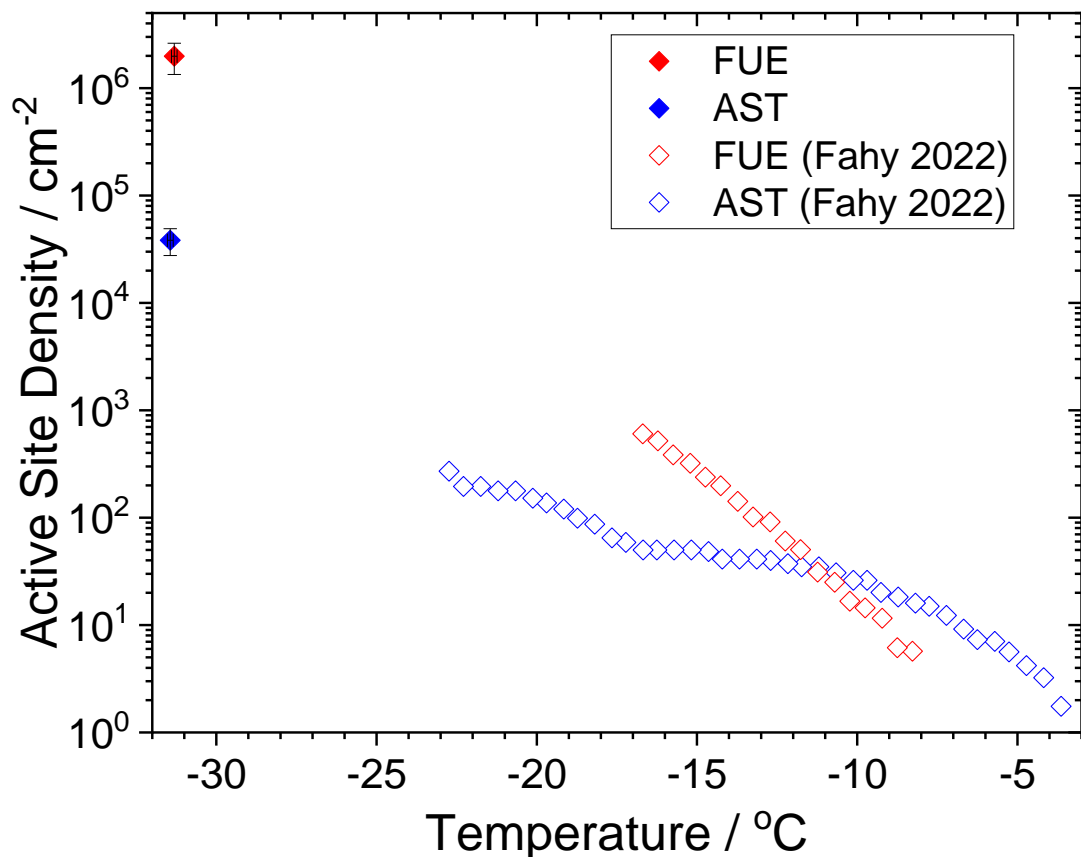


**Figure 4.9:** Comparison between the INA of unaged Fuego and Astroni volcanic ashes measured using the PINE-1B in this study (filled symbols) and the  $\mu\text{L-NIPI}$  by Fahy et al. (2022) (hollow symbols).

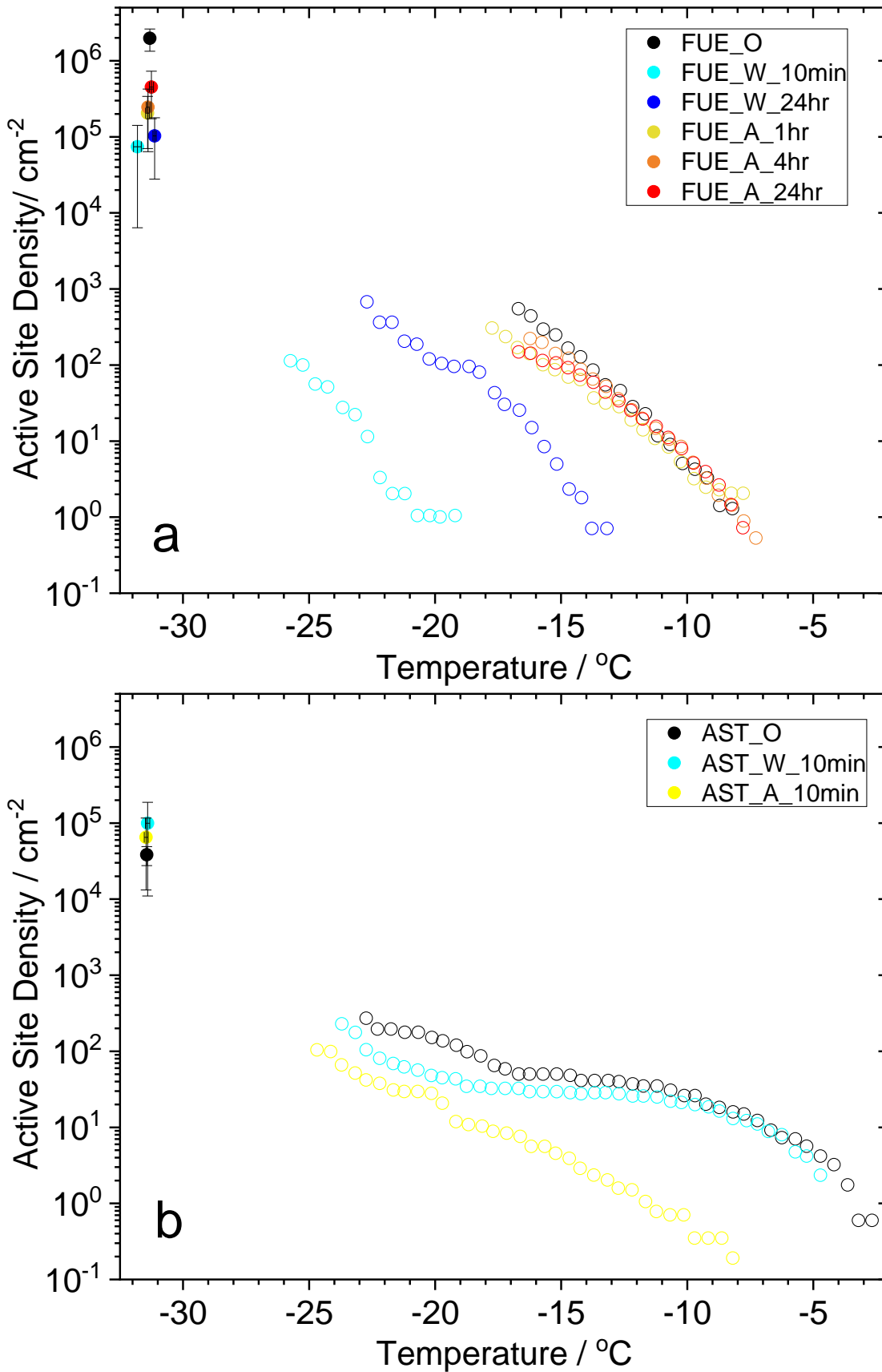


**Figure 4.10:** Comparison between the INA of unaged a) Fuego and b) Astroni volcanic ashes measured using the PINE-1B in this study (filled symbols) and  $\mu$ L-NIPI by Fahy et al. (2022) (hollow symbols). Sample names indicate type of ash, type of ageing and length of ageing.

uncertainties are much greater than this change in the mean value. Fahy et al. (2022) attributed the recovery of the INA of the Fuego ash after longer periods of water-aging to the precipitation of ice-nucleating secondary mineral phases from solution, since measurements of the concentrations of elements in the ageing solutions showed mineral phases such as montmorillonite, kaolinite and gibbsite to be supersaturated. For the acid-aged Fuego ash samples, both the PINE-1B and  $\mu\text{L-NIPI}$  showed a smaller decrease in INA compared to water-ageing, with the  $\mu\text{L-NIPI}$  measurements above  $-15\text{ }^{\circ}\text{C}$  showing effectively no change in INA. In the results reported by Fahy et al. (2022), the 10-minute acid-aged Fuego ash did have a decrease in INA by a factor of 5 to 10, but the activity recovered to unaged values upon longer ageing. The PINE-1B measurements show a slight recovery of the INA of Fuego ash upon longer acid-ageing times, in line with the results from Fahy et al. (2022). The initial loss of the INA of Fuego ash after acid ageing was attributed by Fahy et al. (2022) to the leaching of cations as with water ageing, however the recovery of INA upon longer ageing was suggested to be due to the establishment of a steady state of active site density at the surface of the ash as a result of the dissolution of surface mineral layers revealing new active sites on new mineral layers.

Panel b shows the effects of 10-minute water and acid ageing on Astroni volcanic ash, PINE-1B measurements were only performed on the 10-minute aged samples, so the effects of longer ageing on the INA at  $-31\text{ }^{\circ}\text{C}$  is unknown. Water and acid ageing increased the INA measured by PINE-1B by factors of  $\sim 2$  and  $\sim 3$  respectively, however the mean values are all within the uncertainties of one another, so the changes are not statistically significant. This lack of change in the INA of Astroni ash upon water and acid ageing is consistent with the  $\mu\text{L-NIPI}$  from Fahy et al. (2022), which showed at temperatures below  $-23\text{ }^{\circ}\text{C}$  and  $-17\text{ }^{\circ}\text{C}$  respectively, water and acid ageing had little effect on the INA of Astroni ash. The temperature dependence of the effects of ageing on the Astroni ash was suggested to be due to the presence of different minerals controlling the activity at different temperatures, with K-feldspar controlling the activity at temperatures above  $-17\text{ }^{\circ}\text{C}$  and pyroxene or Na/Ca-feldspar controlling the activity at temperatures below  $-17\text{ }^{\circ}\text{C}$ . As with Figure 4.9, the results in Figure 4.10 shows that the PINE-1B and  $\mu\text{L-NIPI}$  measurements are consistent with one another and so the techniques are complimentary to each other, since the PINE can perform expansions at temperatures lower than the  $\mu\text{L-NIPI}$  can typically reach. Further PINE measurements at temperatures between  $-10$  and  $-35\text{ }^{\circ}\text{C}$  would allow for a clearer comparison with the  $\mu\text{L-NIPI}$

measurements of volcanic ashes and would extend the temperature range of the INA spectra down to homogeneous freezing temperatures.

## 4.5 Conclusions

The results from this study highlight the complexity of volcanic ash in the atmosphere and its ability to nucleate ice. The different INAs of volcanic ashes from different source volcanoes alongside the various effects of ageing, depending on the properties of the unaged ash, the ageing material, and the length of ageing, demonstrates that not all volcanic ash in the atmosphere is the same. In particular, the use of freshly ground ash for laboratory measurements is unlikely to represent the properties of the ash in the atmosphere, since ash emitted from volcanic eruptions is expected to undergo ageing due to its emission alongside various volcanic gases at high temperatures.

The need for a specific range of aerosol sample concentration to make accurate measurements of ice crystal number concentrations demonstrates a weakness in the PINE-1B detection system. Since the specific surface area concentration range needed for accurate measurements will depend on the INA of the measured sample and the temperature of measurements, when making measurements using new materials or conditions, the results should be checked during experiments to ensure that the limits of detection are not being reached. Settings in the Welas OPC can be changed to fit the aims of each given experiment, such as changing the size measurement range. Since this limitation is linked to the measurements and identification of ice crystals in the PINE chamber, alternative methods such as a depolarization detector (Zenker et al., 2017) could be used to distinguish between ice crystals, liquid droplets and aerosol particles in the PINE-1B. However, the addition of alternative detection methods would require a significant redesign of the PINE instrument.

This study also demonstrates the use of PINE to extend the measurements of the  $\mu\text{L-NIPI}$  down to lower temperatures. The results from the PINE-1B were consistent with those from the  $\mu\text{L-NIPI}$  cold stage measurements of the same samples by Fahy et al. (2022) in terms of the changes in INA seen upon ageing of the Fuego and Astroni volcanic ash samples. As shown here, the PINE and  $\mu\text{L-NIPI}$  can be used as complimentary instruments to one another, since the PINE can make measurements at lower temperatures than typically possible with the  $\mu\text{L-NIPI}$  ( $< -25\text{ }^\circ\text{C}$ ) while the  $\mu\text{L-NIPI}$  can make accurate measurements at higher temperatures ( $> -10\text{ }^\circ\text{C}$ ) where the PINE measurements are often

inaccurate due to the low number of ice crystals produced. To allow for the results from different instruments to be clearly compared to one another, future studies using different measurement techniques to measure the same samples should make sure to have measurements at overlapping temperatures. A strength of the PINE is in its ability to make ice nucleation measurements across a wide range of temperatures ( $\sim -10$  to  $-35$  °C) and future measurements using the PINE should endeavour to make full use of this temperature range to characterise INAs across a wide range of temperatures and allow for the best comparisons with measurements from other instruments, like the results for high-latitude mineral dusts shown in chapter 3 of this thesis.

#### 4.6 Appendix

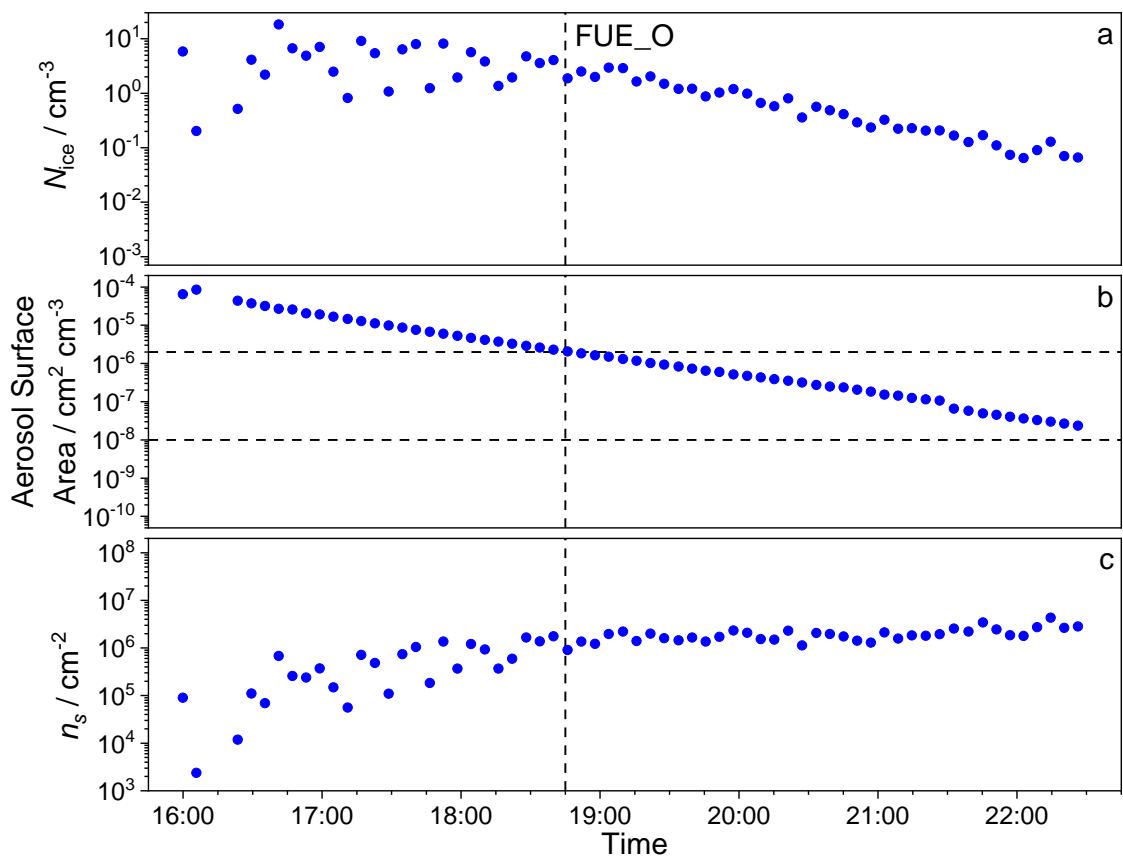


**Figure 4.11:** Same as Figure 4.7 but for unaged Fuego volcanic ash.

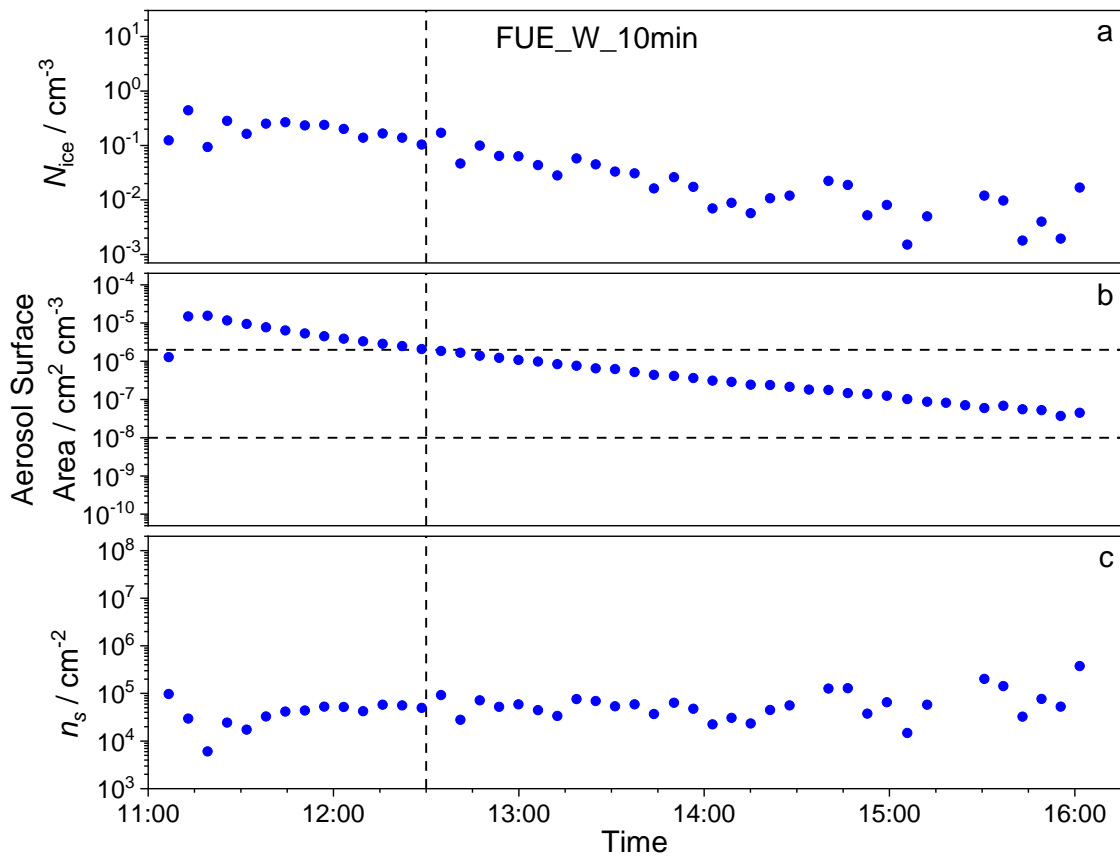


**Figure 4.12:** Same as Figure 4.7 but for 10-minute water-aged volcanic ash.

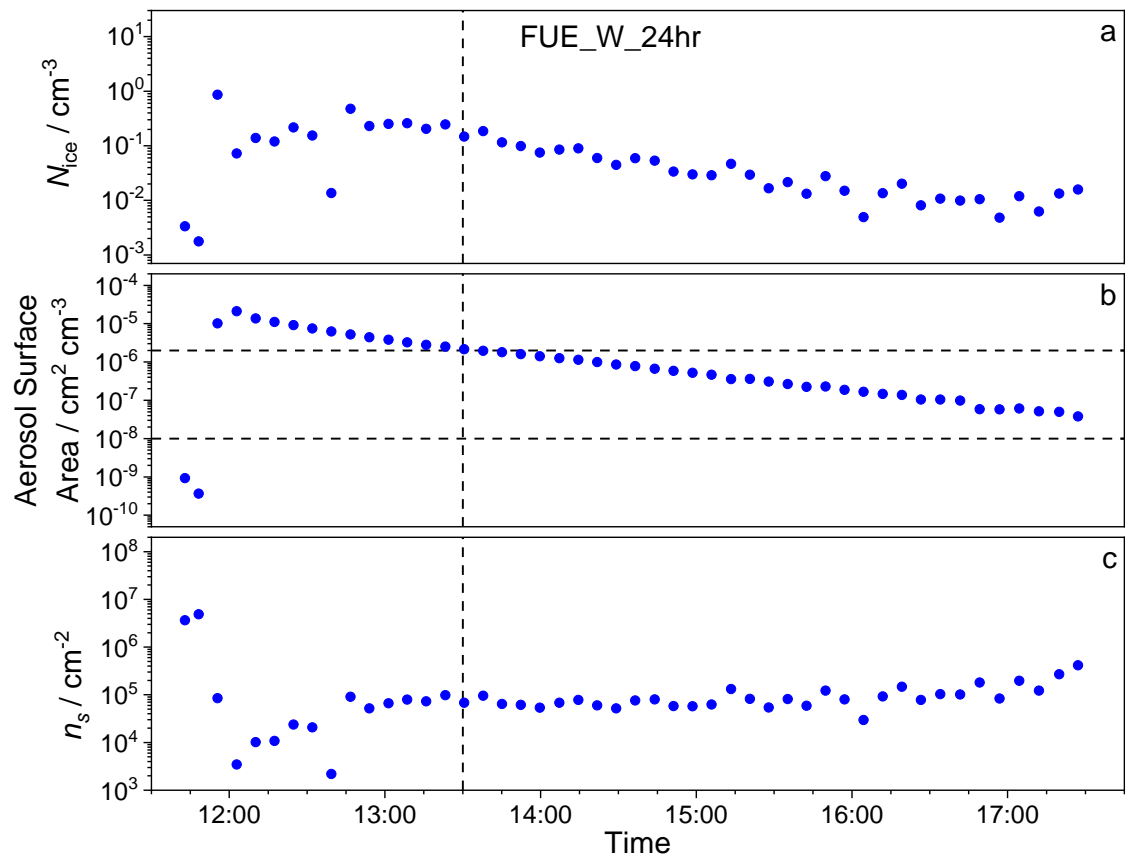


**Figure 4.13:** Same as Figure 4.7 but for 24-hour water-aged Fuego volcanic ash.

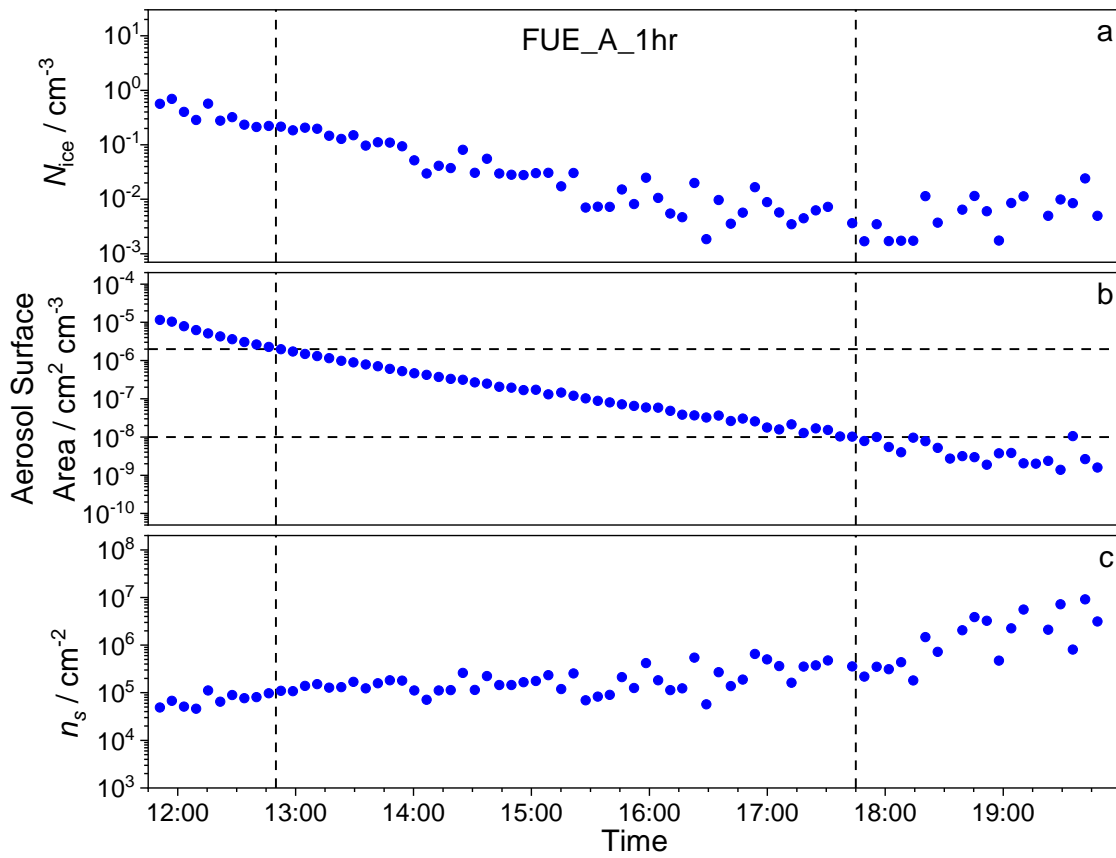


**Figure 4.14:** Same as Figure 4.7 but for 1-hour acid-aged Fuego volcanic ash.

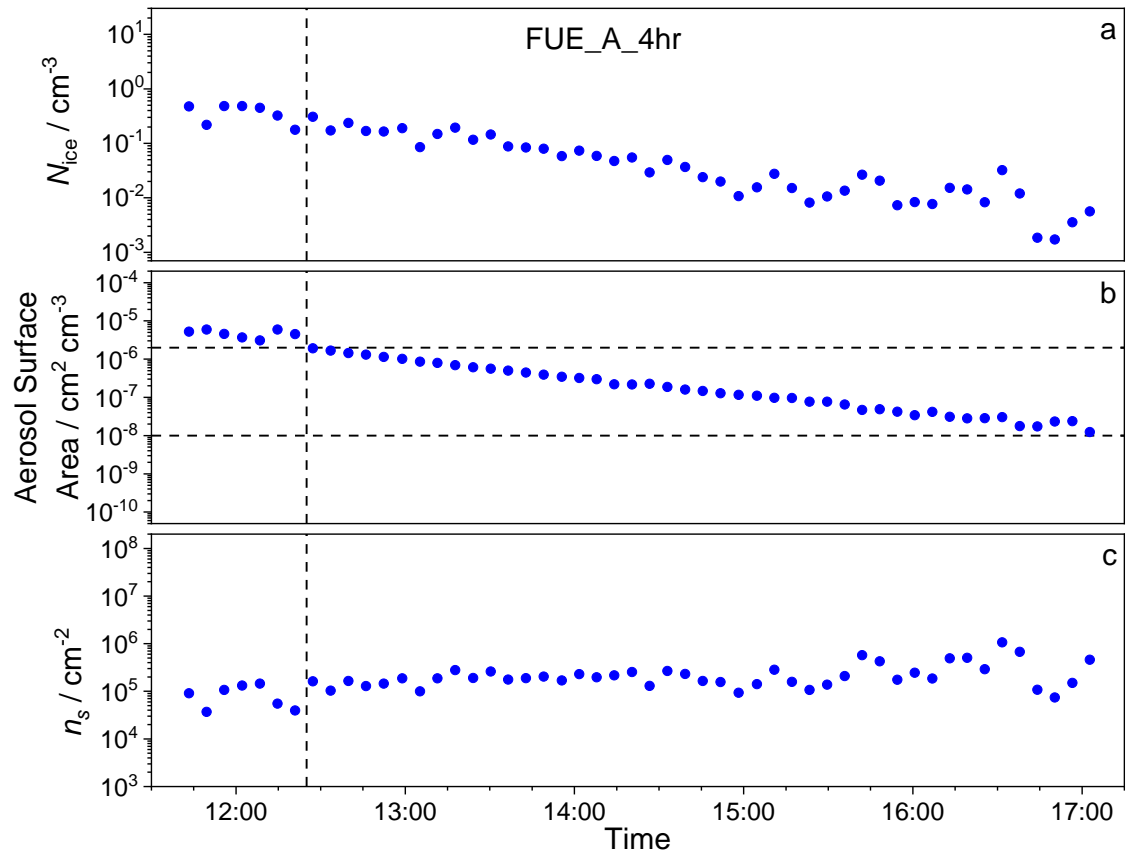


**Figure 4.15:** Same as Figure 4.7 but for 4-hour acid-aged Fuego volcanic ash.

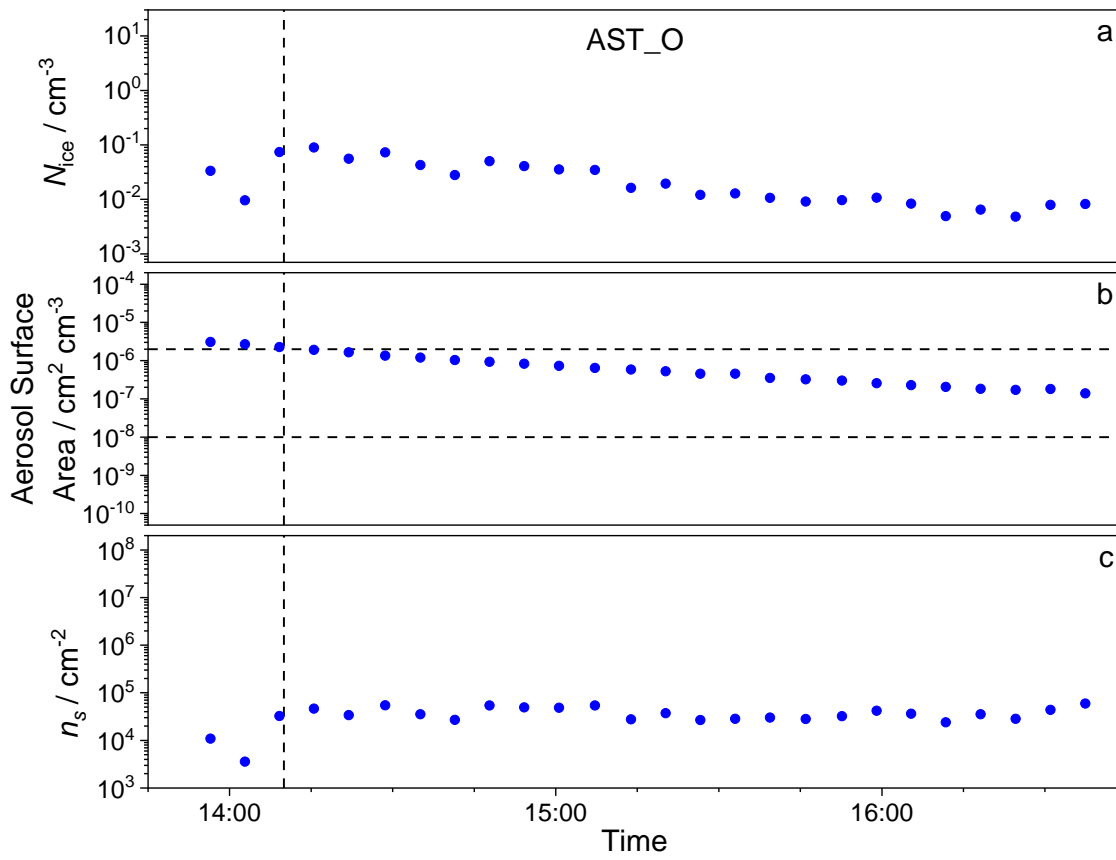


**Figure 4.16:** Same as Figure 4.7 but for unaged Astroni volcanic ash.

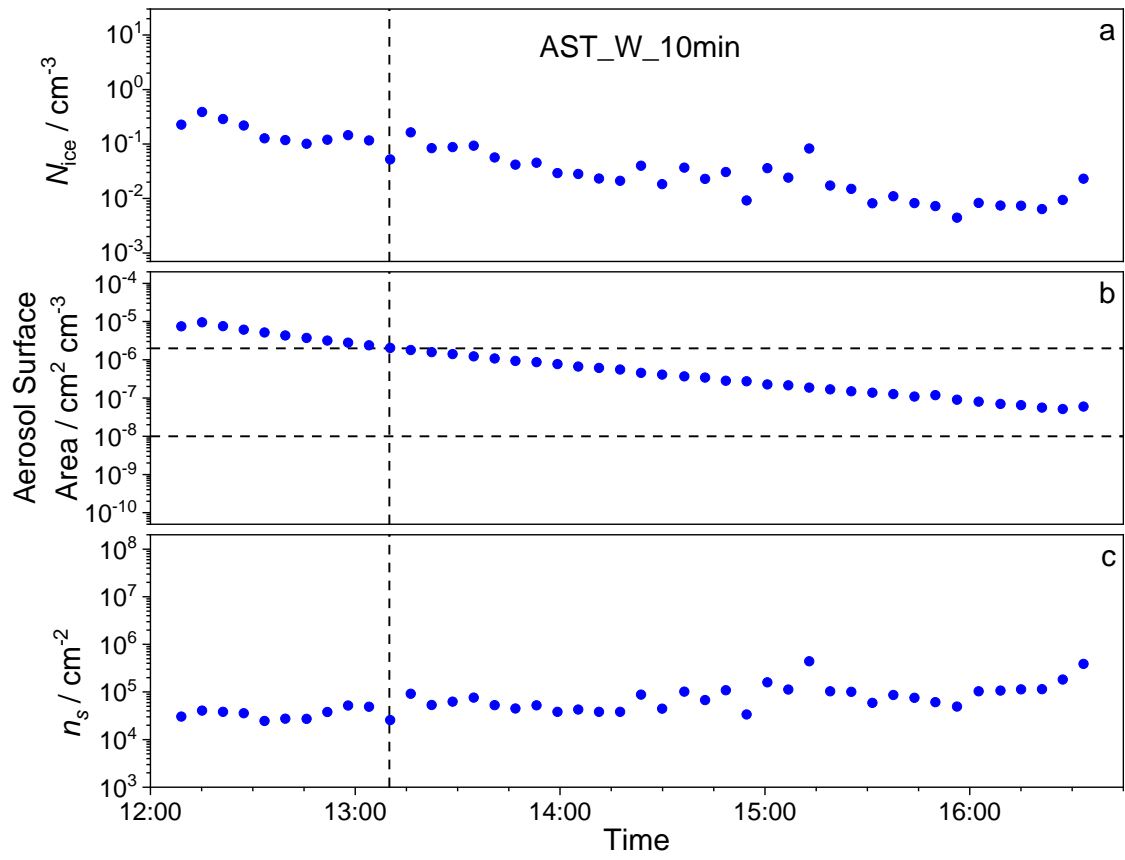


**Figure 4.17:** Same as Figure 4.7 but for 10-minute water-aged Astroni volcanic ash.

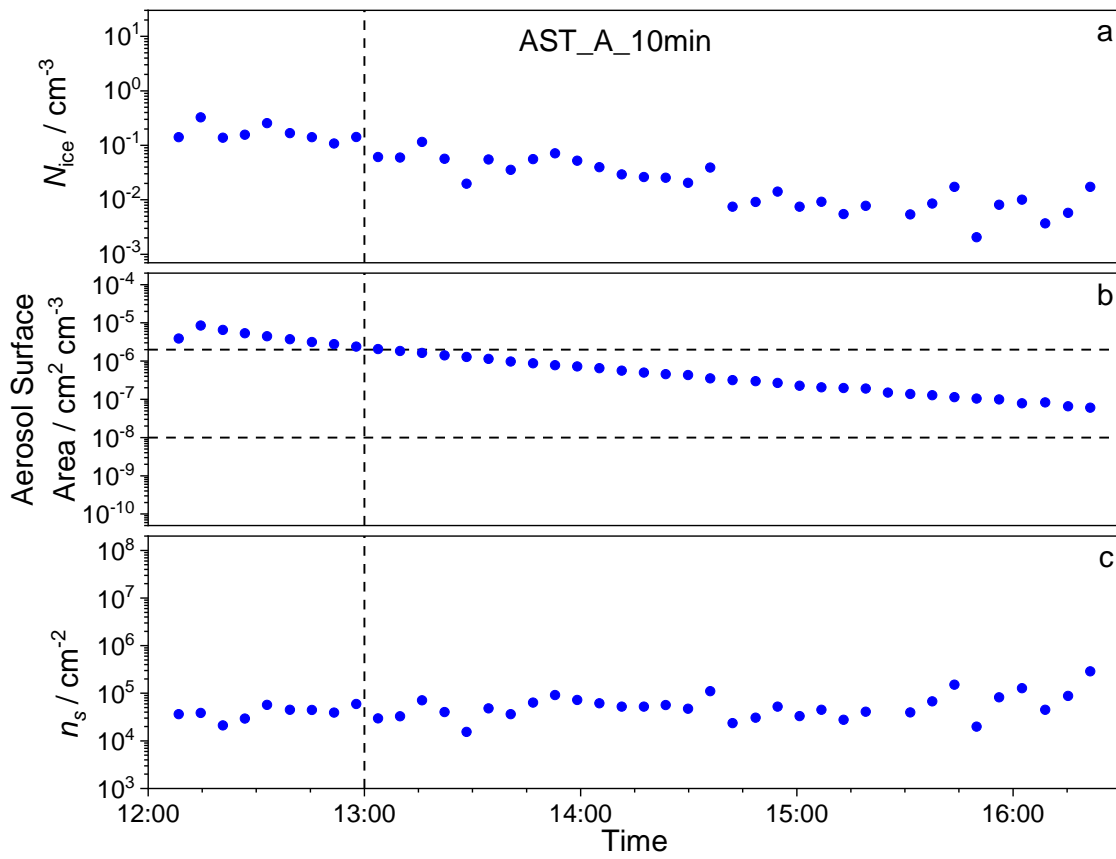
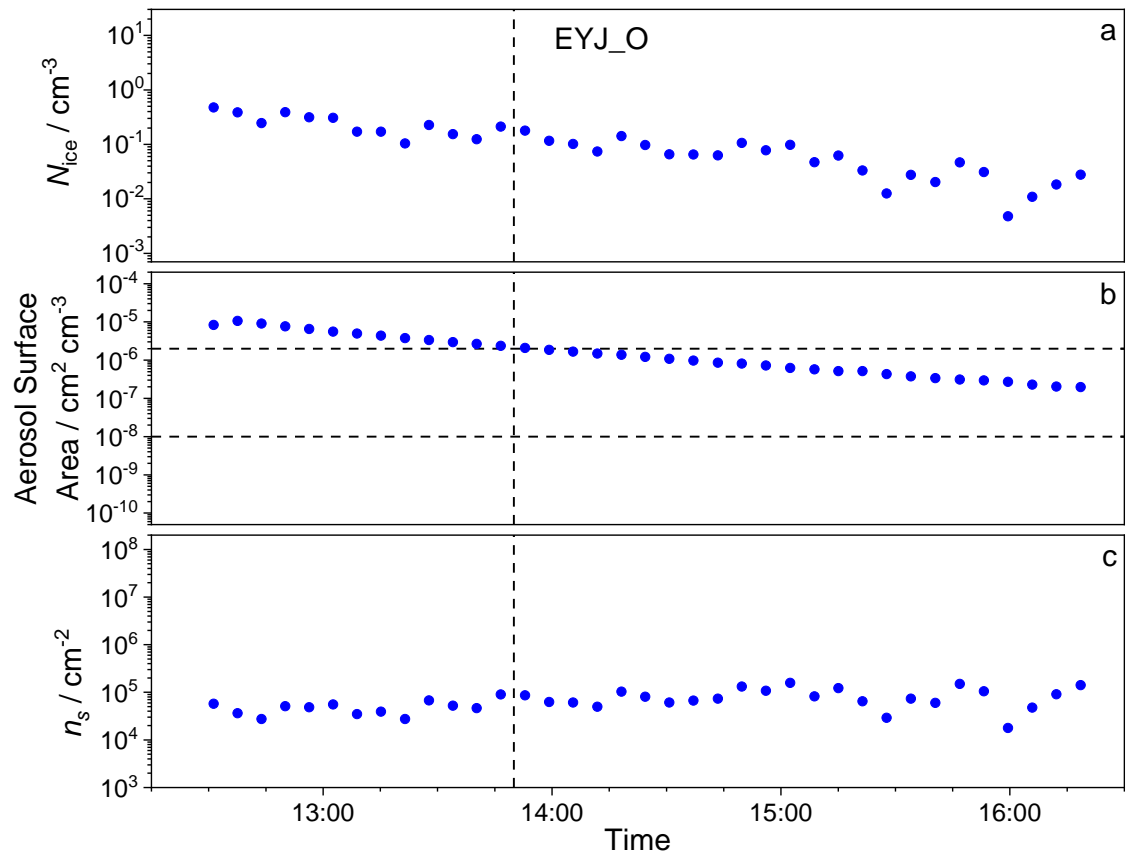


Figure 4.18: Same as Figure 4.7 but for 10-minute acid-aged volcanic ash.



**Figure 4.19:** Same as Figure 4.7 but for unaged Eyjafjallajökull volcanic ash.

## 4.7 References

- Barr, S. L., Wyld, B., McQuaid, J. B., Neely, R. R. and Murray, B. J.: Southern Alaska as a source of atmospheric mineral dust and ice-nucleating particles, *Sci. Adv.*, 9(33), eadg3708, doi:10.1126/sciadv.adg3708, 2023.
- Delmelle, P., Lambert, M., Dufrêne, Y., Gerin, P. and Óskarsson, N.: Gas/aerosol-ash interaction in volcanic plumes: New insights from surface analyses of fine ash particles, *Earth Planet. Sci. Lett.*, 259(1–2), 159–170, doi:10.1016/j.epsl.2007.04.052, 2007.
- Durant, A. J., Shaw, R. A., Rose, W. I., Mi, Y. and Ernst, G. G. J.: Ice nucleation and overseeding of ice in volcanic clouds, *J. Geophys. Res. Atmos.*, 113(9), 9206, doi:10.1029/2007JD009064, 2008.
- Durant, A. J., Bonadonna, C. and Horwell, C. J.: Atmospheric and environmental impacts of volcanic particulates, *Elements*, 6(4), 235–240, doi:10.2113/gselements.6.4.235, 2010.
- Engwell, S. and Eychenne, J.: Contribution of Fine Ash to the Atmosphere From Plumes Associated With Pyroclastic Density Currents, in *Volcanic Ash: Hazard Observation*, pp. 68–85, Elsevier., 2016.
- Fahy, W. D., Maters, E. C., Giese Miranda, R., Adams, M. P., Jahn, L. G., Sullivan, R. C. and Murray, B. J.: Volcanic ash ice nucleation activity is variably reduced by aging in water and sulfuric acid: the effects of leaching, dissolution, and precipitation, *Environ. Sci. Atmos.*, 2(1), 85–99, doi:10.1039/D1EA00071C, 2022.
- Genareau, K., Cloer, S. M., Primm, K., Tolbert, M. A. and Woods, T. W.: Compositional and mineralogical effects on ice nucleation activity of volcanic ash, *Atmosphere (Basel)*, 9(7), 238, doi:10.3390/atmos9070238, 2018.
- Glaze, L. S., Baloga, S. M. and Wilson, L.: Transport of atmospheric water vapor by volcanic eruption columns, *J. Geophys. Res. Atmos.*, 102(5), 6099–6108, doi:10.1029/96jd03125, 1997.
- Grawe, S., Augustin-Bauditz, S., Clemen, H. C., Ebert, M., Eriksen Hammer, S., Lubitz, J., Reicher, N., Rudich, Y., Schneider, J., Staacke, R., Stratmann, F., Welti, A. and Wex, H.: Coal fly ash: Linking immersion freezing behavior and physicochemical particle properties, *Atmos. Chem. Phys.*, 18(19), 13903–13923, doi:10.5194/acp-18-13903-2018, 2018.

- Herbert, R. J., Murray, B. J., Whale, T. F., Dobbie, S. J. and Atkinson, J. D.: Representing time-dependent freezing behaviour in immersion mode ice nucleation, *Atmos. Chem. Phys.*, 14(16), 8501–8520, doi:10.5194/acp-14-8501-2014, 2014.
- Herzog, M., Graf, H. F., Textor, C. and Oberhuber, J. M.: The effect of phase changes of water on the development of volcanic plumes, *J. Volcanol. Geotherm. Res.*, 87(1–4), 55–74, doi:10.1016/S0377-0273(98)00100-0, 1998.
- Hobbs, P. V., Fullerton, C. M. and Bluhm, G. C.: Ice Nucleus Storms in Hawaii, *Nat. Phys. Sci.*, 230(12), 90–91, doi:10.1038/physci230090a0, 1971.
- Hoyle, C. R., Pinti, V., Welti, A., Zobrist, B., Marcolli, C., Luo, B., Höskuldsson, Á., Mattsson, H. B., Stetzer, O., Thorsteinsson, T., Larsen, G. and Peter, T.: Ice nucleation properties of volcanic ash from Eyjafjallajökull, *Atmos. Chem. Phys.*, 11(18), 9911–9926, doi:10.5194/acp-11-9911-2011, 2011.
- Isono, K., Komabayasi, M. and Ono, A.: Volcanoes as a source of atmospheric ice nuclei, *Nature*, 183(4657), 317–318, doi:10.1038/183317a0, 1959.
- Jahn, L. G., Fahy, W. D., Williams, D. B. and Sullivan, R. C.: Role of Feldspar and Pyroxene Minerals in the Ice Nucleating Ability of Three Volcanic Ashes, *ACS Earth Sp. Chem.*, 3(4), 626–636, doi:10.1021/acsearthspacechem.9b00004, 2019.
- Kumar, A., Marcolli, C. and Peter, T.: Ice nucleation activity of silicates and aluminosilicates in pure water and aqueous solutions-Part 3: Aluminosilicates, *Atmos. Chem. Phys.*, 19(9), 6059–6084, doi:10.5194/acp-19-6059-2019, 2019.
- Le Maitre, R. W., Bateman, P., Dudek, A., Keller, J., Lameyre, J., Le Bas, M. J., Sabine, P. A., Schmit, R., Sorensen, H., Streckeisen, A., Woolley, A. R. and Zanettin, B.: A classification of Igneous rocks and glossary of terms: recommendations of the International Union of Geological Sciences subcommission on the systematic of igneous rocks, Oxford Blackwell Sci., 193, 1989.
- Mangan, T. P., Atkinson, J. D., Neuberg, J. W., O’Sullivan, D., Wilson, T. W., Whale, T. F., Neve, L., Umo, N. S., Malkin, T. L. and Murray, B. J.: Heterogeneous Ice nucleation by soufriere hills volcanic ash immersed in water droplets, *PLoS One*, 12(1), e0169720, doi:10.1371/journal.pone.0169720, 2017.

Maters, E. C., Dingwell, D. B., Cimarelli, C., Müller, D., Whale, T. F. and Murray, B. J.: The importance of crystalline phases in ice nucleation by volcanic ash, *Atmos. Chem. Phys.*, 19(8), 5451–5465, doi:10.5194/acp-19-5451-2019, 2019.

Maters, E. C., Cimarelli, C., Casas, A. S., Dingwell, D. B. and Murray, B. J.: Volcanic ash ice-nucleating activity can be enhanced or depressed by ash-gas interaction in the eruption plume, *Earth Planet. Sci. Lett.*, 551, 116587, doi:10.1016/j.epsl.2020.116587, 2020.

Möhler, O., Benz, S., Saathoff, H., Schnaiter, M., Wagner, R., Schneider, J., Walter, S., Ebert, V. and Wagner, S.: The effect of organic coating on the heterogeneous ice nucleation efficiency of mineral dust aerosols, *Environ. Res. Lett.*, 3(2), 025007, doi:10.1088/1748-9326/3/2/025007, 2008.

Nakagawa, M. and Ohba, T.: Minerals in Volcanic Ash 1: Primary Minerals and Volcanic Glass, *Glob. Environ. Res.*, 6(October), 41–51 [online] Available from: <http://www.airies.or.jp/publication/ger/pdf/06-2-06.pdf>, 2003.

Porter, G. C. E., Sikora, S. N. F., Adams, M. P., Proske, U., Harrison, A. D., Tarn, M. D., Brooks, I. M. and Murray, B. J.: Resolving the size of ice-nucleating particles with a balloon deployable aerosol sampler: the SHARK, *Atmos. Meas. Tech.*, 13(6), 2905–2921, doi:10.5194/amt-13-2905-2020, 2020.

Reicher, N., Segev, L. and Rudich, Y.: The Welzmann Supercooled Droplets Observation on a Microarray (WISDOM) and application for ambient dust, *Atmos. Meas. Tech.*, 11(1), 233–248, doi:10.5194/amt-11-233-2018, 2018.

Schill, G. P., Genareau, K. and Tolbert, M. A.: Deposition and immersion-mode nucleation of ice by three distinct samples of volcanic ash, *Atmos. Chem. Phys.*, 15(13), 7523–7536, doi:10.5194/acp-15-7523-2015, 2015.

Sparks, R. S. J.: The dimensions and dynamics of volcanic eruption columns, *Bull. Volcanol.*, 48(1), 3–15, doi:10.1007/BF01073509, 1986.

Steinke, I., Möhler, O., Kiselev, A., Niemand, M., Saathoff, H., Schnaiter, M., Skrotzki, J., Hoose, C. and Leisner, T.: Ice nucleation properties of fine ash particles from the Eyjafjallajökull eruption in April 2010, *Atmos. Chem. Phys.*, 11(24), 12945–12958, doi:10.5194/acp-11-12945-2011, 2011.

Textor, C., Graf, H. F., Herzog, M. and Oberhuber, J. M.: Injection of gases into the stratosphere by explosive volcanic eruptions, *J. Geophys. Res. Atmos.*, 108(19), doi:10.1029/2002jd002987, 2003.

TSI: Model 390069 Data Merge Software Module for Merging and Fitting of SMPS and APS Data Files User's Guide, 2011.

Vernier, J. P., Fairlie, T. D., Deshler, T., Natarajan, M., Knepp, T., Foster, K., Wienhold, F. G., Bedka, K. M., Thomason, L. and Trepte, C.: In situ and space-based observations of the Kelud volcanic plume: The persistence of ash in the lower stratosphere, *J. Geophys. Res.*, 121(18), 11,104-11,118, doi:10.1002/2016JD025344, 2016.

Williams, S. N. and Self, S.: The October 1902 plinian eruption of Santa Maria volcano, Guatemala, *J. Volcanol. Geotherm. Res.*, 16(1–2), 33–56, doi:10.1016/0377-0273(83)90083-5, 1983.

Woods, A. W.: Moist convection and the injection of volcanic ash into the atmosphere, *J. Geophys. Res.*, 98(B10), doi:10.1029/93jb00718, 1993.

Wright, H. M. N., Cashman, K. V., Mothes, P. A., Hall, M. L., Ruiz, A. G. and Le Pennec, J. L.: Estimating rates of decompression from textures of erupted ash particles produced by 1999-2006 eruptions of Tungurahua volcano, Ecuador, *Geology*, 40(7), 619–622, doi:10.1130/G32948.1, 2012.

Zenker, J., Collier, K. N., Xu, G., Yang, P., Levin, E. J. T., Suski, K. J., DeMott, P. J. and Brooks, S. D.: Using depolarization to quantify ice nucleating particle concentrations: a new method, *Atmos. Meas. Tech.*, 10(12), 4639–4657, doi:10.5194/amt-10-4639-2017, 2017.

## 5 Conclusions

### 5.1 Overview

INPs can affect the optical properties and lifetime of clouds (Lohmann and Feichter, 2005) by causing cloud droplets to heterogeneously freeze at warmer temperatures than they otherwise would, so an understanding of the sources and concentrations of INPs as well as the temperatures at which they are active is needed to accurately model the CRE. There are many different types and sources of INPs which can be active at different temperatures (Kanji et al., 2017; Murray et al., 2012), so we need to characterise the INAs of these different INP types to know which may be capable of heterogeneously nucleating ice in the atmosphere. The overarching aim of this thesis was to improve our understanding of specific types of ice-nucleating particles through laboratory experiments. To achieve this aim, three key objectives were outlined: 1) use and develop tools (PINE-1B) for measuring ice nucleation; 2) use these tools to characterise the ice-nucleating activity of high-latitude mineral dusts across a range of temperatures relevant for mixed-phase clouds; 3) use these tools to characterise the ice-nucleating activity of volcanic ash and the effect of aging processes. These objectives were met in chapters 2, 3 and 4 respectively.

#### 5.1.1 Objective 1: The use and development of tools and methods for measuring ice nucleation – the PINE-1B instrument

There are many different instruments and methods used to measure ice nucleation, with each method having advantages and disadvantages. The PINE is one of the newer instruments in this space (Möhler et al., 2021), and as such its development is still ongoing and new methods for using it are still being explored. The PINE offers advantages over other instruments used to measure ice nucleation, in particular its portability and capability to autonomously and continuously measure INP concentrations for periods of weeks to months (Brasseur et al., 2022; Lacher et al., 2024) make it an ideal instrument for measuring ambient INP concentrations around the world. However, the temperature gradient across the vertical length of the PINE's expansion chamber leads to an uncertainty in identifying the temperature relevant for the ice nucleation processes which occur in the chamber during expansions. To improve the accuracy of the measurements made with PINE, in chapter 2 of this thesis the PINE-1B, a prototype model of the PINE instrument, was characterised in terms of its temperature during expansions by observing well-defined phase changes which occur inside the PINE-1B chamber during expansions.

The first phase change explored was the activation of aerosol particles to cloud droplets or the homogeneous freezing of haze droplets if the temperature was cold enough, which were measured using smoke and citric acid as test aerosols. The time at which cloud particles began to form during expansions was determined based upon the size and concentration of particles measured by the PINE's OPC, and the  $RH_i$  in the chamber at that time was calculated using the pressure measurement. Previous studies using PINE have assumed the coldest thermocouple to be representative of the nucleation processes occurring in the PINE chamber during expansions (Möhler et al., 2021). However, the results from the measurements of cloud droplet activation (shown in Figure 2.4) showed that, when using the coldest thermocouple measurement to represent the temperature, the calculated  $RH_i$  was far below water saturation, where cloud droplet activation would be expected to occur. Instead, it was found that using the adiabatic temperature, calculated using the coldest thermocouple measurement at the start of each expansion and the pressure measurement, resulted in  $RH_i$  values consistent with water saturation at the time of cloud droplet activation at temperatures between -5 and -35 °C. Similarly, the homogeneous freezing of haze droplets, which is expected to occur at conditions according to Koop et al. (2000), was found to be best represented by calculating the adiabatic temperature during PINE-1B expansions. The use of adiabatic temperature to represent the temperature inside the PINE chamber assumes that there is negligible heat influx from the chamber walls, however it is expected that after enough time this heat influx would begin to have a noticeable effect and so the accuracy of using the adiabatic temperature is likely dependent on the speed and length of expansions. Test measurements were done to investigate this dependence by measuring the cloud droplet activation of citric acid aerosol at different expansion flow rates. The results of these tests showed that at expansion flow rates of 2 slpm and slower the adiabatic temperature was no longer consistent with the expected conditions of water saturation and therefore no longer accurate. Based upon these tests, an expansion flow rate of 4 slpm was decided as the best flow rate to use to ensure that the adiabatic assumption remained accurate up to and beyond water saturation conditions.

The second phase change explored was the homogeneous freezing of cloud droplets, which was measured using citric acid test aerosol. Again, the time at which homogeneous nucleation began to occur was determined based upon the size of the particles measured by the OPC. As with the results from the cloud droplet activation measurements, when using the thermocouple temperature measurement, homogeneous nucleation occurred at

temperatures  $\sim 5$  °C higher than would be expected based upon parameterisations and model calculations from previous studies (Espinosa et al., 2016; Koop and Murray, 2016; Tarn et al., 2021) (shown in Figure 2.7). Again, the calculated adiabatic temperature was consistent with the temperatures expected for homogeneous nucleation to occur.

The results from the measurements of the phase changes that occur in the PINE chamber during expansions showed that, for the PINE-1B model, the coldest thermocouple measurement was too warm to accurately represent  $T_{\text{exp}}$ . The results also showed that the calculated adiabatic temperature was an accurate representation of  $T_{\text{exp}}$  under certain experimental conditions, which allows for the temperature inside the PINE chamber relevant for expansion measurements to be determined without having to rely on the thermocouple measurements. To further test the use of the adiabatic temperature as a measure of  $T_{\text{exp}}$  during expansions, the INA of K-feldspar, a mineral known for its high ice-nucleating ability, was measured. When using the adiabatic temperature, most measurements of the INA of K-feldspar were consistent with the parameterisation from Harrison et al. (2019) across a temperature range of  $\sim -18$  to  $-33$  °C, further supporting the accuracy of the adiabatic temperature.

The results of these temperature characterisation tests are specific to the PINE-1B, since the positions of the thermocouples in other PINE models may be in slightly different positions than in the PINE-1B, so the accuracy of the temperature measurements in other PINE models may be better or worse than in the PINE-1B. Therefore, it is recommended that all other PINE models be tested using similar methods to determine the accuracy of their temperature measurements. Also, it is not guaranteed that the adiabatic temperature would be an accurate representation of  $T_{\text{exp}}$ , especially in the commercial PINE models which have a different chamber volume and shape to the PINE-1B, so the characterisation tests would also allow for the accuracy of using the adiabatic temperature in other PINE models to be determined. For future PINE models, improvements should be made to the temperature measurements, for example a measure of temperature across the full vertical length of the chamber would allow for the temperature gradient to be fully measured and the coldest temperature in the chamber during expansions would be more likely to be observed by measurements. Other developments such as cooling the air before it enters the main PINE expansion chamber would reduce the temperature gradient and therefore reduce the temperature uncertainty caused by thermocouple positioning.

The objective of developing tools and methods of measuring ice nucleation was achieved by characterising the temperature in the PINE-1B chamber during expansions and

showing through measurements that the adiabatic temperature can be used to accurately represent the temperature controlling nucleation processes during expansions under certain experimental conditions. The techniques and knowledge developed while achieving this objective were then used to help achieve the remaining two objectives.

### **5.1.2 Objective 2: Use PINE to characterise the ice-nucleating activity of high-latitude mineral dusts across a range of temperatures relevant for mixed-phase clouds**

Many high-latitude locations have been identified as sources of atmospheric mineral dust (Meinander et al., 2022) and it is estimated that high-latitude sources account for 1 % to 5 % of the total dust emissions on Earth (Bullard et al., 2016; Meinander et al., 2022). In recent years, several measurement studies have shown dust from northern high-latitude sources to be capable of heterogeneous ice nucleation (Barr et al., 2023; Paramonov et al., 2018; Porter et al., 2020; Sanchez-Marroquin et al., 2020; Tobo et al., 2019; Xi et al., 2022) and modelling studies have shown that these dusts may contribute to the immersion ice nucleation of mixed phase clouds at locations close to the emission sources and under certain conditions (Barr et al., 2023; Sanchez-Marroquin et al., 2020; Shi et al., 2022). HLDs from the Copper River valley, Alaska, and the Kangerlussuaq valley, Greenland, have previously had their INAs measured using the  $\mu\text{L-NIPI}$  cold stage method at temperatures above  $-25\text{ }^{\circ}\text{C}$  by Barr et al. (2023) and Wyld et al. (in prep), respectively. To expand upon the characterisation of the INA of HLDs, in chapter 3 of this thesis the PINE-1B was used to measure the INA of HLD samples from the Copper River valley and the Kangerlussuaq valley at temperatures between  $\sim -15$  and  $-36\text{ }^{\circ}\text{C}$  to extend the measurement range of HLDs from these sources to homogeneous freezing temperatures while also providing a  $\sim 10\text{ }^{\circ}\text{C}$  overlap between the PINE and previous  $\mu\text{L-NIPI}$  measurements to compare the results from the two different methods.

The INAs of the HLD samples measured by the PINE-1B were similar to one another at temperatures between  $-20$  and  $-25\text{ }^{\circ}\text{C}$  but at temperatures below  $-25\text{ }^{\circ}\text{C}$  the Kangerlussuaq sample had a higher INA by approximately 1 order of magnitude (shown in Figure 3.7). The INA of the Kangerlussuaq sample at temperatures below  $-22\text{ }^{\circ}\text{C}$  was similar to that of the Harrison et al. (2019) parameterisation of K-feldspar scaled to the composition of K-feldspar in the Kangerlussuaq sample as measured by QXRD. However, at temperatures above  $-22\text{ }^{\circ}\text{C}$  the INA of the Kangerlussuaq sample was higher than of any of the mineral components in the sample with characterised INAs, indicating the presence of another type of material in the sample controlling its INA at these temperatures (shown

in Figure 3.8). A similar pattern was seen with the Copper River sample where the INA at temperatures below  $-22\text{ }^{\circ}\text{C}$  was consistent with the mineral components, but at temperatures above  $-22\text{ }^{\circ}\text{C}$  the INA was higher than the mineral components. The INA results from the PINE-1B compared well with the  $\mu\text{L-NIPI}$  measurements of samples from the same locations, with the two methods having overlapping measurements at temperatures between  $\sim -15$  and  $-25\text{ }^{\circ}\text{C}$  (shown in Figure 3.9 and Figure 3.10).

A parameterisation for the INA of HLDs at temperatures between  $-6$  and  $-37.5\text{ }^{\circ}\text{C}$  was produced by combining the PINE-1B and  $\mu\text{L-NIPI}$  measurements. It was assumed that the INAs of the samples were controlled by a combination of a mineral component, which controlled the INA at temperatures below  $\sim -25\text{ }^{\circ}\text{C}$ , and a biogenic component, which controlled the INA at temperatures above  $\sim -25\text{ }^{\circ}\text{C}$ . To describe this behaviour, a scaled version of the Harrison et al. (2019) K-feldspar parameterisation was used to represent the mineral component and a power law function was used to represent the biogenic component. The new parameterisation was fitted individually to the Copper River data and the Kangerlussuaq data (shown in Figure 3.12) and both datasets combined (shown in Figure 3.13) to demonstrate that the parameterisation can be used as a tool to describe the INA of individual HLD sample or an average of multiple different HLDs.

The objective of using PINE to characterise the ice-nucleating activity of high-latitude mineral dusts across a range of temperatures relevant for mixed-phase clouds was met through the PINE-1B measurements of the Copper River and Kangerlussuaq dusts at temperatures between  $-15$  and  $-36\text{ }^{\circ}\text{C}$ . By comparing the PINE-1B results with those from the  $\mu\text{L-NIPI}$ , the temperature range of measurements of the INA of these HLDs was extended to lower temperatures and allowed for a parameterisation to be produced which describes the INA of these HLD samples at temperatures from  $-6$  to  $-37.5\text{ }^{\circ}\text{C}$ . In future work, more HLD samples from different sources such as Antarctica should be measured using both the PINE and  $\mu\text{L-NIPI}$  to characterise their INAs across a wide range of temperatures. The results from these measurements could then be used to fit the parameterisation developed in this study to produce a parameterisation which represents the INA of HLD samples from several locations across the globe. This parameterisation could then be used in climate modelling studies to better represent the impact that HLD may have on clouds and climate, which may become increasingly important as the Earth warms and HLD emissions likely increase (Amino et al., 2021).

### **5.1.3 Objective 3: Use PINE to characterise the ice-nucleating activity of volcanic ash and the effect of aging processes**

Volcanic eruptions can release up to tens of thousands of teragrams of ash (Williams and Self, 1983) and a portion of this ash can persist in the atmosphere for months and potentially affect regional and global climate (Durant et al., 2010; Engwell and Eychenne, 2016; Vernier et al., 2016). Laboratory studies have shown that volcanic ash is capable of heterogeneously nucleating ice in the immersion mode and can have a similar INA to other active mineral dusts (Durant et al., 2008; Jahn et al., 2019; Mangan et al., 2017; Steinke et al., 2011). The INAs of different volcanic ashes have been shown to depend on their mineralogy (Genareau et al., 2018; Maters et al., 2019; Schill et al., 2015), crystallinity (Maters et al., 2019) and their interactions with water and volcanic gases in both the gaseous phase (Maters et al., 2020) and the aqueous phase (Fahy et al., 2022), meaning that predicting the INA of volcanic ashes in the atmosphere may require knowledge of the composition and the atmospheric history of the ashes. A previous study by Fahy et al. (2022) investigated the effects of aqueous-phase water and acid ageing on the INAs of volcanic ash samples from Volcán de Fuego (FUE), Guatemala and Astroni (AST) volcano, Italy. They used the  $\mu\text{L-NIPI}$  to measure the INA of these volcanic ash samples both unaged and aged for various lengths of time up to 120 hours at temperatures between  $-3$  and  $-25$  °C. To extend the temperature range of these measurements, in chapter 4 of this thesis the PINE-1B was used to measure the INA of these same volcanic ash samples and a sample from Eyjafjallajökull (EYJ) volcano, Iceland at a temperature of  $-32$  °C. The trends seen in the PINE-measured INAs of the samples upon ageing were also compared to those from the  $\mu\text{L-NIPI}$  measurements to determine the consistency between the two instruments.

The INA of the unaged FUE ash was over 1 order of magnitude higher than the other two unaged ashes (shown in Figure 4.8), indicating that there were unique ice-active sites on the surface of the FUE ash particles which the other ashes lacked. Upon ageing, the INA of the FUE ash decreased, water ageing resulting in a greater decrease than acid ageing and for both types of ageing the INA increased as ageing time increased. Compared to the FUE ash, the INA of the AST ash did not significantly change upon water or acid ageing. The patterns in the INAs of the different volcanic ash samples and the effects of ageing seen in the PINE-1B measurements at  $-32$  °C were consistent with the  $\mu\text{L-NIPI}$  measurements at temperatures below  $-15$  °C by Fahy et al. (2022) (shown in Figure 4.10).

The objective of using the PINE to characterise the ice-nucleating activity of volcanic ash and the effect of ageing processes was met through the PINE-1B measurements of the FUE, AST and EYJ volcanic ash samples at a consistent temperature of -32 °C. The variability in the INA of volcanic ashes depending on the source of the ash and the type and length of ageing with different compounds shows the complexity of accurately predicting the INA of volcanic ashes in the atmosphere. The use of the PINE-1B to measure the INAs of the volcanic ash samples at -32 °C allowed the measurements from Fahy et al. (2022) to be extended to the lower end of the range of temperature relevant for mixed-phase clouds. However, the lack of temperature variation for the PINE-1B measurements meant that the temperature dependence of the INAs of these volcanic ash samples is still not known for temperatures between -25 and -32 °C. The measurements by Fahy et al. (2022) showed that the relative INAs of the ashes and the effects of ageing were different at different temperatures, highlighting the importance of making measurements across a range of temperatures. Also, if the PINE measurements were made at temperatures down to -15 °C, a better comparison with the  $\mu$ L-NIPI results from Fahy et al. (2022) could have been made, similar to what was shown in chapter 3.

## **5.2 Project conclusions**

This research project has met the aim of improving our understanding of specific types of ice-nucleating particles through laboratory experiments by developing new methods for measuring the INAs of aerosol sample using the PINE-1B instrument in chapter 2. These new methods were then utilised to characterise the INA of high-latitude dusts and volcanic ashes in chapters 3 and 4 respectively. Through the development and use of the PINE-1B throughout this research project, the strengths and weakness of the PINE-1B instrument were highlighted.

### **5.2.1 PINE-1B temperature measurement range and consistency with cold stage measurements**

A key strength of the PINE-1B instrument that was utilised in this project was its ability to make measurements across a wide range of temperatures relevant for immersion mode nucleation. In chapters 2 and 3 measurements of the INAs of mineral dusts were measured at temperatures between -13 and -36 °C, a temperature range of over 20 °C. In chapter 3 this temperature range allowed the results from the PINE-1B to directly be compared with those from the  $\mu$ L-NIPI, which can make more accurate measurements than the PINE-1B

at temperatures above  $-15\text{ }^{\circ}\text{C}$  but also has a lower temperature limit of roughly  $-25\text{ }^{\circ}\text{C}$ . Unfortunately, the PINE-1B measurements of volcanic ashes in chapter 4 were only done at a single temperature, although this allowed for many repeat measurements to be made for each sample, it meant that the temperature dependence of the INAs of the ashes was not known. Future studies using the PINE-1B and similar instruments should endeavour to utilise the full temperature measurement ranges of the instruments to allow for temperature dependencies to be known and enable clear comparisons with other instruments and studies. Aside from just extending one another's temperature ranges, the results from the PINE-1B and  $\mu\text{L-NIPI}$  measurements were also consistent with one another, providing validity to the accuracy of the measurements since previous studies intercomparing INA results from different instruments have not always shown consistency between the instruments (DeMott et al., 2018; Hiranuma et al., 2019; Wex et al., 2015). The results from chapters 3 and 4 of this thesis demonstrated the strength of using multiple different measurement techniques to measure the same materials in order to complement each other, and so future studies characterising the INA of new materials should make an effort to use multiple measurement techniques to allow the results to be compared and combined.

### **5.2.2 Limitations of PINE**

The results in this thesis also highlighted experimental limitations under which the PINE-1B can be used to make accurate measurements of ice crystal number concentrations. Ice crystals in the PINE are distinguished from other particles based upon the size measured by the OPC and so a clear distinction is needed between the ice crystals and other particles in the cloud size distribution measurements to be able to assign a threshold diameter above which all measured particles can be counted as ice crystals. In chapter 3, it was shown that there are temperature limits within which accurate measurements of ice crystal number concentrations can be made, with the specific limits depending on the surface area concentration and the INA of the sample being measured. At temperatures below  $\sim -35\text{ }^{\circ}\text{C}$ , homogeneous nucleation of droplets is expected to begin to occur in the PINE (Herbert et al., 2015; Rosenfeld and Woodley, 2000; Westbrook and Illingworth, 2011) and so immersion mode heterogeneous nucleation cannot be measured since heterogeneously frozen ice crystals cannot be distinguished from those homogeneously frozen. This serves as a lower temperature limit of PINE when making measurements of heterogenous nucleation and is independent from sample surface area concentration and INA. The upper temperature limit is a result of the lower detection limit

of ice crystals produced in the PINE-1B during expansions, for the HLD sample measurements, when the minimum expansion adiabatic temperature was above  $\sim -20$  °C only  $\sim 0$  to 5 ice crystals were measured per expansion resulting in a high uncertainty associated with the counting statistics of the ice crystals. Although multiple expansions at these temperatures could be averaged to produce values with lower uncertainty, there was still an upper temperature limit of  $\sim -14$  °C above which ice crystals were no longer detected during expansions. It can be expected that this temperature limit depends on the surface area concentration and INA of the sample being measured, since at higher concentration or higher sample INA at these higher temperatures the number of ice crystals produced during expansions would be expected to be larger and therefore more would be detected and the number of ice crystals could be measured with statistical significance.

The results in chapter 4 showed that there are also sample concentration limitations outside of which the PINE-1B measurements of ice crystal number concentrations can become inaccurate. In chapter 4, a wide range of sample concentrations were used, and it was found that the aerosol surface area concentration needed to be within the range of  $2 \times 10^{-6}$  to  $1 \times 10^{-8}$   $\text{cm}^2 \text{cm}^{-3}$  to produce accurate ice crystal concentration measurements at a temperature of  $-32$  °C. At lower concentrations, the number of ice crystals measured per expansion was too low ( $\sim 0$  to 10), resulting in a high measurement uncertainty similar to the higher temperature expansions in chapter 3. At aerosol surface area concentrations higher than the defined range, the presence of sample aerosol particles up to  $10 \mu\text{m}$  in diameter potentially interfered with the identification of ice crystals based upon their size, leading to uncertainty in the measurements of ice crystal concentrations. This issue of larger aerosol particles interfering with the ice identification could be address for future measurements with the PINE-1B by using a tool such as an impactor when generating or collecting the aerosol sample to ensure there are no particles above a certain size. Like the temperature limitations found in chapter 3, the specific surface area concentration limits defined in chapter 4 will depend on the sample being measured, since samples with higher INA would produce more ice crystals at a given surface area concentration and so result in a lower concentration limit. The PINE-1B measurement limitations seen in chapters 3 and 4 are a consequence of the method of identifying ice crystals solely based upon the size of particles measured by the Welas OPC at the PINE chamber outlet. To address these limitations, future developments of the PINE instrument should consider additional or alternative methods for identifying ice crystal production in the PINE

chamber, for example a depolarization detector to distinguish the phase of the particles (Zenker et al., 2017).

### 5.3 References

Amino, T., Iizuka, Y., Matoba, S., Shimada, R., Oshima, N., Suzuki, T., Ando, T., Aoki, T. and Fujita, K.: Increasing dust emission from ice free terrain in southeastern Greenland since 2000, *Polar Sci.*, 27, 100599, doi:10.1016/j.polar.2020.100599, 2021.

Barr, S. L., Wyld, B., McQuaid, J. B., Neely, R. R. and Murray, B. J.: Southern Alaska as a source of atmospheric mineral dust and ice-nucleating particles, *Sci. Adv.*, 9(33), eadg3708, doi:10.1126/sciadv.adg3708, 2023.

Brasseur, Z., Castarède, D., Thomson, E. S., Adams, M. P., Drossaert Van Dusseldorp, S., Heikkilä, P., Korhonen, K., Lampilahti, J., Paramonov, M., Schneider, J., Vogel, F., Wu, Y., Abbatt, J. P. D., Atanasova, N. S., Bamford, D. H., Bertozzi, B., Boyer, M., Brus, D., Daily, M. I., Fösig, R., Gute, E., Harrison, A. D., Hietala, P., Höhler, K., Kanji, Z. A., Keskinen, J., Lacher, L., Lampimäki, M., Levula, J., Manninen, A., Nadolny, J., Peltola, M., Porter, G. C. E., Poutanen, P., Proske, U., Schorr, T., Silas Umo, N., Stenszky, J., Virtanen, A., Moisseev, D., Kulmala, M., Murray, B. J., Petäjä, T., Möhler, O. and Duplissy, J.: Measurement report: Introduction to the HyICE-2018 campaign for measurements of ice-nucleating particles and instrument inter-comparison in the Hyytiälä boreal forest, *Atmos. Chem. Phys.*, 22(8), 5117–5145, doi:10.5194/acp-22-5117-2022, 2022.

Bullard, J. E., Baddock, M., Bradwell, T., Crusius, J., Darlington, E., Gaiero, D., Gassó, S., Gisladdottir, G., Hodgkins, R., McCulloch, R., McKenna-Neuman, C., Mockford, T., Stewart, H. and Thorsteinsson, T.: High-latitude dust in the Earth system, *Rev. Geophys.*, 54(2), 447–485, doi:10.1002/2016RG000518, 2016.

DeMott, P. J., Möhler, O., Cziczo, D. J., Hiranuma, N., Petters, M. D., Petters, S. S., Belosi, F., Bingemer, H. G., Brooks, S. D., Budke, C., Burkert-Kohn, M., Collier, K. N., Danielczok, A., Eppers, O., Felgitsch, L., Garimella, S., Grothe, H., Herenz, P., Hill, T. C. J., Höhler, K., Kanji, Z. A., Kiselev, A., Koop, T., Kristensen, T. B., Krüger, K., Kulkarni, G., Levin, E. J. T., Murray, B. J., Nicosia, A., O’Sullivan, D., Peckhaus, A., Polen, M. J., Price, H. C., Reicher, N., Rothenberg, D. A., Rudich, Y., Santachiara, G., Schiebel, T., Schrod, J., Seifried, T. M., Stratmann, F., Sullivan, R. C., Suski, K. J., Szakáll, M., Taylor,

H. P., Ullrich, R., Vergara-Temprado, J., Wagner, R., Whale, T. F., Weber, D., Welti, A., Wilson, T. W., Wolf, M. J. and Zenker, J.: The Fifth International Workshop on Ice Nucleation phase 2 (FIN-02): Laboratory intercomparison of ice nucleation measurements, *Atmos. Meas. Tech.*, 11(11), 6231–6257, doi:10.5194/amt-11-6231-2018, 2018.

Durant, A. J., Shaw, R. A., Rose, W. I., Mi, Y. and Ernst, G. G. J.: Ice nucleation and overseeding of ice in volcanic clouds, *J. Geophys. Res. Atmos.*, 113(9), 9206, doi:10.1029/2007JD009064, 2008.

Durant, A. J., Bonadonna, C. and Horwell, C. J.: Atmospheric and environmental impacts of volcanic particulates, *Elements*, 6(4), 235–240, doi:10.2113/gselements.6.4.235, 2010.

Engwell, S. and Eychenne, J.: Contribution of Fine Ash to the Atmosphere From Plumes Associated With Pyroclastic Density Currents, in *Volcanic Ash: Hazard Observation*, pp. 68–85, Elsevier., 2016.

Espinosa, J. R., Navarro, C., Sanz, E., Valeriani, C. and Vega, C.: On the time required to freeze water, *J. Chem. Phys.*, 145(21), 211922, doi:10.1063/1.4965427, 2016.

Fahy, W. D., Maters, E. C., Giese Miranda, R., Adams, M. P., Jahn, L. G., Sullivan, R. C. and Murray, B. J.: Volcanic ash ice nucleation activity is variably reduced by aging in water and sulfuric acid: the effects of leaching, dissolution, and precipitation, *Environ. Sci. Atmos.*, 2(1), 85–99, doi:10.1039/D1EA00071C, 2022.

Genareau, K., Cloer, S. M., Primm, K., Tolbert, M. A. and Woods, T. W.: Compositional and mineralogical effects on ice nucleation activity of volcanic ash, *Atmosphere (Basel)*, 9(7), 238, doi:10.3390/atmos9070238, 2018.

Harrison, A. D., Lever, K., Sanchez-Marroquin, A., Holden, M. A., Whale, T. F., Tarn, M. D., McQuaid, J. B. and Murray, B. J.: The ice-nucleating ability of quartz immersed in water and its atmospheric importance compared to K-feldspar, *Atmos. Chem. Phys. Discuss.*, 1–23, doi:10.5194/acp-2019-288, 2019.

Herbert, R. J., Murray, B. J., Dobbie, S. J. and Koop, T.: Sensitivity of liquid clouds to homogenous freezing parameterizations, *Geophys. Res. Lett.*, 42(5), 1599–1605, doi:10.1002/2014GL062729, 2015.

Hiranuma, N., Adachi, K., Bell, D., Belosi, F., Beydoun, H., Bhaduri, B., Bingemer, H., Budke, C., Clemen, H. C., Conen, F., Cory, K., Curtius, J., Demott, P., Eppers, O., Grawe,

S., Hartmann, S., Hoffmann, N., Höhler, K., Jantsch, E., Kiselev, A., Koop, T., Kulkarni, G., Mayer, A., Murakami, M., Murray, B., Nicosia, A., Petters, M., Piazza, M., Polen, M., Reicher, N., Rudich, Y., Saito, A., Santachiara, G., Schiebel, T., Schill, G., Schneider, J., Segev, L., Stopelli, E., Sullivan, R., Suski, K., Szakall, M., Tajiri, T., Taylor, H., Tobo, Y., Ullrich, R., Weber, D., Wex, H., Whale, T., Whiteside, C., Yamashita, K., Zelenyuk, A. and Möhler, O.: A comprehensive characterization of ice nucleation by three different types of cellulose particles immersed in water, *Atmos. Chem. Phys.*, 19(7), 4823–4849, doi:10.5194/acp-19-4823-2019, 2019.

Jahn, L. G., Fahy, W. D., Williams, D. B. and Sullivan, R. C.: Role of Feldspar and Pyroxene Minerals in the Ice Nucleating Ability of Three Volcanic Ashes, *ACS Earth Sp. Chem.*, 3(4), 626–636, doi:10.1021/acsearthspacechem.9b00004, 2019.

Kanji, Z. A., Ladino, L. A., Wex, H., Boose, Y., Burkert-Kohn, M., Cziczo, D. J. and Krämer, M.: Overview of Ice Nucleating Particles, *Meteorol. Monogr.*, 58, 1.1-1.33, doi:10.1175/amsmonographs-d-16-0006.1, 2017.

Koop, T. and Murray, B. J.: A physically constrained classical description of the homogeneous nucleation of ice in water, *J. Chem. Phys.*, 145(21), 211915, doi:10.1063/1.4962355, 2016.

Koop, T., Luo, B., Tsias, A. and Peter, T.: Water activity as the determinant for homogeneous ice nucleation in aqueous solutions, *Nature*, 406(6796), 611–614, doi:10.1038/35020537, 2000.

Lacher, L., Adams, M. P., Barry, K., Bertozzi, B., Bingemer, H., Boffo, C., Bras, Y., Büttner, N., Castarede, D., Cziczo, D. J., DeMott, P. J., Fösig, R., Goodell, M., Höhler, K., Hill, T. C. J., Jentsch, C., Ladino, L. A., Levin, E. J. T., Mertes, S., Möhler, O., Moore, K. A., Murray, B. J., Nadolny, J., Pfeuffer, T., Picard, D., Ramírez-Romero, C., Ribeiro, M., Richter, S., Schrod, J., Sellegri, K., Stratmann, F., Swanson, B. E., Thomson, E. S., Wex, H., Wolf, M. J. and Freney, E.: The Puy de Dôme ICe Nucleation Intercomparison Campaign (PICNIC): comparison between online and offline methods in ambient air, *Atmos. Chem. Phys.*, 24(4), 2651–2678, doi:10.5194/acp-24-2651-2024, 2024.

Loeb, N. G., Wielicki, B. A., Doelling, D. R., Smith, G. L., Keyes, D. F., Kato, S., Manalo-Smith, N. and Wong, T.: Toward optimal closure of the Earth's top-of-atmosphere radiation budget, *J. Clim.*, 22(3), 748–766, doi:10.1175/2008JCLI2637.1, 2009.

Lohmann, U. and Feichter, J.: Global indirect aerosol effects: a review, *Atmos. Chem. Phys.*, 5(3), 715–737, doi:10.5194/acp-5-715-2005, 2005.

Mangan, T. P., Atkinson, J. D., Neuberger, J. W., O’Sullivan, D., Wilson, T. W., Whale, T. F., Neve, L., Umo, N. S., Malkin, T. L. and Murray, B. J.: Heterogeneous Ice nucleation by soufriere hills volcanic ash immersed in water droplets, *PLoS One*, 12(1), e0169720, doi:10.1371/journal.pone.0169720, 2017.

Maters, E. C., Dingwell, D. B., Cimarelli, C., Müller, D., Whale, T. F. and Murray, B. J.: The importance of crystalline phases in ice nucleation by volcanic ash, *Atmos. Chem. Phys.*, 19(8), 5451–5465, doi:10.5194/acp-19-5451-2019, 2019.

Maters, E. C., Cimarelli, C., Casas, A. S., Dingwell, D. B. and Murray, B. J.: Volcanic ash ice-nucleating activity can be enhanced or depressed by ash-gas interaction in the eruption plume, *Earth Planet. Sci. Lett.*, 551, 116587, doi:10.1016/j.epsl.2020.116587, 2020.

Meinander, O., Dagsson-Waldhauserova, P., Amosov, P., Aseyeva, E., Atkins, C., Baklanov, A., Baldo, C., Barr, S. L., Barzycka, B., Benning, L. G., Cvetkovic, B., Enchilik, P., Frolov, D., Gassó, S., Kandler, K., Kasimov, N., Kavan, J., King, J., Koroleva, T., Krupskaya, V., Kulmala, M., Kusiak, M., Lappalainen, H. K., Laska, M., Lasne, J., Lewandowski, M., Luks, B., McQuaid, J. B., Moroni, B., Murray, B., Möhler, O., Nawrot, A., Nickovic, S., O’Neill, N. T., Pejanovic, G., Popovicheva, O., Ranjbar, K., Romanias, M., Samonova, O., Sanchez-Marroquin, A., Schepanski, K., Semenov, I., Sharapova, A., Shevnina, E., Shi, Z., Sofiev, M., Thevenet, F., Thorsteinsson, T., Timofeev, M., Umo, N. S., Uppstu, A., Urupina, D., Varga, G., Werner, T., Arnalds, O. and Vukovic Vimic, A.: Newly identified climatically and environmentally significant high-latitude dust sources, *Atmos. Chem. Phys.*, 22(17), 11889–11930, doi:10.5194/acp-22-11889-2022, 2022.

Möhler, O., Adams, M., Lacher, L., Vogel, F., Nadolny, J., Ullrich, R., Boffo, C., Pfeuffer, T., Hobl, A., Weiß, M., Vepuri, H. S. K., Hiranuma, N. and Murray, B. J.: The Portable Ice Nucleation Experiment (PINE): A new online instrument for laboratory studies and automated long-term field observations of ice-nucleating particles, *Atmos. Meas. Tech.*, 14(2), 1143–1166, doi:10.5194/amt-14-1143-2021, 2021.

Murray, B. J., O’Sullivan, D., Atkinson, J. D. and Webb, M. E.: Ice nucleation by particles immersed in supercooled cloud droplets, *Chem. Soc. Rev.*, 41(19), 6519, doi:10.1039/c2cs35200a, 2012.

Paramonov, M., David, R. O., Kretzschmar, R. and Kanji, Z. A.: A laboratory investigation of the ice nucleation efficiency of three types of mineral and soil dust, *Atmos. Chem. Phys.*, 18(22), 16515–16536, doi:10.5194/acp-18-16515-2018, 2018.

Porter, G. C. E., Sikora, S. N. F., Adams, M. P., Proske, U., Harrison, A. D., Tarn, M. D., Brooks, I. M. and Murray, B. J.: Resolving the size of ice-nucleating particles with a balloon deployable aerosol sampler: the SHARK, *Atmos. Meas. Tech.*, 13(6), 2905–2921, doi:10.5194/amt-13-2905-2020, 2020.

Rosenfeld, D. and Woodley, W. L.: Deep convective clouds with sustained supercooled liquid water down to - 37.5 °C, *Nature*, 405(6785), 440–442, doi:10.1038/35013030, 2000.

Sanchez-Marroquin, A., Arnalds, O., Baustian-Dorsi, K. J., Browse, J., Dagsson-Waldhauserova, P., Harrison, A. D., Maters, E. C., Pringle, K. J., Vergara-Temprado, J., Burke, I. T., McQuaid, J. B., Carslaw, K. S. and Murray, B. J.: Iceland is an episodic source of atmospheric ice-nucleating particles relevant for mixed-phase clouds, *Sci. Adv.*, 6(26), 8137–8161, doi:10.1126/sciadv.aba8137, 2020.

Schill, G. P., Genareau, K. and Tolbert, M. A.: Deposition and immersion-mode nucleation of ice by three distinct samples of volcanic ash, *Atmos. Chem. Phys.*, 15(13), 7523–7536, doi:10.5194/acp-15-7523-2015, 2015.

Shi, Y., Liu, X., Wu, M., Zhao, X., Ke, Z. and Brown, H.: Relative importance of high-latitude local and long-range-transported dust for Arctic ice-nucleating particles and impacts on Arctic mixed-phase clouds, *Atmos. Chem. Phys.*, 22(4), 2909–2935, doi:10.5194/acp-22-2909-2022, 2022.

Steinke, I., Möhler, O., Kiselev, A., Niemand, M., Saathoff, H., Schnaiter, M., Skrotzki, J., Hoose, C. and Leisner, T.: Ice nucleation properties of fine ash particles from the Eyjafjallajökull eruption in April 2010, *Atmos. Chem. Phys.*, 11(24), 12945–12958, doi:10.5194/acp-11-12945-2011, 2011.

Tarn, M. D., Sikora, S. N. F., Porter, G. C. E., Shim, J. U. and Murray, B. J.: Homogeneous freezing of water using microfluidics, *Micromachines*, 12(2), 1–23, doi:10.3390/mi12020223, 2021.

Tobo, Y., Adachi, K., DeMott, P. J., Hill, T. C. J., Hamilton, D. S., Mahowald, N. M., Nagatsuka, N., Ohata, S., Uetake, J., Kondo, Y. and Koike, M.: Glacially sourced dust as

a potentially significant source of ice nucleating particles, *Nat. Geosci.*, 12(4), 253–258, doi:10.1038/s41561-019-0314-x, 2019.

Vernier, J. P., Fairlie, T. D., Deshler, T., Natarajan, M., Knepp, T., Foster, K., Wienhold, F. G., Bedka, K. M., Thomason, L. and Trepte, C.: In situ and space-based observations of the Kelud volcanic plume: The persistence of ash in the lower stratosphere, *J. Geophys. Res.*, 121(18), 11,104–11,118, doi:10.1002/2016JD025344, 2016.

Westbrook, C. D. and Illingworth, A. J.: Evidence that ice forms primarily in supercooled liquid clouds at temperatures  $>-27^{\circ}\text{C}$ , *Geophys. Res. Lett.*, 38(14), doi:10.1029/2011GL048021, 2011.

Wex, H., Augustin-Bauditz, S., Boose, Y., Budke, C., Curtius, J., Diehl, K., Dreyer, A., Frank, F., Hartmann, S., Hiranuma, N., Jantsch, E., Kanji, Z. A., Kiselev, A., Koop, T., Möhler, O., Niedermeier, D., Nillius, B., Rösch, M., Rose, D., Schmidt, C., Steinke, I. and Stratmann, F.: Intercomparing different devices for the investigation of ice nucleating particles using Snomax® as test substance, *Atmos. Chem. Phys.*, 15(3), 1463–1485, doi:10.5194/acp-15-1463-2015, 2015.

Williams, S. N. and Self, S.: The October 1902 plinian eruption of Santa Maria volcano, Guatemala, *J. Volcanol. Geotherm. Res.*, 16(1–2), 33–56, doi:10.1016/0377-0273(83)90083-5, 1983.

Xi, Y., Xu, C., Downey, A., Stevens, R., Bachelder, J. O., King, J., Hayes, P. L. and Bertram, A. K.: Ice nucleating properties of airborne dust from an actively retreating glacier in Yukon, Canada, *Environ. Sci. Atmos.*, 2(4), 714–726, doi:10.1039/d1ea00101a, 2022.

Zenker, J., Collier, K. N., Xu, G., Yang, P., Levin, E. J. T., Suski, K. J., DeMott, P. J. and Brooks, S. D.: Using depolarization to quantify ice nucleating particle concentrations: a new method, *Atmos. Meas. Tech.*, 10(12), 4639–4657, doi:10.5194/amt-10-4639-2017, 2017.